Nanotechnological Solutions to Combat Malaria

INAUGURALDISSERTATION

zur Erlangung der Würde
eines Doktors der Philosophie
vorgelegt der
Philosophisch-Naturwissenschaftlichen
Fakultät der Universität Basel

von
Adrian Najer
aus Dagmersellen, LU

Basel, 2016

Genehmigt von der Philosophisch-Naturwissenschaftlichen Fakultät
auf Antrag von

Prof. Dr. Wolfgang P. Meier (Universität Basel)
Dissertationsleiter

Prof. Dr. Cornelia G. Palivan (Universität Basel)
Co-Dissertationsleiterin

Prof. Dr. Hans-Peter Beck (Schweizerisches Tropen- und Public Health Institut)
Co-Dissertationsleiter

und

Prof. Dr. Abhay Pandit (National University of Ireland, Galway)
Korreferent

Basel, den 21. Juni 2016

Prof. Dr. Jörg Schibler
Dekan

Nanotechnological Solutions to Combat Malaria

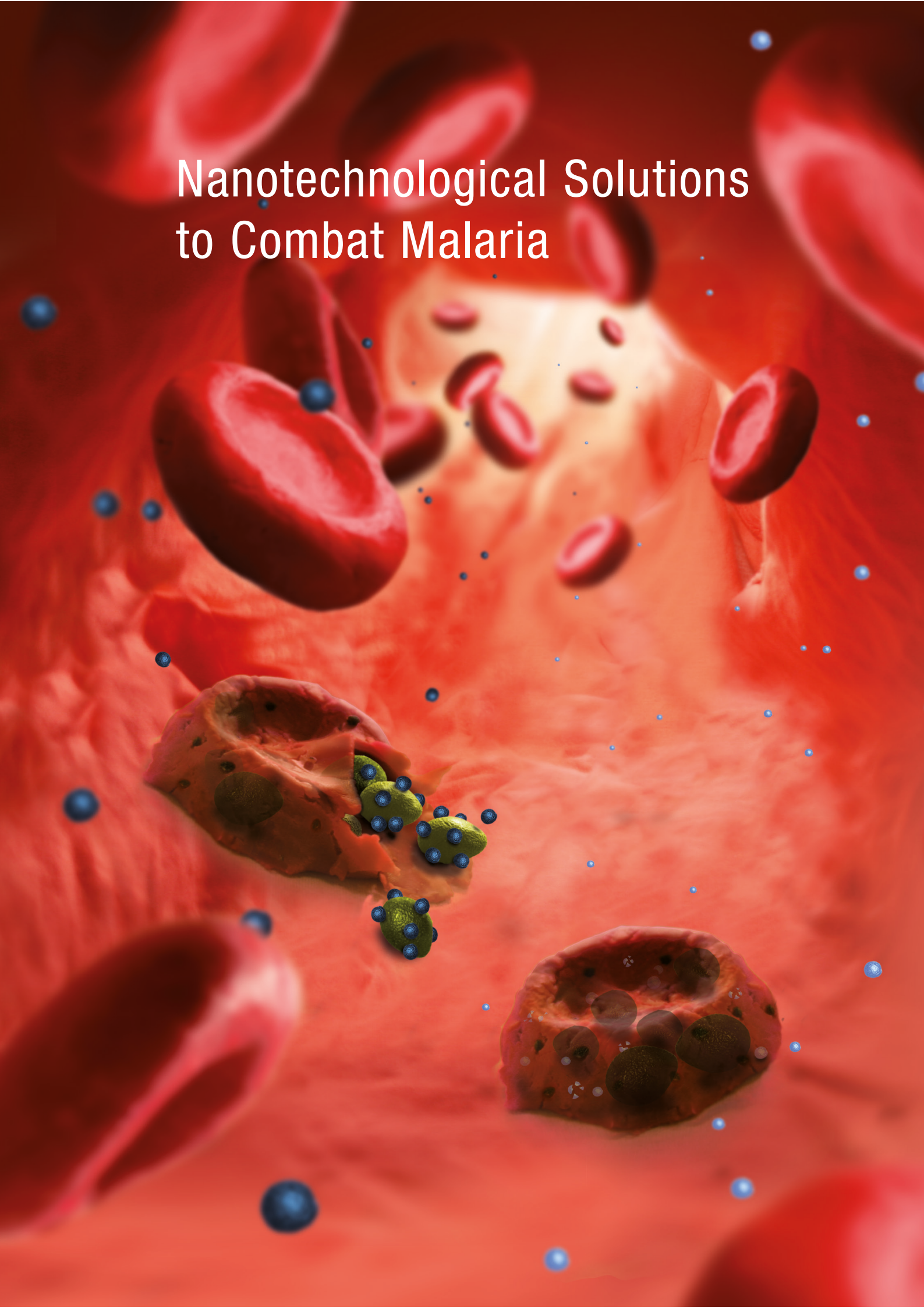

För mini Eltere

SUMMARY

Infectious diseases remain a major cause of death worldwide, despite enormous control efforts. A major problem in the context of antimicrobial drug resistance, which already leads to treatment failures, is the lack of novel antimicrobial drugs. Further, current and future control measures are threatened by the inexistence, unavailability, and failures of vaccines. In this regard, development of novel tools, including new antimicrobial drugs, vaccines, alternative drug/vaccine delivery systems, and other strategies, is urgently needed to keep up the fight against infectious diseases. Malaria is a typical example of an infectious disease to which the above-mentioned problems apply. This disease is caused by *Plasmodium* spp. parasites that are transmitted by *Anopheles* mosquitoes. The life cycle of malaria parasites in humans involves a blood stage cycle that is responsible for disease pathogenesis and includes continuous red blood cell (RBC) invasion, asexual multiplication, and subsequent egress of parasites back into the bloodstream.

In this thesis, two alternative nanotechnological strategies aimed at the malaria blood stage cycle are presented. Both of these strategies are considered valuable alternatives for malaria treatment/prophylaxis compared to conventional drug treatment and experimental vaccination schemes. The first ‘nanomimic strategy’ aims for a dual drug- and "vaccine-like" action using RBC membrane-mimicking nanostructures, termed ‘nanomimics’. The drug action is the inhibition of parasite invasion into RBCs by these nanomimics. "Vaccine-like" activity is achieved through generation of an immune response by exposed extracellular parasites bound to nanomimics as obtained during the drug action. Several amphiphilic block copolymers were designed and synthesized that contain a RBC receptor molecule that is known to be used by the parasite to attach to RBCs. These functional block copolymers were mixed with another type of block copolymer to prepare polymer vesicles (polymersomes) by self-assembly, which served as nanomimics and giant RBC membrane models. Highly potent invasion-inhibitory nanomimics were realized following this procedure as determined by *in vitro* assays using malaria blood stage cultures in suspension. Further analyses revealed

binding of multiple nanomimics to one parasite and multivalent, high-affinity interaction of receptor molecules on nanomimics with a corresponding parasite ligand. Potential adverse effects of nanomimics related to cellular toxicity, anticoagulation property, and endotoxin contamination, were found to be negligible. Preliminary tests on the second "vaccine-like" activity point in a promising direction, but this needs to be further studied in more detail. A potential application of nanomimics is treatment and immune boost for children having one of their first infections, in order to induce protection from subsequent infections. Furthermore, many human pathogens use the same receptor molecule to interact with target cells that is currently presented on the nanomimics prepared in the scope of this thesis. Therefore, the nanomimic strategy has the potential to be directly applied to other infectious diseases, too.

In the second approach, the delivery of a poorly soluble, metabolically instable antimalarial drug candidate to *Plasmodium*-infected RBCs (iRBCs) using functional nanoparticles was examined. For this purpose, a reduction-responsive, degradable, polymeric nanoparticle platform was successfully designed and applied. The highly reducing cytosol environment of iRBCs acts as the trigger for nanoparticle disassembly and subsequent drug release. In contrast, these loaded nanoparticles were stable in extracellular environments. This drug delivery platform is promising in tackling antimalarial resistance, and to deliver any hydrophobic antimicrobial drug candidate at early development stages to corresponding diseased cells.

ZUSAMMENFASSUNG

Infektionskrankheiten gehören immer noch zu den weltweit häufigsten Todesursachen, obwohl enormer Aufwand betrieben wird, sie unter Kontrolle zu bringen. Eines der grössten Probleme stellt das Fehlen neuer Antibiotika dar. Bereits heute führen Antibiotikaresistenzen zu Behandlungsversagen. Zudem bedrohen Inexistenz, mangelnde Verfügbarkeit und ungenügende Wirksamkeit von gewissen Impfstoffen Kontrollstrategien für Infektionskrankheiten. In Zukunft werden dringendst neue Antibiotika, Impfungen, alternative Antibiotika/ Impfstoff-Verteilsysteme und andere Strategien benötigt, um den Kampf gegen Infektionskrankheiten nicht zu verlieren. Malaria ist ein typisches Beispiel einer Infektionskrankheit, die wegen der obengenannten Probleme schwer zu kontrollieren ist. Die Krankheitserreger der Malaria sind *Plasmodium* spp. Parasiten die von Stechmücken der Gattung *Anopheles* übertragen werden. Der Lebenszyklus dieser Parasiten beinhaltet einen Kreislauf im menschlichen Blut, welcher schlussendlich für die Pathogenität dieser Krankheit verantwortlich ist. Dieser Kreislauf im menschlichen Blut charakterisiert sich durch kontinuierliche Invasion von roten Blutkörperchen, asexuelle Vermehrung und anschliessendem Austritt von Parasiten zurück in den Blutstrom.

In dieser Dissertation werden zwei nanotechnologische Strategien vorgestellt, die beide auf den Kreislauf von Malariaparasiten im menschlichen Blut abzielen. Beide Strategien werden als wertvolle Alternativen zu heutigen konventionellen Therapien mit Medikamenten und experimentellen Impfungen zur Malariabehandlung und Prophylaxe in Betracht gezogen. Die erste „Nano-Imitat-Strategie“ zielt auf eine therapeutische und „impfähnliche“ Doppelwirkung ab, wobei Nanostrukturen benutzt werden, die rote Blutkörperchenmembrane imitieren und deswegen auch „Nano-Imitate“ genannt werden. Die therapeutische Wirkung wird erreicht, indem man das Eindringen des Malariaparasiten in seine Wirtszelle (rotes Blutkörperchen) durch die Nano-Imitate blockiert. Die dadurch exponierten Malariaparasiten sollen eine „impfähnliche“ Wirkung erzeugen, indem sie eine Immunantwort auslösen. Dafür wurden zuerst mehrere amphiphile

Block-Copolymere synthetisiert, wobei ein Teil davon ein bekannter Wirtszellrezeptor ist, der von Malariaparasiten benutzt wird um an rote Blutkörperchen anzudocken. Durch das Mischen dieser Block-Copolymere mit einem anderen Block-Copolymer konnten Polymer-Vesikel (Polymersome) mittels Selbstassemblierung hergestellt werden. Diese Polymer-Vesikel fungierten dann als Nano-Imitate und in einer grösseren Version auch als Modelle von roten Blutkörperchen. Dank diesem Vorgehen hat man äusserst potente invasionsblockierende Nano-Imitate erhalten, was man mittels *in vitro*-Tests mit kultivierten Malariaparasiten in Suspension gezeigt hat. Weitere Analysen haben offengelegt, dass mehrere Nano-Imitate an einen Parasiten binden können. Zudem wurden multivalente, hochaffine Interaktionen der Rezeptormoleküle auf den Nano-Imitaten mit den dazugehörigen Parasitenliganden gemessen. Mögliche Nebenwirkungen dieser Nano-Imitate, die durch zelluläre Toxizität, Antikoagulationsaktivität und Endotoxinkontaminierung ausgelöst werden könnten, wurden als vernachlässigbar tief eingestuft. Erste Tests bezüglich der „impfähnlichen" Aktivität weisen in eine vielversprechende Richtung, dies muss aber zuerst im Detail weitergetestet werden. Eine potentielle Anwendung von Nano-Imitaten wäre die Behandlung und Verstärkung der Immunantwort bei Kindern, die eine ihrer ersten Malariainfektion haben, um sie so vor nächsten Infektionen zu schützen. Zudem benützen viele menschliche Krankheitserreger denselben Wirtszellrezeptor, der zurzeit auf unseren Nano-Imitaten präsentiert wird, um mit Wirtszellen zu interagieren. Aus diesem Grund könnten diese Nano-Imitate auch direkt auf andere Infektionskrankheiten angewendet werden.

Die zweite Strategie befasst sich mit einem Medikamenten-Nanoverteilsystem, welches ein schlecht wasserlösliches, metabolisch instabiles Anti-Malaria Medikament spezifisch zu infizierten roten Blutkörperchen bringt. Dieses Nanoverteilsystem besteht aus reduktionssensitiven, abbaubaren Polymer-basierten Nanopartikeln. Das hochreduzierende Zytosol von intrazellulären Malariaparasiten fungiert als Auslöser für den intrazellulären Nanopartikel-Abbau und die dazugehörige Medikamentenfreisetzung. Im Gegensatz dazu sind diese Nanopartikel in extrazellulären Umgebungen stabil. Dieses Medikamenten-Nanoverteilsystem ist eine vielversprechende Plattform, um Resistenzen gegen Malariamedikamente entgegenzuwirken und um gezielt schwerlöslichen Antibiotika, welche sich im Entwicklungsstadium befinden, zu den dazugehörigen befallenen Wirtszellen zu bringen.

CONTENT

Dedication I
Summary III
Zusammenfassung V
Content VII
Abbreviations XI

1 General Introduction 1

1.1 Infectious Diseases: a Contemporary Global Public Health Problem.....1
1.2 Malaria..... 3
1.2.1 Life Cycle of *Plasmodium falciparum* 4
1.2.2 *Plasmodium* Biology: Red Blood Cell Invasion Mechanism 6
1.2.3 Pathogenesis of Malaria and Prophylaxis, Treatment, and Control Strategies..... 9
1.3 Self-Assembled Amphiphilic Copolymers in the Context of Medical Applications 11
1.3.1 Block Copolymers and Self-Assembly Mechanism 11
1.3.2 Polymer Vesicles – Polymersomes 14
1.3.3 Characterization of Nanoassemblies by Fluorescence Correlation Spectroscopy 16
1.3.4 Requirements of Polymer Nanostructures When Used in Medicine 21
1.3.4.1 Biocompatibility and Biodegradability of the Nanostructure Material 22
1.3.4.2 Surface Chemistry 23
1.3.4.3 Size 24
1.3.4.4 Shape 25
1.3.5 A Glimpse at Potential Polymersome Biomedical Applications 25
1.4 Nanotechnology for Infectious Disease Medicine 28
1.4.1 Polymersome-Based Anti-Infectious Strategies 28
1.4.2 Nanotechnological Approaches for Malaria..... 30
1.4.2.1 Antimalarial Drug Delivery..... 30

1.4.2.2 Nanostrategies for Malaria Vaccines....33

2 Motivation and Aim of this Thesis 35

3 Nanomimics of Host Cell Membranes Block Invasion and Expose Invasive Malaria Parasites 39

3.1 Abstract.... 40
3.2 Introduction.... 40
3.3 Results and Discussion....43
3.3.1 Block Copolymer Synthesis....43
3.3.2 Preparation and Characterization of Nanomimics....45
3.3.3 Nanomimics Bind *Plasmodium* Merozoite Proteins Involved in Initial Attachment.... 51
3.3.4 Nanomimics Block Invasion of and Expose *Plasmodium* Merozoites.... 51
3.3.5 Efficacy of Invasion Inhibition by Nanomimics....54
3.4 Conclusions....56

4 Analysis of Molecular Parameters Determining the Antimalarial Activity of Polymer-Based Nanomimics 57

4.1 Abstract....58
4.2 Introduction....58
4.3 Results and Discussion....59
4.3.1 Effect of Amount and Length of Receptor Molecule of Nanomimics on Antimalarial Activity....59
4.3.2 Detailed Analysis of Parasite Protein Interaction with Nanomimics 62
4.3.3 Antimalarial Activity of Modified Nanomimics....64
4.4 Conclusions....67

5 Giant Host Red Blood Cell Membrane Mimicking Polymersomes Bind Parasite Proteins and Malaria Parasites 69

5.1 Abstract....70
5.2 Introduction....70

5.3 Results and Discussion 71
5.3.1 Giant Host RBC Membrane Mimicking Polymersomes Bind *Plasmodium* Proteins 71
5.3.2 Giant Host RBC Membrane Mimicking Polymersomes Bind *Plasmodium* Merozoites 74
5.4 Conclusions 75

6 Further Evaluation of Nanomimics with Respect to Biomedical Applicability 77
6.1 Results and Discussion 77
6.1.1 Anticoagulation Property of Nanomimics 77
6.1.2 Estimation of Endotoxin Contamination 78
6.1.3 *In vivo* Activity and "Vaccine-Like" Action 80

7 An Amphiphilic Graft Copolymer-Based Nanoparticle Platform for Reduction-Responsive Anticancer and Antimalarial Drug Delivery 85
7.1 Abstract 86
7.2 Introduction 86
7.3 Results and Discussion 89
7.3.1 Chemical Structure of Graft Copolymers and Self-Assembly 89
7.3.2 Loading of Various Hydrophobic Model Molecules within Nanoparticles 91
7.3.3 Reduction-Triggered Model Compound Release and Stability of Nanoparticles in Cell Media 92
7.3.4 Drug Delivery to *Plasmodium falciparum*-Infected Red Blood Cells 97
7.4 Conclusions 102

8 Supplementary Experiments on Antimalarial Drug Delivery 103
8.1 Results and Discussion 103
8.1.1 Dye Participation to *Plasmodium*-Infected Red Blood Cells 103
8.1.2 Nanostructure-Based Delivery to *Plasmodium*-Infected Red Blood Cells 104

8.1.3 Additional Data on SHMT Inhibitor Delivery 108

9 General Conclusion and Outlook **111**

10 Experimental Section **115**

11 References **133**

Acknowledgments **149**

Abbreviations

3D-SIM	Super–resolution 3D structured illumination microscopy
ABP	Amphiphilic block copolymer
AIDS	Acquired immunodeficiency syndrome
AMA1	Apical membrane antigen 1
APD	Avalanche photo diode
$CHCl_3$	Chloroform
CLSM	Confocal laser scanning microscopy
CMC	Critical micelle concentration
CPM	Counts per molecule
Cryo-TEM	Cryogenic-transmission electron microscopy
CQ	Chloroquine
CSP	Circumsporozoite protein
D	Diffusion coefficient
DCM	Dichloromethane
DDS	Drug delivery system
D_H	Hydrodynamic diameter
DLE	Drug loading efficiency
DLC	Drug loading content
DLS	Dynamic light scattering
DMF	Dimethylformamide
DMMB	Dimethylmethylene blue
DMSO	Dimethyl sulfoxide
DOX	Doxorubicin
DTT	Dithiothreitol
EBA	Erythrocyte binding antigen
ELISA	Enzyme-linked immunosorbent assay
EPR effect	Enhanced permeation and retention effect
EtOH	Ethanol
f	Ratio
$f_{hydrophilic}$	Hydrophilic to whole copolymer weight ratio
FBS	Fetal bovine serum
FCS	Fluorescence correlation spectroscopy
FCCS	Fluorescence cross-correlation spectroscopy
FTIR	Fourier transform infrared spectroscopy
GPC	Gel permeation chromatography
GPI	Glycosylphosphatidylinositol
GSH	Glutathione
GUV	Giant unilamellar vesicle
$G(\tau)$	Autocorrelation function
$G_x(\tau)$	Cross-correlation function
HeLa cell	Cervical cancer cell from Henrietta Lacks
HIV	Human immunodeficiency virus
HS	Heparan sulfate
iRBC	*Plasmodium*-infected red blood cell
ITO	Indium tin oxide
k_B	Boltzmann constant
K_D	Dissociation constant
kDa	Kilo Dalton
kHz	Kilo Hertz
LAL	Limulus amebocyte lysate
LMWH	Low molecular weight heparin
LPS	Lipopolysaccharide
MCM	Malaria culture medium

MDR	Multiple drug resistance
MeOH	Methanol
MHC	Major histocompatibility complex
MPS	Mononuclear phagocytic system
MTS	3-(4,5-dimethylthiazol-2-yl)-5-(3-carboxymethoxyphenyl)-2-(4-sulfophenyl)-2H-tetrazolium
MWCO	Molecular weight cut-off
N	Number of particles
NA	Numeric aperture
NaOH	Sodium hydroxide
NMR	Nuclear magnetic resonance
NPP	New permeation pathway
OG488-NHS	Oregon Green 488 carboxylic acid, succinimidyl ester, 5-isomer
OmpF	Bacterial outer membrane protein F
PBS	Phosphate buffered saline
PCL	Poly(ε-caprolactone)
PDI	Polydispersity index
PDMS	Poly(dimethylsiloxane)
PEG	Poly(ethylene glycol)
PEO	Poly(ethylene oxide) = poly(ethylene glycol)
*Pf*EMP1	*Plasmodium falciparum* erythrocyte membrane protein 1
*Pf*MSP1$_{42}$	*Plasmodium falciparum* major/merozoite surface protein 1-42
*Pf*RH	Reticulocyte binding-like homologous
PICsome	Polyion complex membrane vesicles
PMOXA	Poly(2-methyl-2-oxazoline)
PMOXA-SH	Thiolated PMOXA
PPCL	Poly(α-pyridyldisulfide-ε-caprolactone)
PPM	Parasite plasma membrane
PQ	Primaquine
PVM	Parasitophorous vacuole membrane
RBC	Red blood cell
RBCM	Red blood cell membrane
RCA	Relative cross-correlation amplitude
R_g	Radius of gyration
R_H	Hydrodynamic radius
ROS	Reactive oxygen species
RPM	Revolutions per minute
RT	Room temperature
SD	Standard deviation
SEC	Size exclusion chromatography
SEM	Standard error of the mean
SHMT	Serine hydroxymethyltransferase
SLS	Static light scattering
SRB	Sulforhodamine B
SUB	Subtilisin-like protease
TEA	Triethylamine
TEM	Transmission electron microscopy
Tfsa	Trifluoromethanesulfonic acid
T_g	Glass transition temperature
THF	Tetrahydrofuran
TVM	Tubovesicular membrane
τ_D	Diffusion time
τ_{trip}	Triplet time
ω_{xy}	Beam waist radius

CHAPTER 1

1 General Introduction

This general introduction provides an overview of some major threats to public health posed by infectious diseases. Malaria is introduced and few biological details relevant to this thesis are given. Specific malaria-related control strategies and accompanying problems are discussed in more detail. Thereafter, self-assembling amphiphilic copolymers are introduced with a specific focus on potential biomedical applications. Finally, nanotechnological approaches, mainly polymer-based systems, for infectious diseases, in particular malaria, are discussed. Contents of the as-yet unpublished parts of this general introduction are being prepared for publication elsewhere.

1.1 Infectious Diseases: a Contemporary Global Public Health Problem

Infectious diseases are a major and continuous threat to human health. Currently, about a quarter of total annual deaths worldwide are attributed to infectious diseases.[1] The main killers being respiratory infections, diarrheal diseases, human immunodeficiency virus (HIV) causing acquired immunodeficiency syndrome (AIDS), tuberculosis, and malaria (Figure 1).[1]

Throughout human history, infectious diseases have had a tremendous impact on civilizations – sometimes even changing the course of history. Some famous, most influential examples of disease outbreaks are the 14th century Black Death (bubonic plague) pandemic in Europe, the 1918 influenza pandemic, and the current HIV/AIDS pandemic.[2] Three main names that should not be missed in the history of infections are Louis Pasteur and Robert Koch, who consolidated the "germ theory" – proposed by Girolamo Fracastoro nearly 350 years earlier – in the late 1870s; a turning point in the history of medicine and the start of the hunt for microbes and the subsequent development of vaccines and antibiotics.[2] Overall, public sanitation, personal hygiene (*e.g.* hand washing), antibiotics, and vaccines

can be considered the main factors that dramatically decreased infant/child mortality during the 20th century and led to human life expectancy being approximately doubled.[3] Nevertheless, infectious diseases remain a contemporary and ongoing challenge to public health, mainly due to the high evolutionary capacity of infectious pathogens that can overcome pressures directed at their elimination quite easily.[1]

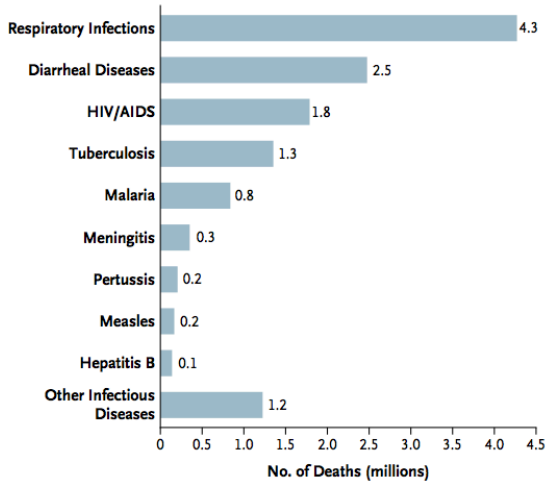

Figure 1. Main infectious diseases causing in total about 15.0 million (26%) deaths of an estimated 58.8 million total global deaths annually. Data does not include secondary infectious causes of death. Reproduced with permission from ref [1]. Copyright (2012) Massachusetts Medical Society.

Recently, the Zika virus pandemic in South/Central America and the 2014 Ebola outbreak in West Africa have received much attention in the mainstream media. However, they are only the tip of the iceberg comprising of all the challenges that are posed by infectious pathogens. In fact, several arthropod-borne viral diseases caused by Dengue, West Nile, Chikungunya, and Zika virus are unexpectedly and rapidly spreading all over the globe at the moment, which highlights the fact that human-caused influences on ecological balances will cause such rapid outbreaks in the future as well.[4] Antibiotic resistance is another, and one of the most worrying examples, demonstrating the necessity for keeping up efforts in infectious disease research and antibiotic development. Systematic misuse and overuse of antibiotics in medicine, but also in food production (veterinary medicine) has caused the current situation.[5] Multiple drug resistant (MDR) pathogens, such as MDR *Staphylococcus aureus*[6] and MDR *Mycobacterium tuberculosis,*[7] are two frightening examples of bacterial pathogens that have become resistant to various antibiotics. MDR tuberculosis affected about 480'000 and killed about 190'000

people in 2014.[8] The recent occurrence and spread of artemisinin-resistant malaria parasites[9] combined with the difficulty in formulating an efficacious malaria vaccine[10] equally represent serious threats to public health (See Chapter 1.2 for more details). This demonstrates the urgency for new antimicrobial drugs or alternative prophylaxis and treatment strategies.[1] To tackle antimicrobial resistance – not only resistant bacteria but also resistant viruses, parasites, and fungi – WHO has recently drafted and published a global action plan, because it is clear that only globally coordinated efforts will have an effect on controlling the spread of antimicrobial resistance.[5] WHO and various leaders in the field strengthen the notion that we might soon enter a post-antibiotic era, if no counteraction is undertaken soon.[5] In a post-antibiotic era, simple infections or injuries might once again lead to death, which is why the overuse of antibiotics *e.g.* in the food sector should be reviewed and changed rapidly.[11] Otherwise, we are in danger of losing the control tools that helped to double our life expectancy,[3] which clearly highlights the relevance and urgency of appropriate countermeasures.

In the context of globalization and climate change, the pattern of infectious disease appearance and distribution will further shift and therefore poses considerable challenges to global human health management.[12] However, the influence of climate change on the occurrence, distribution, and severity of infectious diseases is not predictable, although a shift in vector habitats can clearly spread vector-born diseases to previously disease-free geographic areas.[13] Furthermore, these diseases particularly affect the most vulnerable individuals of a society: children, pregnant women, diseased-, malnourished-, and elderly people. This also highlights an ethical responsibility to boost research on infectious diseases for the development of future control strategies.

1.2 Malaria

Malaria is an infectious disease caused by *Plasmodium* spp. parasites, which are mainly prevalent in developing countries (Figure 2), due to the habitat of their arthropod vector: female *Anopheles* mosquitoes.

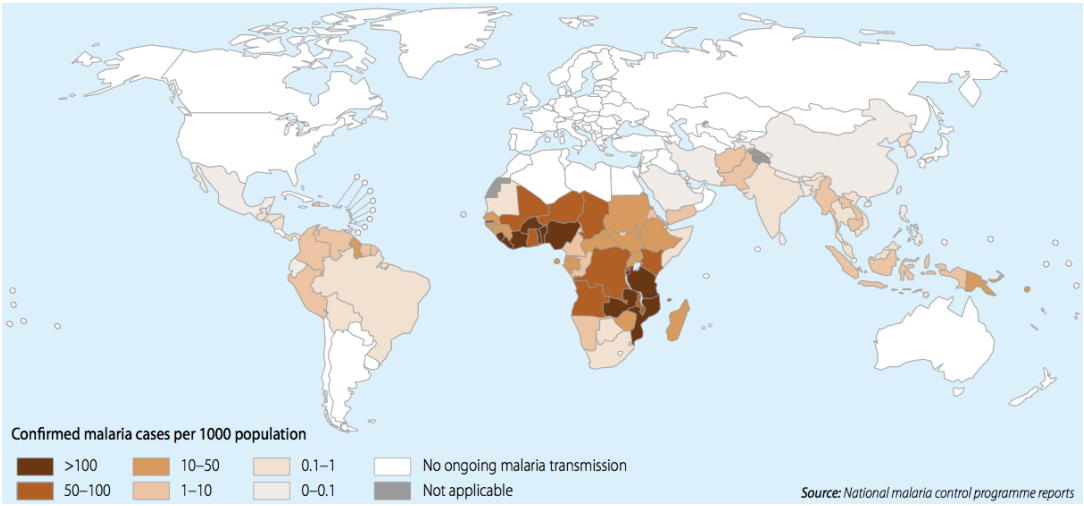

Figure 2. Worldwide distribution of malaria highlighting countries with on-going transmission of malaria in 2013. Reprinted from WHO World Malaria Report 2014.[14]

Several *Plasmodium* species are known to infect humans: *P. falciparum, P. vivax, P. ovale, P. malariae,* and *P. knowlesi.* The most aggressive and life-threatening species is *P. falciparum*, which accounts for most of the malaria-related deaths, and is the main form occurring in Sub-Saharan African countries. *P. vivax* is more prevalent in Asia and South America. This parasite species is less life threatening, but the liver stage of this parasite can remain latent as hypnozoites, which can release pathogens even months or years after infection and cause a relapse of the disease. Of an estimated 198 million malaria cases, about 584'000 ended fatally in 2013.[15] About 90% of all the malaria deaths occurred in Sub-Saharan Africa and 78% were children aged below five years.[15] These numbers highlight the large burden malaria still puts on public health in less developed countries.

1.2.1 Life Cycle of *Plasmodium falciparum*

Plasmodium spp. parasites – belonging to parasitic protists of the phylum Apicomplexa – undergo very complex life cycles, which include arthropod (*Anopheles* mosquito) and human host. Various extracellular (sporozoites, merozoites, ookinetes) and intracellular (intra-erythrocytic and intra-hepatocytic schizonts) forms of the parasite are involved in the life cycle (Figure 3).

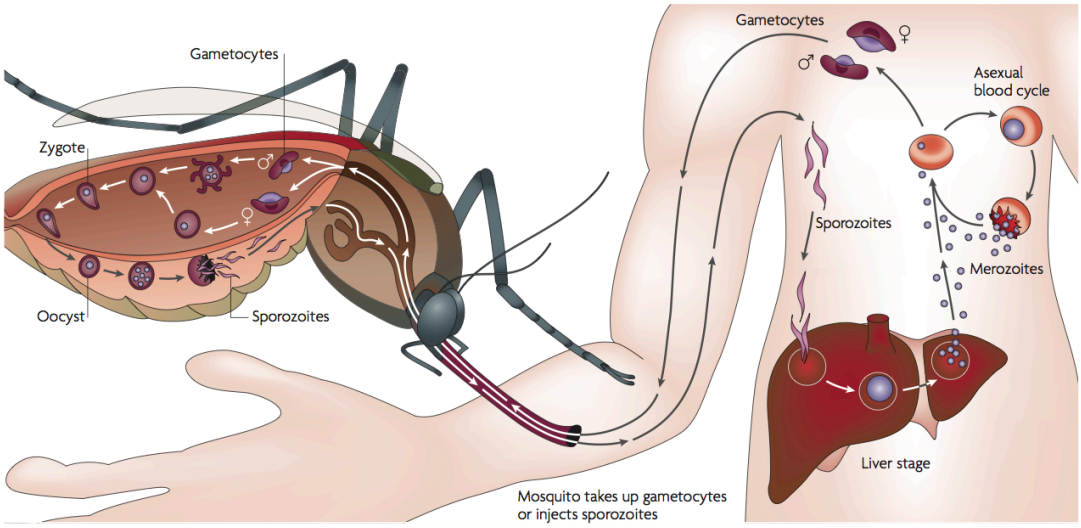

Figure 3. Malaria parasite life cycle. During the blood meal, *Anopheles* mosquitoes can inject sporozoites into the bloodstream of humans or take up gametocytes from infected humans. Info on the life cycle in the mosquito vector and gametogenesis can be found elsewhere.[16] Sporozoites asexually reproduce within hepatocytes in the liver, which release thousands of merozoites back into the bloodstream. Merozoites invade red blood cells (RBCs) where they asexually divide to form more parasites (schizogeny). After about 48 hours (*P. falciparum*), all infected RBCs burst and release the freshly generated parasites that rapidly invade more RBCs. This erythrocytic cycle is responsible for malaria pathogenesis. Reprinted with permission from reference [17]. Copyright (2007) Nature Publishing Group.

Only part of the life cycle of *P. falciparum* that is relevant to this thesis is briefly summarized herein. More information on the mosquito-based stages and gametogenesis needed for transmission from the human host back to the mosquito vector can be found elsewhere.[16] Multiplication within the human host exclusively occurs by mitosis, whereas meiosis is restricted to the replication within the mosquito host.[18] First, infected female *Anopheles* mosquitoes inject from a few dozen up to a few hundred sporozoites into the bloodstream of humans, while taking their blood meal. This extracellular sporozoite form travels through the bloodstream, passes through Kupffer cells in the liver, and finally infects and reproduces within hepatocytes. Each infected hepatocyte releases thousands of merozoites into the bloodstream, after they were formed through asexual cell division. Merozoites are polarized pear-shaped cells with a length of only about 1.5 µm; merozoites belong to the smallest known eukaryotic cells.[19] Merozoites are equipped and primed to attach to and invade red blood cells (RBCs). Therein, this parasite form undergoes schizogeny for about 48 hours to yield about 16 to 32 fresh daughter merozoites within each infected RBC (iRBC) in the case of *P. falciparum*.[20] Daughter merozoites egress from iRBCs to rapidly infect more RBCs. This erythrocytic asexual life cycle of the parasite continues and is finally responsible for malaria pathogenesis.[18]

1.2.2 *Plasmodium* Biology: Red Blood Cell Invasion Mechanism

RBC invasion by the *Plasmodium* merozoite form is a very rapid, complex, and well-coordinated process (Figure 4). Many different receptor-ligand interactions are involved in each step of invasion (Figure 5). Intriguingly, many proteins involved in invasion are first located within specific parasite organelles called micronemes and rhoptries present at the apical side of merozoites. Along with proteolytic enzymes that cleave part of the merozoite surface coat during invasion, other microneme and rhoptry proteins are secreted in a time-controlled manor to allow well-coordinated receptor-ligand interactions after initial attachment. These proteins are mainly members of the erythrocyte binding antigens (EBAs) and reticulocyte binding-like homologous (*Pf*RH).[21] In total, the whole entry process likely happens within only 60 seconds.[20] Detailed information on the sequence of protein interactions during the invasion of RBCs by malaria parasite can be found in recent reviews.[19,21-23] Mechanistic aspects of RBC invasion, including host cell modifications that facilitate parasite entry, have been discussed in a recent review, where the authors suggest that more mechanistic insight into the role of each essential invasion-related protein is necessary to finally understand the invasion process.[24]

A schematic overview of the RBC invasion process by *P. falciparum* is given in Figure 4. Only very few details relating to interactions occurring early in the invasion process are highlighted herein, especially related to merozoite/major surface protein 1 (MSP1) and heparan sulfate host receptor, because these are most relevant for the inhibitory strategy established within this thesis. Involved receptor-ligand interactions were traditionally determined by using enzymatic receptor cleavage; inhibition of binding *via* antibodies, peptides and small molecules; and genetic deletion of parasite ligands (Figure 5).[22]

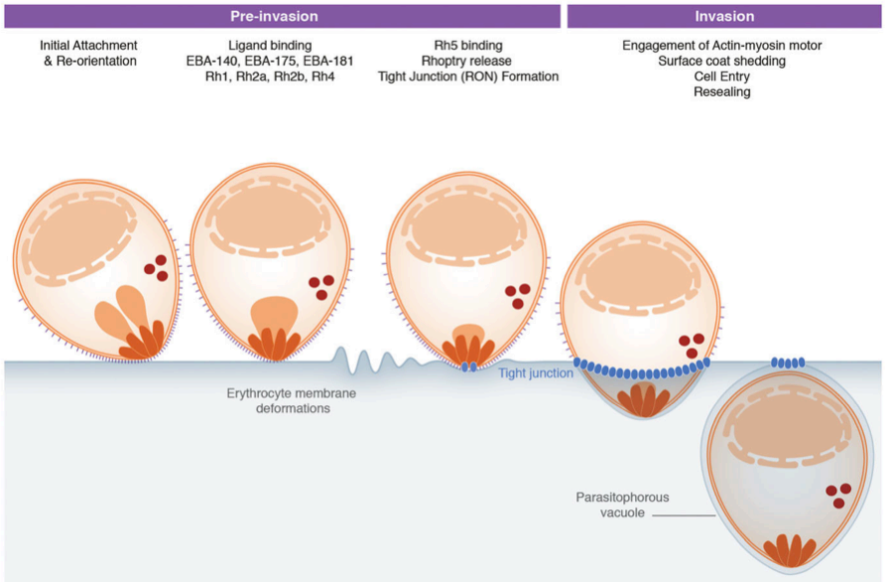

Figure 4. Schematic overview of the RBC invasion process by *P. falciparum* merozoites. After initial attachment to the RBC surface, the merozoite re-orientates to face the apical pole towards the RBC surface. Various, well-coordinated merozoite-RBC interactions occur during the invasion process (highlighted in Figure 5). Finally, the parasite enters through the formed tight junction using its actin-myosin motor. Reprinted with permission from ref [24]. Copyright (2016) Creative Commons Licence 4.0.

MSP1 – the main surface protein covering the whole surface of *Plasmodium* merozoites (MW 180 kDa) – is thought to be responsible for early processes of merozoite and RBCs interaction.[22,25] MSP1 is a glycosylphosphatidylinositol (GPI)-anchored membrane protein and it forms a non-covalent complex with MSP3, MSP6 and MSP7.[19] MSP1 is associated with an important role in merozoite egress from iRBCs and with subsequent invasion processes, which is coordinated by proteases cleaving MSP1 during these processes. A subtilisin-like protease 1 (SUB1) has been identified to process MSP1 into the fragments $MSP1_{83}$, $MSP1_{30}$, $MSP1_{38}$, and the GPI-anchored $MSP1_{42}$ just prior to egress.[21] This processing allows intracellular merozoites to bind the spectrin network of the erythrocyte cytoskeleton *via* processed MSP1 to finally facilitate parasite egress from iRBCs.[26] The second proteolytic cleavage of MSP1 by SUB2 occurs during parasite invasion. After initial contact between merozoite and erythrocyte has been established, the microneme content – including SUB2 – is expelled at the apical end of the merozoite, and SUB2 subsequently migrates along the merozoite surface.[27] SUB2 is responsible for shedding MSP1 and other proteins from the merozoite surface at the tight junction that is formed at merozoite-RBC interaction point.[21] Only the small $MSP1_{19}$ GPI-anchored fragment is finally carried into the RBC.

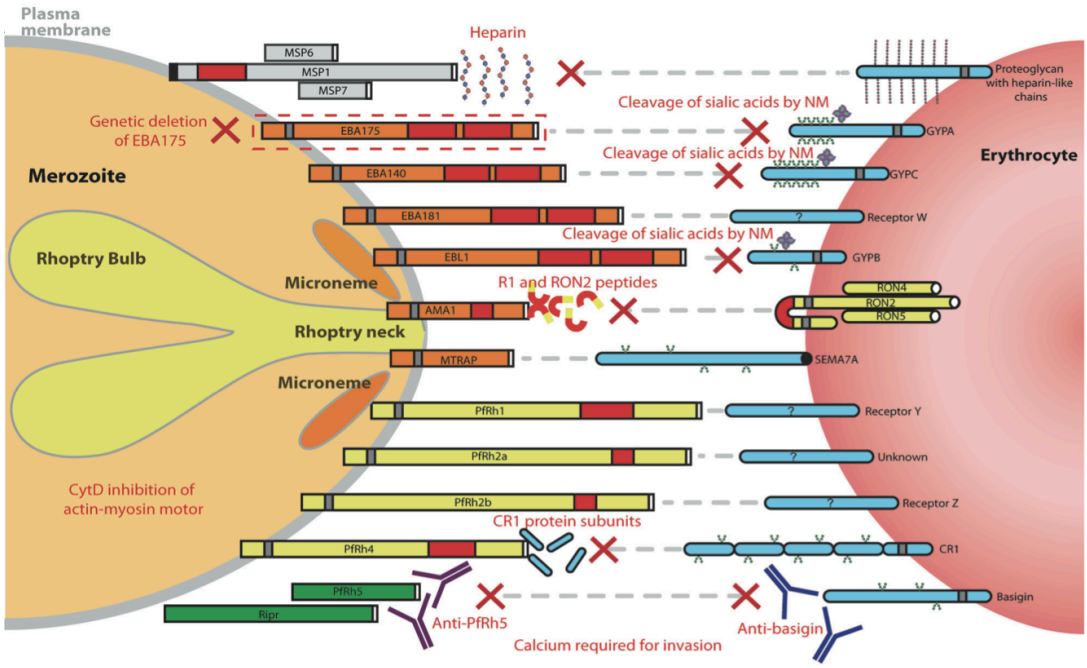

Figure 5. Schematic representation of known merozoite ligands, their interaction partners on the red blood cells, and methods to suppress these interactions. Reprinted with permission from ref [22]. Copyright (2015) Creative Commons Licence 4.0.

MSP1 (more specifically the proteolytic fragment $MSP1_{42}$) was proposed to be responsible for the initial attachment of merozoites to RBCs[25] or in a slightly later stage by mediating weak deformation of the erythrocyte.[22] Since this interaction is inhibited by soluble heparin, the interaction partner on the RBC side is most probably heparan sulfate proteoglycan present on RBCs (Figure 5).[25,28] This initial attachment has long been thought to be of low affinity,[20] but recently it was found that adhesion force prior to reorientation is already as strong as thereafter based on optical tweezers measurements with whole merozoites and RBCs.[29] Besides $MSP1_{42}$, many other interaction partners for heparan sulfate were identified and found having varying affinities towards this receptor; these include BAEBL (also known as EBA-140), *Pf*RH1, *Pf*RH2, *Pf*RH5, apical membrane antigen 1 (AMA1), and more.[30-32]

After initial attachment of merozoite to RBC, *Pf*RH5 has recently been identified to bind basigin on RBCs to anchor the merozoite to the RBC.[33] This allows subsequent interaction of AMA1 with RON2 to initiate tight junction formation, through which the merozoite finally passes, using its actin-myosin motor complex, to enter the RBC.[21] However, others have suggested that the actin-myosin motor is not the sole force governing host cell entry, but rather a combination of parasite machinery and host cell forces and dynamics allows efficient and rapid invasion.[24]

1.2.3 Pathogenesis of Malaria and Prophylaxis, Treatment, and Control Strategies

Pathogenesis is solely related to the blood stage cycle of malaria. Symptoms, which usually appear about 10 to 15 days after infection, and potential establishment of severe malaria, are all attributed to the multiplication and residence of parasites within RBCs. Laboratory manifestations of severe malaria include: severe anemia, acidosis, hyperlactatemia and hypoglycemia, pulmonary edema, and acute kidney injury.[18] Severe *P. falciparum* malaria is responsible for most malaria-related deaths and is mainly caused by sequestration of iRBCs and subsequent dysfunction of various, vital organs.[18] So-called cerebral malaria, which is a syndrome that frequently leads to death, is also related to sequestration, in this case within the brain microvasculature.[34] Sequestration, also called cytoadherence, relates to the adhesion of *P. falciparum* iRBCs (about 12 – 15 h post-invasion) to endothelial cell surfaces in veins and capillaries *via* knob structures on iRBCs. Sequestration leads to interference with microcirculatory flow leading to malfunctioning of the affected organ and ultimately to death, if not treated.[18]

The major adhesion protein in these knob structures of the iRBC surface is *P. falciparum* erythrocyte membrane protein 1 (*Pf*EMP1), which is in fact the main responsible molecule for the disease pathogenesis. Intracellular parasites have the astonishing ability to dramatically change the RBC physicochemical properties during the 48-hour intracellular cycle of *e.g. P. falciparum*. In fact, the intracellular parasite exports about 10% of all its proteins to the host cell cytosol, where a parasite-derived membranous sorting machinery, termed Maurer's clefts, further sends certain proteins, including *Pf*EMP1, to the iRBC surface.[35] Even more astonishing is the fact that the parasite has 60 different *var* genes, which all encode for one specific type of *Pf*EMP1, whereas only one is mutually exclusively expressed at each time point.[36] This allows the parasite to vary cytoadherence by binding to another receptor, which changes pathogenesis and helps the parasite to evade the immune system. Important members of host receptors for different *Pf*EMP1 are chondroitin sulfate A in the placenta, ICAM1 in the brain, and CD36 in many other organs.[18,34]

Another important modification of the host cell, relevant to this thesis, is the large increase of the membrane permeability towards certain small solutes.[37] The activity of so-called new permeation pathways (NPPs) on iRBCs, which were related to reactivation of endogenous dormant protein channels, has been proposed to cause this increase in permeability.[37] Nevertheless, access of even larger proteins and nanoparticles up to 80 nm diameter to the intracellular

parasite, without passing the host cytosol, suggests another yet unclear modification of the host cell to increase permeability; one possibility being a duct pathway that originates from unsuccessful closure of the merozoite entry site.[38-42] Detailed review of other host cell alterations through exported proteins leading to modification of the host's cytoadherence, permeability, and rigidity can be found elsewhere.[35,43]

Malaria can be treated using different combination therapies. The first-line treatment options include the very effective drugs of the artemisinin class in combination with other partner drugs. These drug combinations are also used for prophylaxis in travelers. The current drugs act on the intracellular parasites, no drug is on the market that can inhibit RBC invasion, for example.[44] Similar to other antimicrobials, antimalarials constantly lose their efficacy due to the development and spread of drug resistance. Recently, drug resistance against the artemisinin-based drug combinations emerged in South East Asia,[45] is spreading westwards,[9] and has already led to treatment failures.[46] This explains the constant need for novel antimalarials. Furthermore, there is an urgent need to develop drugs to reduce the high mortality of severe malaria.[47] For final elimination of malaria it will also be necessary to develop drugs that kill gametocytes, therefore blocking transmission, and drugs to eliminate dormant hypnozoites of *P. vivax* to inhibit relapse of the disease months after the infection.[47,48]

There is no malaria vaccine on the market yet. Several are in various stages of clinical trials. The most advanced being RTS,S/AS01 (MosquirixTM), for which a phase 3 clinical trial finished last year,[10] and the European Regulators have approved the use of the vaccine in July 2015. Nevertheless, the vaccine efficacy for this particular vaccine in children and infants was only about 30% after four vaccinations,[10] which is one of the reasons why WHO has only recommended usage in pilot implementation studies; no country-wide implementation has been recommended as yet.[49] In recent years, the whole pathogen vaccination strategy has become more attractive again, especially the attenuated sporozoite vaccine approach, which has regained attention due to new, larger-scale production possibilities and remarkable protection in small studies.[50] However, a very recent study with this sporozoite-based vaccine revealed a protection of about 50% for homologous challenge in adults for at least one year,[51] which is again similar to protection achieved in adults using the RTS,S subunit vaccine.[52] Larger studies are needed to evaluate the sporozoite-based vaccination, especially heterologous challenge to demonstrate clone-independent protection. Nevertheless, issues regarding affordable large-scale production, dosing, administration, storage, distribution, and safety, remain questionable at the moment.[53,54]

Global control measures for malaria, which helped to cut the mortality of malaria by half during the last decade, are the extended use of long-lasting insecticide impregnated bednets, and indoor residual spraying of insecticides.[55] However, these efforts are also greatly challenged by insecticide-resistant mosquitoes that are already prevalent in many malaria endemic areas.[56]

In the following chapters, the focus is shifted to the novel possibilities that are provided by polymer chemistry in combination with nanotechnology to tackle various medical conditions. Especially, specific malaria-related nanotechnological strategies are highlighted. But first, polymers and amphiphilic copolymer-based, self-assembled nanostructures, which are the types of nanoparticles used throughout this thesis, are introduced.

1.3 Self-Assembled Amphiphilic Copolymers in the Context of Medical Applications

In general, the two main areas of biomedically applied polymers are (*i*) "polymer therapeutics" – the polymer exhibits a pharmacological activity – and (*ii*) more inert polymeric constructs that function as drug delivery vehicles. In (*ii*), polymers can act to stabilize/protect therapeutics (*e.g.* small molecular drugs, enzymes, or nucleic acids), to increase *in vivo* circulation times of the drug, to target certain diseased cells, and to allow controlled and triggered drug release inside target cells. Traditionally, the main focus of polymer-based therapeutic systems was the development of novel cancer therapeutics and delivery platforms. Extensive reviews on this topic including examples of type (*i*) and (*ii*) can be found in many recent publications.[57-61] Ever since, applications of polymer-based therapeutics are expanding (See Chapter 1.3.5). Examples include the treatment of infectious diseases (See Chapter 1.4), their use as topical microbiocidals, oral polymeric sequestrants, or in tissue regeneration/repair, demonstrating the broadly applicable concept of polymer-based approaches.[62]

But what is a polymer? Polymers are macromolecules composed of covalently connected repeating units. Herein, the design, assembly, and applicability of such polymers, mainly in the form of block copolymers that self-assemble into supramolecular architectures, are described with an emphasis on intended biomedical uses.

1.3.1 Block Copolymers and Self-Assembly Mechanism

Polymer-based therapeutics relate to various structures ranging from relatively simple linear polymers to more complex copolymer-based macromolecules and

supramolecular assemblies thereof, such as dendrimers, micelles, nanoparticles, and polymer vesicles (polymersomes) (Figure 7).[61,63] These supramolecular assemblies can be obtained *via* self-assembly of amphiphilic block copolymers (ABPs). In general, ABPs relate to a class of copolymers, which contain at least two domains that allows stabilization of an interface between two materials.[64] In most cases this refers to at least one hydrophobic and one hydrophilic domain, with random, block, graft, star, multiblock, *etc.* architecture (Figure 6). These copolymer architectures, which connect hydrophobic and hydrophilic domains, will self-assemble in aqueous solutions to yield supramolecular structures, due to the incompatibility of at least one of the blocks and water.

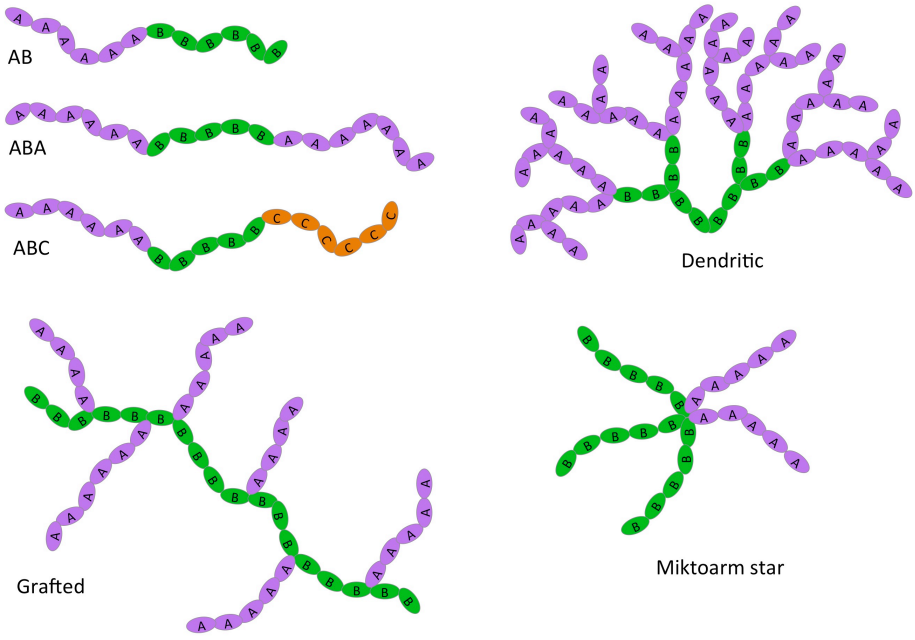

Figure 6. Some examples of possible amphiphilic block copolymer architectures: linear AB, ABA, and ABC copolymers, and more complex grafted, dendritic, and miktoarm star copolymers. A, B, C represent polymer repeating units of different chemical natures.

The concentration limit for amphiphiles to self-assemble into supramolecular structures is called the critical micelle concentration (CMC). The driving force for aqueous self-assembly of such ABPs is mainly the hydrophobic effect,[65] which also explains the self-assembly of lipids, surfactants, and biological membranes.[66,67] The hydrophobic effect describes the tendency of nonpolar molecules to self-assemble in water in order to exclude water molecules, which leads to macrophase separation.[68] In case of amphiphiles, the molecules assemble in such a way that the hydrophobic domains pack together with the hydrophilic domains facing the water

interface. The covalent linkage of hydrophobic and hydrophilic part within amphiphiles causes microscopic phase separation (*e.g.* micellation), in contrast to macroscopic phase separation for purely hydrophobic molecules in water.[68] The forces governing the assembly of amphiphiles are similar to the assembly of purely hydrophobic molecules in water. However, additional entropic effects, arising from the hydrophilic block and the covalent linkage of at least two incompatible blocks, have to be included.[68]

At room temperature, the change in Gibbs free energy (ΔG), which explains the spontaneous self-assembly of ABPs in water, is dominated by entropic forces.[69] This means the self-assemblies described herein are dominated by the fact that water tends to maximize its dynamic hydrogen-bonding network and not due to affinity between the hydrophobic domains.[69] The assembly of hydrophobic molecules in water (a decrease in entropy) is overcompensated by the increase in entropy for the surrounding water molecules. If all amphiphiles would be dissolved, the water molecules, surrounding the amphiphile, would have fewer hydrogen bonds and lower degrees of freedom, which would cause an overall decrease in entropy. Therefore, it is entropically favorable for ABPs to self-assemble instead of dissolving at concentrations above the CMC.

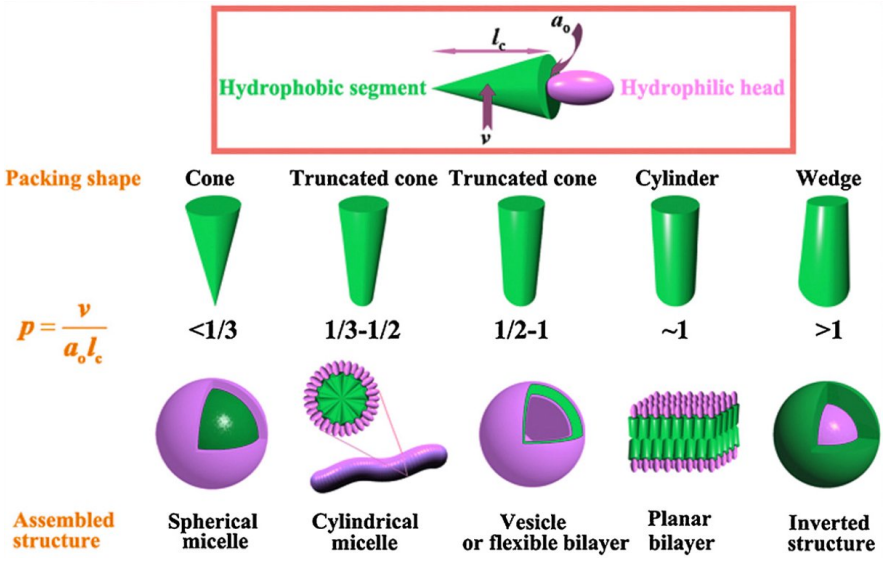

Figure 7. Schematic representation of the influence of amphiphilic block copolymer geometry, with packing parameter *p*, on the self-assembly architecture: from spherical micelles to inverted structures. Reprinted and modified with permission from ref [70]. Copyright (2012) Elsevier. This scheme has been prepared based on the theory of ref [67].

The two main forces governing self-assembly of amphiphiles into distinct structures are the attractive hydrophobic forces at the water-hydrophobic interface

and the hydrophilic head group repulsion, which oppose each other leading to an optimal hydrophilic head area (a_o).[71] Similar to other amphiphiles, such as lipids and surfactants,[67] the chemical nature of the used blocks in ABPs, the absolute length, polydispersity, hydrophilic fraction, and the molecular curvature determine the architecture of the self-assembled structures (Figure 7).[70,72-74] These inherent amphiphile characteristics can be summarized with the so-called packing parameter p (Figure 7), which is the ratio of the hydrophobic domain volume (v) to the optimal hydrophilic head area (a_o) times the length of the hydrophobic block (l_c).[67] The values obtained for p are a key parameter to predict the final structure of the self-assembly. Typical values of p to yield micelles, cylindrical micelles, vesicles, bilayers, and inverted structures are given in Figure 7.[67,70,71]

An even simpler rule for predicting the structure of the self-assemblies is the hydrophilic to total mass fraction ($f_{\text{hydrophilic}}$). ABPs with $f_{\text{hydrophilic}}$ < 25 % favor inverted structures, $f_{\text{hydrophilic}} \approx 35 \pm 10$ % allows vesicle formation, and ABPs with $f_{\text{hydrophilic}}$ > 45 % typically form micelles.[75] The assemblies also depend on pH, temperature, ionic strength, types of ions, ABP concentrations, and presence of homopolymer and surfactants.[71,74] By changing these parameters, the structures can be transformed from one to another. Due to the slow dynamics of ABPs in solution, a global thermodynamic equilibrium is usually not reached. This allows to kinetically trap ABP in a certain self-assembled structure, which is stable due to the inability to thermodynamically equilibrate.[76] The formation of the specific type of ABPs assembly called polymer vesicles is described in a bit more detail, because it was the main structure used in this thesis.

1.3.2 Polymer Vesicles – Polymersomes

This subsection has been published and was reprinted and modified herein with permission from reference [77]. Copyright (2015) CRC Press.

Einfalt, T.; Gunkel, G.; Spulber, M.; ***Najer, A.****; Palivan, C. G. In CRC Concise Encyclopedia of Nanotechnology; Kharisov, B. I.; Kharissova, O. V.; Ortiz-Mendez, U., Eds.; CRC Press, Taylor and Francis Group: Boca Raton, 2016; pp. 1055–1068.*

Polymer vesicles, or polymersomes,[78] are structural analogues to lipid vesicles (liposomes) built from ABPs instead of lipids. In an aqueous environment, these polymers can form spherical, membranous structure (Figure 8). Either spherical mono- (ABA-type polymer) or bilayer membranes (AB-type) enclosing a watery core are formed. The hydrophilic to total mass ratio (f-value) and the packing parameter (p) are key parameters, which govern the self-assembly process

resulting in formation of polymersomes.[75,79] *f*-Ratios in a range of 25 - 45% and *p* parameters between 0.5 and 1 favor formation of polymersomes, when the polydispersity index is as close as possible to 1. The polymerization routes to obtain well-defined amphiphilic copolymers have been reviewed elsewhere.[80-85]

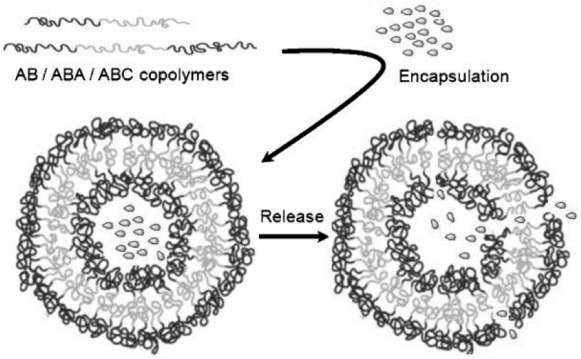

Figure 8. Schematic representation of AB, ABA, and ABC block copolymers, their assembly into polymersomes, and encapsulation of hydrophilic compounds in the vesicle core. Triggered release from polymersomes can be achieved by incorporation of stimuli-responsive bonds. Reprinted with permission ref [86]. Copyright (2009) Wiley and Sons.

While lipid membranes are typically 3 – 5 nm thick; the membrane thickness of polymersomes can be fine-tuned in the range of about 5 to 30 nm by choosing an appropriate copolymer. Polymersomes offer a wide variety of advantages compared to simple liposomes, especially higher mechanic stability, and greater chemical versatility.[78,86,87] While the driving force for nanostructure formation is mostly the hydrophobic effect as described above (Subchapter 1.3.1), there are other interactions, which favor the generation of polymersomes. A special group are vesicles with a polyion complex membrane (PICsomes), which are formed by ionic interactions of oppositely charged polymers.[88] Furthermore, purely synthetic,[79] biohybrid,[88,89] or purely biological[90,91] block copolymers have been employed to from polymersomes. Specific functions, such as targeting properties, can be implemented by including biological entities directly into the block copolymer before vesicle formation[89] or by functionalizing preformed vesicles with targeting ligands.[92,93]

Another critical step is to choose the appropriate polymersome formation technique for each block copolymer. A technique that works for one polymer cannot necessarily be applied to other polymers. Furthermore, the most suitable technique might even change depending on the nature of the desired molecules to be encapsulated, such as nucleic acids, proteins, or enzymes. Currently used

polymersome formation methods are in essence the same as for micelle formation: direct dissolution of dry polymer powder, film rehydration, and solvent switch method.[74,93] In addition, double emulsion technique, and electroformation can be used to generate polymer vesicles.[74,93] The resulting polymersome size is highly dependent on the preparation method. For example, film rehydration yields small multilamellar vesicles, whereas electroformation was specifically developed to produce micrometer-sized polymersomes.[93] Extrusion – separating a polymersome solution through a filter with defined pore sizes – can be applied to obtain smaller polymersomes with a narrower size distribution. Polymersomes made from diblock, but not triblock, copolymers were transformed from unilamellar to bilamellar "double" polymersomes under hypertonic shock, demonstrating the close relation, and the intrinsic differences of polymersomes and liposomes.[94]

The hydrophilic interior of polymersomes and the hydrophobic part of the membrane allow the simultaneous encapsulation of various hydrophilic and hydrophobic compounds, such as drugs, proteins, polysaccharides and nucleic acids. This advantage can be used to formulate multifunctional polymersomes. Our group *e.g.* pioneered the combination of polymersomes with membrane proteins and enzymes to produce nanoreactors that can even function as artificial organelles within cells.[59] The polymersomes used in this thesis are mainly based on the specific ABA-type triblock ABP poly(2-methyl-2-oxazoline)-*block*-poly(dimethylsiloxane)-*block*-poly(2-methyl-2-oxazoline) (PMOXA-*b*-PDMS-*b*-PMOXA). Specific fluorescence-based techniques have been extensively used in this thesis to characterize such polymersomes and other nanoparticles, which is why the next chapter briefly summarizes the concept and applicability of these methods.

1.3.3 Characterization of Nanoassemblies by Fluorescence Correlation Spectroscopy

Fluorescence correlation and cross-correlation spectroscopy (FCS, FCCS) are single molecule detection methods to analyze molecular diffusion properties and interactions of fluorescent molecules and nanostructures. Since its introduction in the early 70s,[95] and upgrade by using confocal setups in the 90s,[96] FCS and FCCS have become powerful tools to investigate a plethora of molecular and nanostructure properties in solution, within membranes, inside cells, and even within living organisms.[97-101] More recently, the introduction of stimulated emission depletion (STED) microscopes allows to measure FCS using even smaller confocal volumes compared to conventional confocal microscopes.[102] FCS/FCCS

can also be applied to study nanoassembly architecture, functionality, and membrane dynamics in detail. As mainly demonstrated by our group, FCS and FCCS can be used to characterize nanostructure hydrodynamic sizes, encapsulation efficacies, release behavior, surface functionality, interaction parameters for targeting ligands on the surface (*e.g.* K_D), molecular dynamics of polymers and membrane proteins within polymersome membranes, and more.[97,103-106] FCS was also used to characterize more biomedically applied surface modification of polymersomes with antibodies.[107]

The schematic measurement setup and analysis principle is summarized in Figure 9. Commercial confocal laser scanning microscopes can be used for these measurements. In contrast to confocal imaging – where the confocal volume is used to scan an image –conventional FCS and FCCS applications use the confocal volume in static condition. The raw signal is the fluorescence intensity fluctuation over time, which occurs due to molecular diffusion of the fluorescent analytes through the small observation volume in the range of about 1 femtoliter (= 10^{-15} L).[108] For conventional confocal laser scanning microscopy (CLSM) the x-y dimension of the confocal volume (ω_{xy}) is solely given by the numerical aperture (NA) of the objective and the laser wavelength (λ):

$$\omega_{xy} = \frac{\lambda}{2 \cdot NA} \qquad \text{Equation 1}$$

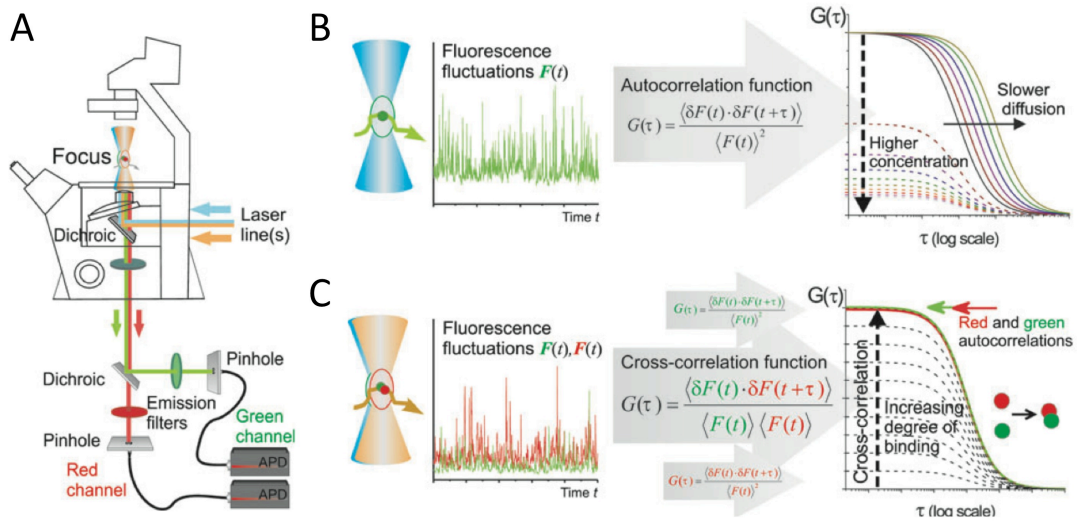

Figure 9. FCS and FCCS setup and principle. (A) Schematic experimental setup. (B) FCS procedure with a single color. Diffusion through the confocal volume induces measurement of fluorescence fluctuation over time, which is auto-correlated to yield autocorrelation curves to finally obtain diffusion times and concentrations. (C) Procedure for dual-color FCCS. Both colors must be spectrally separable to obtain distinct auto- and cross-correlation curves. The closer the cross-correlation amplitude is to the lower auto-correlation the higher is the degree of binding between red and green labeled species. Reprinted with permission from ref [98]. Copyright (2006) Nature Publishing Group.

The measured fluorescence intensity fluctuations are attributed to classical Brownian motion of the suspended molecules/nanostructures through the confocal volume, which occurs due to thermal collisions at temperatures above absolute zero. This irregular and directionless (random) Brownian motion is described using a random walk model, which equals the famous Einstein relation that relates mean-square displacement in the direction of the x axis $\langle x^2 \rangle$ to the diffusion coefficient D and time t:[109,110]

$$\langle x^2 \rangle = 2Dt \qquad \text{Equation 2}$$

Einstein applied van't Hoff's law of osmotic pressure produced by solute molecules in a solvent to free Brownian motion by defining a pressure p that is exerted by Brownian particles in equilibrium. When combined with the Stokes' Law that describes the force exerted on a fixed sphere that is surrounded by moving fluid (velocity υ and viscosity η), the Stokes-Einstein equation is obtained:[109,110]

$$D = \frac{RT}{N}\frac{1}{6\pi\eta R_H} = \frac{k_B T}{6\pi\eta R_H} \qquad \text{Equation 3}$$

T is the absolute temperature, N the Avogadro constant, R the gas constant, k_B the Boltzmann constant, and R_H the hydrodynamic radius of the sphere. This equation relates the diffusion coefficient D to the radius R_H of a particle that moves by Brownian motion within a fluid with viscosity η. This relation is subsequently used when analyzing FCS/FCCS data and calculating R_H of nanoparticles in solution.

For FCS measurements, a solution of fluorescent molecules/nanoparticles, usually in the nanomolar concentration range, is illuminated by a static femtoliter confocal volume on a commercial CLSM. The emitted photons of fluorescent objects present within this confocal volume at any given time point are recorded with high temporal resolution. The pinhole of the confocal setup ensures that out-of-focus light is not collected by the highly sensitive avalanche photo diodes (APDs). The recorded fluorescence intensity fluctuates over time, due to the above described Brownian motion of the suspended molecules/nanoparticles, which enter and leave the confocal volume faster or slower, depending on their size. Examples of raw intensity traces of FCS/FCCS measurements are given in Figure 9B,C. Intensity traces are subsequently auto-correlated ($G(\tau)$, single channel) for FCS and/or cross-correlated ($G_x(\tau)$, red to green channel) for FCCS:[111]

$$G(\tau) = 1 + \frac{\langle \delta I(t) \cdot \delta I(t+\tau) \rangle}{\langle I(t) \rangle^2} \qquad \text{Equation 4}$$

$$G_x(\tau) = \frac{\langle \delta I_i(t) \cdot \delta I_j(t+\tau) \rangle}{\langle I_i(t) \cdot I_j(t) \rangle} \qquad \text{Equation 5}$$

with $\delta I(t) = I(t) - \langle I(t) \rangle$ being the intensity fluctuations with intensity $I(t)$ at time point t, time average fluorescence intensity $\langle I(t) \rangle$, and $\delta I(t + \tau)$ the intensity at time $t + \tau$. In the case of cross-correlation (Equation 5), $I_i(t)$ and $I_j(t)$ correspond to fluorescence intensities recorded by detection channel i (*e.g.* green) and j (*e.g.* red), respectively. The obtained auto- and cross-correlation curves are then fitted using appropriate models, *e.g.* free one-component 3D Brownian motion including triplet state (Equation 7, Chapter 10) or free two-component 3D Brownian motion (Equation 11, Chapter 10). These fits then yield diffusion times (τ_D), number of particles (*N*), fractions of molecules in triplet state, and fractions of molecules with corresponding diffusion time (for two-component fits). These values are then used to calculate hydrodynamic radii R_H (Equations 8, 9, Chapter 10), molecular brightness (counts per molecules (*CPM*) in kHz), concentrations, number of encapsulated molecules, time-dependent release of molecules from nanostructures, surface coverage with targeting ligands, surface interaction parameters such as dissociation constant K_D, colloid aggregation, and more as described in the Experimental Section (Chapter 10).[97,103,104,107] A solution of free dye, for which the absolute diffusion coefficients is known,[112] is first measured to calibrate the confocal volume x-y dimension (ω_{xy}), which is needed to obtain R_H in the end (Equations 8, 9, Chapter 10).

Since the underlying theoretical description – used to calculate specific properties – assumes ideal conditions, such as a perfect Gaussian confocal volume, special attention to setup calibration and data evaluation has to be given to avoid possible artifacts.[113-115] Especially, the problem of a disproportional effect of bright, and slow-diffusing nanostructures on the average autocorrelation curves[114,115] poses hurdles for nanostructure evaluation. For example, a mixture of nanoparticles with diameters of 24 nm (99.4 %) and 100 nm (0.6%, 70 times brighter) yielded an autocorrelation curve characteristic for the 100 nm particles, which were only present in traces.[114] Often, larger nanostructures (*e.g.* polymersomes), which diffuse slower, also contain more dye molecules, which highlights the significance of this problem. This can partly be solved by measuring more short intensity traces instead of few long measurements and exclusion of distorted autocorrelation curves from the averages.[115] Nevertheless, this is subject to introducing subjective bias. Therefore, it should be ensured that only few percentages of all the curves are deleted and the selection process should be based on a number – an automated rejection of distorted curves would be optimal.[115] Otherwise, all the measurements that *e.g.* yield *CPM* values 10 times higher than the average are manually excluded and the total percentage of affected curves are mentioned in the Experimental Section.

In case of analyzing colloidal stability and model dye release from drug delivery vehicles, two-component fits should be accompanied by *CPM* values (Chapter 10). *CPM* gives further indication, whether some molecules were released from the nanostructure, even if the fast-diffusing species does not appear as a second component due to the aforementioned problem. For FCCS measurements even more calibration data are needed. For example, cross-talk from green to red channel has to be minimized and overlap of red and green channel should be optimized.[116]

Despite these hurdles, FCS/FCCS are powerful tools to investigate various nanostructure properties in detail. Especially, qualitative/relative evaluations are relatively simple, fast and often meaningful at a single molecule level. Our group pioneered to use a technique called z-scan FCS[117] to study dynamics of membrane-forming block copolymers, and embedded membrane proteins within giant polymersome membranes.[105,106] In z-scan FCS, the confocal volume is placed at the top of an immobilized giant polymersome. Fluorescence intensity traces are recorded at varying relative z-position to finally calculate parameters of lateral dynamics of copolymers and membrane proteins within the membrane (Figure 10).

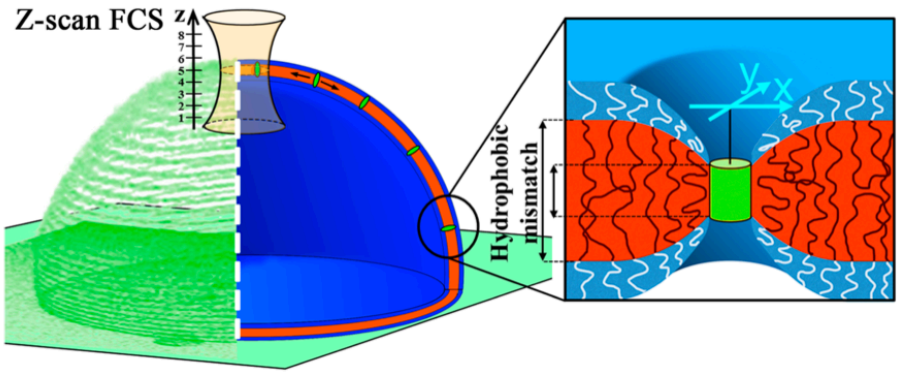

Figure 10. Schematic representation of z-scan FCS applied to measure lateral dynamics of membrane-forming copolymers and embedded membrane proteins (green cylinder). The left half of the immobilized giant (green) are experimental CLSM slices recorded with embedded fluorescently-labeled membrane protein. Hydrophobic mismatch between membrane hydrophobic part and membrane protein height is highlighted. Reprinted with permission from ref [105]. Copyright (2015) American Chemical Society.

Interestingly, our PMOXA-*b*-PDMS-*b*-PMOXA-based giant polymersome membranes revealed relatively fast lateral diffusivity of the copolymers within the membranes compared to other types of copolymer membranes.[106] We argue that this high fluidity of PDMS-based membranes provides the basis for functional

incorporation of membrane proteins even in cases when a large mismatch between protein height and polymer hydrophobic membrane thickness exists.[105] We found that various fluorescently labeled membrane proteins diffuse only about one order of magnitude slower within PDMS-based polymersome membranes compared to protein diffusion within their natural environment, lipid bilayers.[105] This is the basis for the generation of polymeric, membrane-protein-based nanoreactors and artificial organelles.

In the next chapter, the specific requirements of polymer-based nanostructures that should be met when intended for biomedical applications are summarized.

1.3.4 Requirements of Polymer Nanostructures When Used in Medicine

This subsection has been published and was reprinted and modified herein with permission from reference [118]. Copyright (2013) Future Medicine.

***Najer, A.**; Wu, D.; Vasquez, D.; Palivan, C. G.; Meier, W. Polymer Nanocompartments in Broad-Spectrum Medical Applications. Nanomedicine (London, U.K.)* ***2013**, 8, 425–447.*

For use of polymer nanostructures in medicine, for example as drug carriers, nanoreactors or artificial organelles, a complex system of requirements must be fulfilled with reference to (*i*) the material, (*ii*) mechanical properties, *(iii*) size, (*iv*) shape, and (*v*) surface chemistry of the polymeric compartments. These properties determine blood circulation half-life, biodistribution, vascular dynamics, targeting, cell uptake, drug release, and subsequent degradation ((*i, ii*),[119] (*iii*),[120] (*iv*),[121] (*v*)[122]) (Figure 11).

Information on cellular uptake mechanisms of nanocarriers (*e.g.* endocytosis or phagocytosis) can be found in a recent review.[123] Toxicity and immunological aspects should be evaluated carefully, because even small changes in the above mentioned properties alter the properties of a drug delivery system (DDS) in a biological environment *in vitro* and *in vivo*.[124] Because of the limited availability of information specific to polymeric compartments, we selected relevant information concerning the requirements of a DDS from stealth liposome-, general polymer therapeutics-, and nanoparticle literature.

The properties related to the requirements mentioned above will differ drastically, depending on the desired site of action of a DDS or nanoreactor. For example, opposing properties must be exhibited when aiming at a slow-release drug reservoir within cells of the mononuclear phagocytic system (MPS), as compared to targeted drug delivery to a specific site. The former DDS has to be taken up by cells of the MPS, while the latter should be prepared to avoid uptake by these cells.

Specific requirements for nanoreactors in medical applications involve: use of no-, or very dilute organic solvents in order to retain biomolecule function, sufficient robustness of the nanoreactor – even after cellular uptake – and the substrates/products of the enzymatic reaction must be able to cross the polymer membrane of the nanoreactor.[125,126]

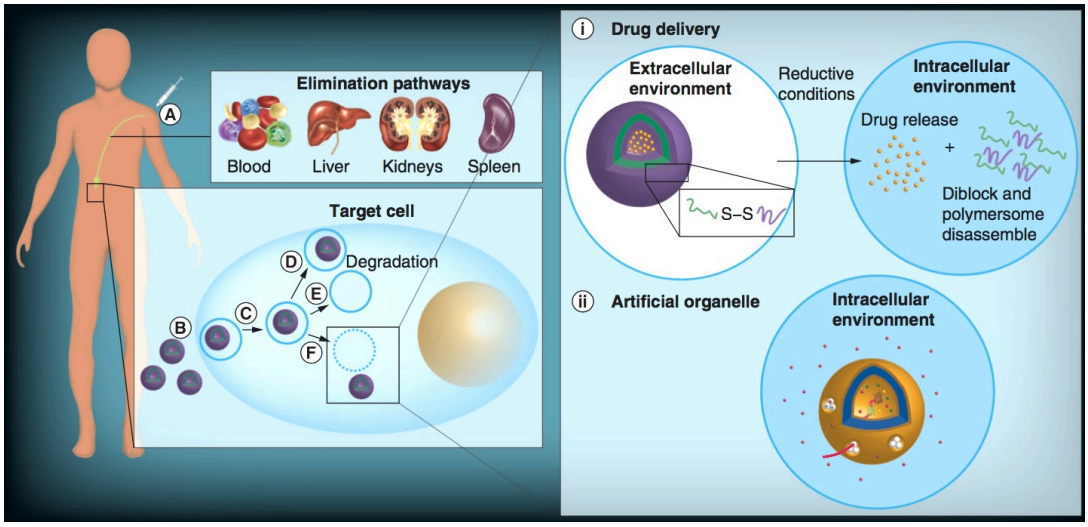

Figure 11. Barriers (blood cells, liver, kidneys and spleen) encountered by polymer nanocompartments after injection and their two functions, either as drug/protein/nucleic acid delivery vehicles or as artificial organelles. (A) To reach target cells, polymer vesicles have to avoid recognition by blood cells, uptake in liver and spleen (phagocytosis or filtration) and renal clearance (kidneys). (B, C) After cellular uptake the polymer vesicles are trafficked in early endosomes. (D) Endocytosed material can be recycled to the cell surface and excreted. Release of cargo is desired for drug/protein/nucleic acid delivery vehicles. This occurs through vesicle degradation (stimuli-responsive vesicles) after fusion with (E) lysosomes or (F) endosomal escape. (i) For example, carriers – sensitive to the cytosolic, reductive environment – release their cargo through degradation after endosomal escape. (ii) Nanoreactors that act as artificial organelles should escape endosomes intact and degradation in the cellular environment must be avoided if activity as artificial organelles is to be carried out. Modified with permission from refs [127,128]. Copyright (2011, 2012) Wiley and Sons.

1.3.4.1 Biocompatibility and Biodegradability of the Nanostructure Material

All polymers designed for use *in vivo* must be biocompatible. Toxicity related to the polymer must be avoided. In the case of a DDS, polymers should be biodegradable as well, or should at least be eliminated from the body. Current knowledge on administration, distribution, metabolism and elimination of general polymer-based therapeutics *in vivo* has recently been summarized.[119] Compared to a polymer-drug conjugate, in which the drug is released *e.g.* upon stimuli-responsive cleavage of the linker between the polymer and the drug, vesicles release their payloads through disruption of the vesicle structure or by transport

through naturally porous membranes or integrated protein channels.[86,129,130] Therefore, either the vesicle-forming polymers themselves should be biodegradable, or the macromolecular assembly should disintegrate into single polymer chains that can be excreted from the body. For example, single poly(ethylene glycol) (PEG) chains smaller than 30 kDa are readily cleared from the body by the kidneys.[131]

DDS are often designed to be responsive to certain stimuli, so that their payload is released only upon proper stimulation at the desired site of action.[86] Polymer assemblies responsive to physical, chemical or biological stimuli have been proposed.[132] In principal, the degradation of a macromolecular assembly could lead to excretion of polymeric material, but the mechanism and the actual fate of these materials should be evaluated carefully.

Other strategies to achieve degradation of the macromolecular assembly are based on the use of natural monomers or polymers such as amino acids, nucleotides, lipids, and carbohydrates to build vesicle-forming block copolymers. If the block copolymer consists of one block made of biological materials (*e.g.* polyglutamic acid, chitosan or dextran),[89,133] and if the second block is made of a synthetic polymer (*e.g.* PEG, PMOXA), this is referred to as biohybrid material. The degradation products of the natural block enter the biochemical pathways in the body. If the remaining synthetic polymer is non-degradable, the kidney will excrete it, as long as the size of the remaining polymers does not exceed the renal excretion cut-off, which is estimated to be 5.5 nm for inorganic nanoparticles, for example.[134]

In the case of artificial organelles, these vesicles must stay intact in the cell environment for effective periods of time in order to perform their tasks; rapid biodegradability is therefore not desirable or needs to be delayed. For example, PMOXA-*b*-PDMS-*b*-PMOXA nanoreactors that contain a dual-enzyme-mimic labeled with sulforhodamine B were stable in THP-1 cells for at least 48 hours.[135] However, as the concept of artificial organelles was introduced only recently and development and optimization inside cells involve extensive testing, there are no examples that report stability of the artificial organelles inside cells for more than 48 hours. If even greater stability is required, cross-linking the polymer chains in the polymeric membrane after vesicle formation can, for example, be performed.[130,136]

1.3.4.2 Surface Chemistry

The surface chemistry of polymeric vesicles is of great importance, especially if *in vivo* applications are intended. For some time now it has been known that

PEGylation of liposomes increases their blood circulation times by reducing opsonisation and uptake of liposomes by MPS cells, because of the protein repellant property of PEG.[137,138] But recently, certain problems have been attributed to the use of PEG; therefore, alternative strategies to PEGylation are gaining ever greater attention.[124,139,140] Proposed, alternative inert surface coatings include PMOXA and poly(2-methacryloyloxyethyl phosphorylcholine).[141,142]

Use of-, or mimicking of the RBC membrane is another strategy to obtain long-circulating DDS. For example, poly(lactic-*co*-glycolic acid) nanoparticles covered with whole RBC membranes exhibited longer half-lives as compared to PEGylated nanoparticles.[143] But, because human RBCs are immunogenic when transferred between patients with different blood groups, personalized DDS need be prepared, or antigens need be eliminated from the membrane.[143] In another strategy to enhance circulation time, charge on the surface of polymersomes was tuned to mimic the negative surface potential of RBCs (-15 mV), whereby a different organ accumulation pattern was found for negatively charged polymersomes as compared to neutral ones, with the former accumulating mainly in the liver.[144] The effect of surface charge on circulation time was studied in tumor-bearing mice using polymersomes made of PEG-*b*-poly(D,L-lactide).[122] The longest circulation time (half-life 47.3 h), lowest liver uptake (27.9% of injected dose), and highest accumulation in the tumor (18.6% of injected dose) was found for 90 – 100 nm polymersomes with a slightly negative surface charge (zeta potential − 7.6 mV). Polymeric vesicles with a more negative surface charge (zeta potential – 38.7 mV) or stealth liposomes were less effective.[122] For clinical therapy, the surface of the DDS should either be neutral or negatively charged, because exposed positive charges are problematic for *in vivo* applications.[145] In order to achieve targeted drug delivery at a specific site, both passive and active targeting strategies are being examined. Using the "enhanced permeability and retention effect" (EPR) in solid tumors, long-circulating DDS will passively accumulate at these tumor sites; no specific surface modifications are necessary.[146] Active targeting strategies require specific targeting ligands on the surface of the DDS. In this regard, different ways to functionalize polymersomes were recently summarized.[92]

1.3.4.3 Size

Vesicle size is another key factor determining biodistribution and circulation half-life in blood.[120,147] The first constraint to long-circulating nanoobjects in blood is the hepatosplenic filtration process. This can be circumvented by not exceeding a 200 nm vesicle diameter, or by introducing flexibility to the assembly.[148,149] The lower size limit depends mainly on the kidneys; only spherical particles with

hydrodynamic diameters greater than 5.5 nm can avoid renal clearance and urinary excretion.[134]

For polymersomes administered in mice, a second size limitation (< 100 nm diameter) was found that was not true for liposomes, influencing biodistribution and circulation.[120] It was observed that polymersomes made of PEG-*b*-polybutadiene at a diameter of 120 nm accumulated far more in liver and spleen than 90 nm vesicles made of the same material (blood half-life of about 24 h). On the other hand, doubling the PEG layer did not alter the circulation time significantly.[120] This strong dependence of pharmaceutical properties on the size of polymeric vesicles enhances the need for vesicle preparation methods that result in defined sizes with low size distributions. Polymer parameters, preparation procedures, and specific methods to obtain defined vesicular structures were summarized recently.[150] Based on the current data, long-circulating polymer vesicles can be produced if prepared in the diameter range of 10 – 100 nm.[120,147] In the case of PICsomes, an optimal size in terms of extended blood circulation and high tumor accumulation was determined to be around 150 nm.[151]

1.3.4.4 Shape

To date, mainly spherical micelles, elongated micelles and spherical vesicles have been investigated for their potential use in drug delivery. It has been determined that shape greatly affects biomedical properties such as toxicity, biodistribution, and cellular uptake of DDS.[121] Worm-like polymeric vesicles were prepared and proposed as a theragnostic tool for cancer, while the influence of their shape on circulation time was not evaluated.[152] Interestingly, when an active targeting strategy was applied by attaching targeting moieties to DDS, differences in shape lost importance.[153] Therefore, it can be speculated that only for DDS with passive targeting strategies does the effect of shape become a significant factor.

After introducing the limitations for polymer-based nanosystems to be applied in medicine, few examples of proposed polymersome-based biomedical applications are summarized in the next chapter.

1.3.5 A Glimpse at Potential Polymersome Biomedical Applications

This subsection has been published and was reprinted and modified herein with permission from reference [77]. Copyright (2015) CRC Press.

Einfalt, T.; Gunkel, G.; Spulber, M.; ***Najer, A.****; Palivan, C. G. In CRC Concise Encyclopedia of Nanotechnology; Kharisov, B. I.; Kharissova, O. V.; Ortiz-*

Mendez, U., Eds.; CRC Press, Taylor and Francis Group: Boca Raton, 2016; pp. 1055–1068.

Applications of ABP-based micelles/nanoparticles can be found in other extensive reviews.[154-157] The main application being the stabilization and delivery of hydrophobic drug molecules for cancer therapy. Compared to micelles, polymersomes have the advantage of allowing the encapsulation/entrapment of both hydrophilic and hydrophobic molecules in the same vesicle due to its intrinsic architecture based on an inner cavity surrounded by a membrane. The ability of polymersomes to simultaneously contain both hydrophobic and hydrophilic molecules allows for the construction of complex systems beyond traditional drug delivery vehicles,[118,127] such as nanoreactors, artificial organelles,[118,126-128,158-160] active surfaces (*e.g.* biosensors)[126] and multicompartment systems mimicking cellular functions.[161]

Polymersomes are a potential candidate to be used as drug delivery system (Figure 11). The robustness large size of their hydrophilic compartment, and their chemical versatility are main advantages of polymersomes compared to other delivery carriers.[162] In addition, by an appropriate selection of the copolymers to contain stimuli-responsive blocks, it is possible to release cargo “on demand”. Common triggers used for stimuli-responsive release from polymersomes are pH, temperature, redox-potential, and concentration gradients of certain molecules (*e.g.* glucose).[86,87,132] Another advantage of polymersomes for drug delivery is their long *in vivo* circulation time, 47.3 h half-life compared to 10.6 h for PEGylated liposomes in mice.[122] The long circulation time was achieved by using the hydrophilic domain PEG, known to reduce adsorption of proteins and subsequent opsonisation by cells.[138] Other factors that support the use of polymersomes for biomedical applications are the biocompatibility/biodegradability of the polymers, the size, shape and surface properties (Subchapter 1.3.4).

Nanoreactor*s* are engineered by encapsulation of active compounds (proteins, enzymes, mimics, or combinations thereof) that perform chemical/biochemical reactions inside the cavity of polymersomes. The membrane permeability allows an exchange of substrates/products with the environment and can be specifically tuned by the chemical nature of copolymers by chemical modifications[163,164] or by incorporation of natural channel proteins.[128,158] Nanoreactors evolved from one-step reactions inside the polymersome,[130,165] to two-step ATP synthesis,[166] to more complex reactions such as three-enzyme cascade reactions,[167,168] or transcription of DNA to mRNA and subsequent translation to yield fluorescent proteins.[169] Nanoreactors were also used to synthesize antibiotics on demand and on site.[170]

Bacterial growth was inhibited by antibiotics (cephalexin), locally produced by nanoreactors containing penicillin acylase, and having a permeable membrane due to the insertion of bacterial outer membrane protein F (OmpF) to allow substrate and product permeation.

The concept of artificial organelles was introduced by reports of nanoreactors performing their enzymatic reactions *in situ* inside cells (Figure 11).[128,171-173] One example is the detoxification of reactive oxygen species (ROS) by artificial peroxisomes. Two enzymes acting in tandem inside the cavity of polymersomes equipped with channel proteins for membrane permeabilization, detoxified superoxide radicals and hydrogen peroxide in cells exposed to oxidative stress. These artificial organelles protected cells from oxidative stress to the same extent as natural peroxisomes.[172]

Another direction of polymersome research is to establish multicompartment systems with a cytosol-mimicking interior including different organelles with the prospect of designing artificial cells.[161,169,174] Controlled production and loading of giant polymersomes was realized by microfluidic techniques. These polymersomes were filled with the whole transcription- and translation machinery in order to synthesize fluorescent proteins from DNA plasmids.[169] Others produced multicompartment systems that mimicked cytosol properties within giant polymersomes.[161,175,176] They produced small polymersomes which were encapsulated in big polymersomes together with a crowding agent (alginate) to mimic the cytosol.[176] Alginate completely arrested movement of the small polymersomes, whereas dextran only slowed down their diffusion. Cascade reactions were also implemented in a multicompartment polymersome system.[168] Two kinds of nanoreactors (containing two different kinds of enzymes) were encapsulated in micrometer-sized polymersomes together with a third enzyme ("cytosolic" enzyme), enabling cascade reactions in this compartmentalized structure with participation of all three enzymes.

Interestingly, even directional movement of polymersome-like structures can be achieved.[177] Polymer stomatocytes, (deformed polymersomes with an opening) encapsulated catalytically active platinum nanoparticles, which catalyzed the production of water and oxygen from hydrogen peroxide. The products were expelled through the controlled opening of stomatocytes, yielding directional movement, demonstrating production of miniature monopropellant rocket engines built from polymersomes.[177]

1.4 Nanotechnology for Infectious Disease Medicine

Nanotechnology is also considered as one of the key technologies to overcome the mentioned threats associated with infectious diseases in the future. More specific, nanotechnology can be used to develop tools to fight drug resistant pathogens and to design more potent vaccines.[178] One example is the use of "nanoantibiotics" against drug resistant bacteria.[179,180] This is particularly important in the context of antibiotic discovery lagging behind rates of drug resistance.[180] Therefore, a current alternative is the delivery of high local antibiotic concentrations to infected sites using DDS. This nanocarrier-based delivery should solve the problems of systemic administration, namely, systemic toxicity and insufficient antibiotic concentrations at the target sites; a known factor to promote antibiotic resistance.[180] Entry inhibition of viruses and bacteria by multivalent nanostructures is a growing and promising strategy for treatment or prophylaxis of infections.[181-185] In general, the inhibitory nanostructure should best be smaller than binder (pathogen).[185] Another example of possible nanotechnology impact on infectious disease control is the formulation of nanovaccines with increased efficacy.[186,187] Carrier systems have long been used for many vaccines in order to modulate the generated immune response, which strongly depends on the nature of the vaccine carrier.

Few examples of polymersome-based anti-infectious strategies are highlighted below. Studies on the application of polymersomes and other polymer-based nanostructures in the field of nanomedicine for infections are clearly limited in contrast to a huge literature on anti-cancer applications. However, polymer-based nanostructures have a great potential to be broadly utilized in the field of anti-infectious strategies as well. Specific advantages of polymer-based strategies are the relatively simple and diverse synthesis possibilities to produce a plethora of degradable/nondegradable polymers, facile post-synthesis modifications/ conjugations, affordability, scale-up, and introduction of stimuli-responsiveness. Triggered nanostructures that respond to a change in their environment (stimuli) are particular examples of sophisticated DDS achievable using polymer-based building blocks.

1.4.1 Polymersome-Based Anti-Infectious Strategies

This subsection has been published and was reprinted and modified herein with permission from reference [59]. Copyright (2016) The Royal Society of Chemistry.

Palivan, C. G.; Goers, R.; ***Najer, A****.; Zhang, X.; Car, A.; Meier, W. Chem. Soc. Rev.* ***2016****, 45, 377–411.*

In addition to cancer therapy, which is the main area of applied polymersome research, there are other possible biomedical applications using triggered polymersomes for diagnostics and therapy. pH-sensitive polymersomes have been tested for the detection of pathogenic bacteria,[188] and for possible intracellular antibiotic therapy.[189,190] Hyaluronic acid-*block*-poly(ε-caprolactone) copolymers are prone to enzymatic degradation by bacteria and can be used for their detection. For example, upon enzymatic cleavage by hyaluronidase, which is common in *Staphylococcus aureus*, a reporter compound is released for detection.[188] Polymersomes based on peptide functionalized chitosan were able to encapsulate and release doxorubicin (DOX) upon proteolytic degradation and act antibacterial at the same time.[191] Thus this system might be applied in the future to deliver drugs and simultaneously protect from bacterial infections. An additional example in the combat of bacterial infection has been proposed for immobilized nanoreactors on implants. They provide the required antibiotic "on site", and only the precursor needs to be administered, thus minimizing side effects.[170] It was also shown that the number of intracellular *Porphyromonas gingivalis*, which infect oral epithelial cells, was reduced by intracellular delivery of metronidazole or doxycycline using acid-sensitive polymersomes,[190] and *Burkholderia pseudomallei*-infected murine macrophages were successfully treated using another type of pH-sensitive polymersomes (Ceftazidim-loaded) that disassembled in endosomes for efficient intracellular drug release.[189]

Oxidation-sensitive polymersomes have been introduced as a valuable vaccine delivery platform because antigen-cross presenting dendritic cells contain oxidative endosomes.[192] In addition, the advantageous architecture of polymersomes allows simultaneous encapsulation of hydrophobic and hydrophilic antigens and adjuvants, and therefore serves as an improved delivery system.[193] First, it was demonstrated that dendritic cells engulfed loaded oxidation-responsive polymersomes *via* endosomes, where they resided for more than 12 h, and then in a second step the payload escaped to the cytoplasm. Endosomal escape of antigen is desirable for entering the 'cytosolic pathway' of antigen cross-presentation *via* major histocompatibility complex 1 (MHC 1), which might be advantageous for adjuvant-induced activation and antigen presentation. Furthermore, enhancement of T cell priming was found when dendritic cells were tested for processing, and cross-presentation of a model antigen on MHC 1 when these polymersomes were used for antigen delivery compared to delivering free antigen to dendritic cells.[193]

1.4.2 Nanotechnological Approaches for Malaria

The current problems associated with malaria discussed in Subchapter 1.2 demand for innovative strategies for future control of this disease. Nanotechnology is increasingly acknowledged as a valuable tool to design novel diagnostic,[194] therapeutic,[195-198] and prophylactic[199,200] approaches for malaria. For detailed examples, readers are referred to the above-mentioned extensive reviews on this topic. Herein, only few examples are highlighted to demonstrate the broad applicability of nanotechnology for possibly controlling malaria in the future.

1.4.2.1 Antimalarial Drug Delivery

Similar to anticancer drug delivery, antimalarials are other valuable carrier molecules to be incorporated within nanoparticles for drug delivery to parasitized cells. In case of malaria, nanoparticle-based drug delivery is being evaluated to reduce drug-related toxicities, fight drug resistance development, increase drug performance, treat severe malaria, and block transmission as exemplified below. Up to now, the main carriers evaluated for antimalarial drug delivery have been liposomes, solid lipid nanoparticles, polymeric nanoparticles, cyclodextrins and dendrimers.[197]

Currently, blood stage parasites are the main target of antimalarial drug delivery. Increasing the drug concentration within intracellular parasites through targeted nanostructure-based drug delivery is thought to be a valuable tool to fight establishment of drug resistance and treatment of drug resistant parasites.[42,201] However, it is an ongoing controversy through which mechanism nanostructures deliver antimalarials to iRBCs. The two main proposed mechanisms are a direct access of nanoparticles (< 80 nm diameter) to intracellular parasites *via* the "leakiness" of iRBCs,[39,40,42,202] and membrane fusion of *e.g.* drug-loaded liposomes with iRBC membranes (iRBCM).[203-205] The main difference between these two mechanisms is the role of the host cell cytosol. With the first mechanism, the DDS bypasses the host cytosol (Figure 12B,C), whereas membrane fusion demands subsequent crossing of the host cytosol by the drug molecule (Figure 12A). Possible explanations for these pathways are summarized in Figure 12.

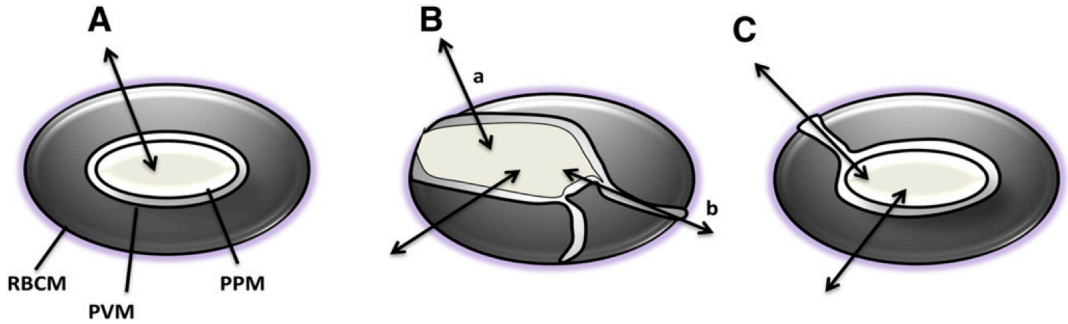

Figure 12. Schematic representation of proposed iRBC morphology causing increased permeability of iRBCs compared to RBCs. (A) Traditional sequential pathway: solutes sequentially cross red blood cell membrane (RBCM), parasitophorous vacuole membrane (PVM), and parasite plasma membrane (PPM) to reach the parasite. (B,C) Alternative models "parallel pathways" for solute transport that does not involve the host cytosol: (B) (a) PVM and PPM are close to RBCM to facilitate solute uptake or (b) tubovesicular membrane (TVM) fuses with RBCM, which allows entry of solutes from extracellular medium. (C) Parasitophorous duct originating from merozoite entry connects the intracellular parasite with the external medium. This scheme is based on ref [206]. Reprinted with permission from ref [197]. Copyright (2013) Elsevier.

The increased permeability of iRBCs to small solutes has been attributed to new permeation pathways (NPP) appearing on iRBC membranes (Figure 12A).[37] However, the size of these channels does not provide a pathway for nanoparticles. Possible sites for the entry of sub-80 nm nanoparticles into iRBCs are the sites where the iRBCM is in close proximity to the parasitophorous vacuole membrane (PVM) and parasite plasma membrane (PPM) (Figure 12B-a).[206] Uptake of nanoparticles could also occur *via* the tubovesicular membrane (TVM) that fuses with the iRBCM (Figure 12B-b). Alternatively, the merozoite entry site might never completely close and therefore provide a parasitophorous duct that allows direct entry from the serum site (Figure 12C).[206]

The second pathway, delivery *via* membrane fusion, calls for a membranous nanostructure, such as liposomes, and active targeting to iRBCs. iRBC-targeting antibodies and polysaccharides presented on liposome surfaces were demonstrated to increase fusion of the nanocarrier with membranes of infected cells.[203,204,207] This strategy reduced the amount of drug needed to kill the intracellular parasites *in vitro* by more than 10-fold compared to free drug, but parasitemia could not completely be eliminated from the cultures.[204] In contrast, targeting liposomes to all RBCs, including non-infected RBCs, also yielded some beneficial effect due to the residence of the antimalarial chloroquine (CQ) already before entry of the parasite.[205,208] Dendrimers have been investigated for antimalarial delivery as well.[42,201] Poly(amidoamine) dendrimers loaded with CQ were much more effective in an *in vivo* model of malaria compared to the free drug.[42] This was attributed to the targeting effect of these dendrimers to iRBCs,

which specifically take up these drug-loaded nanocarriers. Another type of dendrimers, amphiphilic dendrimers, were also loaded with CQ and PQ, which yielded similar beneficial effects as the first example when tested *in vitro* and *in vivo* against malaria.[201] Targeted delivery of high drug concentrations to iRBCs is considered a valuable strategy to tackle development of drug resistance.[42,201]

Another avenue for antimalarial delivery *via* DDS is the optimization of drug performance of existing antimalarials. Nanostructure-based artemisinin delivery was evaluated in a malaria mouse model using PEGylated liposomes *via* parenteral administration. Delivery by this specific carrier showed highest efficiency compared to free artemisinin and conventional liposomal formulation of artemisinin.[209,210] The artemisinin-loaded liposomes yielded much longer blood-circulation times and more stable drug concentration levels in the blood compared to free artemisinin.[209,210] Furthermore, the liposomal formulations had immediate effect on the parasites, whereas free artemisinin decreased parasitemia not before 7 days after the treatment start.[210] In conclusion, the efficacy of an existing drug could be optimized using liposomal nanocarriers.[210]

A further strategy is the development of DDS to reduce the high mortality associated with severe malaria.[211] Liposomes have been tested in a model of a severe pathological event, cerebral malaria.[211,212] In contrast to previous examples, the DDS used in this case did not deliver an antimalarial, but a toxic glucocorticoid prodrug. This DDS reduced cerebral inflammation when administered to mice with experimental cerebral malaria. By first reducing the adverse effects related to the cerebral syndrome using this steroidal nano-drug, the time window for subsequent anti-parasite treatment with conventional antimalarial drugs was significantly increased.[211,212] This sequential treatment completely cured mice from cerebral malaria. The authors conclude that this is a valuable treatment option for this severe form of malaria, even if patients would arrive at a late stage of disease.

Stimuli-responsive nanoparticles that release their cargo upon a change in pH, temperature, redox potential, or concentration of a specific enzyme,[59,213] have not yet been specifically applied to antimalarial drug delivery. The highly reducing cytosol of intracellular malaria parasites[214] provides an endogenous trigger to initiate intracellular nanoparticle disassembly and drug release. This strategy is comparable to reduction-triggered anticancer drug release from DDS within the reducing cytosol of cancer cells.[215] Interestingly, the cytosol of drug-resistant parasite strains (CQ-resistant) were even more reducing (higher glutathione (GSH) levels and glutathione S-transferase activity) compared to drug-sensitive strains.[216] More recent data also revealed the same elevated GSH levels within parasite

cytosols of artemisinin- and mefloquine-resistant strains.[217] This reduction of drug-sensitivity might be overcompensated by delivery of high local concentrations of drugs using reduction-triggered nanoparticles. These triggered carriers might release their payload faster and more effective within the highly reducing-cytosol of drug-resistant parasites.

Other parasite stages that are currently being addressed using nanostructure-based delivery systems are the mosquito stages.[218] One possible way would be the administration of these drug-loaded nanoparticles to humans, which would subsequently delivery the nanoparticles from their blood to the mosquito during their blood meal.[218]

1.4.2.2 Nanostrategies for Malaria Vaccines

Various nanostructures have been proposed and tested as delivery vehicles for malaria vaccines.[199,200] In the context of vaccines, nanostructures are delivery platforms containing a cocktail of antigens (or DNA encoding for antigens), adjuvants, and immunomodulatory molecules. This complex design helps to generate and modulate the immune response.[219] In fact, the most advanced malaria vaccine candidate RTS,S/AS01 from GSK is formulated in liposomes (AS01), which are nanovesicles.[220] RTS,S/AS01 is an example of a subunit protein/peptide vaccine. It mainly consist of the circumsporozoite protein (CSP) of the pre-erythrocytic sporozoite form of *P. falciparum* formulated in a nanostructure (liposome).

Another nanotechnological vaccination possibility that is being followed is the use of viral envelopes, called virosomes, for targeted delivery of incorporated antigens.[221] This strategy was *e.g.* used to successfully induce production of parasite growth-inhibitory antibodies against AMA1 of blood-stage malaria parasites.[221] In even more advanced formulations, epitopes are integrated into designer proteins that self-assemble into “virus-like” nanoparticles themselves.[200] This combines the high immunogenicity of virus-like nanoparticles with the purity of designer proteins; such a self-assembled nanoparticle – based on CSP epitopes – will enter human clinical trials in 2017.[200] DNA vaccination is another alternative. In this case, DNA encoding for certain antigens is used for vaccination. Unfortunately, free DNA suffers from insufficient cellular uptake and low stability in biological fluids. This is circumvented by protection and delivery of the DNA *via* nanocarriers. However, the perfect carrier in combination with the best route of administration has not yet been found.[199]

In general, malaria blood stage protein-based vaccines are challenging to design, due to the difficulty to select and prioritize the antigen or combination of antigens that can induce maximum protective response. Future protein-based malaria vaccine development to achieve a highly effective vaccine, which can either prevent death, disease, or transmission, will need to include new strategies for identification, selection, and formulation of the vaccine.[222] Conserved and essential antigens, which are not necessarily the main targets of naturally acquired immunity, should be selected in the future and most beneficial antigen combinations for protective efficacy should be found.[222] Furthermore, finding improved protein vaccine delivery platforms (nanotechnology) and adjuvants to significantly fine-tune and enhance humoral and cellular immunity is another priority.[222]

In conclusion, we have learned that formulation of an effective subunit protein vaccine for malaria is extremely challenging. For final eradication of malaria a combination of subunit protein vaccines and whole parasite vaccines (See Subchapter 1.2.3) might be the solution.[223]

CHAPTER 2

2 Motivation and Aim of this Thesis

The ongoing challenges to fight infectious diseases, in the context of expanding antimicrobial resistance and the current lack of alternatives for treatment and prophylaxis (See Chapter 1), motivated me to establish nanotechnological approaches for antimicrobial applications, in particular for malaria. Especially since these diseases mainly threaten children, pregnant women, diseased-, malnourished-, and elderly people, I consider finding new ways to treat and/or prevent theses diseases being of highest priority. We will constantly need new drugs, drug/vaccine delivery systems, vaccines, vaccination strategies, or alternative measures to stay ahead of rapidly evolving pathogens. Promising types of biomedically applicable materials are polymer-based nanostructures. These materials can be designed to suit the particular demands by exploiting the broad chemical diversity achievable by polymer chemistry, which allows constructing complex assemblies with multifunctional properties.

The overall aim of this thesis is the development of polymer-based nanostructures for the fight against malaria, while maintaining potential broad-spectrum applicability. The main aim followed herein is the development of functional polymer vesicles (polymersomes) that inhibit malaria parasites from entering RBCs, thereby presenting the extracellular form of the pathogen to the immune system. This strategy is designed to provide multifunctionality due to the combined drug- (invasion inhibition) and "vaccine-like" action (parasite exposed to immune system) (Figure 13). This is straightforwardly addressed by mimicking the host cell surface on the nanostructure. The advantage of this design is a potentially biocompatible structure, because the host is imitated (in this case human), which poses a lower risk of incompatibility with our own body. Moreover, this should allow prolonged circulation time of the nanostructures within the bloodstream. Secondly, the host-mimetic nature of the nanostructures might be advantageous in terms of complicating resistance development by the parasite. Our strategy will work as long as the pathogen binds the specific receptor

presented on nanomimics. In case the pathogen mutates such that it can no longer bind our nanostructure, consequently it cannot bind this specific receptor on the host cell either. Only if the pathogen can use other host cell receptors for attachment and invasion it will still be successful. In this case, the new receptors have to be identified and nanomimics redesigned with another receptor or a combination of several.

For this thesis, the host cell receptor heparan sulfate was chosen to serve as pathogen docking sites on nanomimics. More specific, heparin, which is a polysaccharide very closely related to heparan sulfate, was used for the nanomimic design. This ensures applicability for malaria,[25] but also broad spectrum potential due to the involvement of heparan sulfate in many human infections, *e.g.* HIV-1, hepatitis B and C, Dengue virus, West Nile virus, *Mycobacterium tuberculosis, Staphylococcus aureus,* and *Trypanosoma cruzi*.[224]

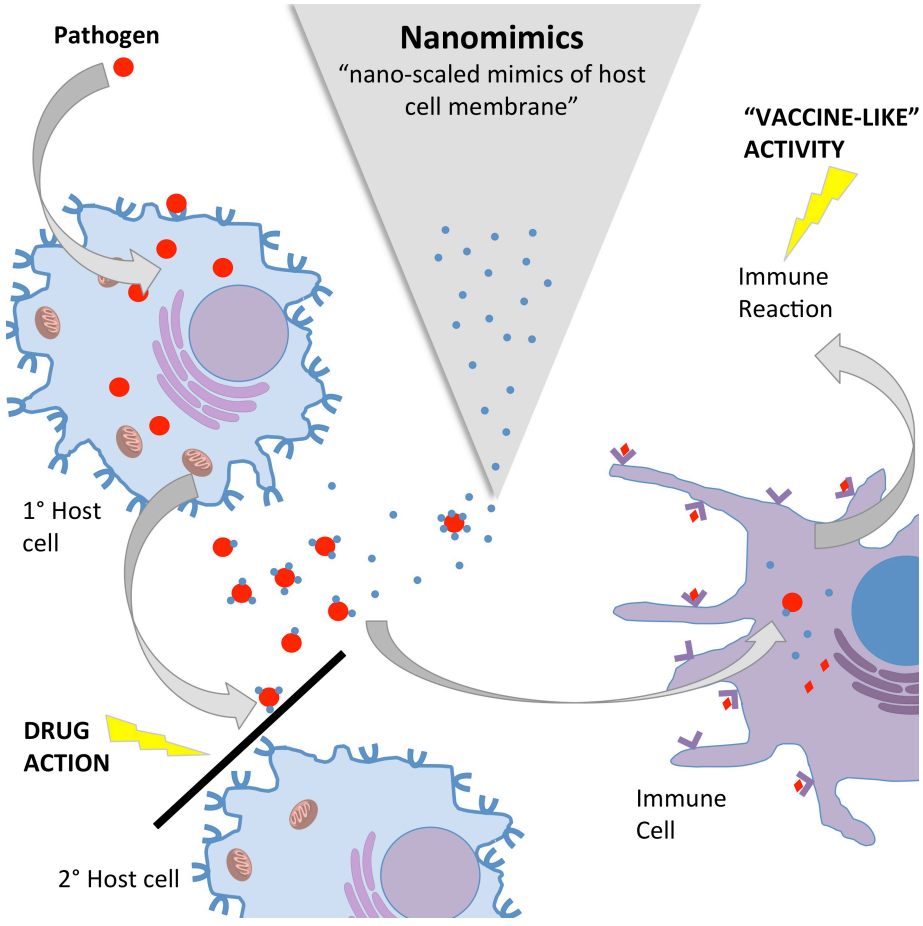

Figure 13. Generalized schematic overview describing the nanomimic strategy, which aims to combine drug- and "vaccine-like" action *in vivo*. The strategy is intended to cure an infection and additionally boost the immune system to protect from secondary infections. This is achieved through inhibition of pathogen entry (drug action) and subsequent exposure and delivery of pathogens to immune cells ("vaccine-like" activity).

The specific experimental steps to realize these objectives are:

- Design and synthesis of amphiphilic block copolymers with heparin as hydrophilic block and receptor molecule (various lengths).
- Self-assembly and analysis of polymersomes obtained by mixing the heparin-based copolymer with vesicle-forming copolymer to yield nanomimics.
- Characterization of interaction of a known heparin-binding parasite protein with nanomimics.
- Establishment of an *in vitro* suspension assay to test nanomimics on suspended *P. falciparum* blood stage cultures.
- Evaluation of nanomimics in the above-established assay and comparison to performance of soluble heparin.
- Analysis of nanomimic-parasite interaction by fluorescence-based techniques and electron microscopy.
- Verification of potential adverse effects of nanomimics: cellular toxicity, anticoagulation property, and endotoxin contamination.
- Preliminary tests on *in vivo* applicability and "vaccine-like" action.

The second aim is the evaluation of degradable, reduction-sensitive, polymer-based nanoparticles for the delivery of an experimental drug candidate with solubility, and metabolic instability problems to *Plasmodium*-infected RBCs. The reducing cytosol of these iRBCs provides a suitable environment for intracellular nanoparticle disassembly and drug release. Specific steps for achieving this aim are:

- Formulation of fluorescent dye-loaded nanoparticles using reduction-sensitive and insensitive copolymers.
- Evaluation of colloidal stability and reduction-triggered model compound release.
- Loading of nanoparticles with an experimental antimalarial compound with the above-mentioned properties.
- Evaluation of drug-loaded nanoparticles in various models of blood stage *P. falciparum*.

CHAPTER 3

3 Nanomimics of Host Cell Membranes Block Invasion and Expose Invasive Malaria Parasites

This study represents the primary evaluation of nano-scaled red blood cell (RBC) membrane mimics (nanomimics) for the inhibition of RBC invasion by malaria parasites of the species Plasmodium falciparum, which is the most dangerous form of Plasmodium parasites that infects humans.

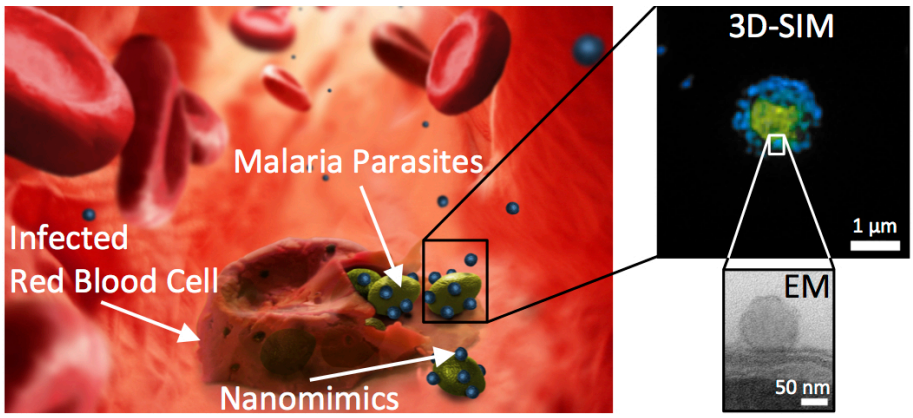

This study has been published and was reprinted and modified herein with permission from reference [225]. Copyright (2014) American Chemical Society.

Najer, A.; Wu, D.; Bieri, A.; Brand, F.; Palivan, C. G.; Beck, H.- P.; Meier, W. *ACS Nano*. **2014**, 8, 12560–12571.

3.1 Abstract

The fight against most infectious diseases, including malaria, is often hampered by the emergence of drug resistance and lack or limited efficacies of vaccines. Therefore, new drugs, vaccines, or other strategies to control these diseases are needed. Here, we present an innovative nanotechnological strategy in which the nanostructure itself represents the active substance with no necessity to release compounds to attain therapeutic effect and which might act in a drug- and vaccine-like dual function. Invasion of *Plasmodium falciparum* parasites into red blood cells was selected as a biological model for the initial validation of this approach. Stable nanomimics – polymersomes presenting receptors required for parasite attachment to host cells – were designed to efficiently interrupt the life cycle of the parasite by inhibiting invasion. A simple way to build nanomimics without postformation modifications was established. First, a block copolymer of the receptor with a hydrophobic polymer was synthesized and then mixed with a polymersome-forming block copolymer. The resulting nanomimics bound parasite-derived ligands involved in the initial attachment to host cells and they efficiently blocked reinvasion of malaria parasites after their egress from host cells *in vitro*. They exhibited efficacies of more than 2 orders of magnitude higher than the soluble form of the receptor, which can be explained by multivalent interactions of several receptors on one nanomimic with multiple ligands on the infective parasite. In the future, our strategy might offer interesting treatment options for severe malaria or a way to modulate the immune response.

3.2 Introduction

Infectious diseases – causing about 25% of total annual deaths worldwide – are a major threat to public health, which is enhanced by the emergence of drug resistance and vaccine failures.[1,226] In the case of malaria, there is no vaccine registered yet and drug susceptibility is decreasing; resistance to artemisinin derivatives, which in combination with other drugs are the recommended first-line treatments, is already spreading across mainland Southeast Asia.[227] An emerging strategy for fighting infectious diseases is to inhibit the initial host-pathogen interaction,[183,184] thus preventing cell invasion as presented here in the case of malaria. A large number of human pathogens use the cell surface heparan sulfate proteoglycan for recognition and primary interaction between host and pathogen.[224] *Plasmodium falciparum*, which causes malaria and is responsible for > 600'000 deaths annually[228] uses heparan sulfate as the receptor for initial binding of sporozoites to hepatocytes[229] and merozoites to host red blood cells

(RBCs).[25] Highly sulfated polysaccharides such as heparin (closely related to heparan sulfate) or K5 polysaccharide are potent inhibitors of merozoite invasion of RBCs *in vitro*. Although different strains of *P. falciparum* use different pathways for RBC invasion, six different parasite strains were tested and were inhibited by these sugars.[25] It has been shown that soluble heparin *in vitro* and *in vivo* can also reverse binding required for sequestration and rosetting in *P. falciparum* infections which are the major pathogenic events.[230,231] However, the use of these polysaccharides in malaria infections is hindered by short *in vivo* circulation half-lives (about 30 min to 2 h),[232,233] limited efficacy, and anticoagulation properties, which led to intracranial bleedings (in the case of heparin).[231,234] Naturally acquired immunity to malaria is largely directed against extracellular merozoites,[235] and protects semi-immune individuals from developing severe forms of the disease. Yet, there is no drug that targets the process of invasion of erythrocytes,[44] although some candidates are known.[236] The recent advent of whole attenuated parasite vaccines is accompanied by concerns about production, distribution and safety,[53] while the limited protection obtained after vaccination with subunit vaccines[237,238] emphasizes the need for alternative treatment and vaccination strategies.

Nanotechnology provides promising tools for designing innovative structures that could be used to combat complex infections,[178,179,239] but as yet has been applied only sparsely to malaria, and was focused on systems for drug or vaccine delivery.[195] With other pathogens, mainly bacteria and viruses, few lipid-based nanostructures have been evaluated for inhibition of host-pathogen interactions.[183] However, liposomes, which are the most simple membranous nanostructures that ensure lateral mobility of receptors for multivalent ligand interaction, possess poor stability and structural integrity *in vivo*.[183] Polymer-based vesicles (polymersomes) composed of amphiphilic block copolymers represent an alternative 3D membranous structure for host cell membrane-nanomimics to interact with or to neutralize pathogens in the bloodstream. They have the advantage of a biomimetic membrane structure, a higher stability than liposomes,[240] and long *in vivo* circulation times.[122] Polymersomes have been extensively studied as carriers for active compounds ranging from low molecular mass drugs to proteins and nucleic acids, and they can compartmentalize *in situ* reactions resulting in the development of nanoreactors and artificial organelles.[118] So far, polymersomes have been designed to present viral receptors on their surface for virus-assisted loading of polymersomes[241] or to study viral protein binding.[242] In addition, heparin has been used at the surface of solid nanoparticles to achieve long circulation times in bloodstream for drug delivery in cancer therapy.[243,244]

Here, we introduce nanomimics based on polymersomes that present attachment receptors and thus mimic RBC membranes as a nanotechnological strategy for blocking invasion (drug action) and increased exposure of the infective form of *P. falciparum* to the immune system (vaccine-like action) (Scheme 1).

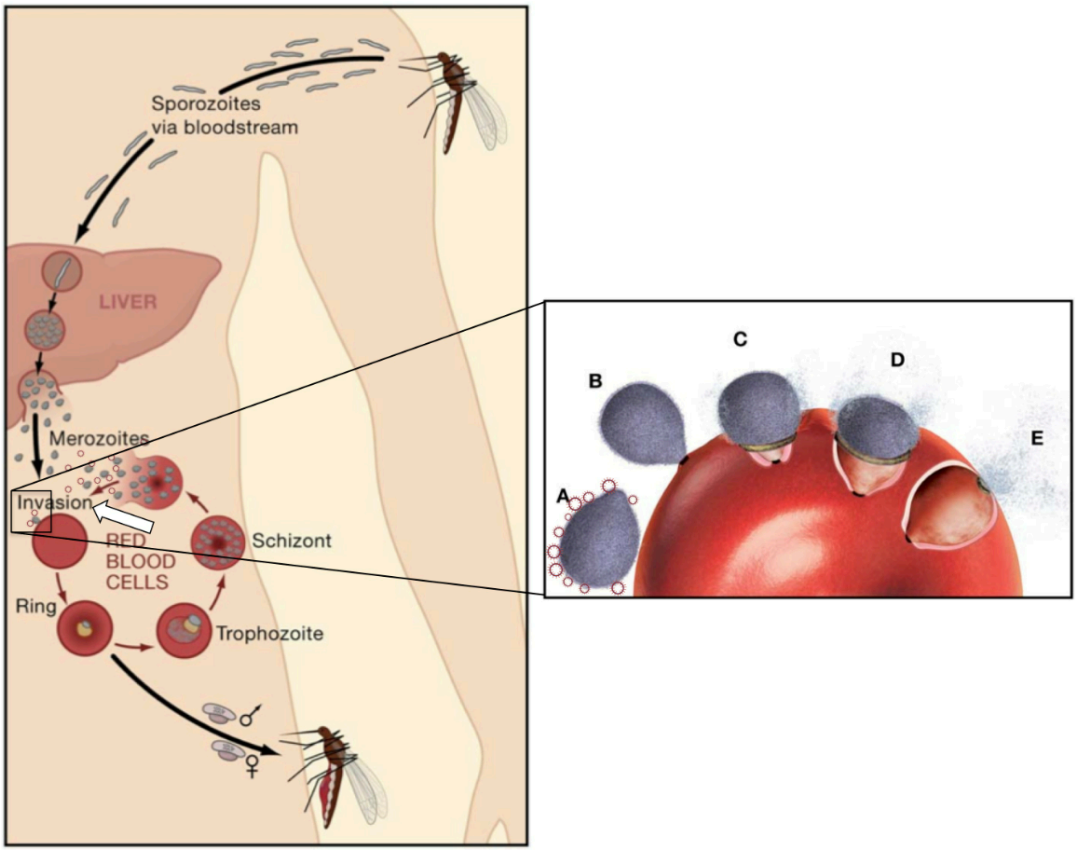

Scheme 1. Schematic presentation of the nanomimic concept. (Left) Life cycle of *P. falciparum* in the human host: an *Anopheles* mosquito injects sporozoites, which pass through Kupffer cells and invade hepatocytes in which merozoites develop and are released into the bloodstream to invade red blood cells (RBCs) after specific attachment to heparan sulfate.[25] In infected RBCs (iRBCs) merozoites develop through schizogeny releasing 16 – 32 daughter merozoites after 48 h, which subsequently invade new RBCs (asexual blood-stage). (Right) Schematic merozoite invasion into RBCs. (A) Initial attachment through binding of the processed ligand $MSP1_{42}$ to heparan sulfate on RBCs.[25] Competing nanomimics (red circles) block fresh merozoites before they enter new RBCs (white arrow) (modified with permission from ref [20]).

Nanomimics were built by self-assembly of a mixture of a polymersome-forming block copolymer with a copolymer based on a hydrophobic block and the host cell receptor as hydrophilic domain. We used *Plasmodium* merozoites as a model to exemplify the concept of efficient blockage of pathogen reinvasion after egress from their host cells *in vitro*. The intrinsic 3D architecture of nanomimics combined with the specificity of heparin selected as receptor represents an essential step to gain efficacy by exposing multiple receptors on one nanomimic,

which serve to block the parasite in a multivalent binding fashion. Due to the use of this key receptor of host cell membranes, it is expected to open efficient directions in addressing other infections that rely on the same receptor and have a similar way of reproduction.

3.3 Results and Discussion

3.3.1 Block Copolymer Synthesis

Heparan sulfate has been shown to play a critical role as a receptor for the initial attachment of merozoites to RBCs;[25,28] therefore we selected the closely related heparin, which is a potent inhibitor of merozoite invasion of RBCs *in vitro,*[25] for exposure on the exterior surface of nanomimics. Heparin is commercially readily available and has a closely related chemical structure to other sugar chains that have been reported as bioactive without anticoagulation property (*e.g.,* K5 polysaccharide).[25] We prefer heparin as a receptor model to be exposed on nanomimics, as it is a very well-known macromolecule, which serves as a straightforward proof of concept; related polysaccharides such as K5 or nonanticoagulant heparin will be then used for the optimization of nanomimics.

To produce model nanomimics, two different block copolymers were synthesized. The biocompatible, polymersome-forming ABA block copolymer poly(2-methyl-2-oxazoline)-*block*-poly(dimethylsiloxane)-*block*-poly(2-methyl-2-oxazoline) (PMOXA-*b*-PDMS-*b*-PMOXA, Table 1, Figure 15A, **1**) was synthesized as previously published,[136,245] and the PDMS-*b*-heparin block copolymer (Figure 15A, **2**) was synthesized by coupling a commercial PDMS block with the commercial heparin polysaccharide (Scheme 2).

Table 1. Polymer characteristics. Mw/Mn was calculated using the corresponding GPC data. Block lengths and molecular weight were determined from ^{1}H NMR.

Composition (NMR)	M_n (GPC) [g/mol]	M_w (GPC) [g/mol]	M_w/M_n	M_n (^{1}H-NMR) [g/mol]
$PMOXA_5$-$PDMS_{64}$-$PMOXA_5$	2920	7311	2.5	5587
$PMOXA_5$-$PDMS_{58}$-$PMOXA_5$	2730	6662	2.4	5143
$PMOXA_9$-$PDMS_{67}$-$PMOXA_9$	3455	7482	2.2	6490

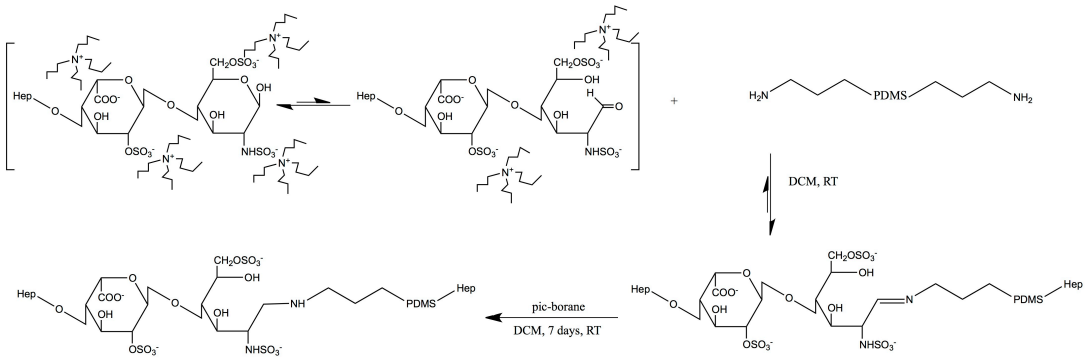

Scheme 2. Scheme for PDMS-*b*-heparin (**2**) synthesis. Tetrabutylammonium salt of heparin reacted with PDMS(NH_2)$_2$ in DCM with 2-picoline borane as reducing agent for 7 days yielded PDMS-*b*-heparin.

A critical step was the solubilization of heparin in organic solvents, which is not possible with commercial sodium salt of heparin, but was needed for PDMS-*b*-heparin synthesis and nanomimic formation. Therefore, it was first hydrophobized by ion exchange from sodium to tetrabutylammonium,[246] which exchanged again with sodium during nanomimic purification. ^{1}H NMR after reaction, purification, and ion exchange indicated successful coupling of PDMS with heparin (Figure 14C).

The reductive amination used for PDMS-*b*-heparin synthesis is a mild reaction; the reducing agent is specific to imines.[247] This specific reaction ensured that heparin was modified with PDMS only at its natural anchor point – leaving the rest of the chain unmodified. Farndale microassays, in which positively charged dye molecules align on heparin chains resulting in a metachromatic shift in the absorption spectrum, were performed in ethanol to obtain a rough estimation of the number of saccharide units per PDMS chain (5 kDa). Tetrabutylammonium heparin in ethanol was used to generate a calibration curve, and by comparing to the absorption values found for PDMS-*b*-heparin the number of saccharide units per PDMS chain was calculated to be about 25 (in total 11 kDa).

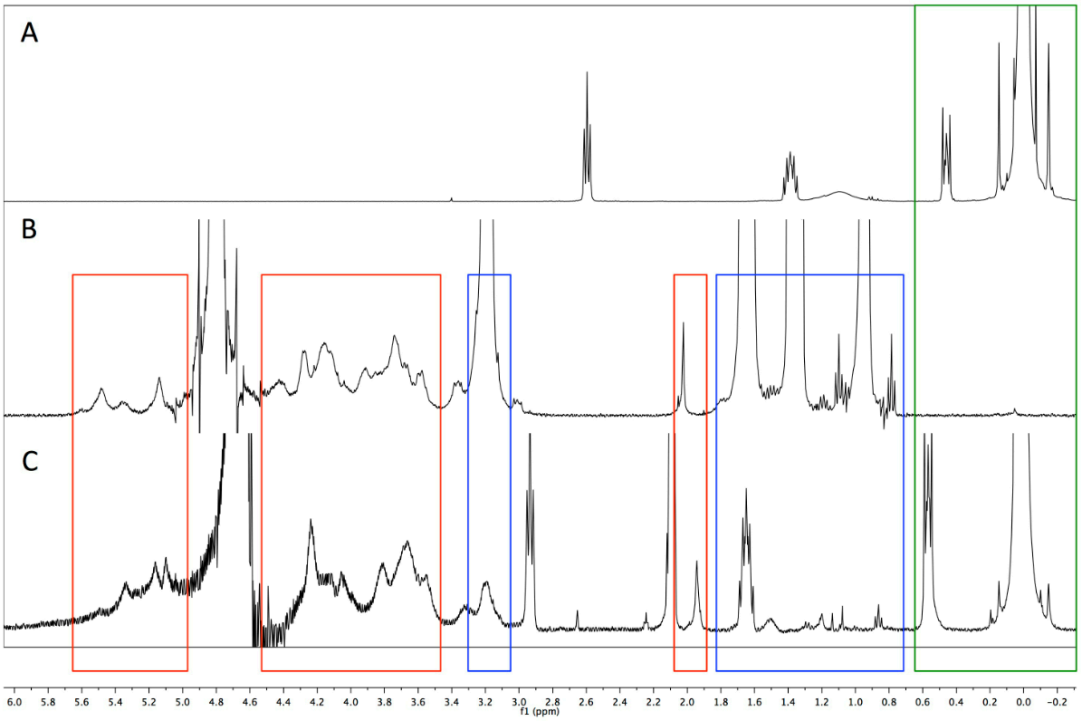

Figure 14. Comparison of ^{1}H NMR (400 MHz, δ) spectra of PDMS(NH_2)$_2$ (A, $CDCl_3$), tetrabutylammonium salt of heparin (B, D_2O) and PDMS-*b*-heparin after purification and ion exchange to Na^+ (2, C, D_2O/acetone-d_6 (3:1)). Red squares indicate anomeric protons (5.6 – 5.0 ppm), fingerprint region (4.5 – 3.4 ppm), and *N*-acetyl (CH_3) of heparin. Blue squares show the protons of tetrabutylammonium. Green square represents protons of siloxane units and adjacent methylene protons. Integrals and corresponding numbers of protons are not indicated, because solubilization of the product (2) was not optimal; the two blocks have opposite characteristics (hydrophobic, very hydrophilic). D_2O was needed to observe the characteristic heparin peaks in the copolymer, but this is a bad solvent for PDMS, leading to line broadening for the PDMS part. Nevertheless, the characteristic peaks of heparin (anomeric-, fingerprint-, *N*-acetyl protons) and PDMS were observed after reaction, purification and ion exchange.

3.3.2 Preparation and Characterization of Nanomimics

Nanomimics were self-assembled by the bulk rehydration technique using a mixture of PMOXA-*b*-PDMS-*b*-PMOXA with 25 % (w/w) PDMS-*b*-heparin block copolymer. Since heparin (mean 11 kDa, 25 saccharide units) of PDMS-*b*-heparin is a longer polymer than PMOXA (max. 0.8 kDa, 5 to 9 oxazoline units) of PMOXA-*b*-PDMS-*b*-PMOXA and PDMS blocks were similar in both copolymers (mean 5 kDa, 63 siloxane units), only a small part of heparin was shielded by PMOXA, while the rest was accessible for protein interaction (Figure 15D,E).

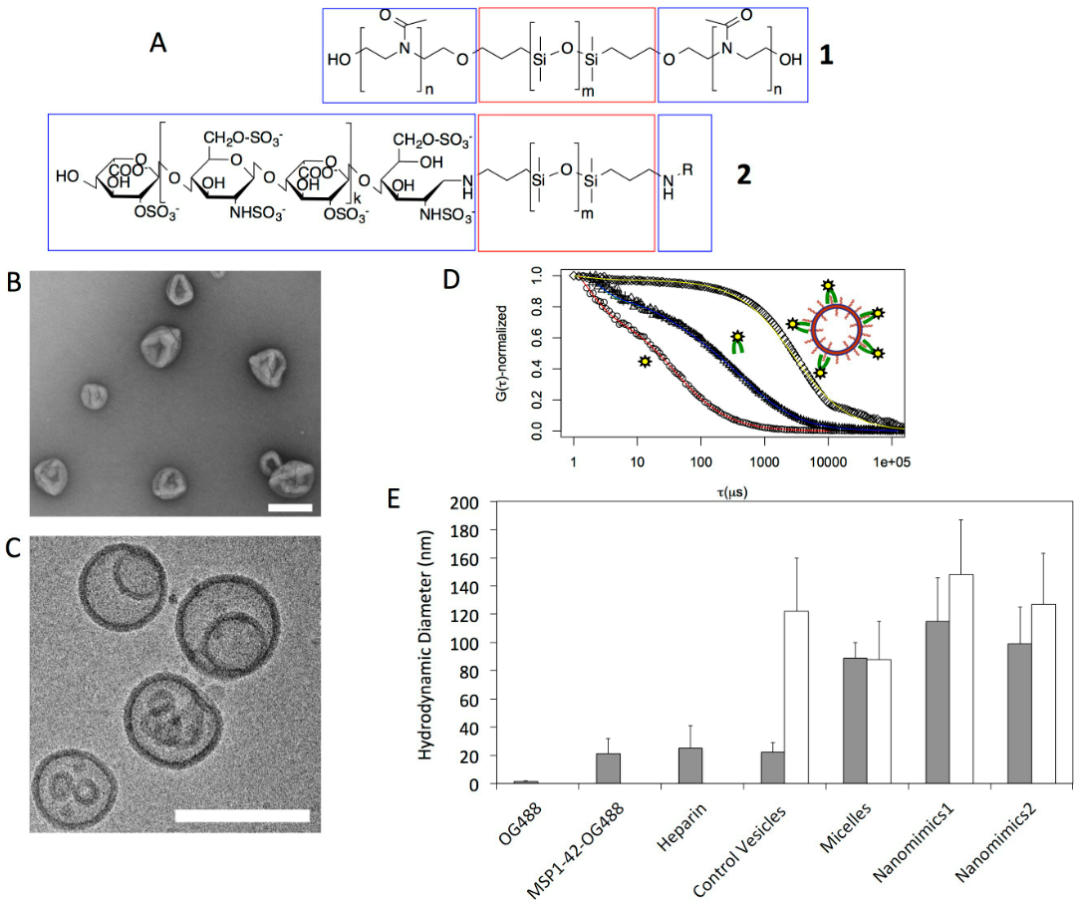

Figure 15. Characteristics of nanomimics. (A) Chemical structure of PMOXA-*b*-PDMS-*b*-PMOXA (1) and PDMS-*b*-heparin (2). R is either a proton or another heparin chain. (B) TEM image of nanomimics. (C) Cryo-TEM of the same nanomimics. Scale bars 200 nm. (D) Normalized autocorrelation curves from FCS data in PBS: free OG488 (red), free *Pf*MSP1$_{42}$-OG488 (blue), control polymersomes with *Pf*MSP1$_{42}$-OG488 (green), and nanomimics with *Pf*MSP1$_{42}$-OG488 (yellow). (E) Hydrodynamic diameters (D_H) obtained from mixtures of *Pf*MSP1$_{42}$-OG488 with controls (free heparin or control polymersomes) and nanomimics (gray bars). Data from dynamic light scattering are included for the nanostructures for comparison (white bars). Only when heparin was present on the surface of nanostructures (micelles, nanomimics) and mixed with *Pf*MSP1$_{42}$-OG488 did the diffusion time shift to the corresponding nanostructure–size, indicating that *Pf*MSP1$_{42}$-OG488 bound to the nanostructures. Mixtures with free heparin or control polymersomes yielded no difference from free *Pf*MSP1$_{42}$-OG488 diffusion (errors are ± standard deviation).

Dynamic light scattering (DLS) revealed hydrodynamic nanomimic diameters (D_H) of about 132 ± 34 nm (average of eight independent samples ± standard deviation) (Table 2). DLS and static light scattering (SLS) performed on four representative nanomimic samples provided R_g/R_H values of ρ = 0.90 – 0.99, as expected close to the value of 1.0 for ideal hollow spheres (vesicles),[248] and thus indicating the vesicular structure of nanomimics (Table 2).

Table 2. Sample characteristics: heparin content (Farndale microassays), hydrodynamic diameters (D_H) from FCS and DLS measurements. D_H and diameter of gyration (D_g) and corresponding ρ-value from DLS/SLS measurements. Diameters from TEM and cryo-TEM images. (Values are mean ± standard deviation)

	Heparin content (µg/ml)	FCS D_H (nm)	DLS1 D_H (nm)	DLS2 D_H (nm)	SLS D_g (nm)	ρ-value = R_g/R_H	TEM D (nm)	cryo-TEM D (nm)
Nanomimics1-A	49.3	203±102	148±39	262±15	244±5	0.93	111±38	101±33
Nanomimics1-B	55.3	-	123±30	212±2	190±4	0.90	120±34	-
Nanomimics1-C	63.8	170±67	126±35	-	-	-	119±29	-
Micelles1	43.1	-	77±25	-	-	-	-	-
Nanomimics2-A	69.8	188±40	150±32	193±3	192±3	0.99	125±39	-
Nanomimics2-B	45.5	-	127±36	-	-	-	123±40	-
Nanomimics2-C	72.6	182±69	132±30	179±2	163±2	0.91	116±33	-
Nanomimics2-D	34.6	184±78	125±35	-	-	-	105±28	-
Micelles2	86.2	-	88±27	-	-	-	-	-

Transmission electron microscopy (TEM) and cryogenic-TEM (cryo-TEM) confirmed these vesicle sizes and illustrated the membranous structure of these nanomimics (Figure 15B,C, Figure 16). TEM micrographs showed collapsed nanomimics (D = 111 ± 38 nm, Figure 15B), which clearly distinguished them from filled nanoparticles. Nanomimics retained their spherical structure (D = 101 ± 33 nm, Figure 15C) during cryo-TEM imaging and revealed a vesicle-in-vesicle structure and a membrane thickness of 10.9 ± 1.4 nm. By increasing the PDMS-*b*-heparin content in nanomimics a transition to micelles was observed. Nanomimics prepared with increasing PDMS-*b*-heparin content (35 % - 65 % w/w) yielded mixtures of polymersomes and worm-like micelles (35 %, 45 %) and finally aggregated micelles (55 %, 65 %) (Figure 17). Self-assembly of PDMS-*b*-heparin copolymer alone yielded aggregated micelles with a D_H of about 83 ± 26 nm (DLS) (Table 2, Figure 16D,H). This demonstrates that nanomimics (25 % w/w) consist of a real mixture of both copolymers; otherwise we would have observed aggregated micelles in the samples containing those nanomimics. Nanomimics with 25 % (w/w) PDMS-*b*-heparin were used in all subsequent experiments. Furthermore, stopped-flow measurements on nanomimics revealed their permeability for water but not solutes. This was concluded due to nanomimic shrinkage upon applied osmotic pressure by doubling the salt concentration outside of nanomimics.[35]

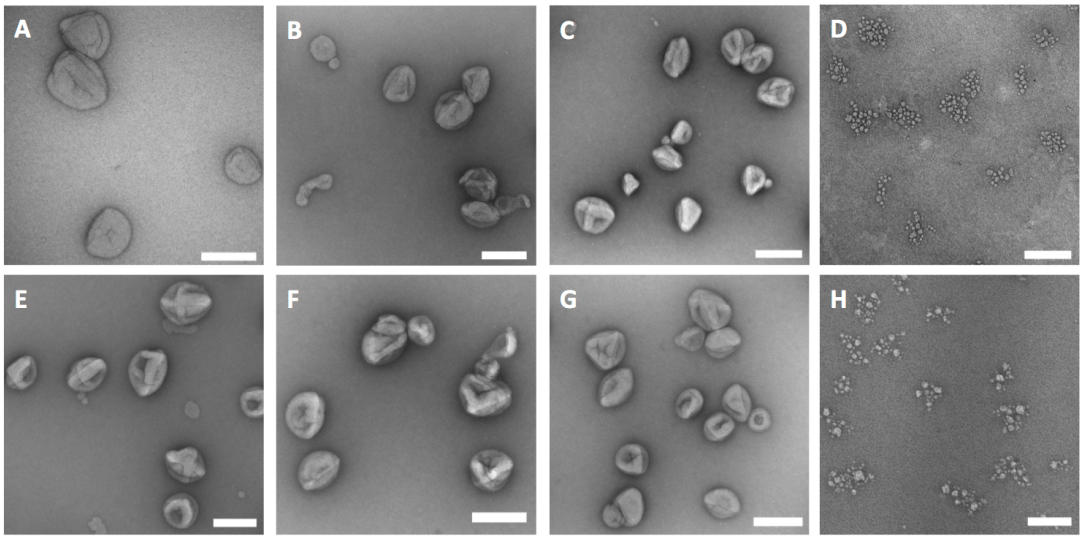

Figure 16. Transmission electron microscopy (TEM) of different preparations of nanomimics and micelles. (A) Control polymersomes built from PMOXA-*b*-PDMS-*b*-PMOXA. (B, C, E-G) Nanomimics (25% (w/w) PDMS-*b*-heparin) prepared from different mixtures of different batches for both polymers. (D, H) PDMS-*b*-heparin aggregated micelles. (Scale bars 200 nm)

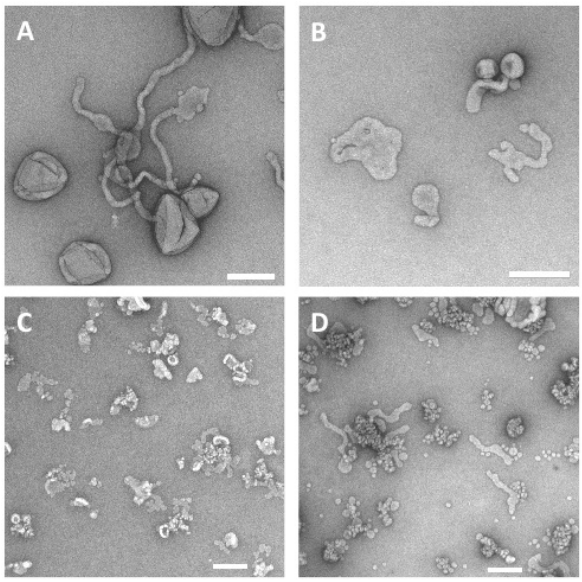

Figure 17. Transmission electron microscopy (TEM) of nanomimic preparations using higher ratios of PDMS-*b*-heparin to PMOXA-*b*-PDMS-*b*-PMOXA. Nanomimics with 35% (w/w) PDMS-*b*-heparin (A), 45% (w/w) PDMS-*b*-heparin (B), 55% (w/w) PDMS-*b*-heparin (C), and 65% (w/w) PDMS-*b*-heparin (D). (Scale bars 200 nm)

Hydrophilic sulforhodamine B (SRB) was encapsulated in the aqueous core of nanomimics for visualization and both D_H and the concentration of the nanomimics were obtained with fluorescence correlation spectroscopy (FCS) by comparing diffusion time of the free dye with that of the encapsulated dye. The concentration of the nanomimics obtained by FCS was 71 ± 18 nM (2.8 mg/mL PMOXA-*b*-PDMS-*b*-PMOXA, 0.93 mg/mL PDMS-*b*-heparin); this value was

subsequently used to calculate the number of nanomimics necessary to obtain an effect in the antimalarial assay (Figure 22).

Farndale microassays in aqueous solution were performed to quantify the amount of surface-accessible heparin on nanomimics after purification (Figure 18). Calibration curves (Figure 18A) were produced with the same heparin solution that was subsequently used in *in vitro* assays (Figure 22) to ensure comparability of assays. PMOXA-*b*-PDMS-*b*-PMOXA polymersomes did not influence the absorbance spectrum of the dye in the range of interest (Figure 18B). Due to the random character of the self-assembly process underlying nanomimic formation, not all PDMS-*b*-heparin added led to surface-exposed heparin in the final nanomimics; a fraction of the heparin chains will face toward the vesicle core, few will be hidden in the membrane or in the nanomimic core (vesicle-in-vesicle structures), and a few free PDMS-*b*-heparin or free heparin chains not incorporated in the membrane were removed during purification. However, Farndale microassays allowed us to quantify the amount of heparin exposed at the outer surface of the nanomimics.

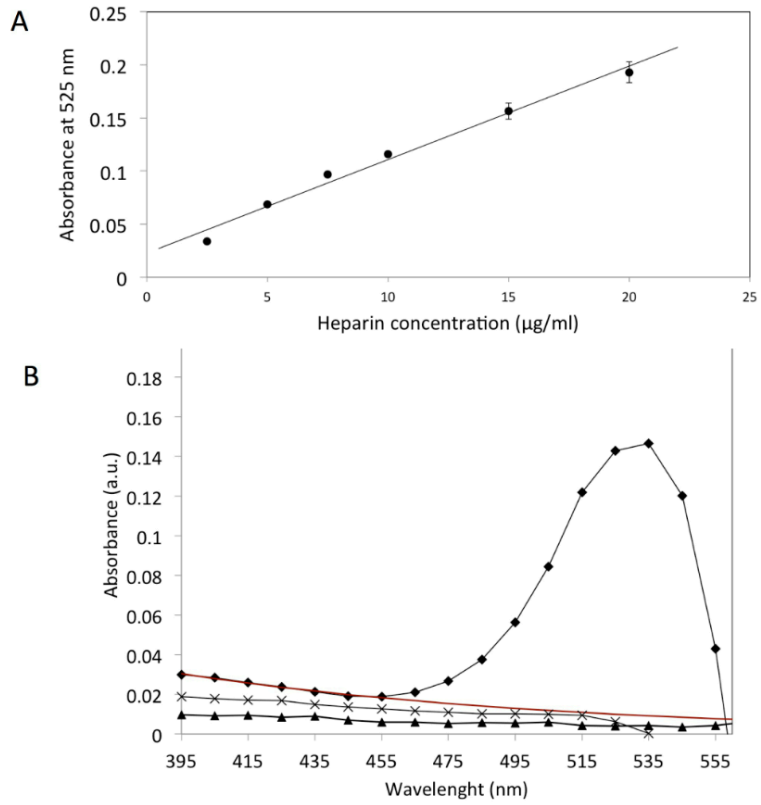

Figure 18. Farndale microassay. (A) Calibration curve produced with a series of free heparin concentrations in duplicates. (B) Example of a UV-Vis absorbance curve for nanomimics (black squares), control polymersomes (black triangles), and control polymersomes with encapsulated tetrabutylammonium heparin (black crosses). Baseline was corrected due to light scattering of the nanomimic-samples (red curve).

Importantly, nanomimic formation yielded detectable amounts of heparin being incorporated in the membrane after purification, whereas formation with PMOXA-*b*-PDMS-*b*-PMOXA and the tetrabutylammonium salt of heparin did not (Figure 18B). In total, three independent PDMS-*b*-heparin and three PMOXA-*b*-PDMS-*b*-PMOXA batches were used (Table 1). Nanomimics1 and micelles1 were built from the same batch of PDMS-*b*-heparin; nanomimics2 and micelles2 were made from two other batches of PDMS-*b*-heparin. Typical nanomimic samples, theoretically containing 2.5 mg/mL PMOXA-*b*-PDMS-*b*-PMOXA and 0.83 mg/mL PDMS-*b*-heparin copolymer, yielded 57 ± 13 µg/mL (mean ± standard deviation) surface-exposed heparin after purification (Table 2). If combined with the nanomimic concentrations obtained by FCS measurements, there are about 74 ± 30 heparin chains (11 kDa) exposed on the outer surface of one nanomimic. Zeta potential measurements performed on nanomimics (-32.4 ± 4.1 mV, average of eight nanomimic samples) and control polymersomes (+5.4 ± 0.2 mV) confirmed the presence of negatively charged groups on nanomimics in contrast to pure PMOXA-*b*-PDMS-*b*-PMOXA vesicles.

To validate the toxicity of nanomimics on cultured cells, a cell viability test was performed using HeLa cells and a representative nanomimic sample (2.9 mg/L PMOXA-*b*-PDMS-*b*-PMOXA, 49.3 µg/mL accessible heparin) (Figure 19). This test demonstrated the absence of any cell toxicity of nanomimics up to the maximum concentration of 290 µg/mL PMOXA-*b*-PDMS-*b*-PMOXA and 4.9 µg/mL surface-exposed heparin, which was an even higher concentration than the highest concentration used in the antimalarial assays (Figure 22).

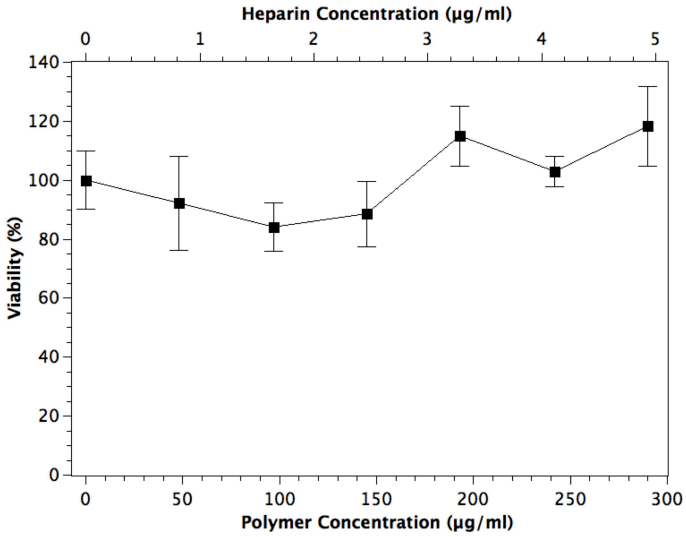

Figure 19. Cell toxicity test with nanomimics. HeLa cell viability is shown versus polymer (bottom) and heparin (top) concentration using a representative nanomimic sample.

3.3.3 Nanomimics Bind *Plasmodium* Merozoite Proteins Involved in Initial Attachment

FCS also allows the analysis of protein binding to nanoobjects by comparing diffusion times of freely diffusing and bound proteins labeled with fluorescent molecules.[97] For the FCS measurements, OregonGreen was used to label the *P. falciparum* (clone 3D7) major surface protein 1-42 (*Pf*MSP1_{42}-OG488), which has been identified as the ligand for heparin-like receptors.[25] The difference in diffusion times between *Pf*MSP1_{42}-OG488 and *Pf*MSP1_{42}-OG488 bound to nanomimics was used to verify that the surface of nanomimics contained accessible heparin molecules, and that they were able to bind merozoite proteins (Figure 15D,E). No binding of *Pf*MSP1_{42}-OG488 occurred with polymersomes without heparin. In contrast, nanomimics and PDMS-*b*-heparin micelles bound significant amounts of *Pf*MSP1_{42}-OG488 (from 5 up to 12 *Pf*MSP1_{42}-OG488 per nanomimic, Figure 15D,E). Therefore, strong multivalent binding of several *Pf*MSP1_{42}-OG488 on one parasite with several heparin chains on one nanomimic is possible, which is an important parameter for invasion inhibition. Furthermore, the interaction of *Pf*MSP1_{42}-OG488 with heparin on artificial membranes seems to be a high-affinity interaction; otherwise no binding would have been observed by FCS.[98] Although heparin has a slightly different structure compared to heparan sulfate, the FCS results provided evidence for high-affinity binding in contrast to previous suggestions that the initial attachment of merozoites to RBCs is a low-affinity interaction.[20] Thus, it is possible that the low abundance of heparan sulfate on RBCs (~2000 chains per RBC)[28] providing only one or a few sugar chains per merozoite for initial attachment is sufficiently strong not only to attach to the RBC but also to allow for subsequent interaction with other receptors for stronger attachment and subsequent reorientation (Scheme 1).

3.3.4 Nanomimics Block Invasion of and Expose *Plasmodium* Merozoites

To test whether our nanomimics could competitively bind freshly egressed merozoites and therefore block RBC invasion *in vitro*, we incubated a mixture of RBCs and late stages of infected RBCs (iRBCs) with these nanomimics for 3 h. During this time, merozoites start to be released and invade new RBCs. After incubation with fluorescent nanomimics fluorescence imaging showed both binding of nanomimics to merozoites and lack of RBC invasion (Figure 20C-E). Extracellular merozoites lose their invasive capacity after 5 min at 37 °C;[249] therefore if merozoites with surface-bound nanomimics appear in culture, they already lost their ability to infect new RBCs (Figure 20C-E). In addition, agglutination of merozoites and nanomimics (Figure 20C) and nanomimic binding

to iRBC just during merozoite egress were observed (Figure 20B), whereas intact iRBCs and RBCs did not bind nanomimics. Polymersomes without heparin did not bind any of the cells present (RBCs, iRBCs, or merozoites) and could therefore not block invasion; only very few merozoites can be found in the controls (Figure 20A).

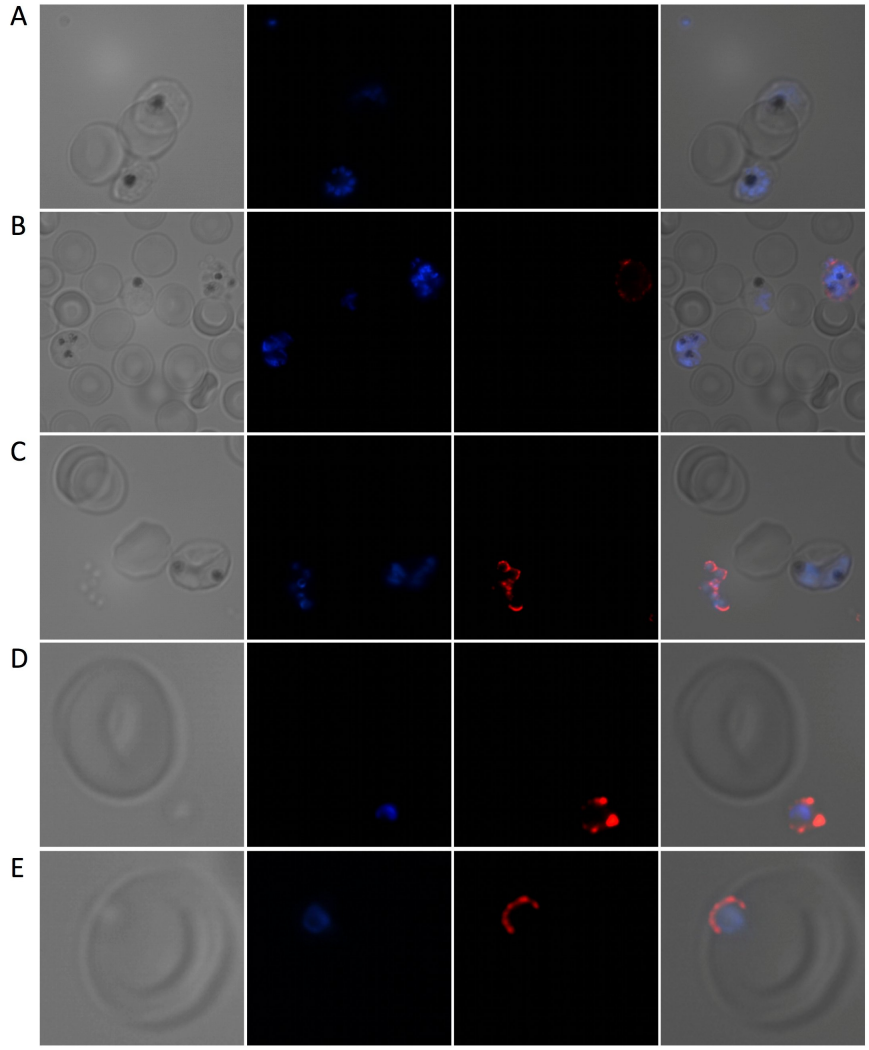

Figure 20. Inhibition of merozoite invasion by nanomimics. (A) Control polymersomes (PMOXA-*b*-PDMS-*b*-PMOXA only) did not bind to merozoites, RBCs, and iRBCs. (B) SRB-filled nanomimics (red) bound to schizonts during merozoite egress, but not to intact iRBCs (all stages) and RBCs; iRBCs and RBC appear normal. (C-E) Merozoites (blue) were inhibited by nanomimics (red) from entering into fresh RBCs. Left: DIC, middle: DAPI (blue) and SRB (red), right: merge. In these images and all the following images with *in vitro* malaria cultures, RBCs serve as the scale bar. RBC diameter is about 7 µm. iRBCs can be distinguished from RBCs by black appearing hemozoin crystals present within iRBCs, originating from hemoglobin digestion and subsequent hematin crystallization.

The merozoite-nanomimic interaction was further examined by super–resolution 3D structured illumination microscopy (3D-SIM), and electron microscopy (EM) of ultrathin sections of merozoite-nanomimic complexes (Figure 21). 3D

reconstruction of merozoites with surface-bound nanomimics showed that several dozens of nanomimics bound to a single merozoite (Figure 21A). The EM images of ultrathin sections revealed nanomimics attached to the outer membrane of merozoites (Figure 21C), which was not found in a preparation without nanomimics (Figure 21B). This revealed that nanomimics blocked the docking sites on merozoites, whereas no fusion of nanomimic- and parasite membrane occurred.

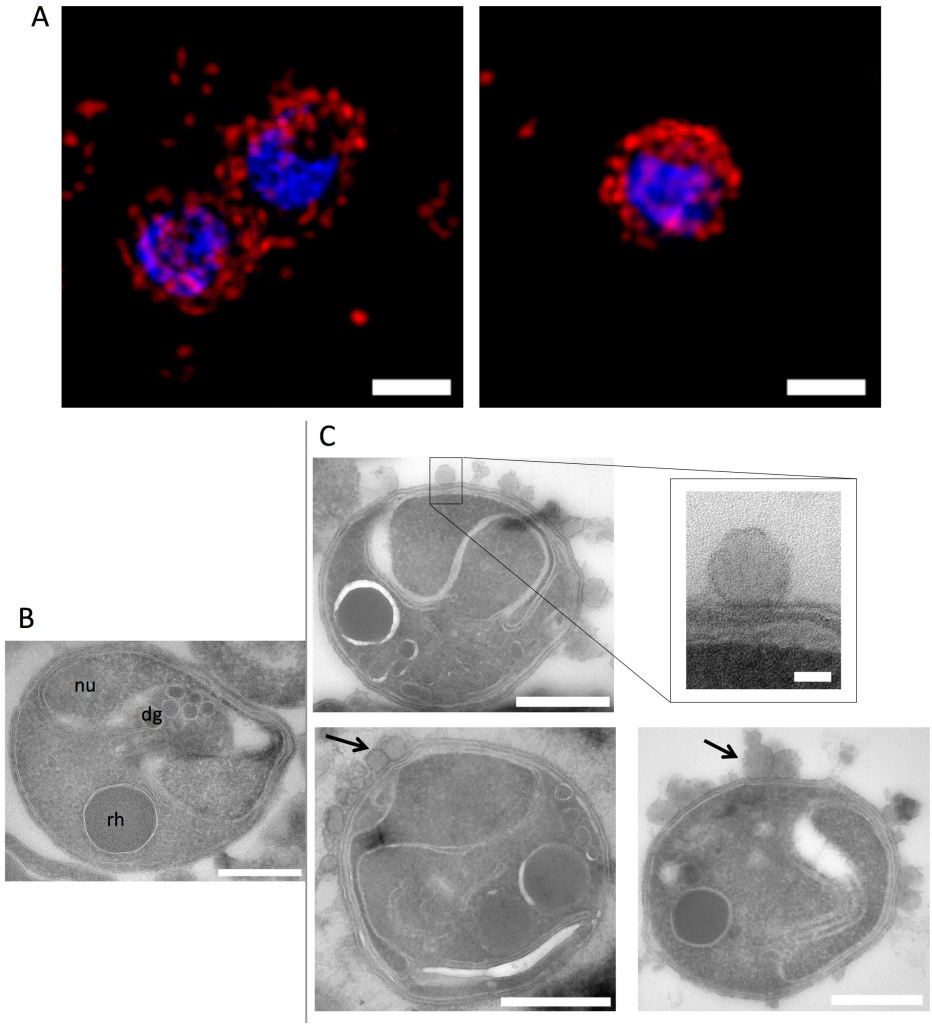

Figure 21. Merozoites bound with nanomimics. (A) Projections of merozoites (DAPI, blue) blocked by SRB-filled nanomimics (red, scale bars, 1 µm) recorded with super–resolution 3D structured illumination microscopy (3D-SIM). (B) TEM of an ultrathin section of a control merozoite (scale bar, 500 nm). (C) TEM of ultrathin sections of merozoites with nanomimics on the surface (scale bars, 500 nm) and higher magnification of a surface-bound nanomimic (scale bar 50 nm). Lipid membranes (light) can be distinguished from the polymer membrane of nanomimics (dark) and the size of the surface-bound nanomimics is in agreement with the diameters of nanomimics (Figure 15B,C). Rhoptries (rh), nucleus (nu) and dense granules (dg) of merozoites can be seen clearly. Some nanomimics are indicated with a black arrow.

3.3.5 Efficacy of Invasion Inhibition by Nanomimics

The inhibitory effect of nanomimics on the parasite life cycle was determined by a growth inhibition assay using a *P. falciparum* (clone 3D7) suspension culture in 24-well plates, which better mimics the *in vivo* situation by using suspension cultures with a higher hematocrit than usually used for measurements of drug effects (typically 1 %).[250] Invasion–inhibition curves with free heparin, nanomimics, and PDMS-*b*-heparin micelles (Figure 22) show a significant difference in IC_{50} values between free heparin and nanomimics or PDMS-*b*-heparin micelles (Figure 22A).

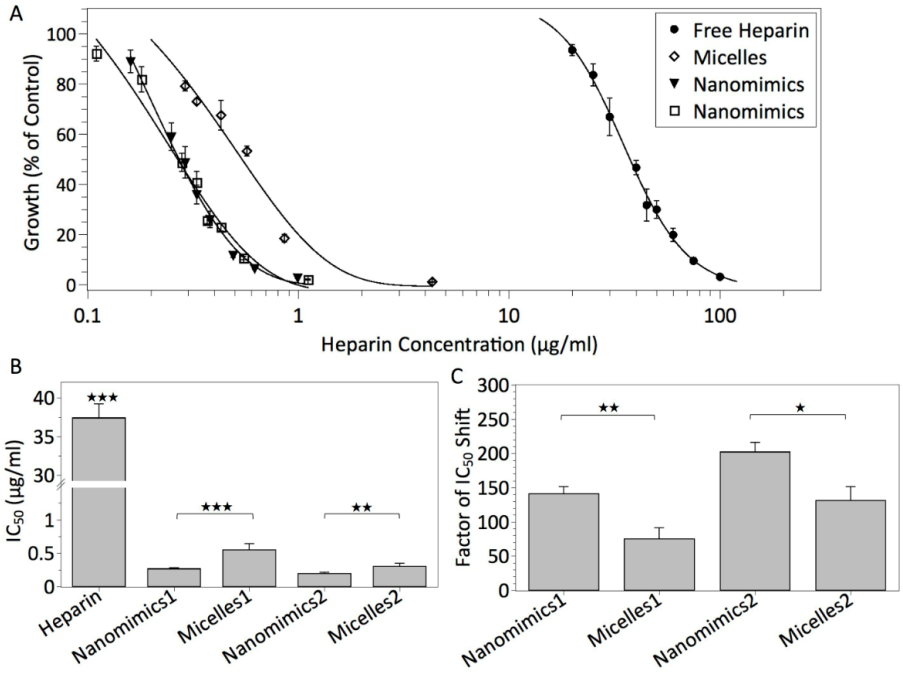

Figure 22. Growth inhibition by free heparin and nanomimics. (A) Free heparin inhibits growth of *P. falciparum* (3D7) in the suspension assay. Micelles built from PDMS-*b*-heparin and nanomimics inhibit merozoite invasion more efficiently than free heparin (data from five independent invasion inhibition experiments, all data points are mean growth ± standard error from at least three duplicate assays for each), presented as percentage of control (PBS)). (B) IC_{50} values for free heparin (n = 7) compared to heparin-loaded nanomimics (n1 = 9, n2 = 12) or micelles (n1 = 4, n2 = 3) indicating the importance of nanostructured heparin for increased activity. Nanomimics1 and micelles1 were built from the same batch of PDMS-*b*-heparin; nanomimics2 were made from two other batches of PDMS-*b*-heparin (mean values ± standard error for three independent experiments for each sample). (C) Comparison of nanomimics and micelles expressed as factor of x difference in IC_{50} values for nanostructures compared to free heparin (mean values ± standard error for three independent experiments for each sample). Statistics were analyzed using Student's *t*-test: $^{\star}p< 0.05$, $^{\star\star}p< 0.01$, $^{\star\star\star}p< 0.001$.

All parasites were blocked at the highest heparin, nanomimic, or micelle concentrations. IC_{50} values dramatically decreased from 37.4 ± 4.7 µg/mL (2.5 µM for free heparin) to 0.197 ± 0.047 µg/mL for the best preparation of nanomimics

(13 nM of heparin on nanomimics2) (Figure 22B). This corresponded to a decrease in IC_{50} value of more than 2 orders of magnitude (Figure 22C), which indicates a very highly efficient inhibitory effect of the nanomimics. The highest concentration of nanomimics tested contained about 60 µg/mL of the polymersome-forming PMOXA-*b*-PDMS-*b*-PMOXA and about 1 µg/mL surface-accessible heparin. Polymersomes consisting of PMOXA-*b*-PDMS-*b*-PMOXA without PDMS-*b*-heparin or PMOXA-*b*-PDMS-*b*-PMOXA vesicles with encapsulated tetrabutylammonium heparin had no effect on the parasite life cycle at similar concentrations (60 µg/mL); parasitemia reached the same values as in control wells with PBS only. A solution of free tetrabutylammonium heparin after size exclusion chromatography (as we do with nanomimics) was also not active at concentrations similar to the highest heparin concentration used in the case of nanomimics (about 1 µg/mL). The IC_{50} value for free heparin was 2-fold higher than previously published,[25] most probably due to the higher hematocrit (5%) and suspension culture. Nanomimics with different ratios of PDMS-*b*-heparin to PMOXA-*b*-PDMS-*b*-PMOXA were also tested in order to find the optimum mixture. Nanomimics containing 25 % (w/w) PDMS-*b*-heparin provided the best balance in terms of efficacy and control over self-assembly (exclusively spherical vesicles). Nanomimics were also significantly more effective than micelles self-assembled from PDMS-*b*-heparin only, most likely because the membranous structure of the nanomimics allowed lateral diffusion of receptors for multivalent interactions.[183] This demonstrates the advantage of using membranous nanomimics compared to micellar or solid nanostructures.

Considering that the active inhibitors are nanomimics themselves – no drug is released from the nanostructure – then IC_{50} value can also be presented in "nanomimic-concentrations". The nanomimic concentration was determined by FCS in PBS (71 ± 18 nM for nanomimics at 2.8 mg/mL PMOXA-*b*-PDMS-*b*-PMOXA and 0.93 mg/mL PDMS-*b*-heparin concentrations). Combining this value with the antimalarial assay results in an IC_{50} value of 0.27 ± 0.09 nM for the nanomimics (five independent samples, three invasion inhibition assays). Therefore, one nanomimic is about as active as 10'000 heparin chains. This significantly higher inhibitory activity of nanomimics compared to free heparin (> 2 orders of magnitude) is explained by multivalent interactions between a multitude of heparin molecules exposed on a single nanomimic with a multitude of *Pf*MSP1_{42} molecules on each merozoite (max. 12 *Pf*MSP1_{42}-OG488 per nanomimic measured), confirming results from binding assays. Indeed, nanomimics represent "macroscopic" objects when compared to free heparin, and thus the binding of a few nanomimics was sufficient to block merozoites from entering fresh RBCs,

while a very large number of free heparin molecules (~10'000 times more) was required for such an effect. Our nanomimics block pathogens using the combined effect of a spatial architecture with a specific, exposed receptor of host cell membranes.

3.4 Conclusions

Nanomimics of host cell membranes were successfully produced by a simple self-assembly procedure without postformation modifications, which uses a mixture of polymersome-forming block copolymer with a copolymer that consists of a hydrophobic block and a specific host cell receptor. The resulting 3D-nanoobjects (nanomimics) very efficiently blocked invasion of RBCs by *P. falciparum* merozoites as compared to soluble receptors, which can be explained by strong multivalent binding of nanomimics to merozoites. This might offer an interesting treatment option for severe malaria when prevention of reinvasion of parasites is of highest priority. Simultaneously, similar to soluble heparin such nanomimics treatment would be expected to reverse the two major pathogenic events in *P. falciparum* infections – sequestration and rosetting – *in vitro* and *in vivo* and thus immediately would reduce pathology.[230,231]

As an additional benefit, our nanomimic strategy will keep a large number of merozoites artificially extracellular after egress. Circulation of a large number of free merozoites does not naturally occur, and it might be speculated whether these merozoites bound to nanomimics represent a strong immunogen and might elicit a strong immune response against all merozoite antigens. Because this would happen during a natural or controlled[251] infection, it would avoid many problems associated with subunit or attenuated merozoite vaccines.[53] However, it remains to be tested as to whether such induced immunity is superior to responses derived from any natural infection or from recombinant antigens.

Thus, our strategy of interrupting the parasite life cycle using nanomimics and then subsequently eliciting an immune response represents a promising alternative to current drug treatment and vaccination strategies.[251] Further, nanomimics offer theoretically a unique possibility of encapsulating high concentrations of adjuvants or other immune modulators, which could be released after phagocytosis to enhance immunogenicity. We have used these nanomimics to interrupt the life cycle of malaria parasites as a proof of principle, but a variety of other pathogens also use host cell heparan sulfate for initial attachment;[224] therefore this technology might be much more widely applied to inhibit other infections.

CHAPTER 4

4 Analysis of Molecular Parameters Determining the Antimalarial Activity of Polymer-Based Nanomimics

This chapter contains the description of nanomimic variants with more, less, or shorter receptor molecules presented on the surface and the corresponding effect on antimalarial activity. Furthermore, interaction parameters of the nanomimic receptor with the parasite ligand was studied in detail and revealed high affinity interactions.

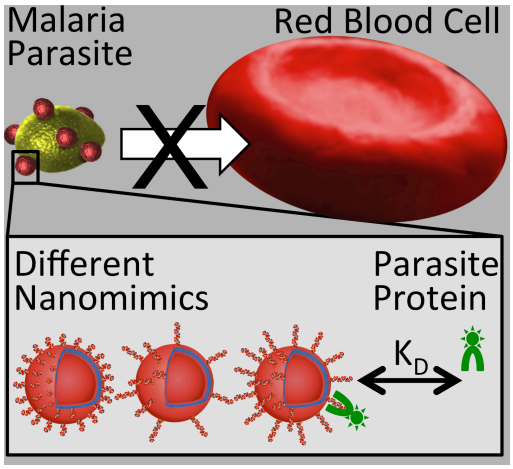

This study has been published and was reprinted and modified herein with permission from reference [252]. Copyright (2015) Wiley and Sons.

Najer, A.; Thamboo, S.; Duskey, J. T.; Palivan, C. G.; Beck, H.-P.; Meier, W. *Macromol. Rapid Commun.* **2015**, 36, 1923–1928.

4.1 Abstract

Malaria and other infectious diseases are major global public health problems, which need to be tackled using new technologies to cope with the lack of efficacious vaccines and emerging drug resistance. A recently developed anti-infectious concept based on nanomimics tested with *Plasmodium falciparum* was analyzed for the molecular parameters determining its applicability. Nanomimics – nano-scaled polymer-based mimics of host cell membranes – were designed with a reduced number of surface-exposed malaria parasite receptor molecules (heparin), resulting in less potent invasion inhibition as determined in antimalarial assays. In contrast, when shorter receptor molecules were used to form nanomimics, more molecules were needed to obtain nanomimic potency similar to nanomimics with longer receptor molecules. The interaction of heparin on nanomimics with the processed *Plasmodium falciparum* merozoite surface protein 1-42 (*Pf*MSP1$_{42}$) had a high affinity, K_d = 12.1 ± 1.6 nM, as measured by fluorescence cross-correlation spectroscopy (FCCS). This detailed characterization of nanomimics and their molecular variants is an important step towards defining and optimizing possible nanomimic therapies for infectious diseases.

4.2 Introduction

Polymer vesicles (polymersomes)[240] made form amphiphilic block copolymers are suitable nanocompartments for many biomedical applications such as drug delivery,[61,253] sensing,[254,255] performing reactions in confined spaces (nanoreactors),[118] artificial organelles,[172] and very simplified cell mimics (Chapter 3).[161] To apply polymersomes in the biomedical domain, the introduction, or modification, of surface functionality on the polymersome structure is of great importance in order to prevent deleterious interactions with non-target cells while promoting targeting interactions,[93] obtain long-circulating polymersomes,[144] or block invading pathogens (Chapter 3). Different methods to prepare functionalized polymersomes are based on either introducing the functionality before self-assembly, or modifying pre-formed vesicles.[93] Usually, biomolecules (*e.g.* targeting ligands) are attached to the hydrophilic blocks of block copolymers, but we have shown that using a biomolecule (in this case heparin) as the sole hydrophilic block is another suitable strategy (Chapter 3). However, this strategy requires a sufficiently long – longer than the hydrophilic block of the membrane-forming block copolymer – and hydrophilic receptor molecule in order to yield modified vesicles with surface-exposed receptors; too short or hydrophobic molecules might be hidden in the membrane and would not be accessible for surface interactions.

Because of the difficulties to develop efficacious vaccines against malaria[256] and other infectious diseases, and the constant threat of emerging drug resistance,[9] innovative approaches to curb these diseases are needed and new technologies will play an important role.[178,239] Malaria is caused by apicomplexan parasites *Plasmodium* spp. and is responsible for more than 600'000 deaths each year.[257] When the parasite reaches the blood-stage in human hosts, the invasive parasite form, called merozoites, invade and reproduce in human red blood cells (RBCs).[20] In the previous Chapter 3, we demonstrated the successful design of host RBC membrane nanomimics, which are polymersomes exposing heparin on the surface, to block malaria parasites from entering host RBCs. This nanomimic concept is based on the interaction of heparin molecules on the surface of nanomimics and merozoite surface proteins (Subchapter 3.3.3). Different merozoite proteins are known to bind to heparan sulfate (HS) on RBCs and soluble heparin, which is a sulfated polysaccharide very closely related to HS.[25,30-32]

Here, we analyzed in detail the interactions of heparin exposed on nanomimics with *Plasmodium falciparum* merozoite surface protein 1 (*Pf*MSP1), in particular the processed 42 kDa fragment *Pf*MSP1$_{42}$, which is one of the most abundant merozoite surface protein that binds HS and heparin.[25,32] We selected fluorescence cross-correlation spectroscopy (FCCS) as a suitable single-molecule detection method to evaluate receptor-ligand interactions.[97,98,258,259] The interaction parameters found allowed to describe the potent invasion inhibitory activity of nanomimics. Furthermore, we studied whether the invasion inhibitory effect of nanomimics against *Plasmodium* parasites was dependent on the total amount, and the length, of surface-accessible heparin exposed on nanomimics. The interaction parameters and activity of modified nanomimics are important to establish a comprehensive framework for future optimization and application of nanomimics against infections.

4.3 Results and Discussion

4.3.1 Effect of Amount and Length of Receptor Molecule of Nanomimics on Antimalarial Activity

To study how the length of the receptor molecule (heparin) exposed on nanomimics affects their antimalarial activity, different PDMS-heparin block copolymers were synthesized based on our previously established method (Chapter 3) and then mixed with polymersome-forming PMOXA-*b*-PDMS-*b*-PMOXA to yield nanomimics. The synthesis of PDMS-*b*-Heparin was first conducted using full-length heparin (mean MW = 15 kDa) to get PDMS-*b*-Hep and

second using low molecular weight heparin (LMWH, mean MW = 5 kDa) to obtain PDMS-*b*-ShortHep, while the hydrophobic block poly(dimethylsiloxane) (PDMS) was kept constant in both block copolymers (5 kDa, 65 repeating units). After purification, ^{1}H-NMR of PDMS-*b*-ShortHep showed characteristic peaks for PDMS- and heparin block demonstrating successful connection of the two blocks, similar to PDMS-*b*-Hep (Chapter 3, Figure 14). Due to solubility problems, peaks from ^{1}H-NMR were not used to calculate the number of repeating units for heparin containing block copolymers. Another method, a Farndale microassay in ethanol, was used to estimate the length of heparin chains and the corresponding number of repeating units per PDMS block (Table 3). For PDMS-*b*-Hep and PDMS-*b*-ShortHep, the average of three different batches form three independent syntheses is given. For PMOXA-*b*-PDMS-*b*-PMOXA, the average number of repeat units was calculated by ^{1}H-NMR and are only presented for one hydrophilic PMOXA-block, to compare to PDMS-Heparins. Clearly, PDMS-*b*-Hep contained a 3- to 4-fold longer heparin chain compared to PDMS-*b*-ShortHep, while the hydrophobic blocks were similar.

Table 3. Average relative lengths of individual blocks of block copolymers used to form nanomimics.

Block	**Hydrophobic units**	**Hydrophilic units**	**Hydrophilic part [kDa]**
PMOXA-*b*-PDMS-*b*-PMOXA	63	6	0.5
PDMS-*b*-Hep	65	23 ± 10	10.1 ± 4.1
PDMS-*b*-ShortHep	65	6 ± 3	2.6 ± 1.3

To expose long or short heparin chains on nanomimics, they were formed using mixtures of 75 wt% PMOXA-*b*-PDMS-*b*-PMOXA with 25 wt% PDMS-*b*-Hep (nanomimics-25%) or 25 wt% PDMS-*b*-ShortHep (nanomimics-ShortHep-25%). To test the effect of the number of heparin chains on nanomimic antimalarial potency, another mixing ratio of the functional copolymer (heparin-containing) and polymersome-forming copolymer was used with 95 wt% PMOXA-*b*-PDMS-*b*-PMOXA and 5 wt% PDMS-*b*-Hep (nanomimics-5%). For comparison, pure PDMS-*b*-ShortHep-based micelles (100 wt% PDMS-*b*-ShortHep) were formed as well. Transmission electron micrographs (TEM) of the corresponding nanomimics and

micelles were taken and hydrodynamic diameters (D_H) were determined using dynamic light scattering (DLS) (Figure 23).

TEM images of nanomimics-25% and nanomimics-5% revealed vesicular character of the nanostructures with diameters of 70 – 200 nm (Figure 23A,B); the two block copolymers mixed well during film formation, otherwise more micelles similar to PDMS-*b*-ShortHep micelles (Figure 23D) would have been observed, which were already described for PDMS-*b*-Hep (Chapter 3). Nanomimics-ShortHep-25% also mainly formed vesicles, but some micelles were found (Figure 23C) similar to nanomimics formed using more than 25 wt% PDMS-*b*-Hep (Chapter 3, Figure 17). In fact, nanomimics-ShortHep-25% contain shorter, but also more heparin chains on the surface compared to nanomimics-25%, because the molecular weight of PDMS-*b*-ShortHep is lower than that of PDMS-*b*-Hep (Table 3), which explains the morphological differences between these samples. DLS data confirmed nanomimic sizes found in TEM (Figure 23A-C) also in solution. The schematic images (Figure 23) illustrate the morphology, as well as number and length, of heparins exposed on various nanomimics. Cryo-TEM images of nanomimics-25% confirmed the membranous structure (Chapter 3, Figure 15C) and collapsed nanomimics presented in TEM images (Figure 23A-C) were spherical vesicles in solution as visualized by cryo-TEM. Due to the aqueous core of nanomimics, the drying procedure and ultra-high vacuum used in conventional TEM explains the collapsed structures seen in Figure 23A-C. In conclusion, polymersomes were successfully prepared, which appeared similar to previous nanomimics (Chapter 3), using shorter or fewer receptor molecule-containing (heparin) copolymers.

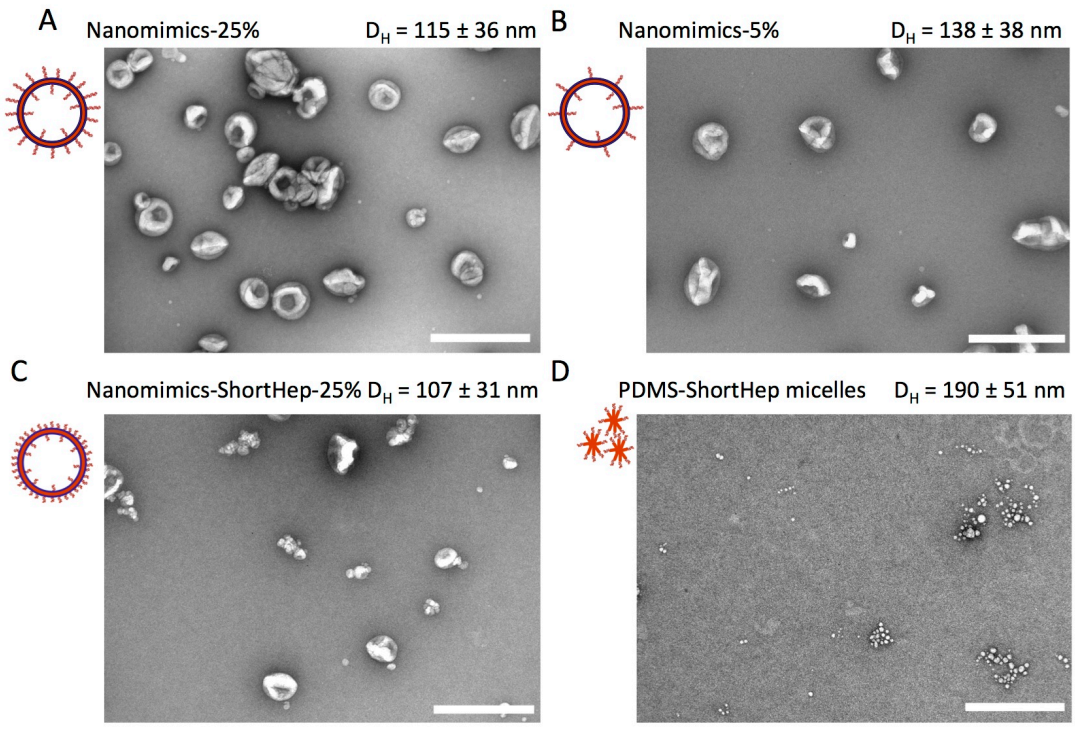

Figure 23. TEM images, hydrodynamic diameters (D_H) from DLS measurements and schematic representations of the nanostructures are shown for (A) nanomimics-25%, (B) nanomimics-5%, (C) nanomimics-ShortHep-25%, and (D) PDMS-ShortHep micelles. The scale bars are 500 nm.

4.3.2 Detailed Analysis of Parasite Protein Interaction with Nanomimics

To further characterize the invasion inhibition mechanism for nanomimics, the interaction of heparin on nanomimics with *Pf*MSP1$_{42}$ was analyzed in detail by fluorescence correlation spectroscopy (FCS) and FCCS (Figure 24).

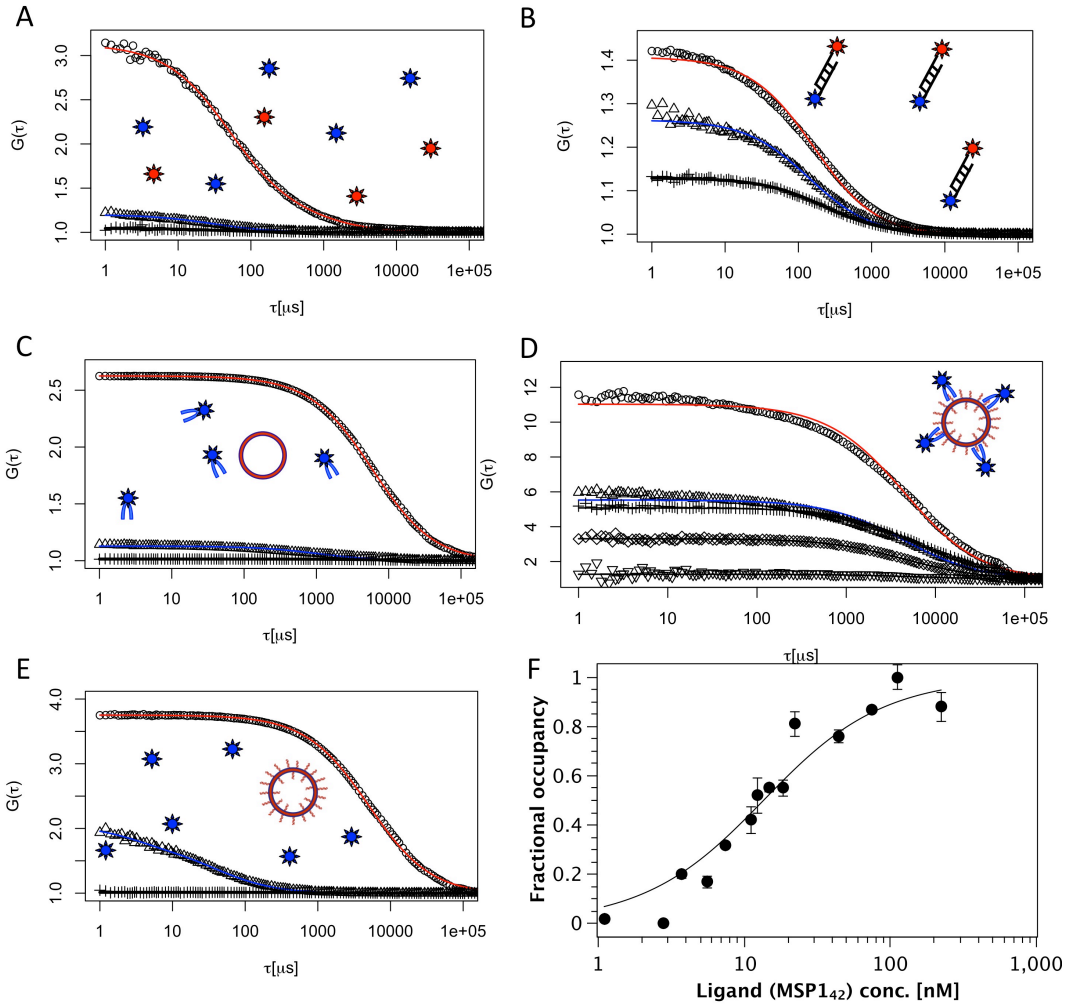

Figure 24. FCS and FCCS data for the evaluation of the nanomimic-*Pf*MSP1$_{42}$ interaction. (A) FCS and corresponding FCCS curve (black) for a mixture of the two used dyes (OG488 (blue) and Bodipy630 (red)) and (B) for a standard sample (IBA standard, double labeled DNA) to obtain the relative minimum (about 3 %) and maximum cross-correlation amplitude (about 33 %). (C) Non-functionalized vesicles (FCS, red) mixed with *Pf*MSP1$_{42}$-OG488 (FCS, blue) and corresponding cross-correlation curve (black); (E) Nanomimics-25% (FCS, red) mixed with OG488 (FCS, blue) and corresponding cross-correlation curve (black); (D) Nanomimics-25% (FCS, red) mixed with *Pf*MSP1$_{42}$-OG488 (FCS, blue) and corresponding cross-correlation curve representing three different *Pf*MSP1$_{42}$-OG488 concentrations: crosses (22.2 nM), diamonds (18.5 nM), triangles pointing down (2.8 nM). (F) Fractional occupancy of heparin on nanomimics-25% by *Pf*MSP1$_{42}$-OG488 normalized versus total *Pf*MSP1$_{42}$-OG488 ligand concentration. Fit was obtained by applying Equation (14, Chapter 10) to the data points in order to obtain K_d.

First, FCCS calibration data were recorded (Figure 24A,B). Both, pure PMOXA-*b*-PDMS-*b*-PMOXA polymersomes-Bodipy630 mixed with *Pf*MSP1$_{42}$–OG488, and nanomimics-25%-Bodipy630 incubated with free Oregon Green 488 (OG488) yielded no significant cross-correlation amplitudes (Figure 24C,E). Therefore, no unspecific binding of *Pf*MSP1$_{42}$–OG488 to the surface of non-functionalized polymersomes (without heparin) was observed, nor did the dye OG488 bind

nanomimics. To study the interaction of *Pf*MSP1$_{42}$ with heparin on nanomimics, red fluorescent nanomimics-25%-Bodipy630 were mixed with different concentrations of green fluorescent *Pf*MSP1$_{42}$–OG488, and the diffusion of fluorescent species were recorded in two detection channels simultaneously (Figure 24D). Titration of *Pf*MSP1$_{42}$–OG488 into a solution of nanomimics, and analysis of the corresponding relative cross-correlation amplitudes yielded a typical ligand-receptor saturation curve (Figure 24F).[97,98,258,259] Different mixtures of *Pf*MSP1$_{42}$–OG488 with nanomimics-25%-Bodipy630 yielded various cross-correlation amplitudes depending on the respective *Pf*MSP1$_{42}$–OG488 concentration used (Figure 24D). Additionally, these binding events were observed in the auto-correlation curves (FCS). For mixtures of nanostructures with fluorescent molecules that did not interact with the nanostructure (Figure 24C,E), the auto-correlation curves represented two distinct diffusion times (triangles: free *Pf*MSP1$_{42}$–OG488 or OG488, circles: polymersome/nanomimic diffusion). When *Pf*MSP1$_{42}$–OG488 was mixed with nanomimics-25%-Bodipy630 (Figure 24D), both auto-correlation curves showed nanomimic diffusion, demonstrating diffusion of nanomimics and *Pf*MSP1$_{42}$–OG488 as one single component. At the highest *Pf*MSP1$_{42}$-OG488 concentration tested, four *Pf*MSP1$_{42}$–OG488 were bound to each nanomimic, which was calculated by comparing the signal per molecule (*CPM* = 6.8 kHz) of *Pf*MSP1$_{42}$–OG488 to *CPM* of the nanomimic-*Pf*MSP1$_{42}$–OG488 complex (*CPM* = 29 kHz). A constant concentration of 2.8 nM *Pf*MSP1$_{42}$–OG488-binding heparins on nanomimics in the titration experiment was calculated. This value was fixed for the fitting of the normalized ligand-receptor saturation curve (Figure 24F).

Fitting the saturation curve of *Pf*MSP1$_{42}$-OG488 with heparin on nanomimics-Bodipy630 (Figure 24F) yielded a K_d of 12.1 ± 1.6 nM for the interaction, confirming the hypothesis that the interaction of *Pf*MSP1$_{42}$ with nanomimics is based on a high affinity interaction (Chapter 3). This also explains the efficient invasion inhibitory effect of nanomimics against malaria parasites (Figure 26C,D). Interestingly, the interaction strength of another merozoite ligand (BAEBL/EBA-140) with HS was estimated to have a K_d of 8.18 ± 2.54 nM,[30] which is very similar to the binding affinity determined here.

4.3.3 Antimalarial Activity of Modified Nanomimics

We further tested the invasion inhibition process and potency of the modified nanomimics (shorter or less heparin on the surface) and compared them to nanomimics-25% by analyzing invasion inhibition using fluorescence microscopy (Figure 25) and testing the dose-response in antimalarial suspension assays

(Figure 26). Fluorescence imaging, after incubation of late stage *Plasmodium falciparum*-infected RBCs (iRBCs), RBCs, and modified nanomimics, revealed invasion inhibition as demonstrated by modified nanomimic binding to merozoites and subsequent trapping of the malaria parasite in its extracellular merozoite form (Figure 25). In quantitative anti-malarial suspension experiments, all tested nanomimics were very potent invasion inhibitors with much lower IC_{50} values compared to soluble heparin chains (Figure 26). Nevertheless, in more complex fluids (*e.g.* human whole blood), it might be necessary to modify the surface-exposed heparin or exchange it with a more specific receptor of the malaria parasite to circumvent unspecific binding, which would interfere with the antimalarial activity and could also produce side effects.

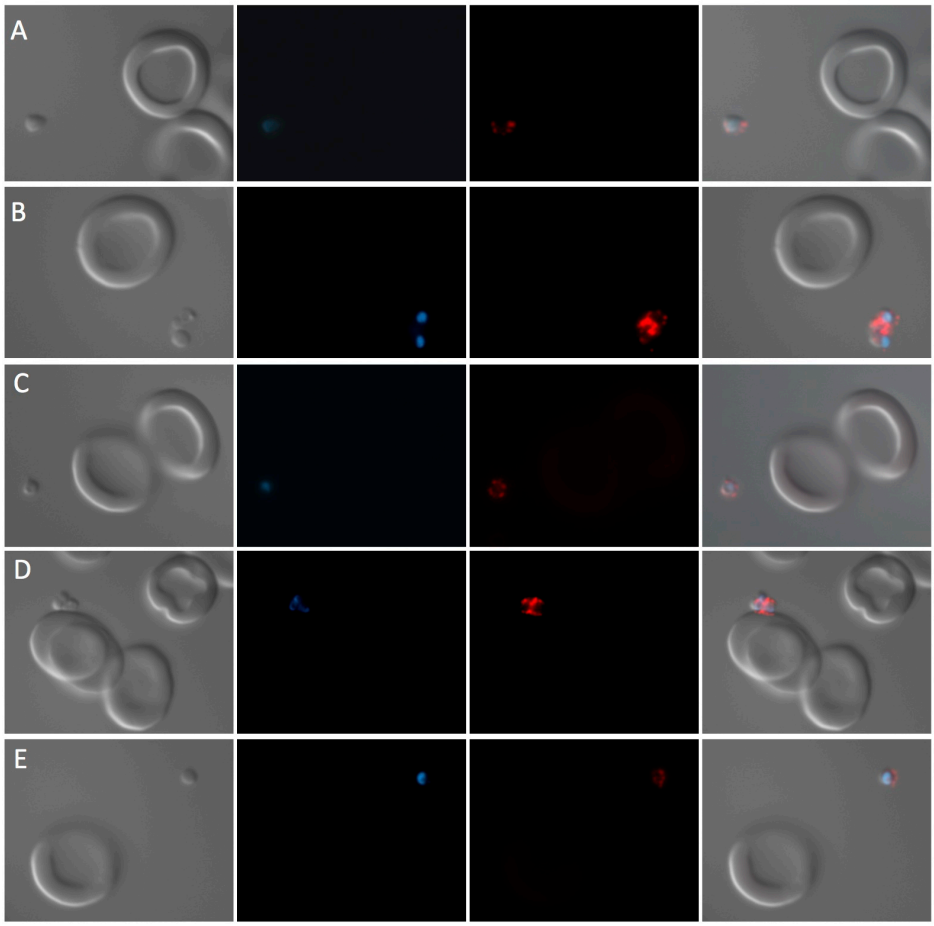

Figure 25. Fluorescence imaging of RBCs, and merozoites (blue) blocked by nanomimics (red) after incubation of late iRBCs, RBCs and fluorescent nanomimics, (A,C,D) nanomimics-ShortHep-25%; and (B,E) nanomimics-5%. (Left: DIC, middle left: merozoite DNA stain, middle right: nanomimics, right: merge)

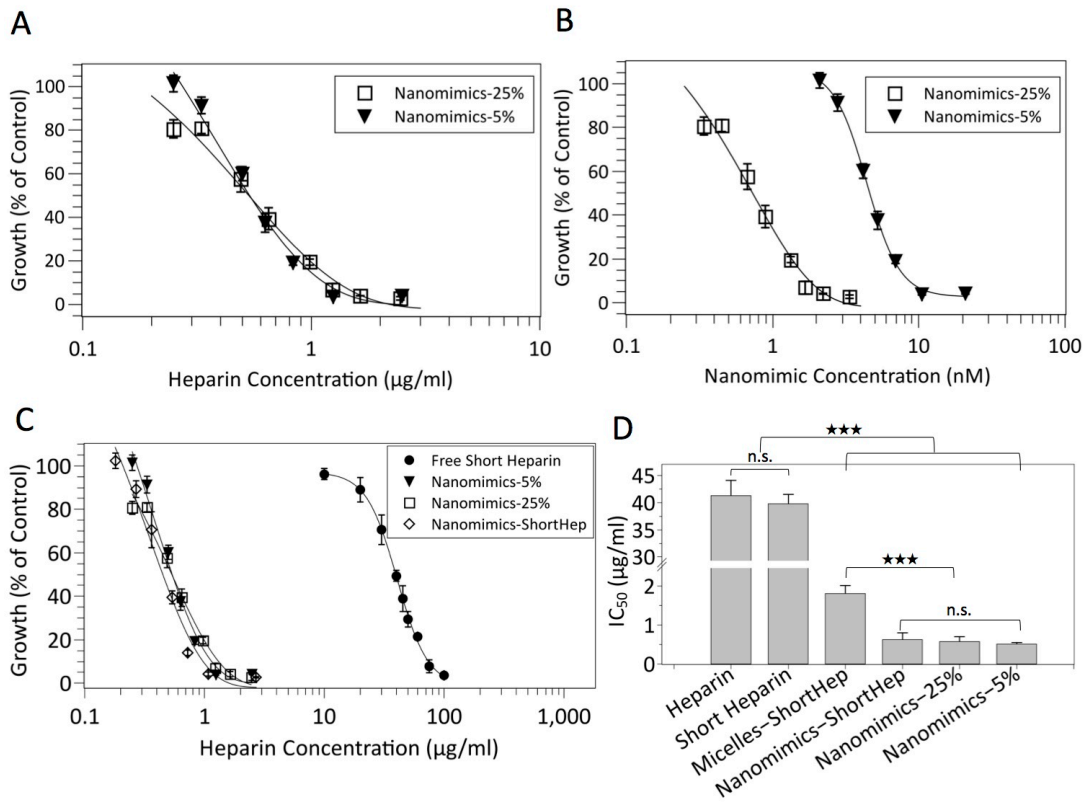

Figure 26. Dose-response curves from antimalarial suspension assays. All data points are mean growth ± standard error, from at least two duplicate assays for each sample, presented as percentage of control (PBS). (A) Dose-response curves for nanomimics-25% and nanomimics-5% represented based on the heparin concentration. (B) Dose-response curves for nanomimics-25% and nanomimics-5% represented based on nanomimic concentration. (C) Dose-response curves for comparison of all nanomimics and free heparin. (D) Comparison of the IC_{50} concentration of free heparin or nanostructured-heparin to inhibit parasite growth based on total heparin amount (µg/mL). Statistics were analyzed using Student's *t*-test: ★★★$p < 0.001$, not significant (n.s.).

When less heparin chains were exposed on a single nanomimic, which was the case for nanomimics-5%, more nanomimics were needed to obtain the same antimalarial effect as with nanomimics-25%, which becomes visible when these samples are compared based on the nanomimic concentration rather than the heparin content (Figure 26A,B). Therefore, nanomimics with less heparin chains, but with identical lengths, are less potent invasion inhibitors in comparison to nanomimics with more heparin chains on the surface.

Interestingly, nanomimic-ShortHep was very potent in invasion inhibition, although the exposed heparin chains were short (Table 3). The antimalarial activity of these nanomimics with short, but more heparin chains on the surface was similar to nanomimics-25%, which were assembled using less, but longer heparin block copolymers. For soluble heparin it has previously been reported that the antimalarial activity drops for very short chains with a number of repeat units

(monosaccharides) below six.[25] Our findings of very potent ShortHep-based nanomimics can be explained by the multivalent presentation of heparin chains on a single nanomimic, which allow strong enough interactions to block invasion. In case of both, long and short heparin block copolymers, the known flexibility and fluidity of PDMS-based membranes –[106] the fundamental basis for the lateral diffusion of biomolecules (membrane proteins) embedded within PDMS-based membranes as described recently –[105] can further promote recruitment of more heparin chains upon initial binding of one chain to the parasite by diffusion of PDMS-heparin within the nanomimic membrane to yield stronger multivalent binding.

4.4 Conclusions

Modified nanomimics with fewer or shorter malaria receptor molecules (heparin) on the surface were successfully self-assembled. All these modified nanomimics were efficient invasion inhibitory nanostructures in the anti-malarial suspension assay. Based on the heparin concentration, all had similar activity, but exposing fewer heparin chains per nanomimic reduced the potency of the nanostructure and for shorter heparins, more chains were needed to yield nanomimics with similar activity to nanomimics with long heparins. Furthermore, the interaction of a merozoite surface protein (*Pf*MSP1$_{42}$), a known heparin-binding protein, with nanomimics was studied and a high affinity interaction was obtained. This high affinity binding is essential to understand and optimize the antimalarial activity of nanomimics in the future.

CHAPTER 5

5 Giant Host Red Blood Cell Membrane Mimicking Polymersomes Bind Parasite Proteins and Malaria Parasites

This chapter describes the interaction of giant versions of the nanostructures of Chapters 3, 4 with the same malaria parasite proteins and whole malaria parasites. This demonstrates the suitability of giant polymersomes as a model to study membrane mimics and confirms data obtained with the corresponding nanostructures.

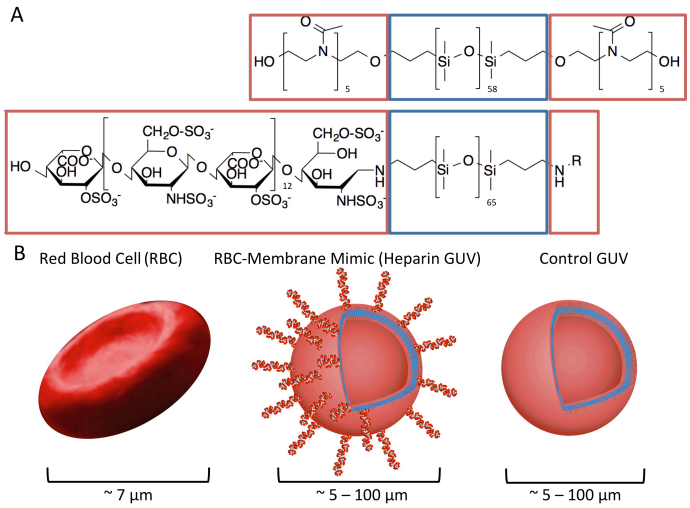

This study has been published and was reprinted and modified herein with permission from reference [260]. Copyright (2016) Neue Schweizerische Chemische Gesellschaft.

Najer, A.; Thamboo, S.; Palivan, C. G.; Beck, H.-P.; Meier, W. *CHIMIA*. **2016**, 70, 288–291.

5.1 Abstract

Malaria is an infectious disease that needs to be addressed using innovative approaches to counteract spread of drug resistance and to establish or optimize vaccination strategies. With our approach, we aim for a dual action with drug- and "vaccine-like" activity against malaria. By inhibiting entry of malaria parasites into host red blood cells (RBCs) – using polymer vesicle-based (polymersome) nanomimics of RBC membranes – the life cycle of the parasite is interrupted and the exposed parasites are accessible to the host immune system. Here, we present that host cell-sized RBC membrane mimics, formed with the same block copolymers as nanomimics, also bind the corresponding malaria parasite ligand and whole malaria parasites, similar to nanomimics. This was demonstrated using fluorescence imaging techniques and confirms the suitability of giant polymersomes (GUVs) as simple mimics for RBC membranes.

5.2 Introduction

Block copolymer-based vesicles, called polymersomes[78] – due to their increased mechanical stability compared to liposomes and broad chemical versatility to introduce *e.g.* stimuli-responsiveness – are considered ideal candidates for drug delivery purposes, as nanoreactors, as artificial organelles inside cells, or as simple cell mimics.[59,253] Our above described nanomimic strategy against infectious diseases is based on such polymer vesicles imitating a host cell membrane at the nanoscale (nanomimics), which was achieved by mixing two distinct block copolymers: vesicle-forming PMOXA-*b*-PDMS-*b*-PMOXA, and PDMS-*b*-heparin (Chapters 3, 4). Giant polymersomes (giant unilamellar vesicles, GUVs), with several micrometers in diameter, are increasingly acknowledged as interesting model systems of very simplified cell mimics.[161]

Malaria, a disease caused by *Plasmodium* spp. parasites that are transmitted by *Anopheles* mosquitoes – killing more than 600'000 people each year –[257] is our current target. When reaching the blood stage cycle, the malaria parasite form called merozoite attach to and enter red blood cells (RBCs), where the parasite asexually divides to form more parasites, which egress from the infected RBC (iRBC) after about 48 hours and infect more RBCs.[19] Heparan sulfate (very similar to heparin) on RBCs is considered as being responsible for the initial attachment of merozoite to the RBC by interaction with *Plasmodium falciparum* merozoite surface protein 1-42 (*Pf*MSP1$_{42}$).[25] With our approach we block the malaria blood stage life cycle using RBC-membrane-mimicking polymersomes, which block the

parasite after egress from iRBCs, inhibit invasion, and expose the infective merozoites to the immune system. If successful *in vivo*, this artificial inhibition of merozoite invasion might lead to an immune boost against extracellular merozoites (Chapter 3).

Here, we demonstrate that RBC membrane mimics formed at a larger size, but similar hollow sphere architecture (heparin GUVs), can also bind the parasite protein *Plasmodium falciparum* merozoite surface protein 1-42 (*Pf*MSP1$_{42}$) and the whole *Plasmodium* parasite (merozoite form) in a similar fashion as their nano-sized counterparts, the nanomimics (Chapters 3, 4). This indicates that GUVs indeed represent a suitable model of small polymersomes, with the advantage of a size close to that of RBCs. Certain aspects, *e.g*. binding of *Pf*MSP1$_{42}$ to polymersomes can be studied with GUVs using methods that would not be suitable for the nanostructure (*e.g*. CLSM to study protein binding).

5.3 Results and Discussion

5.3.1 Giant Host RBC Membrane Mimicking Polymersomes Bind *Plasmodium* Proteins

In the previous Chapters 3, 4, we demonstrated that polymersome-based nanomimics of host RBC membranes efficiently block malaria parasite invasion into host RBCs *in vitro*; nanomimics were more than two orders of magnitude more potent invasion inhibitors compared to soluble receptor-like molecules (heparin), when IC_{50} values were compared based on the heparin concentration in the assays. Furthermore, we measured that several heparin chains on a single nanomimic bound parasite ligands *Pf*MSP1$_{42}$-OG488 with a high affinity (K_d of 12.1 ± 1.6 nM) using fluorescence cross-correlation spectroscopy (FCCS) of green labeled ligand and red labeled nanomimics. This multiple binding with high affinity is the basis for a strong multivalent interaction of nanomimic and merozoite, explaining the potent invasion inhibition by nanomimics.

Herein, host RBC membrane-mimicking polymersomes were formed at a larger size (micrometer scale, heparin GUVs) to study malaria protein and whole parasite interaction with RBC-sized polymersome-based mimics. The same two block copolymers previously used for nanomimic formation were also used to form these giant mimics. PDMS$_{65}$-*b*-heparin$_{12}$ was mixed with PMOXA$_5$-*b*-PDMS$_{58}$-*b*-PMOXA$_5$ (or PMOXA$_9$-*b*-PDMS$_{67}$-*b*-PMOXA$_9$) using 15 wt% of the first block copolymer and subsequent electroformation, yielding heparin GUVs. GUVs made

from $PMOXA_5$-*b*-$PDMS_{58}$-*b*-$PMOXA_5$ without the heparin-functionalized copolymer were used as controls.

Formation of GUVs and heparin GUVs was successfully achieved in both cases using electroformation. Usually, a large number of mainly unilamellar, univesicular polymersomes were formed, whereas only few giants with multivesicular structures were found. Interestingly, these artificial and flexible membranes possess a thickness of about 11 nm (Subchapter 3.3.2), while all the membrane components can laterally diffuse within the membrane,[105,106] but still form stable vesicles with several tens of micrometers in diameter. We performed CLSM to study the interaction of fluorescently labeled *Plasmodium* ligand *Pf*$MSP1_{42}$-OG488 and heparin, the receptor-like molecule known to bind *Pf*$MSP1_{42}$,[25] on the surface of heparin GUVs. This is only possible with GUVs and not with the nanomimics, because of resolution limitations. The membrane of control GUVs and heparin GUVs were labeled with the hydrophobic dye Bodipy630 for visualizing all the membranes in the red channel (Figure 27). The hydrophobic dye spontaneously incorporates into the hydrophobic part of the membranes (PDMS).

The receptor-ligand interaction was followed after mixing control GUVs and heparin GUVs with green-labeled *Pf*$MSP1_{42}$-OG488, respectively. In the control experiments, where GUVs without the receptor-like saccharide were used, no significant interaction with the parasite protein was observed as expected (Figure 27C,D). Only the heparin GUVs, which mimic the host RBC membrane, were covered with *Pf*$MSP1_{42}$-OG488 proteins on the surface, which appeared as green rings, while the exact same imaging settings as in the experiments with GUVs were used (Figure 27A,B). Therefore, we could successfully observe the interaction of heparin on GUVs with the *Plasmodium* ligands *Pf*$MSP1_{42}$ using conventional CLSM imaging.

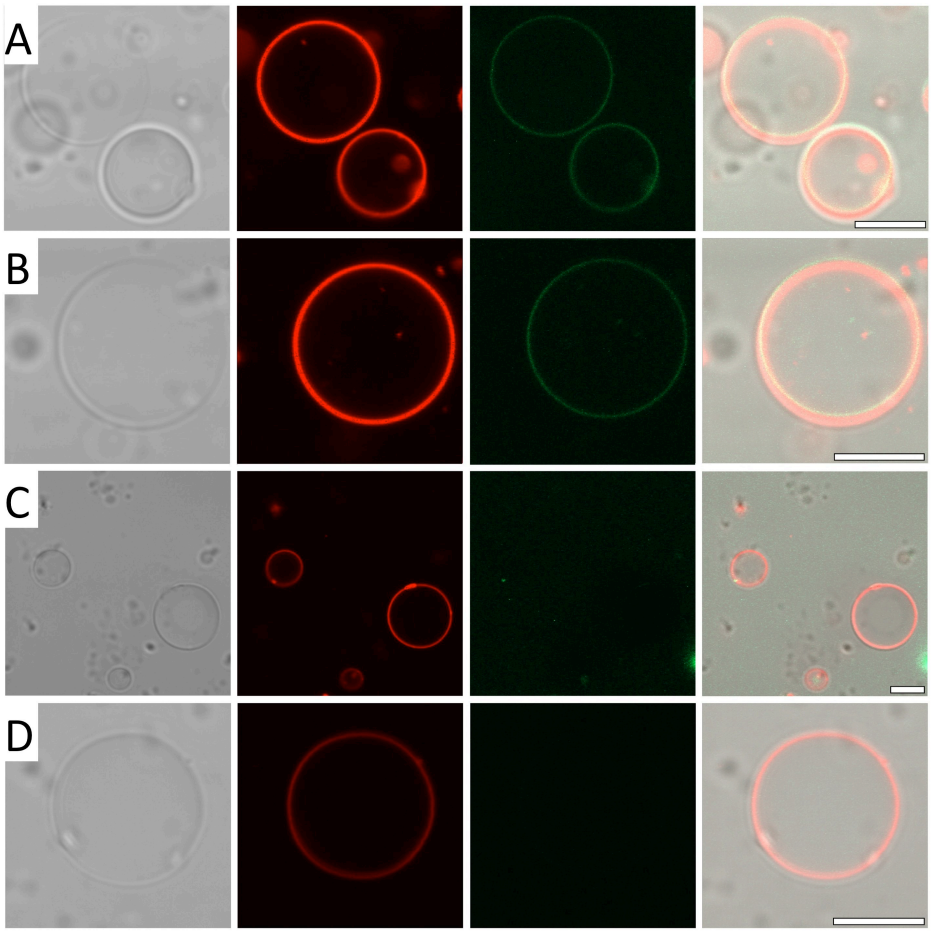

Figure 27. CLSM images of heparin GUVs (A, B) and control GUVs (C, D), which were mixed with the *Plasmodium* parasite ligand *Pf*MSP1$_{42}$-OG488 to investigate the ligand-receptor interaction; only when the receptor was presented on the surface (heparin GUVs), the parasite ligand bound to the GUVs, control GUVs showed no non-specific interaction with the protein. Left: DIC image. Middle left: Bodipy630 in the hydrophobic part of the GUV membranes. Middle right: OG488 on *Pf*MSP1$_{42}$. Right: Merge. Scale bars: 10 µm.

This confirms measurements performed using nanomimics and fluorescence-based diffusion measurements (fluorescence correlation spectroscopy (FCS), and FCCS) with the same *Pf*MSP1$_{42}$-OG488 ligands of merozoites (Chapters 3, 4). This indicates that the membrane-bound receptor-like molecules (heparin) were also exposed on the large heparin GUVs after electroformation, similarly to the nano-scaled versions thereof (nanomimics). Therefore, GUVs are well suited to study certain biophysical aspects of the interaction between the parasite proteins and membrane mimics with a size relevant biologically, which support the conclusions already reported for the corresponding nanoversion system (nanomimics) (Chapters 3, 4).

5.3.2 Giant Host RBC Membrane Mimicking Polymersomes Bind *Plasmodium* Merozoites

Successful binding of parasite proteins to heparin GUVs encouraged performing experiments with whole *Plasmodium* merozoites to check for binding of viable parasites to heparin GUVs. This was studied using fluorescence microscopy after incubation of heparin GUVs with purified, viable *Plasmodium falciparum* merozoites, which is the most aggressive, life-threatening species of malaria parasites. The membrane of heparin GUVs was again visualized by red, hydrophobic dye (Bodipy630). Fluorescence images clearly demonstrate that merozoites also bind to RBC-sized host membrane-mimetic polymersomes (Figure 28). In both examples shown, the merozoites slightly indented the membrane of heparin GUVs upon binding. This deformation of the polymersome structure upon merozoite binding was also seen with nanomimics as previously demonstrated by electron microscopy of ultrathin slices of merozoite-nanomimic complexes (Chapters 3, Figure 21).

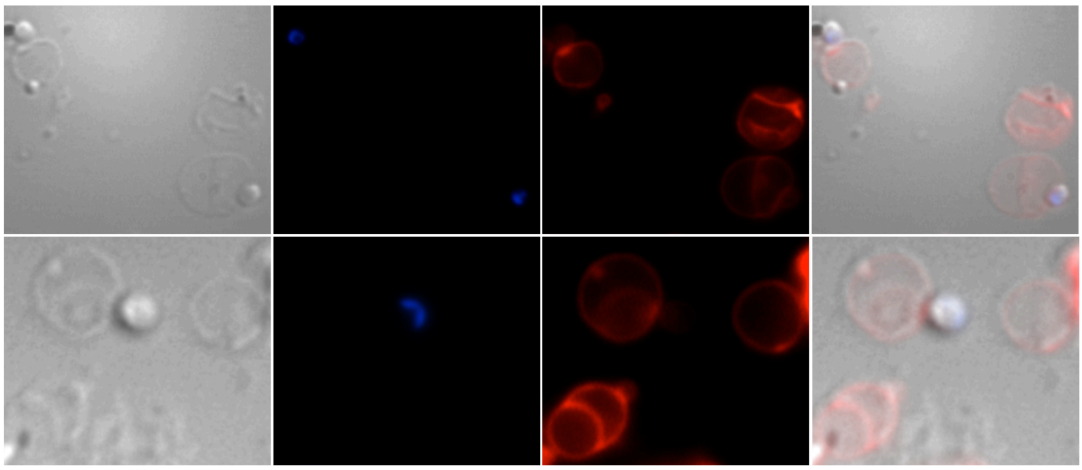

Figure 28. Fluorescence microscopy images of giant host RBC-mimicking polymersomes (red) that bound *Plasmodium* merozoites (blue, DNA stain). Left: DIC image. Middle left: Hoechst, DNA stain. Middle right: Bodipy630, staining polymersome membranes. Right: Merge. Merozoites are about 1.5 µm long.

This confirms that large scaled polymer vesicles can mimic – at a very primitive stage – the membrane of the host RBC to such an extent that binding of *Plasmodium* proteins and whole malaria parasites is achieved. The large size of GUVs allows the analysis of certain aspects by conventional imaging methods. Naturally, for a real *in vivo* application the nano-scaled versions are preferable, but certain aspects are difficult to analyze using only nano-sized structures.

5.4 Conclusions

Host RBC-membrane-mimicking polymersomes (heparin GUVs) were successfully formed at a corresponding RBC size (about 7 μm disk diameter) using two block copolymers and electroformation technique. Only when the second copolymer, containing the receptor-like molecule (heparin), was present in the GUV membrane, the parasite ligand *Pf*MSP1$_{42}$ bound to the GUVs. Furthermore, whole, viable, and RBC-infecting *Plasmodium falciparum* merozoite interacted and deformed these large-sized RBC membrane mimics (heparin GUVs). These are important steps towards understanding and defining this concept and to advance closer to a real biomedical application.

CHAPTER 6

6 Further Evaluation of Nanomimics with Respect to Biomedical Applicability

This chapter summarizes additional data characterizing nanomimics properties in prospect of biomedical applications. This includes anticoagulation property, estimation of endotoxin contamination, and initial in vivo tests regarding invasion inhibition and secondary "vaccine-like" activity of the nanomimic strategy. Parts of this chapter are being prepared for publication.

6.1 Results and Discussion

6.1.1 Anticoagulation Property of Nanomimics

When heparin is intended for a medical purpose other than preventing blood clots, such as anti-infection applications, its anticoagulation property turns out to be a major drawback. Furthermore, heparin-induced bleeding, which is directly linked to its anticoagulation effect, is the most important adverse effect when heparin is used in medical applications.[261] Soluble heparin has previously been used as adjunct therapy for severe malaria, but it was discontinued due to serious side effects, such as intracranial bleeding.[231,262] Therefore, heparin-containing samples (nanomimics) were tested for anticoagulation property. The obtained values were related to the amount of surface-exposed heparin as measured by Farndale microassays.

Control vesicles (only PMOXA-*b*-PDMS-*b*-PMOXA), four independent samples of nanomimics-25% (26, 78, 102, and 146 µg/mL surface-exposed heparin) and one sample nanomimics-12.5% (50 µg/mL) were tested. Only one sample, nanomimics-25% (102 µg/mL heparin), showed a slight anticoagulation activity (0.15 UI/mL); all other samples did not reach activities above the detection limit (0.1 UI/mL). In order to calculate the maximum expectable percentage of anticoagulation activity possible in nanomimic samples, the heparin concentration

was converted from 102 µg/mL to 19.7 UI/mL based on the initial activity of the heparin used for polymer synthesis (193 UI/mg). The measured activity (0.15 UI/mL) revealed that nanomimics-25% (102 µg/mL) exhibit only 0.8 % of the calculated activity. The whole procedure of synthesis and nanomimic formation yielded final nanostructures with much reduced anticoagulation property (only 0.8 % of the expected activity was left). The anticoagulation activity of heparin depends on the interaction of antithrombin III with a specific heparin pentasequence, which is only present in about one third of all the heparin chains of the sodium salt starting material used for synthesis.[263] Moreover, the pentasequence is likely to be occluded in the nanomimics. In conclusions, PDMS-*b*-heparin synthesis and the nanomimic formation technique are responsible for the much reduced anticoagulation activity.

In mice, the minimum blood concentration of soluble heparin, needed to achieve anticoagulation property, was found to be at least 4 µg/mL.[207] Thus, based on our calculations, nanomimics could be injected up to a blood concentration of about 500 µg/mL heparin concentration without reaching the threshold concentration needed for anticoagulation activity in mice. This indicates that anticoagulation property of our nanomimics can be neglected at the current development stage, but has to be kept in mind and tested more thoroughly. However, heparin on nanomimics might specifically interact with other heparin-binding proteins, which might lead to a reduction of circulation time and/or anti-infectious activity. To overcome this drawback, modified or alternative receptor molecules that have less interaction partners than heparin might be considered as building block for nanomimics.

6.1.2 Estimation of Endotoxin Contamination

Most engineered biomaterials suffer from contamination with endotoxins, better known as lipopolysaccharides (LPS), originating from the outer cell membrane of Gram-negative bacteria. Our body strongly reacts to very low endotoxin concentrations, which can cause endotoxin shock and even death. Therefore, FDA regulations strictly demand that all medical solutions intended for intravenous application have to be tested for endotoxins and confirmed to contain less than 0.5 EU/mL endotoxin, which corresponds to only 0.05 ng/mL LPS.[264]

The chromogenic kinetic limulus amebocyte lysate (LAL) assay is a standard method to estimate endotoxin levels, but it is in general rather tricky to perform these assays with nanoparticle-containing solutions.[265] Spiking nanoparticle samples with known amounts of endotoxin is used to determine interference of the sample with the assay; spike recovery of 50 – 200 % indicates suitability of the

assay.[265] Heparin is also known to interfere with the assay, but this can be overcome by adding $MgCl_2$.[266] Furthermore, when high concentrations of nanoparticles are added to the assay solution, light scattering by the nanoparticles influences the absorbance measurements. This is corrected by redefining the onset time (normally the time to reach 0.2 A.U.) by the time to increase by 0.2 A.U., which equals a baseline correction at time point 0. Despite these difficulties, we tested our nanostructures for endotoxin contamination using standard LAL chromogenic kinetic assays (Lonza).[267] Initial measurements of nanoparticle samples that were prepared under standard sterile conditions yielded large amounts of endotoxins (> 5 EU/mL). The main source of endotoxin contamination was found to be the column material used for nanostructure purification and the plastic column itself. After incrementally testing each preparation step, strategies to avoid high endotoxin contaminations in polymersome and nanomimics production were established as follows.

Ultra-pure, endotoxin-free water should be used in all steps of synthesis, assembly, and purification. Endotoxins are eliminated from glassware by heating at 250 °C overnight. Alternatively, glassware and magnetic stirrers are decontaminated by washing in 0.5 M NaOH overnight and subsequent rinsing with EtOH and/or sterile, endotoxin-tested PBS in a sterile hood. Column material, Sepharose 2B, has to be washed in 0.5 M NaOH overnight and then rinsed with sterile, endotoxin-tested PBS. The column is packed within a sterile hood using sterile syringes, needles, and a sterile 10 mL plastic pipette, which served as column (Figure 29). For nanomimic extrusion, the extruder parts are first washed in 0.5 M NaOH overnight and rinsed with sterile, endotoxin-tested PBS before use.

Following these procedures, we obtained nanomimic (146 µg/mL accessible heparin, ~ 5 mg/mL polymer, D_H = 91 ± 24 nm) and polymersome samples that contained less than 0.005 EU/mL endotoxins, which is well below the FDA-limit of 0.5 EU/mL. Spike recovery with a nanomimic sample yielded about 86 % (0.05 EU/mL added), which is within the acceptable range confirming suitability of this assay for our samples.[265] More detailed analysis of endotoxin contamination will be needed, if projects involving polymersomes and nanomimics are continued in the direction of biomedicine.

Figure 29. Digital image of the column set-up used for nanomimic purification to avoid high endotoxin contamination. Sterile 10 mL plastic pipettes, syringes, needles, and freshly cleaned column material (washed in 0.5 M NaOH overnight) had to be used to yield nanomimic samples with endotoxin contamination below 0.005 EU/mL.

6.1.3 *In vivo* Activity and "Vaccine-Like" Action

Encouraged by the promising *in vitro* data we decided to run preliminary tests of the activity of nanomimics in an acute malaria mouse model. 200 µL of a nanomimics-25% (D_H = 85 ± 26 nm, Zeta-Potential = −36.3 ± 1.1 mV, 78 µg/mL heparin) or a nanomimics-12.5% (D_H = 108 ± 33 nm, 50 µg/mL heparin) solution in PBS was injected twice a day for four days after mice have been infected with *P. berghei*. Unfortunately, parasitemia in the test mice reached similar values as in control mice. Although we could not yet demonstrate *in vivo* activity of these nanomimics with *P. berghei* no apparent toxic effects of nanomimics injections were found and all mice survived throughout the assay. It is possible that the lack of effect on *P. berghei* is due to a short circulation time of the nanomimics, which has not yet been tested. Synchronized parasites (as is the case in natural human malaria) and timed nanomimic injection could be used to account for the short circulation time. Additionally, huge numbers of parasites are typically used in this acute malaria mouse model. Even if many parasites were blocked by nanomimics, this might not become visible at high parasitemia. Moreover, *P. berghei* might not be the best model to test whether or not structures inhibit invasion, as indicated by a failure to achieve parasite reduction despite high antibody titers induced by vaccination.[268]

Following our idea of a dual drug- and "vaccine-like" action, another research group recently attempted to inhibit merozoite entry using sulfated polysaccharides.[269] This study showed antimalarial activity of heparin-like sulfated polysaccharides from marine organisms, with IC_{50} values in the range of heparin, but with reduced anticoagulation property. It also reported some *in vivo* activity and the induction of antibody production, but only in one mouse.[269] Clearly, more work is needed to evaluate the *in vivo* effect of sulfated polysaccharides on malaria infection. Structures with increased inhibitory properties have to be formulated or found to exploit the full potential of the nanomimic strategy.

Interestingly, the aforementioned group also formulated a primaquine-loaded nanostructure with heparin non-covalently attached to the surface, mainly for targeting iRBCs.[207] The nanostructure was a liposome with positive surface charges that bound heparin chains to the surface by electrostatic interactions. A concentration of 10 µM heparin was needed for reaching the IC_{80} (growth at 20 % compared to a control), when no drug was additionally encapsulated.[207] In our case, 27 nM of surface-exposed heparin on nanomimics was sufficient to achieve IC_{80} (Subchapter 3.3.5). The 370-fold lower heparin concentration results from the nature of the nanostructure and the different chemical conjugation of heparin. On nanomimics, heparin is covalently attached in its natural conformation *via* its reducing end, which allows for strong multivalent interactions of the nanomimics with the merozoites. Liposomes[207] with heparin electrostatically wrapped around the positively charged surface might not warrant a stable and structurally optimal nanostructure for the inhibition of merozoites.

In the scope of this thesis, another preliminary experiment was performed to assess the "vaccine-like" action of nanomimics. For simplicity, only one merozoite protein rather than the whole pathogen was used for this initial test. The nanomimic-*Pf*MSP1$_{42}$ complexes were injected intravenously to mimic the situation when merozoites would be inhibited in the human bloodstream (Figure 30). Enzyme-linked immunosorbent assay (ELISA) endpoint titers clearly show that anti-*Pf*MSP1$_{42}$ IgG antibodies were produced after intravenous injection of nanomimic-*Pf*MSP1$_{42}$ complexes (Figure 31).

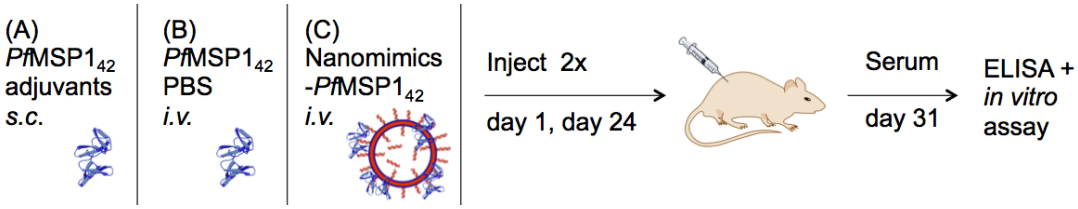

Figure 30. Experimental procedure to test "vaccine-like" activity of the nanomimic strategy.

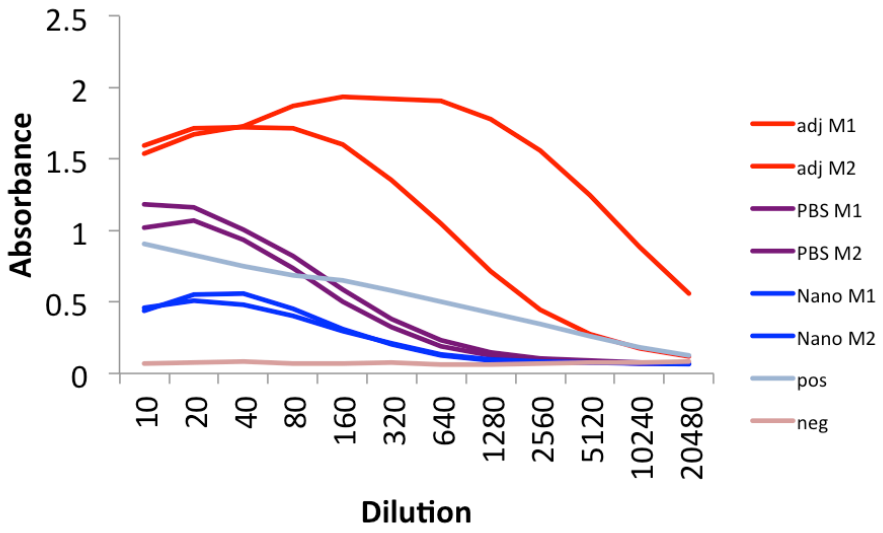

Figure 31. Determination of anti-*Pf*MSP1$_{42}$ IgG antibodies by ELISA. Curves correspond to mouse sera taken on day 31 after immunization. Adj. M1/M2 belong to procedure A (Figure 30), PBS M1/M2 to B, and Nano M1/M2 to C.

However, when parasite invasion is inhibited *in vivo*, not only one protein (as demonstrated here with *Pf*MSP1$_{42}$) but in fact the whole pathogen – with all its antigenic proteins – will be exposed in the bloodstream. Thus, even if antibody levels would be as low as induced with *Pf*MSP1$_{42}$ alone, the diversity of antibodies against a multitude of merozoite proteins could still be highly inhibitory. However,

if the whole pathogen were to be exposed on nanomimics, the fate of the complex would be dominated by the pathogen because it is much bigger than the nanomimics, whereas the *Pf*MSP1$_{42}$ complex is dominated by the nanomimics due to the smaller size of the protein alone compared to nanomimics. Size and antigenic diversity could affect the host immune response against merozoites when blocked by nanomimics *in vivo*.

Initial experiments to examine whether the sera of mice previously injected with nanomimics-*Pf*MSP1$_{42}$ interfere with malaria parasites, we carried out *in vitro* growth inhibition assays using *P. falciparum* in suspension. Immune sera were compared to preimmunization sera and to sera of untreated BALB/c mice (Figure 32).

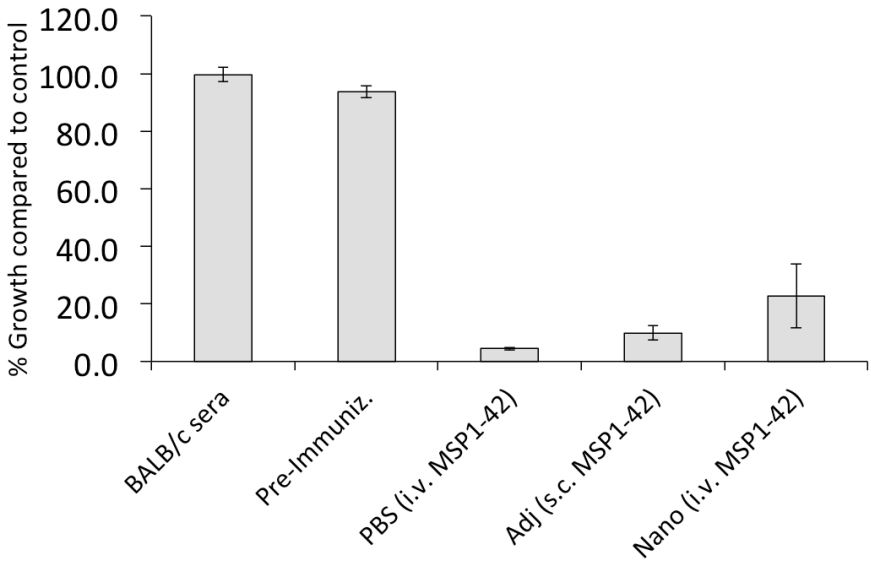

Figure 32. *In vitro* growth inhibition of *Plasmodium falciparum* by mouse sera before and after immunization. The immunization procedure is shown in Figure 30. (n = 2)

Interestingly, all post-immunization sera did inhibit parasite growth in this preliminary test when compared to pre-immunization sera (Figure 32). Although only two independent experiments could be performed with the limited amount of serum available, the different immunization schedules did not reveal sera with significantly different effect on *P. falciparum* growth inhibition. The nature of the inhibitory structures present in these sera remains to be identified. Nevertheless, these preliminary data suggest that the nanomimic strategy might indeed produce an immune response that could potentially protect from a secondary infection. This promising concept will be further explored in the future.

CHAPTER 7

7 An Amphiphilic Graft Copolymer-Based Nanoparticle Platform for Reduction-Responsive Anticancer and Antimalarial Drug Delivery

This chapter demonstrates how environment-sensitive, biodegradable nanoparticles can be used to stabilize an experimental antimalarial compound. Further, our nanoparticle platform delivers the compound to Plasmodium-infected red blood cells.

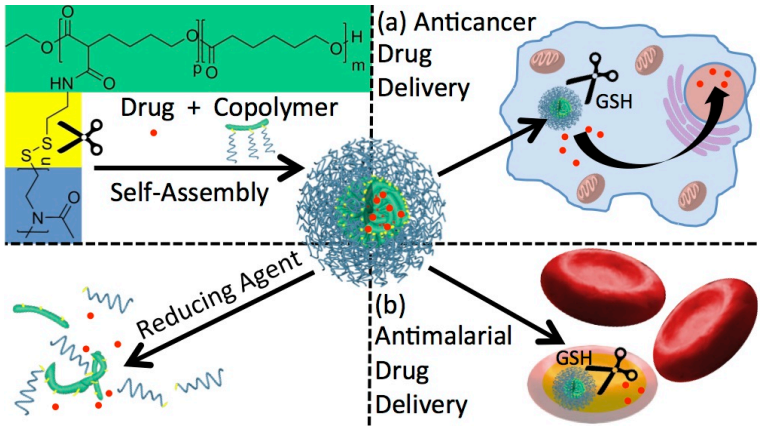

This chapter is part of a study[270] that has been submitted.

Najer, A.[+]; Wu, D.[+]; Nussbaumer, M. G.; Schwertz, G.; Schwab, A.; Witschel, M. C.; Schäfer, A.; Diederich, F.; Rottmann, M.; Palivan, C. G.; Beck, H.-P.; Meier, W. **2016**. *Submitted*.

[+] These authors contributed equally

7.1 Abstract

Medical applications of anticancer and antimalarial drugs often suffer from low aqueous solubility, high systemic toxicity, and metabolic instability. Smart nanocarrier-based drug delivery systems provide means of solving these problems at once. Herein, we present such a smart nanoparticle platform based on self-assembled, reduction-responsive amphiphilic graft copolymers, which were successfully synthesized through thiol-disulfide exchange reaction between thiolated hydrophilic block and pyridyl disulfide functionalized hydrophobic block. These amphiphilic graft copolymers self-assembled into nanoparticles with mean diameters of about 30 – 50 nm and readily incorporated hydrophobic guest molecules. Fluorescence correlation spectroscopy (FCS) was used to study nanoparticle stability and triggered release of a model compound in detail. Long-term colloidal stability and model compound retention within the nanoparticles was found when analyzed in cell media at body temperature. In contrast, rapid, complete reduction-triggered disassembly and model compound release was achieved within a physiological reducing environment. The synthesized copolymers revealed no intrinsic cellular toxicity up to 1 mg/mL. Drug-loaded reduction-sensitive nanoparticles delivered a hydrophobic model anticancer drug (doxorubicin, DOX) to cancer cells (HeLa cells) and an experimental, metabolically unstable antimalarial drug (the serine hydroxymethyltransferase (SHMT) inhibitor (±)-**1**) to *Plasmodium falciparum*-infected red blood cells (iRBCs), with higher efficacy compared to similar, non-sensitive drug-loaded nanoparticles. These responsive copolymer-based nanoparticles represent a promising candidate as smart nanocarrier platform for various drugs to be applied to different diseases, due to the biocompatibility and biodegradability of the hydrophobic block, and the protein-repellant hydrophilic block.

7.2 Introduction

Nanoparticle-assisted drug delivery allows for tuning pharmacokinetics, toxicity, absorption, distribution, metabolism, and excretion profile of drugs leading to different needs for dosage and duration of treatment.[271] This concept has been widely applied for improving clinical outcome of anticancer therapy through increasing drug accumulation at the target site while decreasing drug distribution to off-target sites.[272,273] Passive targeting of tumor tissue can be obtained using non-functionalized, drug-loaded nanoparticles *via* the enhanced permeability and retention (EPR) effect, which allows nanoparticle accumulation in tumors after intravenous application.[146,274] In terms of size, passive accumulation within tumor

tissue *via* the EPR effect is efficiently achieved with long-circulating nanoparticles ranging from 10 to 100 nm in diameter.[149] However, small sized nanoparticles (sub-50 nm diameter) have been shown to better target *e.g.* lymph node metastatic cancer.[275]

Amphiphilic block copolymer (ABP)-based nanomaterials are one promising type of materials with broad applicability in drug delivery.[272,273] Various self-assembled nanostructures ranging from micelles to worm-like micelles to polymer vesicles can be obtained in aqueous environments by carefully choosing the type, architecture, lengths, and hydrophilic/hydrophobic block ratio of ABPs.[61,72,276] ABP-based nanoparticles benefit from lower critical micelle concentrations (CMC), higher mechanical stability, simple introduction of stimuli-responsiveness within the ABP architecture, and modification with targeting moieties when compared to lipid based systems such as liposomes.[59,273,277] Degradability of ABP-based nanoparticles is introduced by using polypeptides or polyesters, such as poly(ε-caprolactone) (PCL), as ABP hydrophobic building blocks.[278] Poly(ethylene glycol) (PEG) and poly(2-methyl-2-oxazoline) (PMOXA) are two readily used biocompatible polymers for the hydrophilic part of ABPs; both provide non-fouling properties needed for long-circulating nanoparticles.[279]

Another challenging aspect of nanoparticle-based drug delivery is the efficient release of the drug in the target cell, while retaining the drug inside the nanostructure in the extracellular environment. This is elegantly addressed by spatiotemporal- and dosage-controlled delivery using stimuli-responsive materials and corresponding nanostructures.[213,280,281] Commonly used endogenous triggers for stimuli-responsive delivery are changes in pH, redox potential, and enzyme concentration.[213] Reduction-responsive ABP-based nanoparticles represent a unique class of smart materials based on their effective delivery mechanism for a wide range of molecules, such as nucleic acids[282,283] and low molecular weight chemical drugs.[284-287] The building blocks of these nanostructures contain one or more disulfide linkage/s in their main- or side-chains. This allows forming drug-loaded nanoparticles with stable morphology in circulation and extracellular environments. After cellular uptake, rapid cleavage of the disulfide linkage/s and subsequent nanoparticle disassembly in the reductive cell cytosol promote drug release.[288] The large gradient of the reducing agent glutathione (GSH) across cell membranes – the cytosolic concentration (2 – 10 mM) is three orders of magnitude higher than the extracellular concentration – serves as the basis for reduction-responsive anticancer drug delivery.[215]

Solubility, stability and toxicity problems are well known for anticancer drugs,[289] but the same problems equally apply to anti-infectious agents, such as antimalarials.[290,291] Malaria is an infectious disease caused by *Plasmodium* spp. parasites, transmitted by *Anopheles* mosquitoes. The disease causing stages of the parasite infect and asexually divide inside of human red blood cells (RBCs).[19] The need for novel antimalarials or strategies against resistance development is increasingly recognized. Especially since the recent development and spread of resistance against the first-line treatment with artemisinin combination,[9] which already led to treatment failures.[46] One proposed approach to overcome the development of resistance is the delivery of high local concentrations of antimalarials using *e.g.* nanoparticles.[42,201] Current antimalarial drug delivery strategies are focused on commercial antimalarials that have already been optimized for *in vivo* applications.[195,196]

Surprisingly, there is evidence that proteins, such as antibodies,[41] and small nanoparticles up to about 80 nm diameter have direct access to the parasite inside the RBC.[39,40,42] Similarly to passive tumor targeting *via* the EPR effect, this controversial "leakiness" of *Plasmodium*-infected RBCs (iRBCs)[39,40,42] can be exploited *via* a passive targeting strategy using non-functionalized, antimalarial-loaded nanoparticles. Also here, smaller sized nanoparticles (sub-80 nm diameter) are needed, because the size-cutoff to efficiently reach intracellular malaria parasites of iRBCs is about 80 nm.[39,40,42] The highly reducing parasite cytosol of iRBCs[214] equally represents a valuable trigger for smart drug delivery of antimalarials *via* reduction-triggerable nanoparticles, similar to reduction-triggered anticancer drug delivery.

Herein, we report the synthesis of a library of biodegradable, reduction-responsive ABPs composed of hydrophilic PMOXA and hydrophobic PCL with grafted molecular architecture, poly(2-methyl-2-oxazoline)-*graft*(SS)-poly(ε-caprolactone) (PMOXA-*g*(SS)-PCL), in which the reduction-responsive disulfide group acts as the linker between PMOXA and PCL. Aqueous self-assembly of these graft copolymers into nanoparticles and loading of cargo using model hydrophobic dye molecules (Bodipy630, NileRed), anticancer drug (doxorubicin, DOX), and antimalarial (serine hydroxymethyltransferase (SHMT) inhibitor (±)-**1**)[291] were studied (Figure 33). A single molecule detection method, FCS, was used to demonstrate high stability and model dye retention within self-assembled nanoparticles in protein-containing cell media over four days and fast disassembly and model compound release upon treatment with reducing agent. Furthermore, the biocompatibility of these copolymers was tested on HeLa cells in the range of 0.1 mg/mL to 1 mg/mL. Anticancer drug-loaded reduction-sensitive nanoparticles

were evaluated for delivery of their payload to cancer cells (Hela) and compared to non-sensitive nanoparticles based on similar polymers with linear architecture, PMOXA-*b*-PCL. Similarly, we explored the nanoparticle-based delivery of a non-optimized, hydrophobic, and metabolically unstable antimalarial compound, which is in preclinical drug development stage, to iRBCs. We consider this as a valuable additional avenue to medicinal chemistry traditionally used to modify pharmacokinetic properties of compounds *via* changing the chemical structure of the compound itself.

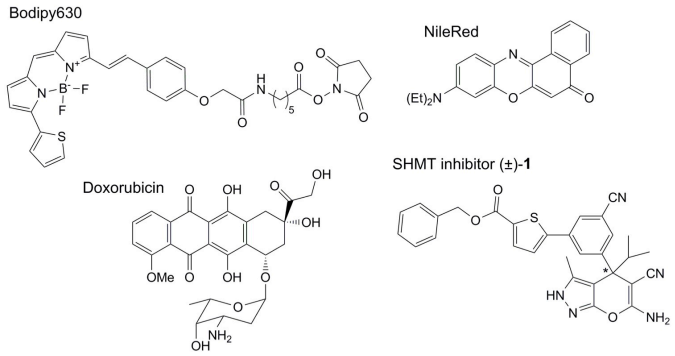

Figure 33. Chemical structures of model hydrophobic cargo molecules used for incorporation in nanoparticles.

7.3 Results and Discussion

7.3.1 Chemical Structure of Graft Copolymers and Self-Assembly

Only a short summary is given here. Full synthesis of the graft copolymer, polymer characterization, aqueous self-assembly, reduction-triggered disassembly, and anticancer activity can be found elsewhere: Dalin Wu, PhD Thesis. Amphiphilic Block Copolymers: Synthesis, Self-assembly and Applications, Basel, CH, 2015.

A library of reduction-sensitive graft copolymers PMOXA-*g*(SS)-PCL and reduction-insensitive linear copolymer PMOXA-*b*-PCL was synthesized (Table 4, Figure 34). Chemical structures were analyzed by ^{1}H NMR, FTIR, and GPC. Aqueous self-assembly of the graft copolymers yielded mean diameters ranging from about 27 nm to 51 nm with narrow PDI of 0.09 to 0.18 for all three graft copolymers according to dynamic light scattering (DLS) measurements in PBS (Figure 34). Transmission electron micrographs (TEM) confirmed the size and morphology of the assembled spherical nanoparticles (Figure 34C). These obtained nanoparticle sizes lie within the optimum range of 10 to 100 nm to be used as

passively targeted drug delivery vehicles.[149] The relatively small average size of maximum 50 nm provides the basis for targeting cancer metastasis[275] and iRBCs in case of malaria.[39,40,42]

Table 4. Chemical Characteristics of synthesized PMOXA-*g*(SS)-PCL.

Polymer	^{1}H NMR				GPC				CMC
	Block ratio	*M*n	$f_{(PMOXA)}$[a]		*M*w	*M*n	PDI		mg/mL
PMOXA-*g*(SS)-PCL-2	88:238	34800	22%		22300	13000	1.72		$0.05*10^{-3}$
PMOXA-*g*(SS)-PCL-1	127:165	30000	36%		18400	13260	1.38		$0.20*10^{-3}$
PMOXA-*g*(SS)-PCL-3	135:135	27000	43%		–[b]	–	–		$0.29*10^{-3}$

[a] The values of $f_{(PMOXA)}$ were calculated by the equation $\frac{Mn\ of\ PMOXA}{Mn\ of\ whole\ copolymer}$

[b] Due to solubility problems of PMOXA-*g*(SS)-PCL 3 in THF, no GPC data were obtained.

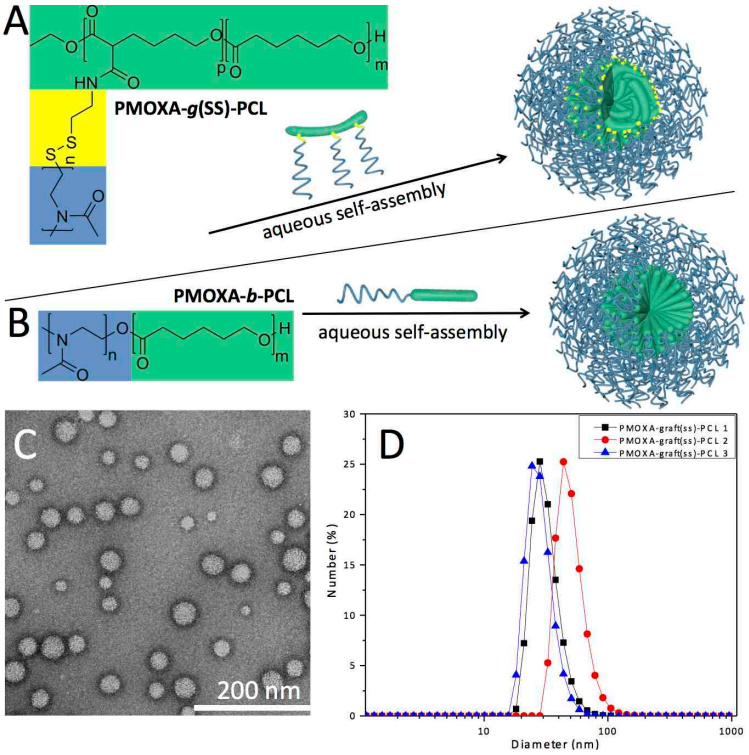

Figure 34. Chemical structure of PMOXA-*g*(SS)-PCL (A), PMOXA-*b*-PCL (B), and schematic self-assembly in aqueous solution. (C) Morphology of nanoparticles self-assembled from PMOXA-*g*(SS)-PCL 2 imaged by transmission electron microscopy (TEM). (D) Hydrodynamic diameter and number distribution of nanoparticles in PBS measured by DLS. More TEM images, and DLS size distributions are shown in Figure 36, 37.

7.3.2 Loading of Various Hydrophobic Model Molecules within Nanoparticles

Various hydrophobic cargo molecules were chosen to be incorporated within the hydrophobic core of self-assembled nanostructures for stabilization and protection purposes. The fluorescent dye molecules Bodipy630 and NileRed, the anticancer drug doxorubicin (DOX), and the experimental, metabolically unstable antimalarial (SHMT inhibitor (±)-**1**)[291] were the selected compounds for encapsulation in nanoparticles formed by reduction-sensitive PMOXA-*g*(SS)-PCLs and PMOXA-*b*-PCL. Non-triggered PMOXA-*b*-PCL-based nanoparticles served as biodegradable, but reduction insensitive control nanostructures. All these hydrophobic molecules were readily incorporated into the hydrophobic core of all the different nanoparticles. Drug loading efficiencies (DLE) of 15%, 30%, 40%, and 55% for NileRed, Bodipy630, DOX, and SHMT inhibitor (±)-**1**, respectively, were measured by fluorescence (DOX) and UV-Vis absorbance (dyes and antimalarial, Figure 35) measurements for reduction-sensitive nanoparticles. DLS measurements of drug/dye-loaded nanoparticles revealed typical average diameters of 42 ± 11 nm for reduction-sensitive nanoparticles and 74 ± 24 nm for similar, non-sensitive nanoparticles (Figure 37). TEM images confirmed these sizes (Figure 36, 37).

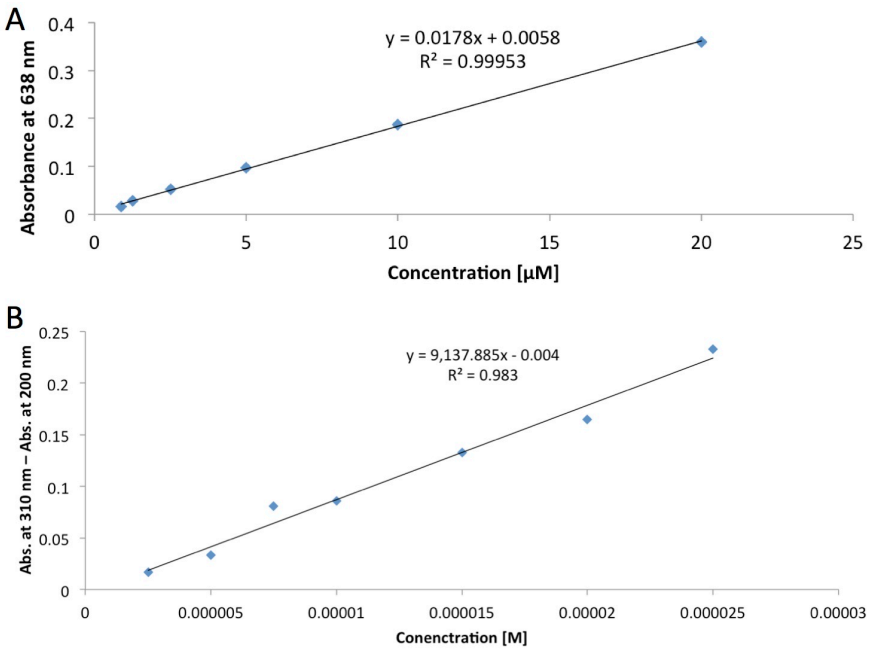

Figure 35. Calibration curve for Bodipy630 in PBS and SHMT inhibitor (±)-**1** in PBS used to calculate amount of encapsulated dye/drug in nanoparticle samples. Due to drug aggregation, the values for SHMT inhibitor (±)-**1** absorbance at peak maximum (310 nm) had to be corrected for light scattering by subtracting the value at 200 nm; nanoparticle calculations were performed similarly.

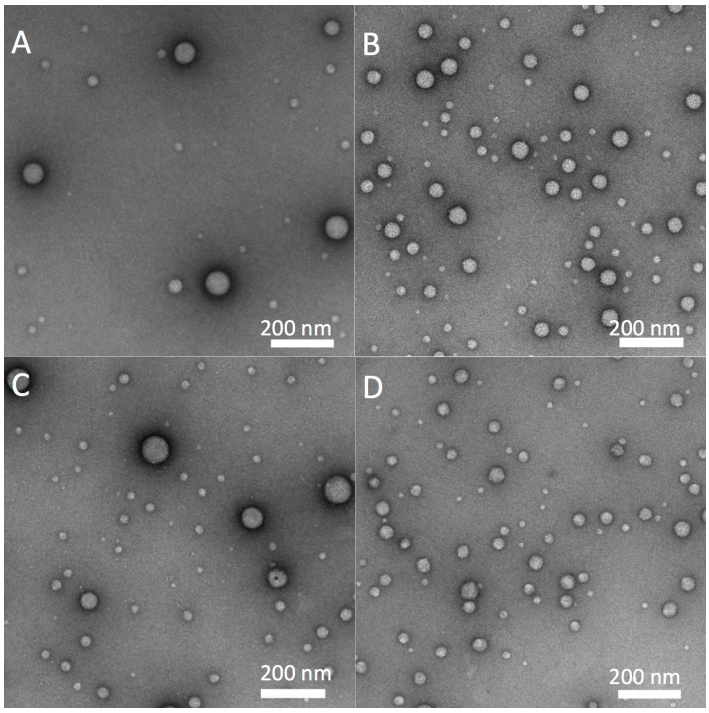

Figure 36. TEM images of Bodipy630 (1 µM)-loaded nanoparticles – used for triggered release studies – self-assembled from (A) PMOXA-*b*-PCL, (B) PMOXA-*g*(SS)-PCL 1, (C) PMOXA-*g*(SS)-PCL 2, and (D) PMOXA-*g*(SS)-PCL 3.

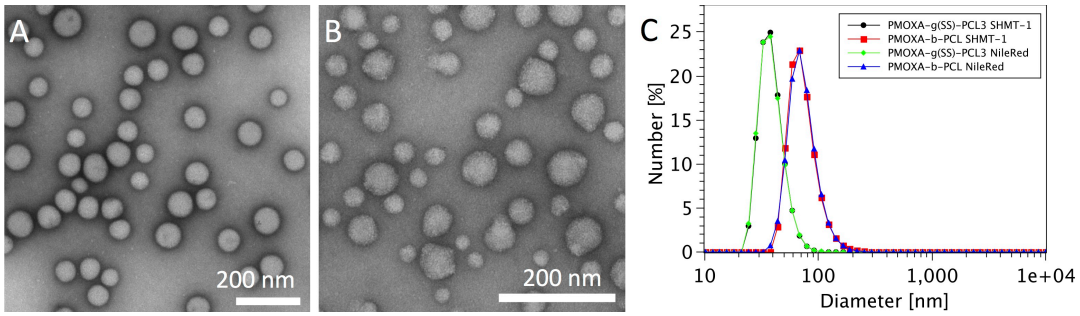

Figure 37. Morphology of drug-loaded (SHMT inhibitor (±)-**1**) nanoparticles self-assembled from PMOXA-*b*-PCL (A), and PMOXA-*g*(SS)-PCL 3 recorded by transmission electron microscopy (TEM). (C) Hydrodynamic diameter and number distribution of dye- (NileRed) and drug-loaded (SHMT inhibitor (±)-**1**) nanoparticles in PBS measured by DLS.

7.3.3 Reduction-Triggered Model Compound Release and Stability of Nanoparticles in Cell Media

The design of smart drug delivery vehicles demands for stable nanostructures, which do not aggregate, keep the drug within the carrier prior to cellular uptake, and subsequently release the payload upon reaching cellular compartments that provide the desired trigger. Fluorescence correlation spectroscopy (FCS) is a method that allows to study dye encapsulation, stability and triggered release on a single molecule level.[97,292] FCS was used herein to first follow the reduction-

triggered release behavior of a model hydrophobic cargo (Bodipy630) upon dithiothreitol (DTT)-induced disintegration of reduction-responsive nanoparticles formed from PMOXA-*g*(SS)-PCLs. It can be determined whether the dye is encapsulated or freely diffusing by following the diffusion times (τ_D) of fluorescent molecules. Time series of FCS curves were recorded in the presence or absence of reducing agent to follow reduction-triggered model compound release from triggered nanoparticles compared to a non-triggered nanoparticle version (Figure 38, 39).

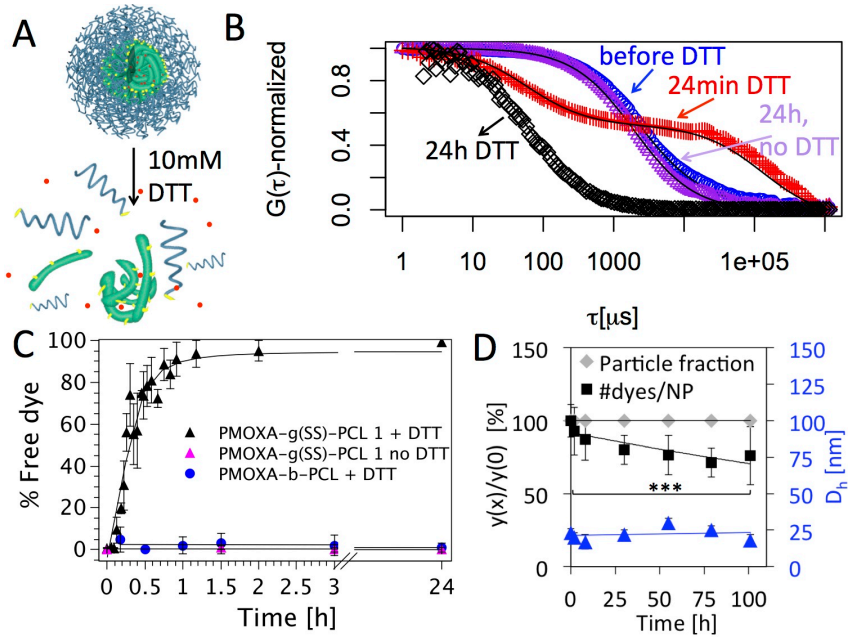

Figure 38. Reduction-triggered disassembly and dye release from PMOXA-*g*(SS)-PCL nanoparticles and nanoparticle cell medium stability studied by fluorescence correlation spectroscopy (FCS). (A) Schematic disassembly and dye release from reduction-sensitive nanoparticles. (B) Normalized autocorrelation curves (symbols) and fits (lines) from FCS measurements using Bodipy630-loaded PMOXA-*g*(SS)-PCL 1 nanoparticles in absence and presence of 10 mM DTT in PBS: t = 0 min (blue circles, 0% free dye fraction), t = 24 min (red crosses, 46% free dye fraction), t = 24 h (black diamonds, 100% free dye fraction), t = 24 h without DTT (magenta triangles, 0% free dye fraction). (C) Time series of the percentage of free dye fraction from FCS curves of nanoparticles with the following conditions: PMOXA-*g*(SS)-PCL 1 in PBS without DTT at 37 °C (magenta triangles), PMOXA-*g*(SS)-PCL 1 in PBS containing 10 mM DTT at 37 °C (black triangles), and PMOXA-*b*-PCL in PBS containing 10 mM DTT at 37 °C (blue circles). Free dye was only appearing for PMOXA-*g*(SS)-PCL in presence of 10 mM DTT, whereas incubation in PBS or non-sensitive PMOXA-*b*-PCL-nanoparticles in 10 mM DTT did not show free dye up to 24 h incubation. Values are mean of three independent measurements ± SEM for each time point. (D) Stability of PMOXA-*g*(SS)-PCL 3 Bodipy630-loaded nanoparticles in malaria culture medium (MCM) at 37 °C under shaking conditions for four days; nanoparticle fraction from two-component autocorrelation curve fitting compared to time point 0 (grey diamonds), change in number of dye molecules per nanoparticles calculated from molecular brightness (*CPM*) data compared to time point 0 (black squares), and hydrodynamic nanoparticle diameter (D_h) calculated from obtained diffusion times (blue triangles). Values are mean of 30 curves ± SD at each time point. Statistics was analyzed using two-tailed Student's *t*-test.

The fraction of free dye versus encapsulated dye was followed using a two-component fit of the obtained autocorrelation curves (Figure 38B). Simultaneously, the hydrodynamic diameters of the nanoparticles and the number of dye molecules per single nanoparticle were calculated from the diffusion times (τ_D) and molecular brightness (counts per molecule, *CPM* in kHz), respectively, by comparing values of nanoparticles to values obtained for free dye. The obtained nanoparticle hydrodynamic diameters using FCS (Figure 38D, 39C, 40) are in good agreement with values measured by DLS and TEM (Figure 34, 36, 37). Furthermore, the reducing agent-induced increase of nanoparticle sizes for the reduction-sensitive copolymers was confirmed by FCS (Figure 39C).

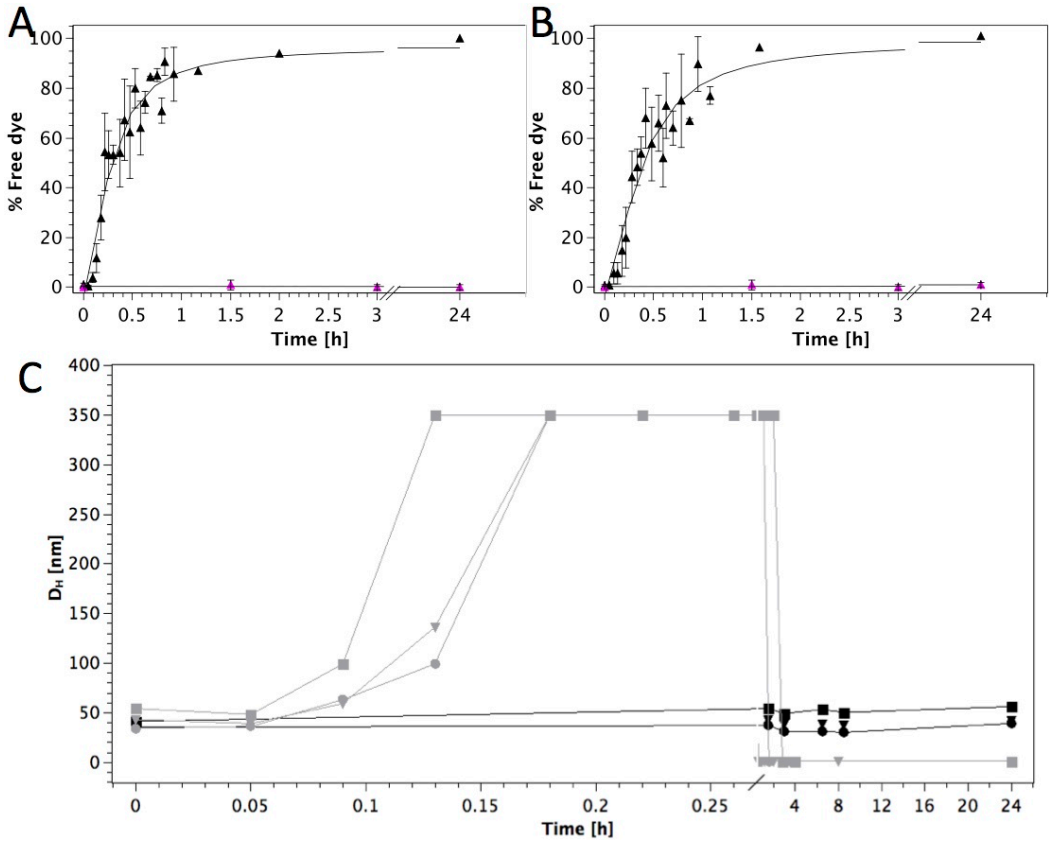

Figure 39. (A) Time series of the percentage of free dye (Bodipy630) fraction from FCS curves of nanoparticles with the following conditions: PMOXA-*g*(SS)-PCL 2 in PBS without DTT at 37 °C (magenta triangles), PMOXA-*g*(SS)-PCL 2 in PBS containing 10 mM DTT at 37 °C (black triangles). (B) Same as (A) but for PMOXA-*g*(SS)-PCL 3. Values are mean of three independent measurements ± SEM for each time point. (C) Development of hydrodynamic diameters calculated from FCS diffusion times: PMOXA-*g*(SS)-PCL 1 (down triangles), PMOXA-*g*(SS)-PCL 2 (squares), PMOXA-*g*(SS)-PCL 3 (circles) in PBS containing 10 mM DTT at 37°C under shaking condition (grey symbols and curves), and in PBS without DTT at 37°C under shaking condition (black symbols and curves). Diameters of aggregates above 350 nm are shown at 350 nm, because accurate size information is only possible for particles/aggregates smaller than the confocal volume.

The reduction-triggered release of a model cargo (Bodipy630) from all reduction-sensitive nanoparticles compared to stable, non-sensitive nanoparticles was successfully achieved as demonstrated by FCS measurements (Figure 38B, C, 39A, B). The free dye population obtained from two component fits was only increasing over time – reaching more than 90% free dye after 1.5 h – in case of PMOXA-*g*(SS)-PCL nanoparticles in the presence of DTT (10 mM). The same samples incubated without DTT or non-sensitive nanoparticles (PMOXA-*b*-PCL) with DTT (10 mM) did not reveal a free dye population in FCS curves even after 24 h. This smart drug release from nanoparticles at physiological, cytosolic reducing agent concentration at 37 °C sets the basis for triggered delivery of hydrophobic and unstable drug molecules to cancer cells and malaria parasite infected RBCs. Before cell experiments were conducted, the stability of the loaded nanocarriers was studied in detail on a single molecule level using FCS. These measurements were performed at physiological temperature (37 °C) under shaking conditions in the complete cell media (containing proteins), which were subsequently used for assays with cancer cells and malaria parasites. Reduction-sensitive and non-sensitive nanoparticles were both highly stable in terms of nanoparticle size, colloidal stability, and dye retention within the nanoparticles in both cell media for the whole tested time window of four days (Figure 38D, 40), which was the maximum incubation time used in cell assays.

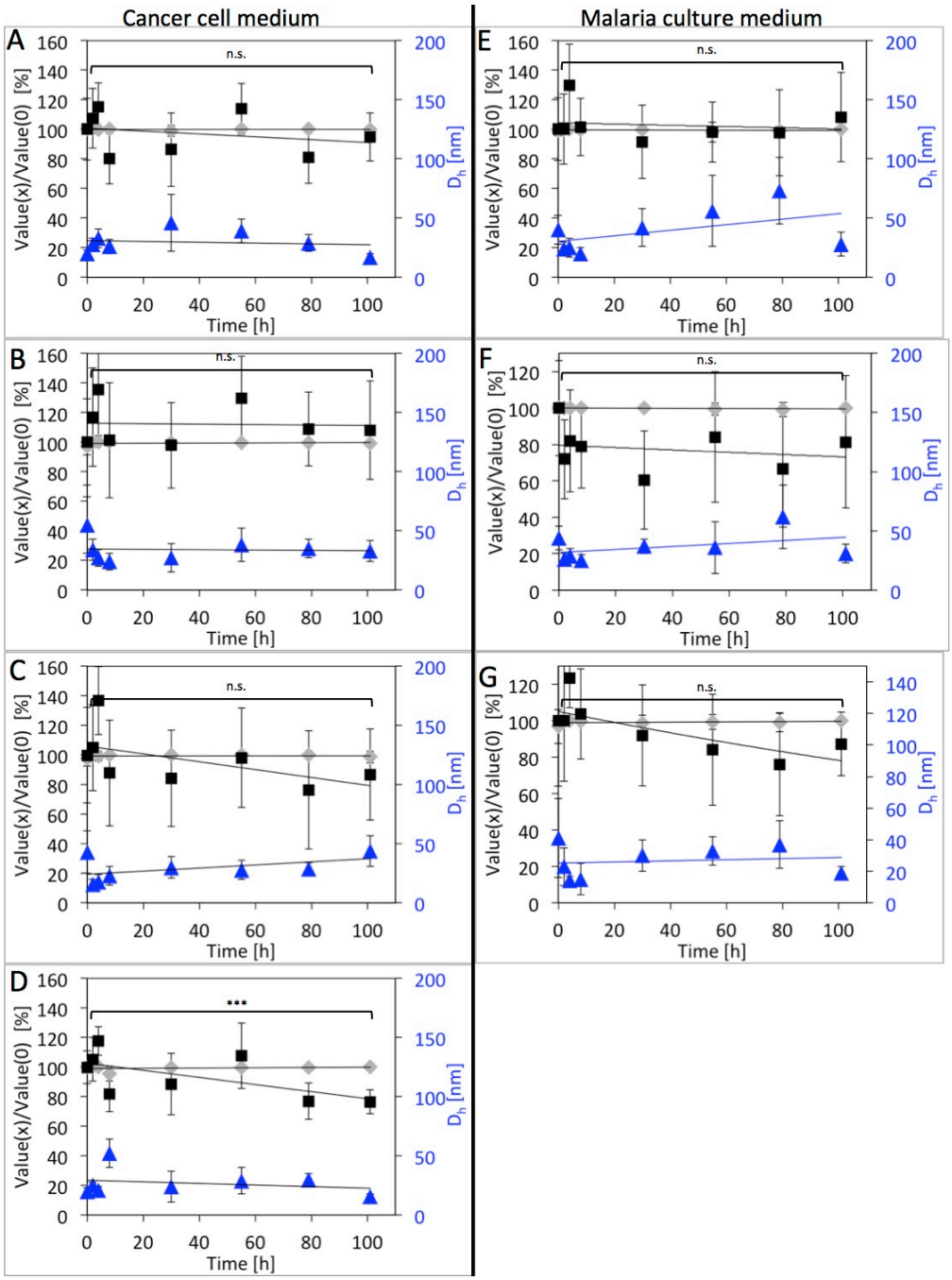

Figure 40. Stability of dye-loaded (Bodipy630) nanoparticles in cancer cell medium (left) and malaria culture medium (right) at 37 °C under shaking condition for 4 days: nanoparticle fraction from two-component autocorrelation curve fitting compared to time point 0 (grey diamonds), change in number of dye molecules per nanoparticles calculated from molecular brightness (*CPM*) data compared to time point 0 (black squares), and hydrodynamic nanoparticle diameter calculated from obtained diffusion times (blue triangles). (A,E) PMOXA-*b*-PCL nanoparticles (stock containing 2.5 µM Bodipy630). (B,F) PMOXA-*b*-PCL nanoparticles (133 µM Bodipy630). (C,G) PMOXA-*g*(SS)-PCL 2 nanoparticles (2.5 µM Bodipy630). (D) PMOXA-*g*(SS)-PCL 3 nanoparticles (56 µM Bodipy630). Values are mean of 30 curves ± SD at each time point. Statistics were analyzed using two-tailed Student's *t*-test.

Overall, all the nanoparticle samples did not reveal any dye release throughout the whole assay time as calculated from two component fits of autocorrelation curves, which did not yield any significant fractions of fast diffusing species (grey diamonds, Figure 38D, 40). The diffusion time of this fast diffusing component was fixed to typical values of about 300 µs, which is different to free dye diffusion due to interaction of media proteins with hydrophobic dye molecules as calibrated by FCS of dye in complete cell media. An average of 18% and 2% dye release was calculated at the end of the four-day assay in case of reduction-sensitive and non-sensitive nanoparticles, respectively, when comparing the change in the number of dye molecules per nanoparticle, *via CPM* comparison of free dye to nanoparticle values over time. But these small differences compared to time point zero were mostly not significant (Figure 40). The nanoparticle hydrodynamic diameters (D_h) remained similar for all samples over the whole time course of four days, remaining in the optimal size window of D_h = 10 to 100 nm needed for optimal drug delivery *via* passive targeting.[149] This was expected due to the protein-repellant PMOXA[139,140] hydrophilic blocks exposed on the nanoparticle surfaces. This is an important aspect, since nanoparticle aggregation would significantly hamper accessibility of nanoparticles to tumor sites and iRBCs. Blood circulation times *in vivo* – needed for efficient passive accumulation of the drug-loaded nanoparticles at tumor sites or within iRBCs – would also be reduced due to increased hepatosplenic filtration. This demonstrates the high potential of triggered nanoparticles based on PMOXA hydrophilic blocks that can be seen as valuable alternatives to overcome problems associated with PEG-based nanoparticles.[124]

7.3.4 Drug Delivery to *Plasmodium falciparum*-Infected Red Blood Cells

Another disease model was used to study the broad applicability of the reduction-sensitive PMOXA-*g*(SS)-PCL nanoparticle platform for smart drug delivery. First, a model hydrophobic molecule, NileRed, was encapsulated in reduction-sensitive PMOXA-*g*(SS)-PCL 3 nanoparticles and PMOXA-*b*-PCL nanoparticles to study delivery of a model compound *via* fluorescence microscopy. This hydrophobic dye molecule additionally serves as a model for drug molecules with very low aqueous solubility, a property of many experimental drugs at early stages of drug development. After a short 2 h incubation of either free dye or encapsulated dye with a mixture of RBCs and iRBCs (about 4%), a clear intracellular parasite staining was observed in all cases, demonstrating the possible delivery of a model molecule to iRBCs using small nanoparticles (Figure 41B, 42). This fast delivery of a model compound to iRBCs without any targeting ligands on the nanoparticle

surface indicates the potential of inert, protein-repellant PMOXA-coated nanoparticles for passively targeted antimalarial delivery to *Plasmodium*-infected RBCs.

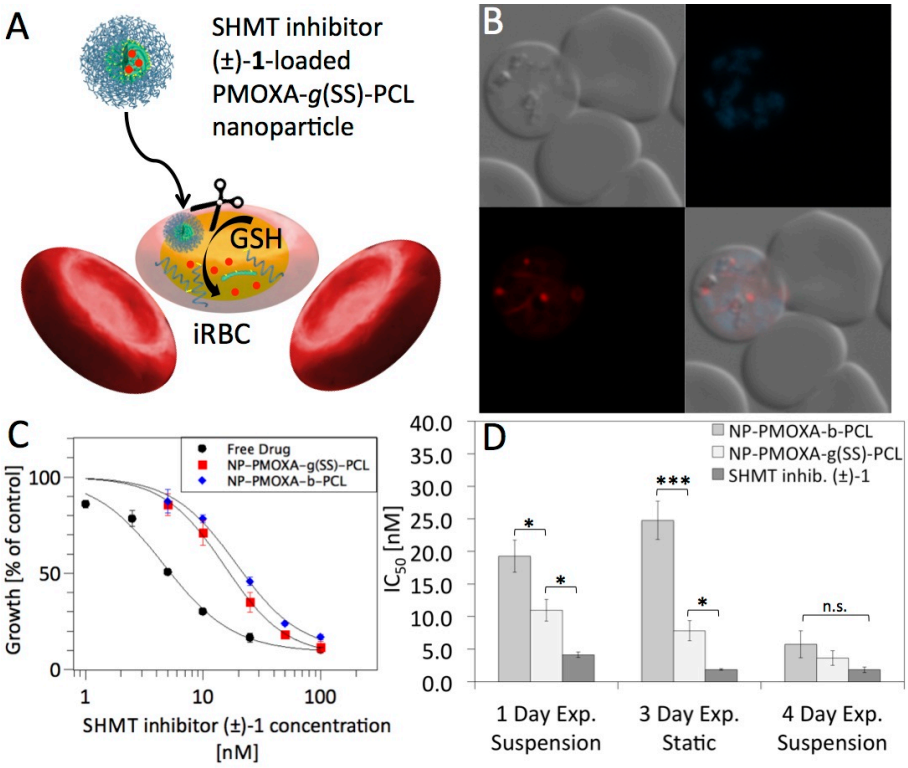

Figure 41. Dye and drug delivery to Plasmodium-infected red blood cells (iRBCs). (A) Schematic representation of SHMT inhibitor (±)-**1** delivery to iRBCs using reduction-responsive PMOXA-*g*(SS)-PCL nanoparticles. (B) Fluorescence imaging demonstrating delivery of hydrophobic model molecule, NileRed, using PMOXA-*g*(SS)-PCL 3 nanoparticles: DIC (top left), Hoechst DNA-stain (top right), NileRed signal (bottom left), merge (bottom right). (C) Example of dose-response curves for one-day suspension antimalarial assay with free SHMT inhibitor (±)-**1** or nanoparticle-based delivery. (D) Comparison of IC_{50} values for all the different antimalarial assay conditions and samples presented as the average ± SEM (n ≥ 3). Statistics were analyzed using two-tailed Student's *t*-test: $^{*}p<0.05$, $^{**}p<0.01$, $^{***}p<0.001$.

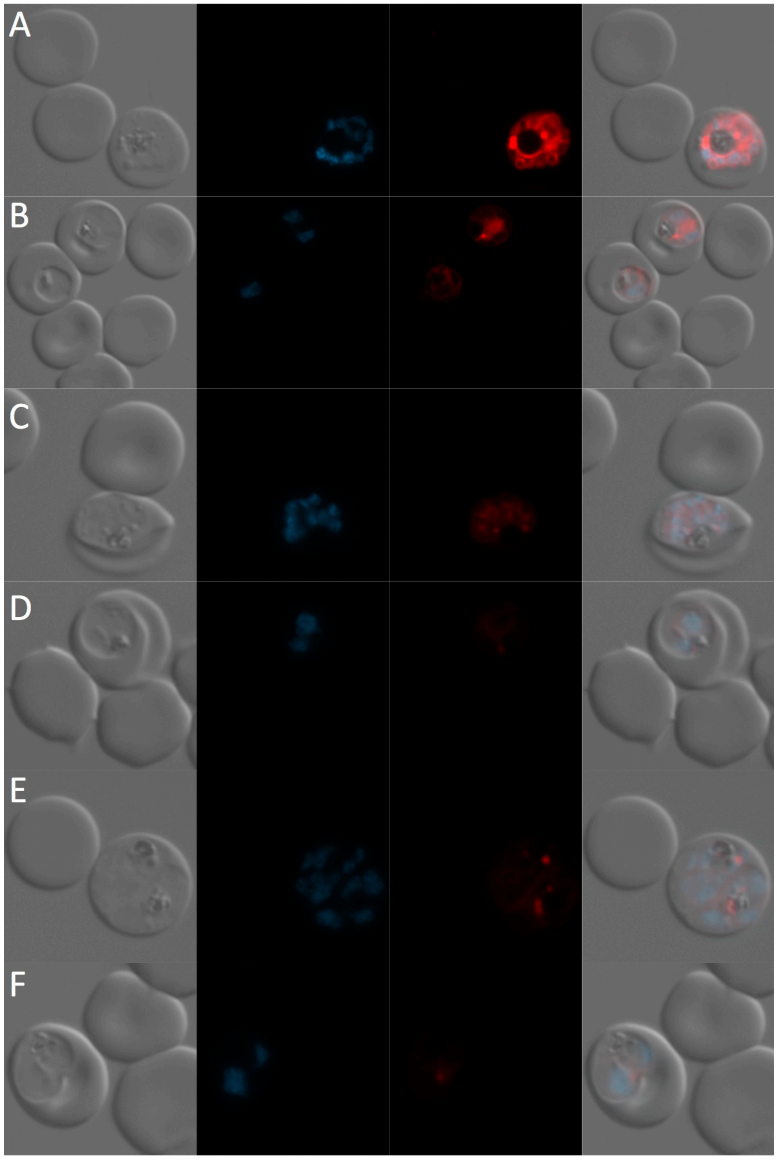

Figure 42. Fluorescence imaging demonstrating delivery of hydrophobic model molecule, NileRed, to iRBCs using no carrier (A, B); PMOXA-*g*(SS)-PCL 3 nanoparticles (C, D); PMOXA-*b*-PCL nanoparticles (E, F): DIC (left), Hoechst DNA-stain (middle left), NileRed signal (middle right), merge (right). Same dye concentrations (final 2.5 µM) and microscopy settings were used for all images.

Fluorescence intensities were in general higher within schizonts compared to trophozoite stage parasites (Figure 42). The staining pattern shows accumulation of the dye in certain parasite compartments. This specific dye is known to accumulate in neutral lipid bodies, which were proposed to be storage organelles for lipid intermediates.[293] The observation of this lipid body staining also in nanoparticle samples suggests successful release of the dye from nanoparticles. Combined with the high medium stability of both particles for several days (Figure 38D, 40) it can be speculated that nanoparticles are taken up and the dye is subsequently released. This delivery mechanism was also proposed by other

research groups.[39,40,42] To reflect the potency of nanoparticle-based stabilization and delivery of small compounds, a one-day-old NileRed aqueous solution was additionally tested in the same way and compared to a fresh NileRed solution. It clearly showed that this model hydrophobic compound was not stable enough in solution for one day; it did not readily appear in the iRBCs compared to fresh dye (Figure 43).

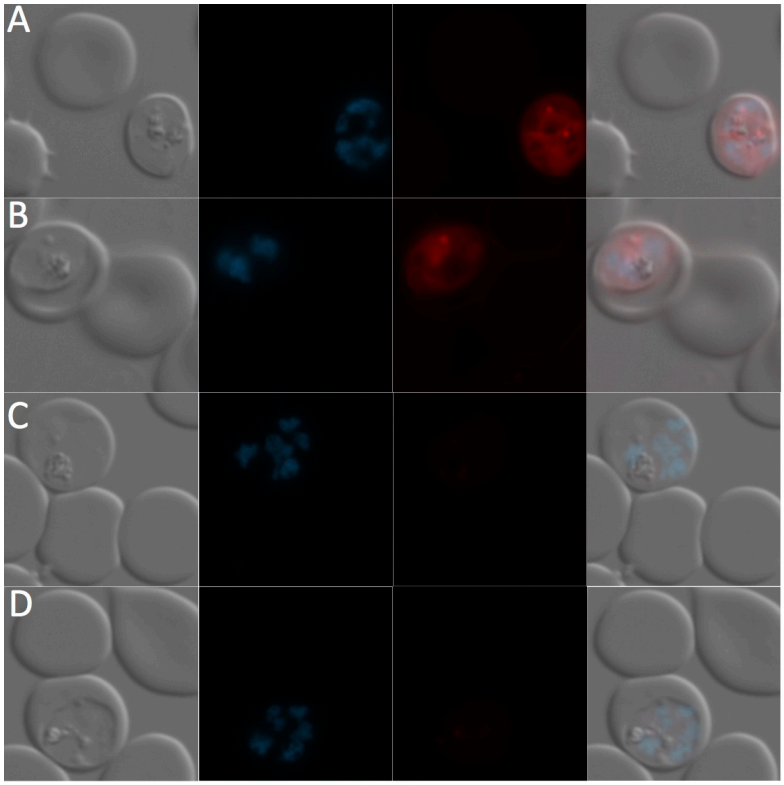

Figure 43. Fluorescence imaging demonstrating uptake of hydrophobic dye by iRBCs using freshly prepared NileRed solution in PBS (A, B), and 1 day incubated NileRed solution in PBS: DIC (left), Hoechst DNA-stain (middle left), NileRed signal (middle right), merge (right). Same dye concentrations (final 2.5 µM) and microscopy settings were used for all images.

Similarly, an experimental antimalarial compound (SHMT inhibitor (±)-**1**, Figure 33),[291] which is very active *in vitro*, but with an intrinsic solubility and metabolic stability problem that hampers successful *in vivo* application,[291] was incorporated within reduction-sensitive and non-sensitive nanoparticles. With our nanoparticles, we could stabilize the drug up to concentrations of about 300 µM, whereas the free drug was not readily soluble in PBS, it visibly precipitated as shown in digital images at a concentration of 10 µM drug in PBS (Figure 44).

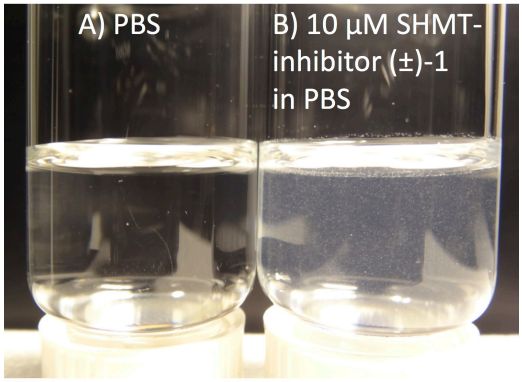

Figure 44. Digital image of a PBS solution (A) and a 10 µM SHMT inhibitor (±)-**1** in PBS (B) after 30 minutes at RT, prepared from a 10 mM stock in DMSO, demonstrating precipitation of the hydrophobic drug in aqueous solution.

iRBCs and uninfected RBCs under shaking conditions were used as an *in vitro* system that more closely simulates the *in vivo* situation compared to standard static drug testing for antimalarials (Subchapter 3.3.5), which was additionally performed (Figure 41C, D). Only PMOXA-*g*(SS)-PCL 3 and PMOXA-*b*-PCL nanoparticles were used for antimalarial testing, because there were no significant differences found for the three graft copolymers in terms of drug delivery to cancer cells. Solubilization and potential protection from metabolic degradation are the main reasons for SHMT inhibitor (±)-**1** encapsulation in nanoparticles. We demonstrated that over two parasite cycles (four day suspension assay, 5% hematocrit) the drug reached its full potential when delivered *via* nanoparticles (Figure 41D). For shorter incubation times (one day suspension assay, 10% hematocrit, Figure 41C, D), which better mimic the natural situation, the drug was more active followed by drug delivery *via* reduction-sensitive nanoparticles and non-sensitive nanoparticles. The results were similar when tested in standard antimalarial drug testing assays (three day static assay, 1.25% hematocrit). In this *in vitro* setting, where no other cells apart from RBCs and iRBCs were present, developed antimalarials intrinsically target the iRBCs and uptake of bigger nanoparticles is slower compared to small molecule uptake. This explains the delivery profile obtained with our drug delivery system. Our nanoparticle platform holds the promise to efficiently solubilize and delay fast liver degradation of this experimental drug,[291] by providing a hydrophobic core to shield it from the environment and deliver it to iRBC in the bloodstream. These observations provide the basis for further optimization and application of nanoparticles for stabilizing, protecting, and delivering water-insoluble, labile drugs already at early stages of drug development. This represents a highly promising alternative to optimization of the drug itself and can be applied to other anticancer or anti-infectious drugs.

7.4 Conclusions

A library of reduction responsive PMOXA-*g*(SS)-PCL amphiphilic block copolymers was synthesized through the thiol-disulfide exchange reaction between thiolated PMOXA (PMOXA-SH) and pyridyl disulfide functionalized poly(ε-caprolactone) (PCL-*co*-PPCL). This type of copolymers self-assembled into nanoparticles with sizes around 50 nm. These nanoparticles did not reveal any cytotoxicity in the tested concentration range, providing a biocompatible, biodegradable, and reduction-triggerable platform for smart drug delivery. Detailed stability and release studies using nanoparticle-incorporated model compounds demonstrated high colloidal stability and guest molecule retention within the nanostructures when incubated in various cell media at physiological temperature for four days. Rapid release of the guest molecules was achieved upon treatment with biologically relevant reducing agent concentrations. This designed nanoparticle platform was successfully used to delivery hydrophobic, toxic anticancer drugs to cancer cells. Additionally, this nanoparticle platform was evaluated to solubilize and deliver a hydrophobic, metabolically unstable, experimental antimalarial drug to *Plasmodium*-infected RBCs, which was successfully achieved. Our new reduction-sensitive amphiphilic copolymers are promising candidate materials for targeted drug delivery purposes to tackle cancer and malaria with a sophisticated smart delivery platform.

CHAPTER 8

8 Supplementary Experiments on Antimalarial Drug Delivery

This chapter contains more data on antimalarial drug delivery to iRBCs including first in vivo trials. In particular, dye uptake and nanoparticle-assisted delivery to iRBCs is examined in more detail. Parts of this chapter are being prepared for publication.

8.1 Results and Discussion

8.1.1 Dye Participation to *Plasmodium*-Infected Red Blood Cells

In the previous Chapter 7, staining of iRBCs with the hydrophobic dye NileRed was demonstrated. In fact, most small molecular compounds (dyes, drugs) that were used within this study accumulated within iRBCs compared to normal RBCs. We speculate that this is the case for most antimalarial compounds and established drugs. Here, selected examples of dye/drug accumulation in iRBCs are presented (Figure 45). In essence, *in vitro* cultures of *P. falciparum* were mixed and incubated for a few hours with dye/drug solutions, and then examined by live imaging without any washing steps.

Rhodamine 6G, Bodipy630, and DNA-intercalating Hoechst 33342, as well as the cytotoxic anticancer drug DOX were taken up by the parasites. The uptake of DOX by iRBCs reveals why several anticancer drugs are also potent antimalarials and vice versa.[294,295] Reason for the increased uptake of various compounds by iRBCs might be NPPs activated on iRBC membranes, which take up molecules with various chemical makeups from the surrounding medium.[37] Furthermore, the controversial “leakiness” of iRBCs might provide openings that allow for passive accumulation of these compounds within iRBCs.[39,40,42]

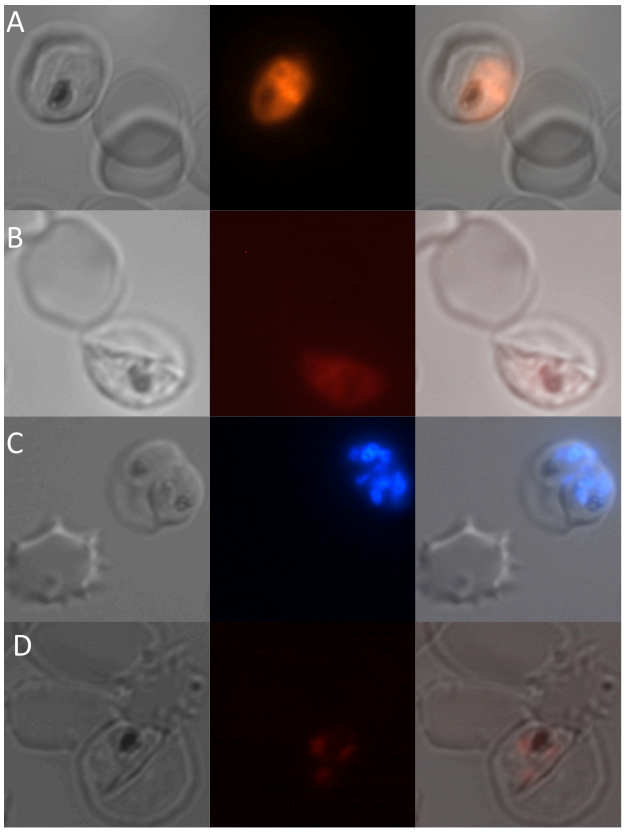

Figure 45. Uptake of various dye molecules by iRBCs revealed by live cell fluorescence imaging without washing steps. (A) 50 nM Rhodamine 6G, (B) 7.5 µM Bodipy630, (C) 2.5 µM Hoechst 33342, and (D) 50 nM DOX. DIC (left), corresponding fluorescence channel (middle), merged images (right).

Only one specific dye, SRB, did not specifically accumulate within iRBCs. Before washing the culture, the cell-surrounding medium was as bright as iRBCs (Figure 48A). Before washing, homogenous fluorescence was predominantly observed in the medium and within iRBCs in cultures incubated with SRB. Only after washing, it became apparent that SRB also entered iRBCs, albeit without accumulating over time. Therefore, SRB serves as a model compound to compare uptake of free dye versus dye-loaded nanostructures as further described below.

8.1.2 Nanostructure-Based Delivery to *Plasmodium*-Infected Red Blood Cells

Uptake of molecules, antibodies, and nanoparticles (up to about 80 nm diameter) by iRBCs has previously been demonstrated by several groups.[39-42] Nevertheless, these data remain a controversy, especially due to the specific dye uptake by iRBCs even without conjugation or incorporation to/within nanoparticles (Figure 42, 45). Based on previous reports that demonstrated specific uptake of polystyrene

nanobeads by iRBCs,[39] we first repeated uptake experiments with commercial, fluorescently labeled polystyrene nanobeads (Sigma, L5155).

Size distribution and diameters of the commercial nanobeads were examined by TEM (Figure 46A) and FCS, yielding bead diameters of 25 ± 6 nm and 24 nm (*CPM* = 20 kHz), respectively. Fluorescence imaging after a two-hour incubation with nanobeads clearly showed that only *Plasmodium*-infected RBCs were labeled (Figure 46B).

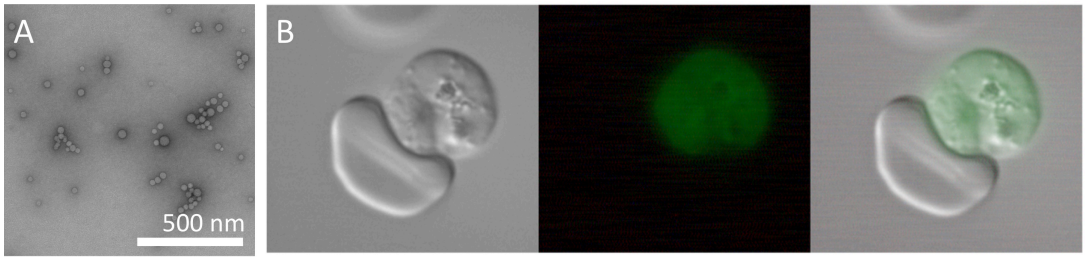

Figure 46. (A) TEM image of green fluorescent polystyrene beads (25 ± 6 nm, Sigma, L5155). (B) Uptake of green fluorescent polystyrene beads (Sigma, L5155) by *P. falciparum*-infected red blood cells (iRBCs). DIC (left), green fluorescence channel (middle), merged image (right).

It is also possible that the fluorescent dye leaks from the nanostructures, which would lead to staining of iRBCs provided the free dye accumulates in iRBCs (Figure 42, 45). SRB is an exception because being a highly hydrophilic dye; it can be stably encapsulated by nanostructures forming a hydrophilic compartment (*e.g.* polymersomes and nanomimics). Therefore, SRB can be used to compare delivery of loaded nanostructures versus free dye. Various SRB-loaded polymersomes and nanomimics were tested for uptake by iRBCs (Figure 47, 48, 49). Samples were diluted 1 to 10 within the final parasite culture medium.

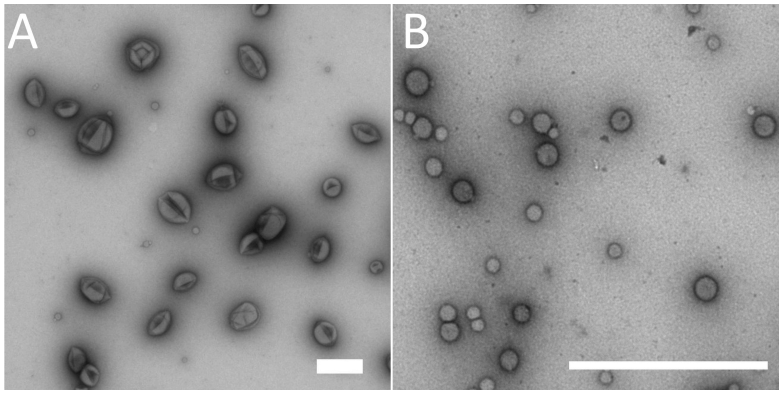

Figure 47. TEM micrographs of (A) large PMOXA-*b*-PDMS polymersomes, and (B) small nanomimics used for uptake experiment shown below. Scale bars are 500 nm.

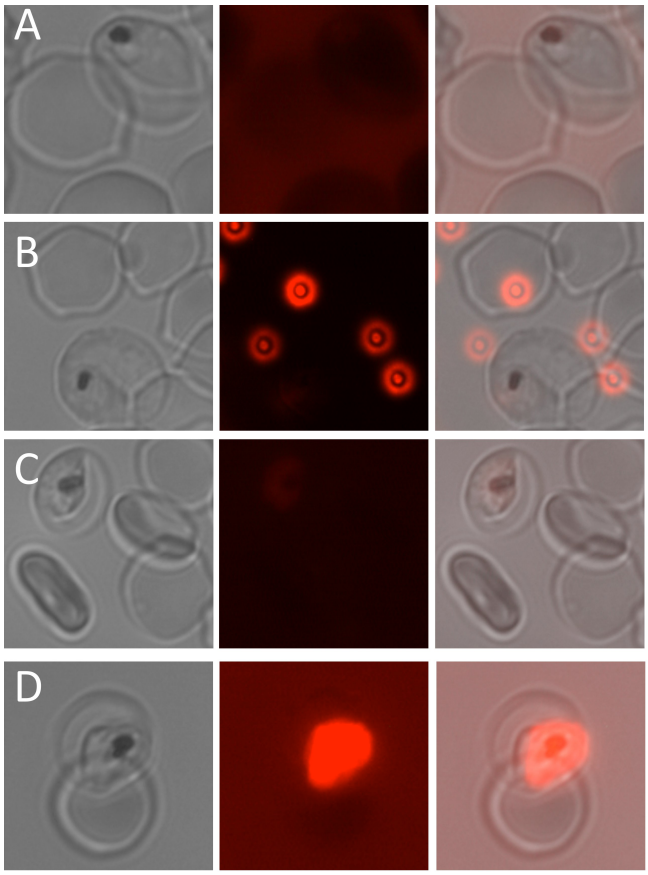

Figure 48. Fluorescence live cell imaging of SRB uptake by *P. falciparum*-infected RBCs. Samples were incubated for 21 hours with free and encapsulated SRB and directly imaged without washing. (A) 500 nM SRB, (B) large, SRB-loaded PMOXA-*b*-PDMS-based polymersomes (D_H = 225 nm, 170 nM SRB), (C) middle-sized, SRB-loaded PMOXA-*b*-PDMS-based polymersomes (D_H = 140 nm, 90 nM SRB), (D) small, SRB-loaded nanomimics (D_H = 56 nm, 360 nM SRB). DIC (left), SRB channel (middle), merge (right). Imaging parameters were identical for all images.

Fluorescence images of parasite cultures incubated with different SRB-loaded vesicles revealed the same trend that has previously been found:[39,40,42] Small sized nanostructures (< 80 nm diameter) readily reached intracellular parasites (nanomimics, 56 nm mean diameter, Figure 48D), followed by middle-sized polymersomes (140 nm mean diameter, Figure 48C). In contrast, large polymersomes (225 nm mean diameter) did not end up within iRBCs but are detected in a different focal plane (Figure 48B). Importantly, free SRB – added at higher concentration than SRB concentrations of all nanostructure samples – did not reveal clear parasite staining before washing (Figure 48A).

The efficient delivery of SRB to parasites *via* nanomimics might be related to the heparin-mediated targeting of the nanostructures to iRBC as has been demonstrated by others.[207] However, we observed only partial targeting of iRBCs by nanomimics (Chapter 3). We consider the difference in size between nanomimics and polymersomes to a more likely explanation for the increased

delivery efficiency. Despite extensive extrusion using 50 nm pores, only nanomimics remained close to this size whereas polymersomes usually rearranged to larger sizes after extrusion. Some more detailed images of washed samples incubated with nanomimics also revealed early stage parasite staining of a triple-infected RBC (Figure 49).

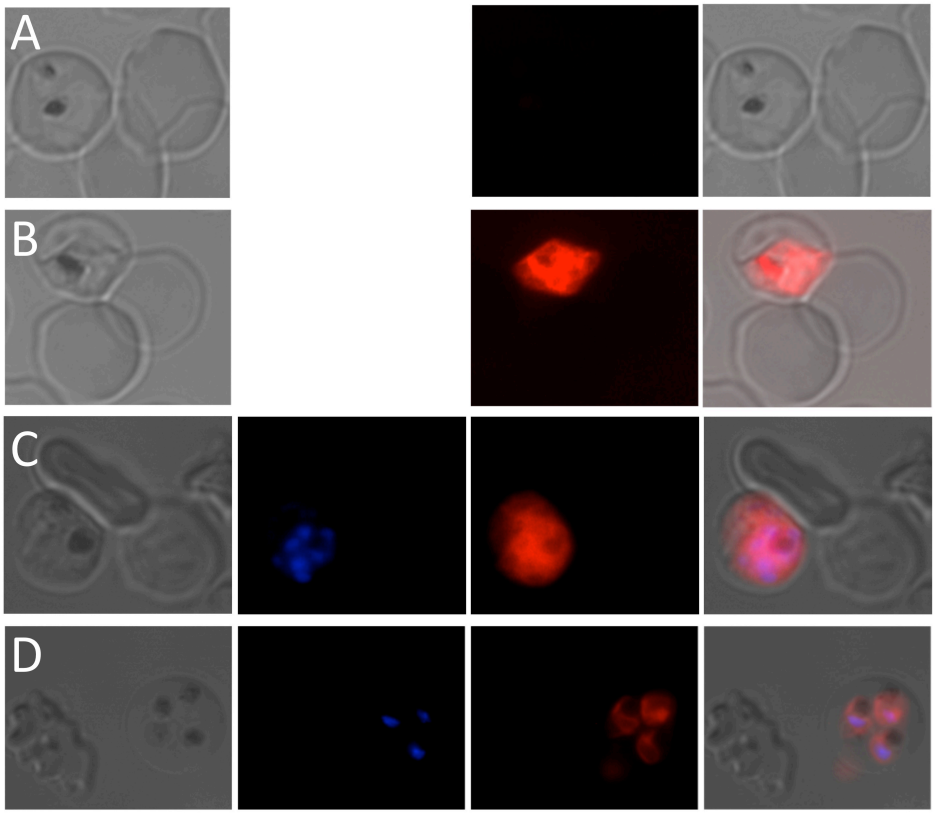

Figure 49. Fluorescence live cell imaging of samples incubated for 21 hours containing (A) 500 nM SRB, and (B) small nanomimics (D_H = 56 nm, 360 nM SRB), without including washing steps after incubation. (C, D) Imaging of nanomimic-assisted SRB delivery (D_H = 56 nm, 360 nM SRB). Parasite-infected RBC cultures were incubated for three days, washed twice with PBS and then imaged. Panels: DIC (left), Hoechst (middle left), SRB channel (middle right), merge (right).

An antimalarial drug candidate that exhibits a similar distribution pattern as SRB is likely to benefit from nanoparticle-assisted delivery as lower amounts of the drug would be needed to achieve a similar effect as with the free drug. Additional advantages offered by nanoparticle-assisted antimalarial drug delivery include solubilization, stabilization, and protection from metabolic degradation.

To follow the uptake of nanocarriers by iRBCs, SRB-conjugated copolymers were used in the assembly of the nanostructure rather than encapsulating the dye. PMOXA-*b*-PDMS-*b*-PMOXA micelles were formed using the solvent injection method (from EtOH to PBS) with 95 wt% unlabeled copolymer and 5 wt% SRB-

labeled copolymer.[106] Importantly, micelles do not provide a hydrophilic compartment for encapsulation of any residual free SRB present in the solution. Accordingly, SRB visualized in iRBCs is part of the micelle itself. FCS measurements revealed hydrodynamic diameter of about 26 nm and about five dye-conjugated copolymers per micelle. Consistent with other reports on nanoparticle uptake by iRBCs,[39-42] faint iRBC staining was observed (Figure 50) after a 2h incubation of SRB-nanoparticles with a parasite culture.

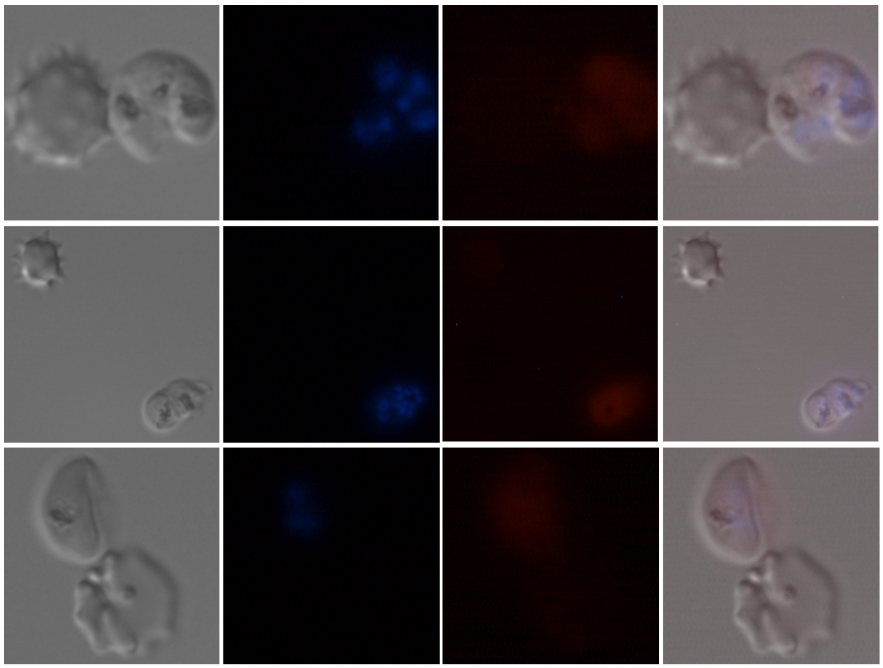

Figure 50. Uptake of PMOXA-*b*-PDMS-*b*-PMOXA micelles consisting of 5 wt% SRB-conjugated copolymer. iRBCs appeared reddish after two hours incubation and 2 x PBS wash. DIC (left), Hoechst DNA-stain (middle left), SRB signal (middle right), merge (right).

8.1.3 Additional Data on SHMT Inhibitor Delivery

SHMT inhibitor (±)-**1**-loaded PMOXA-*b*-PDMS-*b*-PMOXA micelles (D_H = 34 ± 10 nm) were also tested in *in vitro* suspension growth inhibition assays with *P. falciparum* (4 day assays). Data showed IC_{50} values of about 3 – 4 nM, which is similar to the values obtained for inhibitor delivery *via* other nanoparticles (Chapter 7).

First *in vivo* experiments using a *Plasmodium berghei* acute malaria mouse model were carried out with micelles (PMOXA-*b*-PDMS-*b*-PMOXA, 550 µM loaded SHMT inhibitor (±)-**1**, D_H = 26 ± 7 nm), reduction-sensitive nanoparticles (PMOXA-*g*(SS)-PCL, 50 µM and 5 µM loaded SHMT inhibitor (±)-**1**, D_H = 52 ± 14

nm), and insensitive nanoparticles (PMOXA-*b*-PCL, 300 µM, 50 µM and 5 µM loaded SHMT inhibitor (±)-**1**, D_H = 70 ± 22 nm). Despite rather high drug doses, none of the samples led to a significant reduction in parasitemia after four days. The mouse malaria parasite *P. berghei*, unfortunately, cannot be cultured *in vitro*. Therefore, it is difficult to establish whether nanoparticle stability and circulation time *in vivo* were inadequate or whether *P. berghei* is not a corresponding model for *in vivo* testing of *in vitro* activity previously observed with *P. falciparum*. For instance, *P. berghei*-infected mouse RBCs might not provide the same "leakiness" as human *P. falciparum*-infected RBCs, which might significantly hamper accessibility of nanoparticles to iRBCs. Moreover, the mouse parasites might not be susceptible to SHMT inhibitor(±)-**1**. Accordingly, the drug failed to reduce parasitemia when applied without a carrier, although this has mainly been attributed to the rapid metabolic degradation of the drug.[291] Nevertheless, no apparent toxic effects of the *i.v.* applied drug-loaded nanoparticles were observed; all mice survived until the end of the assay. This indicates the large potential for a broad use of such nanostructures in biomedical applications. Future studies must assess nanoparticle stability, drug-retention and circulation time *in vivo* before final conclusions on the suitability of this nanoparticle platform for the delivery of antimalarials can be drawn.

CHAPTER 9

9 General Conclusion and Outlook

In this thesis, two alternative nanotechnological approaches for potential malaria treatment/prophylaxis were established. The first approach, called 'nanomimic strategy' involved the synthesis of simple, functional polymersome with potent parasite invasion inhibitory property. These polymersomes served as nanomimics of RBC membranes to bind to malaria parasites and thereby blocking RBC invasion. In *in vitro P. falciparum* blood stage suspension cultures, these nanomimics performed about two orders of magnitude better than soluble receptor molecules. The multivalent presentation of receptor molecules on nanomimics allows strong parasite-nanomimic interactions, which explains the highly potent performance of nanomimics. Furthermore, a high affinity interaction of heparin on nanomimics with *Pf*MSP1_{42} was measured, which provides important information on the parasite invasion mechanism. In contrast to the currently accepted common view, our data suggest that initial attachment might already be of high affinity. We further showed that cellular toxicity, anticoagulation property, and endotoxin contamination is very low for nanomimics, which render them ideal candidates for biomedical applications. Preliminary data on the secondary "vaccine-like" activity are very promising and warrant further, comprehensive exploration. The nanomimic concept clearly provides an interesting alternative to conventional drugs and vaccines. Considering the limited efficacy of malaria vaccine candidates and the difficulties associated with antimalarial drug resistance, the nanomimic strategy might be a valuable option to treat children, having one of their first infections, and thereby, boosting the immune system to generate semi-immunity more rapidly than multiple natural infections do.

As a next step, *in vivo* applicability of nanomimics needs to be extensively explored. Specifically, blood circulation time of nanomimics has to be scrutinized. This information will help to determine whether synchronous parasites, where all infected cells would burst at about the same time, and timed nanomimics injection

are sufficient to potentially ensure that enough nanomimics are present in the bloodstream, when parasites are egressing from iRBCs. Alternatively, other receptor/receptor-like molecules might be considered in the design of nanomimics to yield more specific pathogen inhibition and longer blood circulation times.

The secondary "vaccine-like" activity has to be examined in more detail, preferentially with whole merozoites. If the immune response is not sufficient to protect from secondary infections, adjuvants, secondary targeting ligands (for specific immune cells), and immunostimulatory molecules might be integrated in the nanomimic formulation. This is readily accomplished by taking advantage of the polymersome-nature of nanomimics, which provides a hydrophobic membrane and a hydrophilic core for incorporation of various hydrophilic and/or hydrophobic substances. On the other hand, if the “vaccine-like” activity can be confirmed, but the infection, which is used to generate the immune response, is not sufficiently treated by nanomimics (based on the large number of parasites in the bloodstream), it might be necessary to combine nanomimics with a common antimalarial, which is not a problem.

Other interesting future analyses include detailed studies of the processes induced or inhibited in merozoites by nanomimic-binding, and of the stage(s) at which the merozoite is arrested. Merozoites are primed to invade RBCs; several sequential alterations on the merozoite occur during egress and subsequent invasion of fresh RBCs.[21-24] Therefore, binding of nanomimics to merozoites might either prevent binding of RBCs, or it might inhibit shedding of MSP1 by SUB2, for example. This is especially important in the context of the secondary "vaccine-like" activity, which will depend on the state of the merozoite surface-proteins. In other words, this nanomimic approach can be regarded as a platform for the antigenic display of whole merozoites produced during a natural infection. Problems associated with merozoite protein-based vaccination strategies, in particular the difficulty to find the best antigen or mixture of antigens and delivery vehicle[21] to induce maximum long-term protective response, might be circumvented. However, the nanomimic approach might only induce clone-specific immunity and infection with another clone might not be inhibited. Due to the current design of our nanomimics, which present a receptor that is used by all yet tested clones, such a new infection with a different clone could be treated with the same nanomimics again.

The design of the current nanomimics should entail broad-spectrum activity. Therefore, nanomimics should be tested on several other pathogens that use heparan sulfate for host cell interactions, *e.g.* HIV-1, hepatitis B and C, Dengue virus, West Nile virus, *Mycobacterium tuberculosis, Staphylococcus aureus, and*

Trypanosoma cruzi.[224] If surface binding alone cannot interfere with the life cycle of these pathogens, additional hydrophilic/hydrophobic drugs can easily be incorporated within nanomimics. Such nanomimics can be considered targeted drug delivery systems, which first bind to the extracellular pathogen, and then release toxic compounds within the host cell after cellular uptake of nanomimic-pathogen complexes.

In the second part of the thesis it was demonstrated that reduction-triggered, degradable, polymer-based nanoparticles stabilize an experimental antimalarial drug candidate and deliver it to infected RBCs. Excellent nanoparticle stability and reduction-triggered release properties were found for our nanoparticle drug delivery platform. The anticipated trigger for nanoparticle disassembly, the reducing cytosol of iRBCs, provides a basis for future optimization of carrier chemistry and loading. Moreover, we hypothesize that experimental antimalarial drugs in particular might benefit from nanoparticle-based delivery. Compounds identified to inhibit parasite growth *in vitro* often exhibit low aqueous solubility and instability, which hampers biomedical applications. An elegant way to tackle these problems is by incorporation within nanostructures: amphiphile-based nanostructures provide a hydrophobic core for solubilization of the drug and protection from the environment. However, if nanoparticle-assisted drug delivery is to be developed for treatment of uncomplicated malaria, another significant hurdle has to be considered, namely how orally administered nanoparticles reach the bloodstream. The transport of nanoparticles from an oral dose into the bloodstream is a considerable challenge, but it might be a valuable avenue to pursue. For cases of severe malaria associated with high mortality, where oral bioavailability is neither required nor applicable the formulation of nanoparticle-based drugs should be adapted correspondingly. Another avenue of possible nanoparticle-based antimalarial delivery is the fight of antimicrobial resistance.

Other interesting candidates for targeted drug delivery *via* nanocarriers are *P. falciparum* gametocytes and *P. vivax* hypnozoites. This is particularly relevant with regard to malaria eradication.[296] In the last steps of eradication, *P. vivax* hypnozoites must be totally eliminated to avoid relapse of infection in a few people, which might restart transmission to mosquitoes and cause further infections. Additionally, *P. falciparum* gametocytes should be attacked to block transmission from human to mosquito. One marketed drug, primaquine (PQ), can kill both, *P. falciparum* gametocytes and *P. vivax* hypnozoites, but its use is limited due to severe side effects.[296] PQ can lead to hemolysis in glucose 6-dehydrogenase (G6PD)-deficient patients, which are as frequent as 5 to 20 % in populations in malaria endemic areas of Sub-Saharan Africa and Asia.[297]

Nanoparticle-based delivery of PQ to hypnozoites and/or gametocytes is a promising strategy as it allows for much lower drug concentrations which, in turn, would largely reduce side effects.[298] Results on blood stage malaria, where CQ-concentration could be reduced 10-fold when delivered *via* nanostructures support this notion.[204]

This thesis has clearly demonstrated that a vast range of possibilities exist to tackle infectious diseases, in particular malaria, using nanomedicine approaches, which is much underexplored to date, but should be actively continued to finally find novel alternatives to treat/prevent infections in the future.

CHAPTER 10

10 Experimental Section

This chapter contains all experimental procedures, which were reproduced and modified with permission from the corresponding references [225,252,260,270].

PMOXA-*b*-PDMS-*b*-PMOXA (1) Synthesis. PMOXA-*b*-PDMS-*b*-PMOXA (**1**) was synthesized according to previously published protocols.[74,136,245] Briefly, bifunctional poly(dimethylsiloxane) (PDMS from ABCR GmbH, Karlsruhe, Germany) was vacuum stripped in a Schlenkflask overnight. Anhydrous hexane was subsequently added, and the stirred solution was dried by bubbling argon through it for 1 h. After bubbling, freshly distilled triethylamine (TEA) was added, and the mixture was cooled to −20 °C. PDMS was then reacted with trifluoromethanesulfonic acid (Tfsa) for 3 h at −20 °C, resulting in a bifunctional triflic PDMS macroinitiator. The reaction mixture was filtered through a cooled G4 filter under argon. From the filtrate hexane was removed under vacuum and replaced by dry ethyl acetate. Adding distilled 2-methyl-2-oxazoline resulted in a cationic ring-opening polymerization of poly(2-methyl-2-oxazoline) (PMOXA) on the PDMS macroinitiator. Termination was performed after 60 h at 40 °C by adding a 2:8 mixture of TEA/water resulting in bifunctional OH-terminated PMOXA-*b*-PDMS-*b*-PMOXA. Finally, the solvent was removed by vacuum distillation. Purification was performed by resolubilizing the polymer in 1:1 ethanol/water mixture and ultrafiltration through a 5 kDa membrane. The final product was dried under vacuum.

PDMS-*b*-heparin (2) Synthesis. Heparin sodium salt from porcine intestinal mucosa (15 kDa, 197 U/mg, 375095) was purchased from Merck KGaA (Darmstadt, Germany), and aminopropyl-terminated poly(dimethylsiloxane) ($PDMS(NH_2)_2$) (5 kDa, AB109371) from ABCR GmbH (Karlsruhe, Germany).

The tetrabutylammonium salt of heparin was obtained using a published protocol.[246] Briefly, 500 mg of heparin sodium salt was dissolved in a minimum

amount of water (approximately 3 mL) and passed through a freshly packed Dowex Marathon MSC column (H^+ form, 6 mL, Sigma-Aldrich, 428787). The pH was adjusted to pH 7 using a tetrabutylammonium hydroxide solution (54.0-56.0% in H_2O, Sigma-Aldrich, 86863). After reducing the volume on a rotary vacuum evaporator, the product was dialyzed against water for at least 48 h (Spectrum Laboratories Inc., Rancho Dominguez, CA, USA, MWCO 3.5 – 5 kDa). The product was subsequently dried under vacuum. To use as a control in the antimalarial assay, tetrabutylammonium heparin was first precipitated in cold diethyl ether, dried under vacuum, dissolved in PBS, and then passed through a size exclusion column (Sepharose 2B, Sigma-Aldrich, 2B300) equilibrated in PBS. The final concentration of heparin was then determined using the Farndale microassay.

For PDMS-*b*-heparin (**2**, Scheme 2, Chapter 3) synthesis, 100 mg of tetrabutylammonium heparin (~ 22 kDa) was dissolved in a 50 mL round-bottom flask in 25 mL dichloromethane (DCM), and a hundred-fold excess of $PDMS(NH_2)_2$ was added under stirring. Furthermore, a 10-fold excess of 2-picoline borane (Sigma-Aldrich, 654213) was dissolved in a small amount of DCM, added to the reaction mixture, and stirred for 7 days at room temperature (25 °C). After the third and fifth day of the reaction another 10-fold excess of 2-picoline borane was added, respectively. After 7 days, DCM was evaporated on a rotary evaporator and the product was washed in diethyl ether. The washed product was dried under vacuum and redissolved in a minimum amount of ethanol. Adding the solution dropwise into 4 x 15 mL diethyl ether in glass centrifugal tubes precipitated the product; unreacted $PDMS(NH_2)_2$ and reducing agent were soluble in diethyl ether. The precipitate was collected by centrifugation for 5 min (2000 RCF) and discarding the supernatant. This precipitation process was repeated two times. The final product was dissolved in ethanol, filtered and dried under vacuum. For ^1H NMR about 20 mg of the product was dissolved in 10% ethanol and passed through a freshly packed Dowex Marathon MSC column (Na^+ form, 2 mL, Sigma-Aldrich, 428787), and the volume was reduced to about 2 mL on a rotary evaporator, dialyzed against water for 24 h (Spectrum Laboratories Inc., Rancho Dominguez, CA, USA, MWCO 8-10 kDa), dried under vacuum and redissolved in D_2O/acetone-d_6 (v/v 3:1).

PDMS-*block*-Short-Heparin (PDMS-*b*-ShortHep) was synthesized similarly to PDMS-*b*-heparin, but using shorter heparin (ShortHep, 4 – 6 kDa) for the synthesis instead of full-length heparin (15 kDa).

Polymersome and Nanomimic Formation. Control polymersomes (PMOXA-*b*-PDMS-*b*-PMOXA only) were formed by the film rehydration technique.[74] A 1 mL amount of PMOXA-*b*-PDMS-*b*-PMOXA (6 mg/mL in ethanol) was put in a 5 mL round-bottom flask, and ethanol was removed on a rotary evaporator (100 mbar, 40 °C, 120 rpm). Subsequently, the thin polymer film was rehydrated using PBS or 1 mM SRB (Sigma-Aldrich, S1402) in PBS and stirred at least overnight.

Nanomimics were prepared using the bulk rehydration technique.[74] PMOXA-*b*-PDMS-*b*-PMOXA (6 mg/mL) and PDMS-*b*-heparin (4 mg/mL) were dissolved in ethanol (both yielded clear solutions) and mixed in a 5 mL round-bottom flask in the desired ratio. The solvent was evaporated on a rotary evaporator (100 mbar, 40 °C, 120 rpm) and the film was further dried at high vacuum overnight. The polymer film was subsequently destroyed using a spatula. The bulk polymer was hydrated in PBS and stirred for at least 12 h. To yield fluorescent polymersomes and nanomimics, they were incubated with 200 nM Bodipy630 (hydrophobic dye) in PBS after the vesicle formation procedure for FCS/FCCS, or the polymer mixture was hydrated using a 1 mM SRB (Sigma-Aldrich, S1402) solution in PBS. To use as a control in the antimalarial assay, tetrabutylammonium heparin, which was first precipitated in diethyl ether, dried under vacuum and dissolved in ethanol, was encapsulated in control polymersomes by adding 0.54 mL (4 mg/mL in ethanol) of the tetrabutylammonium heparin solution to 1 mL of PMOXA-*b*-PDMS-*b*-PMOXA (6 mg/mL in ethanol) with subsequent vesicle formation as described above for nanomimics (bulk rehydration[44]).

Micelle Formation. PDMS-*b*-heparin and PDMS-*b*-ShortHep micelles were formed similar to nanomimics but by using only PDMS-*b*-heparin or PDMS-*b*-ShortHep (100%) instead of a mixture with PMOXA-*b*-PDMS-*b*-PMOXA.

Nanostructure Extrusion and Purification. The polymersome, nanomimic, and micelle solutions were extruded at least 15 times through a 0.1 μm Nucleopore track-etch membrane (Whatman, GE Healthcare, UK) using a LIPEX extruder (Northern Lipids Inc., Canada). The final solution of nanostructures was passed through a size-exclusion column containing Sepharose 2B (Sigma-Aldrich, 2B300) equilibrated with PBS.

Giant Polymersome Formation. Giant polymersome (GUV) formation was accomplished according to the standard electroformation technique[299] using a Nanion Vesicle Prep Pro setup (Nanion Technologies, Munich, Germany). A freshly cleaned ITO-coated glass slide was first plasma-treated (Plasma Cleaner, PDC-002, Harrick Plasma, Ithaca, New York, USA), and then, a thin polymer film

was deposited on it. For control GUVs (only PMOXA-*b*-PDMS-*b*-PMOXA) a solution of PMOXA-*b*-PDMS-*b*-PMOXA in ethanol (6 mg/mL, 40 μl) was dispersed on the ITO-coated side of the glass slide and ethanol was subsequently evaporated using a vacuum chamber for 30 min (Plasma Cleaner, PDC-002, Harrick Plasma, Ithaca, New York, USA). For the heparin GUVs a mixture of PMOXA-*b*-PDMS-*b*-PMOXA in ethanol (6 mg/mL, 40 μl) and PDMS-*b*-heparin in ethanol (4 mg/mL, 10 μl) corresponding to a ratio of wt/wt 85:15 was used. Afterwards, a greased O-ring was put around the polymer film on the glass slide to form a chamber and then an aqueous sucrose solution (300 mM, 600 μl) was added to hydrate the polymer film. After covering by another ITO-coated glass slide, the sample was exposed to an ac current (3.0 V, 3.0 Hz) at room temperature. For control GUVs we performed electroformation overnight and for heparin GUVs electroformation was conducted for one hour. Finally, the GUV solutions were transferred to Eppendorf tubes and stored at 4 °C.

Protein Labeling. Water-soluble proteins were fluorescently labeled *via* amine groups using Oregon Green 488 carboxylic acid, succinimidyl ester, 5-isomer (OG488-NHS, Invitrogen, Carlsbad, CA, USA, O-6147) using established protocols (Invitrogen). The buffer of *P. falciparum* major surface protein 1-42 (*Pf*MSP1$_{42}$ (3D7)) was exchanged with 0.1 M carbonate buffer (pH 8.3) at a concentration of 2 mg/mL by using Amicon Ultra-0.5 mL (10K) centrifugal filters. OG488-NHS was dissolved in water-free DMSO (19.6 mM) and a 12-fold excess of OG488-NHS was added to the protein solution. After shaking for at least 2 h at room temperature, free OG488 was separated from labeled proteins on HiTrap desalting columns (Sephadex G25) using PBS as running buffer. The labeled proteins were stored in aliquots at −20 °C.

Nanoparticle Formation and Critical Micelles Concentration (CMC). Nanoparticles of PMOXA-*g*(SS)-PCL were prepared by first dissolving 5 mg of copolymer in 300 μL DMF, then 1 mL of filtered PBS buffer was added drop wise under continuous stirring. The solution was subsequently dialyzed against PBS buffer for 24 h with changing PBS buffer solution three times.

The critical micelle concentration (CMC) values of three PMOXA-*g*(SS)-PCL samples were determined by using pyrene as the fluorescence probe. The concentration of graft copolymers was varied from $1*10^{-5}$ mg/mL to 0.5 mg/mL, while preserving the same concentration of pyrene at 0.8 μM. After mixing the graft copolymer solution with pyrene, the solution was kept in the dark at 37 °C for 12 h before measuring. Fluorescence spectra were recorded using fluorescence spectroscopy at an excitation wavelength of 330 nm. Fluorescence emission at 372

and 383 nm were monitored. The CMC was estimated as the cross-point when extrapolating the intensity ratio I_{383} / I_{372} at low and high concentration regions.

Loading of Nanoparticles Formed by PMOXA-*g*(SS)-PCL and PMOXA-*b*-PCL. SHMT inhibitor (±)-**1**-, Bodipy630-, and NileRed were loaded into PMOXA-*g*(SS)-PCL and PMOXA-*b*-PCL by the solvent switch technique. First, PMOXA-*g*(SS)-PCL was dissolved in DMF (150 µL), and PMOXA-*b*-PCL in THF (150 µL). Subsequently, the drug or dye was dissolved in DMSO (SHMT inhibitor (±)-**1**, 10 mM, Bodipy630, 7.9 mM) or THF (NileRed, 8 mM) and added to the dissolved polymers in the desired ratio. In case of PMOXA-*g*(SS)-PCL, 0.5 mL PBS was then added dropwise under stirring. For PMOXA-*b*-PCL, the polymer-drug/dye mixture was dropwise added to 0.5 mL stirred PBS. The mixtures were transferred into dialysis tubes (Spectrum Laboratories Inc., Rancho Dominguez, CA, USA, MWCO 300 kDa) and extensively dialyzed against 0.15 M NaCl for at least three days, while changing the solution at least eight times, and in the last step of purification dialysis was performed against PBS (Sigma). After purification, samples were sterile filtered using sterile 0.45 µm syringe filters.

Drug loading efficiency (DLE) and drug loading content (DLC) were calculated according to the following formulas:

DLE (%) = (weight of loaded drug / weight in feed) * 100%

DLC (wt%) = (weight of loaded drug / weight of polymer+drug) * 100%

Loading content in SHMT inhibitor (±)-**1**-, Bodipy630-, and NileRed-loaded nanoparticles was determined using UV-Vis absorption measurements at corresponding absorbance maxima and comparing to drug/dye calibration curves in PBS (Figure 35).

Farndale Microassay. Farndale microassays were performed based on Farndale *et al.*[300] with slight modifications. To obtain the amount of saccharide units per PDMS chain (5 kDa) an ethanolic solution of dimethylmethylene blue (DMMB) was prepared (15.8 µg/mL). A 250 µL sample of this solution was pipetted into each well of a 96-well plate and 50 µL of ethanol (blank), tetrabutylammonium heparin in ethanol (100, 50, 25, 10 µg/mL), and PDMS-*b*-heparin in ethanol (100, 50 µg/mL) were mixed into each well in duplicates. The UV-vis absorbance was measured from 495 nm to 605 nm immediately after mixing. The tetrabutylammonium heparin standard curve was generated using the absorbance at the peak maximum at 565 nm. Absorbance at 565 nm of the PDMS-*b*-heparin samples and the calibration curve were used to calculate the relative tetrabutylammonium heparin content (*R*) in PDMS-*b*-heparin and the molecular

weight of tetrabutylammonium heparin (MW) per PDMS while assuming a constant length of PDMS (5 kDa) and using

$$R = \frac{c(assay)}{c(added)} = \frac{Mw}{(Mw + 5kDa)} \qquad \text{Equation 6}$$

The number of tetrabutylammonium saccharide units per PDMS chain was obtained using MW and a tetrabutylammonium saccharide unit molecular weight of 440 g/mol (300 g/mol[36] x 3/2).

For Farndale microassays in aqueous solutions, the DMMB-solution was prepared as suggested.[301] A 250 µL sample of the DMMB solution was pipetted into 96-well plates. A 50 µL amount of PBS, heparin standards (20, 10, 7.5, 5, 2.5 µg/mL), and diluted nanomimic and control polymersome samples (typically 5-fold diluted) were mixed with the DMMB solution in duplicates. The UV-vis absorbance was measured from 395 nm to 595 nm immediately after mixing. The heparin standard curve was generated using the absorbance at 525 nm, and this curve was used as a calibration curve. In the nanomimic samples a baseline correction (exponential decay) was performed and the corrected absorbance value at 525 nm was used to calculate the amount of surface-accessible heparin.

UV–Vis Spectrometry. UV–vis absorbance measurements were performed on a SpectraMax Plus M5e (Molecular Devices, Sunnyvale, CA, USA) using 0.1 mL cuvettes or 96-flat-bottom-well plates.

Nuclear Magnetic Resonance. ^{1}H NMR spectra were recorded on a Bruker DPX-400 NMR spectrometer in D_2O, D_2O/acetone-d_6-mixture or $CDCl_3$ at room temperature. The spectrometer was operated at 400 MHz and 16 or 128 NMR cycles were recorded for each sample.

Gel Permeation Chromatography. Gel permeation chromatography (GPC) was performed on a Viscotek GPCmax system equipped with two PLgel Mixed-c 5 µm columns (300 x 7.5 mm) and THF as eluent (flow rate = 1 mL min^{-1}) at 40 °C and recorded by refractive index. Polymer molecular weights and polydispersity indices (PDI) were determined using polystyrene standards for calibration.

Transmission Electron Microscopy. Nanostructure samples were negatively stained with 2% uranyl acetate for TEM imaging. Ultrathin sections of parasites were stained with a mixture of 4% uranyl acetate/methylcellulose (ratio 1:9). Imaging was carried out on a transmission electron microscope (Philips CM100) at an acceleration voltage of 80 kV. Size measurements were performed using ImageJ software.

Cryogenic Transmission Electron Microcopy. A 4 µL amount of nanomimic sample (3 mg/mL) was adsorbed on a holey carbon-coated grid (Quantifoil, Germany), blotted with a Whatman 1 filter paper and vitrified in liquid nitrogen-cooled liquid ethane using an FEI Vitrobot MK4 (FEI Company, The Netherlands). Frozen grids were transferred to a Philips CM200-FEG electron microscope, which was operated at an acceleration voltage of 200 kV. Digital electron micrographs were recorded with a 4k x 4k TemCam-F416 CMOS camera (TVIPS Company, Germany).

Zeta Potential. Zeta potential measurements were performed using a Zetasizer Nano ZSP (Malvern Instruments Ltd., UK) at 20 °C. Nanomimics or control polymersomes (about 3 mg/mL polymer concentration) prepared and purified in PBS were 40-fold diluted in 300 mM glucose (75 µg/mL polymer and less than 5 mM salt).

Fluorescence Correlation Spectroscopy. FCS measurements were performed on a commercial Confocor2 (Carl Zeiss, Jena, Germany) using an Ar+ laser for the 488 nm wavelength and two HeNe lasers for 543 nm and 633 nm, respectively. The laser beam was focused onto the sample through a 40x C-Apochromat water immersion objective with a numeric aperture of 1.2 and the appropriate filter sets. Finally, the fluorescence intensity was recorded with an avalanche photodiode (APD). All measurements were performed at 20 °C. Typically, 5 µL samples were used. Measurement series of 30 x 5 s (fast diffusing species) or 30 x 10 s (slow diffusing species) were taken for each sample. Raw data were processed with the ConfoCor3 software. R Statistics was used for normalization and graphs. The following fit function was used to fit samples with one component and including a triplet state:

$$G(\tau)_{fit} = 1 + \left(1 + \frac{T}{1-T} e^{-\frac{\tau}{\tau_{\text{trip}}}}\right) \frac{1}{N} \left[\frac{1}{1 + \frac{\tau}{\tau_{\text{D}}}} \frac{1}{\sqrt{1 + R^2 \frac{\tau}{\tau_{\text{D}}}}} \right] \qquad \text{Equation 7}$$

τ_D is the diffusion time. T represents the fraction of fluorophores in triplet state with the corresponding triplet time τ_{trip}. N is the number of particles and R the structural parameter. R was set to 5 if fit results yielded R smaller than 3 or bigger than 8. The relation between the x–y dimension of the confocal volume (ω_{xy}) and τ_D was used to calculate diffusion coefficients (D).

$$\tau_{\text{D}} = \frac{{\omega_{\text{xy}}}^2}{4D} \qquad \text{Equation 8}$$

The Einstein-Stokes equation was utilized to calculate hydrodynamic radii (R_H). k_B is the Boltzmann's constant, T the absolute temperature, and η the viscosity of the surrounding medium.

$$D = \frac{k_B T}{6\pi\eta R_H} \qquad \text{Equation 9}$$

R_H was calculated for each of the 30 curves, and data are presented as mean ± standard deviation. To obtain nanomimic concentrations, calibration of the confocal volume was needed. This was obtained by measuring a series of dye solutions with known concentrations from 1 to 100 nM. A linear fit of dye concentration versus N – obtained from amplitudes of FCS curves – yielded the size of the confocal volume (approximately 0.5 fL). This calibrated value was subsequently used to determine nanomimic concentrations.

For binding studies, *Pf*MSP1_{42}-OG488 was mixed with controls or nanomimics, incubated under shaking at 37 °C for 2 h, cooled to RT (20 °C), put on the cover slide, and incubated 5 min, and FCS curves were recorded. Autocorrelation curves that could not be fitted due to big diffusing aggregates were excluded from the mean (max. 3 of 30 curves, 10%). Brightness (counts per molecule, *CPM*) of free *Pf*MSP1_{42}-OG488 was compared to *CPM* obtained from the mixtures with nanostructures in order to calculate the number of *Pf*MSP1_{42}-OG488 per nanostructure.

Reduction-Triggered Release and Medium Stability of Dye-loaded Nanoparticles Formed from PMOXA-*g*(SS)-PCL and PMOXA-*b*-PCL. Bodipy630-loaded PMOXA-*g*(SS)-PCL and PMOXA-*b*-PCL nanoparticles were prepared as described above using theoretical final dye concentrations in the nanoparticle stock solutions of 1 µM for FCS release studies, 25 µM and 140 µM for FCS studies in cell media.

For release measurements, aliquots of 20 µL nanoparticle solution (containing 1 µM Bodipy630) were added to 200 µL pre-warmed (37 °C) PBS, or 11 mM DTT in PBS and subsequently incubated under shaking (500 RPM) at 37 °C in an Eppendorf Thermomixer Comfort. 5 µL of these mixtures were transferred for subsequent FCS measurements at each time point. 20 x 5 s FCS curves were recorded for each sample at each time point. Resulting FCS curves were fitted with a two-component system, whereas one diffusion parameter was fixed to free dye diffusion (typically about 50 – 60 µs). FCS curves that could not be fitted correctly by the program were excluded from the average (less than 1% of all curves). The following formula for autocorrelation curve fitting was used for one-component fits (for *e.g.* calibration measurements with free dye):

$$G(\tau)_{1comp-fit} = 1 + \frac{1}{N}\left[\frac{1}{1+\frac{\tau}{\tau_D}}\frac{1}{\sqrt{1+R^2\frac{\tau}{\tau_D}}}\right] \quad \text{Equation 10}$$

Two-component fits were used for nanoparticle stability and release measurements, with one diffusion component being fixed to free dye diffusion (typically about 50 – 60 µs) for release and stability measurements in PBS, or protein-dye complex diffusion (typically about 300 µs) for stability measurements in cell media, respectively:

$$G(\tau)_{2comp-fit} = 1 + \frac{1}{N}\left[\frac{f_1}{1+\frac{\tau}{\tau_{D1}}}\frac{1}{\sqrt{1+R^2\frac{\tau}{\tau_{D1}}}}\right] + \frac{1}{N}\left[\frac{f_2}{1+\frac{\tau}{\tau_{D2}}}\frac{1}{\sqrt{1+R^2\frac{\tau}{\tau_{D2}}}}\right]$$

Equation 11

With diffusion times (τ_{D1} and τ_{D2}), number of particles N, the fraction f of molecules with the corresponding diffusion time, and R, the structural parameter, which was always fixed to 5. Number of dye molecules per nanoparticle was calculated based on the molecular brightness (counts per molecule, *CPM* in kHz) when only one component was found (medium stability measurements):

$$\frac{\#\text{dye}}{\text{nanoparticle}} = \frac{CPM_{nanoparticle}}{CPM_{dye}} \quad \text{Equation 12}$$

Percentage of free dye is presented as average ± SEM from three independent measurements using two independent samples for each copolymer. Hydrodynamic diameters (D_H) were calculated using Einstein-Stokes equation; diffusion constants obtained for the nanoparticles and free Atto655 in PBS as a calibration for the confocal volume.

For FCS measurements in cell medium, the following four representative dye-loaded nanoparticle stock solutions were used: PMOXA-*g*(SS)-PCL 2 (2.5 µM Bodipy630), PMOXA-*g*(SS)-PCL 3 (56 µM Bodipy630) and PMOXA-*b*-PCL (2.5 µM, and 133 µM Bodipy630), with the following dilutions in the corresponding pre-warmed (37 °C) cell culture medium: 1 to 10 (2.5 µM stocks), and 1 to 50 (56 µM, 133 µM stocks). Samples were kept under constant shaking (500 RPM) at 37 °C in an Eppendorf Thermomixer Comfort for four days. At each time point, 5 µL of these mixtures were transferred for subsequent FCS measurements of 30 x 5 s. Each curve was fitted using a two-component model with one component being fixed to protein-dye complex (typically about 300 µs) obtained from measurements of a Bodipy630 solution in cell culture media. Few curves with bright and slow diffusing aggregates were excluded from the average (< 1% of all

curves), due to their disproportional effect on the average.[114] Average values for 30 curves at each time point and corresponding standard deviation (SD) are presented. R Statistics and Excel were used for preparing graphs.

Fluorescence Cross-Correlation Spectroscopy. FCCS measurements were also performed on a commercial Confocor2 (Carl Zeiss, Jena, Germany) – equipped with an Ar+ laser for the 488 nm wavelength and a HeNe laser for 633 nm – according to previous protocols.[97,98,259,302] The lasers were simultaneously focused onto the sample through a 40x C-Apochromat water immersion objective with a numeric aperture of 1.2 and the appropriate filter sets (Green: BP 505-550 nm, red: LP 650 nm) to separate the two colors (green/red). All measurements were performed at 20 °C. FCCS calibration data to test the relative minimal cross-correlation amplitude, which is given by the cross-talk from one channel to the other, was estimated using a mixture of the two used dyes (OG488 and Bodipy630) and the relative maximum cross-correlation amplitude using a standard sample (IBA standard, double labeled DNA). Different concentrations of *Pf*MSP1$_{42}$–OG488 were mixed with diluted control polymersomes (PMOXA-*b*-PDMS-*b*-PMOXA) or nanomimics-25% that were both stained with Bodipy630, immediately added onto the sample plate, and incubated at 20 °C on the glass plate for 5 min before recording fluorescence intensity fluctuations in both detection channels (green/red) 30x for 10 seconds each. This procedure was repeated in three independent experiments for each concentration. Intensity fluctuations recorded in both channels were auto- (FCS) and cross-correlated (FCCS) on the ConfoCor3 software to yield auto-correlation and cross-correlation curves. R Statistics was used for preparing graphs. FCCS data was analyzed using the following procedure. All auto- and cross-correlation curves were fitted using the one-component model without triplet state. R was fixed to 5.

Relative cross-correlation amplitudes (RCA) were calculated to obtain the fractional occupancy of the binding sites on nanomimics:[98]

$$\mathrm{RCA} = \frac{G_c(0) - 1}{G_{r,g}(0) - 1} \qquad \text{Equation 13}$$

Where $G_c(0)$ is the cross-correlation amplitude and $G_{r,g}(0)$ the auto-correlation amplitudes of the respective red or green auto-correlation curves. The average data of normalized RCA (n = 3 for each concentration) and corresponding standard errors were plotted against the total ligand concentration (*Pf*MSP1$_{42}$-OG488) and fit using the following formula in QtiPlot (http://soft.proindependent.com/qtiplot.html) to obtain K_d for the interaction.[97,303]

$$\mathrm{RCA} = \frac{[AB]}{[A_0]} = \frac{[A_0] + [B_0] + K_d - \sqrt{([A_0] + [B_0] + K_d)^2 - 4[A_0][B_0]}}{2[A_0]} \quad \text{Equation 14}$$

Where [AB] is the complex concentration, $[A_o]$ the accessible heparin concentration (2.8 nM fixed), $[B_o]$ the *Pf*MSP1$_{42}$-OG488 concentration, and K_d the dissociation constant. Quantitative fluorescence correlation spectroscopy (FCS) measurements were used to calculate concentrations of nanomimics in solution by first measuring a series of known dye concentrations to calibrate the confocal volume.

Static and Dynamic Light Scattering. DLS was performed on a Zetasizer Nano ZSP (Malvern Instruments Ltd, UK) at 20 °C. SLS/DLS was carried out to determine the hydrodynamic radius (R_H), the radius of gyration (R_g) and the value $\rho = R_g/R_H$ of nanomimics in solution. SLS and DLS experiments were performed on an ALV goniometer (ALV GmbH, Germany), equipped with an ALV He-Ne laser (λ = 632.8 nm). Measurements were performed in 10 mm cylindrical quartz cells at angles of 30 – 140° at 20 °C. Data processing was performed using ALV static and dynamic fit and plot software (version 4.31 10/01). SLS data were processed using the Berry model.

Stopped-Flow Measurements. The effect of osmotic pressure on nanomimic size was determined using a stopped-flow apparatus (Bio-Logic SAS, France). Changes in light scattering were monitored at an emission wavelength of 600 nm. As a control, nanomimics in 1 x PBS were mixed equally with 1 x PBS. Osmotic pressure was generated using 2 x PBS as the mixing medium with nanomimics in 1 x PBS. At least four measurements were conducted for each mixture at 20°C. Experimental curves were fitted using exponential fits in QtiPlot (http://soft.proindependent.com/qtiplot.html).

Viability MTS Assay. HeLa cells (2000 cells per well) were seeded in a 96-well plate, and incubated at 37 °C, 5 % CO_2 for 24 h in DMEM containing 10 % fetal calf serum and 1% penicillin/streptomycin. After 24 h, nanomimics were added to triplicate wells at concentrations ranging from about 50 - 300 µg/mL in a total volume of 100 µL per well (90 µL media mixed with 10 µL nanomimic solution in PBS). Cells were incubated in the presence of nanomimics for an additional 24 h. Cell viability was determined using the MTS assay. Briefly, 20 µL MTS assay solution was added to each well and incubated at 37 °C for 3 h. Cell viability was determined by measuring absorbance at 490 nm using a microplate reader SpectraMax Plus M5e (Molecular Devices) and comparing to a PBS control (100 % cell viability) to obtain the percentage of living cells. All samples were corrected against controls containing only media and PBS or an SRB solution in PBS.

Suspension Culture Assay. *Plasmodium falciparum* 3D7 strain was maintained in culture as described elsewhere.[304] Malaria culture medium (MCM) was RPMI medium supplemented with 0.5 % Albumax (Chapter 3, 7)[305] or 0.5% CellMaxx bovine albumin (Chapter 4). Synchronization was performed using 5 % sorbitol.[306] Invasion inhibition experiments were carried out in standard 24-well flat-bottom culture plates (Falcon 353047, Becton Dickinson, NJ, USA). Starting parasitemia was about 0.1 % (Chapter 3, 7) or 0.2 % (Chapter 4) ring/trophozoite stages at 5 % hematocrit in MCM and parasitemia reached ~ 2 – 4 % after 96 hours. Total volume added to each well was 500 µL of parasite culture plus 55 µL PBS or test samples. Plates were placed in a plastic box with wet paper (for humidification) and cultured under continuous and simultaneous rocking (140 RPM, ProBlot 25 Rocker, Labnet International Inc., NJ, USA) and shaking (105 RPM, Lab-Therm LT-W, Kühner, Switzerland) at 37 °C for 96 hours by fixing the ProBlot 25 Rocker onto the shaking plate of the Lab-Therm shaking incubator. The maximum tilt angle was increased to 15° by putting one side of the plastic box on a 3 cm thick spacer. This setup ensures continuous suspension of RBCs and iRBCs over the 96-hour incubation period. Each sample was tested in at least 3 independent assays in duplicates. After 96 hours, parasitemia was determined by flow cytometry (FACSCalibur, BD Biosciences) using dihydroethidium to stain parasite DNA. In total, 100'000 cells were counted for each well. Data are presented as mean growth ± standard error with respect to PBS controls. Statistical comparison of free heparin versus nanostructured heparin was performed using Student's *t*-test (two-tailed, type 2) in Microsoft Excel. Graphs were drawn using QtiPlot (http://soft.proindependent.com/qtiplot.html). To obtain IC_{50} values, experimental growth inhibition curves were fitted using logistic or exponential curves in QtiPlot.

Malaria Parasite Growth Inhibition Assays with Drugs. 10 mM SHMT inhibitor (±)-**1** stock in DMSO and SHMT inhibitor (±)-**1**-loaded nanoparticle samples in PBS were diluted in PBS immediately before use in the assays. Briefly, four-day suspension assays were conducted in 24-well plates under continuous agitation at 37 °C. Hematocrit was 5 % and starting parasitemia (% of iRBCs, 3D7 strain) was about 0.1 %. After 96 hours, control wells (PBS added) reached about 2 - 4 % iRBCs as measured by flow cytometry (FACSCalibur, BD Biosciences). For each well, 100'000 cells were counted and parasitemia was compared to PBS control wells to obtain mean growth ± standard error (SEM). Each sample was tested in at least three independent assays in duplicates. Statistical comparison was performed using Student's *t*-test (two-tailed, type 2). Graphs were prepared using QtiPlot (http://soft.proindependent.com/qtiplot.html). To obtain IC_{50}

values, experimental growth inhibition curves were fitted using logistic fits in QtiPlot with fixed maximum value A1 = 100.

Three-day static assays were performed in 96-well plates using 1.25 % hematocrit and 0.3 % parasitemia (NF54 strain) at the beginning. After 48 h, 0.25 μCi [^{3}H]hypoxanthine was added to each well, and the assay was continued for an additional 24 h. After a total of three days incubation, parasites were harvested onto glass-fiber filters, and radioactivity was counted using a Betaplate liquid scintillation counter (Wallac, Zurich). The results were recorded and expressed as a percentage of the untreated controls. Fifty percent inhibitory concentrations (IC_{50}) were estimated by linear interpolation.[307]

One-day suspension inhibition assay was performed and evaluated similarly to the four-day suspension assay but using 10 % hematocrit and 1 % starting parasitemia with late stage parasites (3D7 strain). IC_{50} values had to be baseline-corrected in this case, because dead parasites remained within the culture for this short one-day incubation periods and therefore still appeared in the flow cytometry measurements. Thin blood smears revealed only dead late stages and no ring stage parasites at high drug concentration after one-day incubation, which confirms that the slightly increased baseline was due to remaining dead parasites (iRBCs) and not due to incomplete drug action.

Preparation of Parasites for Fluorescence Microscopy with Nanomimics. Mature 3D7 parasites (trophozoites/schizonts) were purified by Percoll density gradient.[308] Then, purified late stages were mixed again with RBCs to yield a mixture at 20 % parasitemia. Polymersomes or nanomimics (both filled with fluorescent dye SRB) were then added to this mixture and incubated at 37 °C for 3 hours under static conditions. After incubation, cells were fixed using 2 % paraformaldehyde/0.2 % glutaraldehyde in phosphate buffer 0.1 M (pH 7.4) at 4 °C overnight. Then, fixed samples were centrifuged at high speed (13.5 kRPM) and redissolved in a small amount of PBS and finally mounted on a slide using Vectashield supplemented with DAPI (Vector Laboratories).

Preparation of Malaria Parasite Cultures for Imaging with Delivery Vehicles. 0.36 mL malaria parasite culture (4% parasitemia, late stages, 5% hematocrit) in MCM was transferred to Eppendorf tubes and 40 μL of 25 μM Nile Red solution in PBS (freshly prepared from a 10 mM stock in THF and immediately added), 25 μM Nile Red in PMOXA-*g*(SS)-PCL 3 nanoparticles, and 25 μM Nile Red in PMOXA-*b*-PCL nanoparticles. The gas in the tubes was exchanged by the culturing gas mixture and then incubated under shaking conditions at 37 °C for 1.5 h. Then, 1 μL of 1 mg/mL Hoechst DNA-stain was

added and incubation was continued under static condition for 0.5 h. After centrifugation, 5 µL of the pellet was mounted on a microscopy slide and images were taken using a 60x oil immersion objective. First, the appropriate filters and exposure times were adjusted for the free dye sample. Then, parasites were searched in DIC mode and automatic overlays were taken for each sample using the exact same setting in order to have comparable brightness data.

Preparation of Parasites for TEM and 3D-SIM. For TEM and 3D-SIM imaging, merozoites were mechanically released from mature schizonts using a published protocol.[249] Briefly, 3D7 mature parasites were purified by Percoll density gradient and incubated with 10 µM E-64 inhibitor. After 6 – 8 hours incubation, mature schizonts were filtered through 1.2 µm filters to release merozoites mechanically, immediately mixed with nanomimics and incubated for 20 min at 37 °C. Then, merozoites were fixed in 2% paraformaldehyde/0.2 % glutaraldehyde in phosphate buffer 0.1 M (pH 7.4) at 4 °C overnight. For TEM, samples were prepared according to Tokuyasu.[309] Briefly, merozoite-nanomimic complexes were washed in PBS, embedded in 12 % gelatin and thin blocks were infiltrated with 2.3 M sucrose overnight at 4°C. Each centrifugation step was performed at high speed (13.5 kRPM). Ultrathin sections (80 to 100 nm) were prepared on a FC7/UC7-ultramicrotome (Leica) at -120 °C. For 3D-SIM fixed merozoites were collected by fast centrifugation (13.4 kRPM) and then mounted on a slide using Vectashield with DAPI as mounting medium.

Fluorescence Microscopy and Super–Resolution 3D Structured Illumination Microscopy (3D-SIM). Fluorescence micrographs were taken on a Leica DM 5000B fluorescence microscope. Image processing was performed on GIMP software. In case of dye delivery, images were cropped using GIMP software; no other adjustments of original images were performed.

3D-SIM was performed on a microscope system (DeltaVision OMX-Blaze version 4; Applied Precision, Issaquah, WA) equipped with 405, 445, 488, 514, 568 and 642 nm solid-state lasers. Images were acquired using a Plan Apo N 60× 1.42 NA oil immersion objective lens (Olympus) and 4 liquid-cooled sCMOs cameras (pco Edge, full frame 2560 x 2160; Photometrics). Exciting light was directed through a movable optical grating to generate a fine-striped interference pattern on the sample plane. The pattern was shifted laterally through five phases and three angular rotations of 60° for each z section. Optical z-sections were separated by 0.125 µm. The laser lines 405 and 568 nm were used for 3D-SIM acquisition. Exposure times were typically between 3 and 50 ms, and the power of each laser was adjusted to achieve optimal intensities of between 7,000 and 10,000 counts in

a raw image of 15-bit dynamic range at the lowest laser power possible to minimize photobleaching. Multichannel imaging was achieved through sequential acquisition of wavelengths by separate cameras. Raw 3D-SIM images were processed and reconstructed using the DeltaVision OMX SoftWoRx software package (Applied Precision[310,311]). The resulting size of the reconstructed images was 128 x 128 px from an initial set of 64 x 64 raw images. The channels were aligned in the image plane and around the optical axis using predetermined shifts as measured using a target lens and the SoftWoRx alignment tool. The channels were then carefully aligned using alignment parameter from control measurements with 0.5 μm diameter multi-spectral fluorescent beads (Invitrogen, Molecular Probes)

Fluorescence Microscopy of Giant Polymersomes. Fluorescence imaging of protein interaction with giant polymersomes was performed on a confocal laser scanning microscope (Zeiss CLSM 510-META/Confocor2, Carl Zeiss, Jena, Germany). A freshly plasma-cleaned 8-well microscopy chamber (Nunc Lab-Tek Chamber Slide System, Thermo Fisher Scientific) was filled with PBS (200 μl, pH 7.2), GUVs (20 μl in 300 mM sucrose), Bodipy630 (10 μl, 72 mM) in PBS, and *Pf*MSP1$_{42}$-OG488 in PBS (5 μl, 2.5 μM). For the CLSM measurements a water immersion objective (C-Apochromat, 40 x magnification, NA of 1.2) was used. The OG488 signal was obtained by excitation with an Ar laser (λ= 488 nm) with dichroic mirrors HFT (main beam splitter) 488 and NFT (secondary beam splitter) 490 with the band-pass BP 500-550 filter. HFT 488/543/633, NFT 545 and the long-pass LP 650 filters were used to collect the fluorescence signal of Bodipy630. The pinhole size was set to 70 μm for the green channel, and 90 μm for the red channel, respectively. All settings (including laser power, detector gains) were kept constant for imaging of positive and negative samples.

Fluorescence imaging of heparin GUVs with merozoites was performed on a Leica DM 5000B fluorescence microscope using the appropriate filters.

Study Interaction of Giants and Merozoites. A 30 mL petri dish filled with human RBCs at 5 % haematocrit and 5 – 6 % parasitemia (iRBC late stages) was used for merozoite isolation. First, late stage iRBCs were separated from RBCs and young iRBCs by Percoll density gradient. After maturation to schizont stage parasites, they were concentrated to 1 mL in malaria culture medium, and viable merozoites were mechanically released using 1.2 μm syringe filters. They were immediately mixed with 300 μL of a heparin GUV solution in 300 mM sucrose, gently shaken, and incubated under static conditions at 37 °C for 15 min. Subsequently, 2 μL of 1 mg/mL Hoechst (DNA stain) was added and

merozoite/giant mixture was fixed in 2% paraformaldehyde/0.2% glutaraldehyde in 150 mM phosphate buffer (pH 7.4) overnight. After gentle centrifugation (3500 RCF) for 5 min, 10 µL of the pellet was mounted on a microscopy slide.

Anticoagulation Property of Nanomimics. Anticoagulation property of heparin-containing samples was measured using a chromogenic anti-Xa assay (Biophen Heparin (LRT) kit and manual) at the University Hospital Basel (Prof. D. Tsakiris). The detection limit is 0.1 UI/mL.

Estimation of Endotoxin Contamination. Commercial Limulus Amebocyte Lysate (LAL) Kinetic QCL assay (Lonza) was performed using established protocols.[266,267] Briefly, 100 µL of known endotoxin concentrations (5 – 0.005 EU/mL) in LAL water, undiluted nanostructure samples in PBS, endotoxin spiked (0.05 EU/mL) nanomimics, and nanomimics in 10 mM $MgCl_2$ in PBS were pipetted into sterile 96-well plates. After incubation at 37 °C for at least 10 min, 100 µL of the Kinetic-QCL reagent was pipetted to each well and absorbance (405 nm) was immediately measured at 37 °C for about 1.5 h. Onset time was defined as time for absorbance to increase by 0.2 A.U. and was compared to the calibration performed with known endotoxin concentrations.

Experiment on "Vaccine-Like" Action of Nanomimics with Surface-Bound Immunogen. 3x2 BALB/c mice (12 weeks old) were immunized on day 0 with either a) 150 µL of 0.1 mg/mL *Pf*MSP1_{42} (3D7) in PBS intravenously (i.v.), b) 150 µL of 0.1 mg/mL *Pf*MSP1_{42} (3D7) in PBS containing 50% Sigma-Adjuvant subcutaneously (s.c.), or c) 150 µL of nanomimics-25% that were first incubated with 0.1 mg/mL *Pf*MSP1_{42} (3D7) in PBS and then injected i.v. On day 24 a second shot was given *via* the same routes for a)-c) but with slightly lower protein concentrations (150 µL, 0.065 mg/mL each). All mice were terminally bled on day 31. The collected blood was centrifuged, the sera was separated and stored at -20°C. Induced IgG antibody titers were quantified using ELISA. Briefly, Nuc-Maxisorb ELISA plates were coated with 3 µg/mL *Pf*MSP1_{42} (3D7) in PBS (50 µL/well) at 4° for 48 h. Plates were washed and blocked with 3% BSA in PBS (100 µL/well) at RT for 1 h. Test-sera were diluted 1:10 in 1% BSA TNT and serially diluted on the plate up to 1:20'048. Serum dilutions were incubated at RT for 2 h. Plates were washed and incubated with anti-mouse IgG alkaline phosphate labeled antibodies (1:5000) 1% BSA TNT at RT for 1h. Plates were developed with 1mg/mL pNPP in carbonate buffer pH 8.6 for 20 minutes and absorbance was measured at 405nm. Antibody endpoint titers are given for the last dilution where the absorbance was two times the absorbance of the negative control. All *in vivo*

studies conducted at the Swiss TPH were adhering to local and national regulations of laboratory animal welfare in Switzerland.

Activity Tests in *Plasmodium Berghei* Mouse Model. Heparinized blood (containing 50 µL of 200 UI/mL heparin) was taken from a donor mouse with approximately 30% parasitemia, and it was diluted down to 10^8 parasitized erythrocytes per mL using physiological saline. 0.2 mL of this suspension was injected intravenously (i.v.) into experimental groups of 3 mice, and a control group of 5 mice. 6, 24, 48 and 72 hours post-infection, the experimental groups were treated with a single daily dose (i.v.) of 0.2 mL SHMT inhibitor (±)-**1**-loaded nanoparticles in case of drug-loaded nanostructures. For nanomimics, 0.2 mL i.v. injection was performed twice daily for four days. 24 hours after the last drug treatment, 1 µL tail blood was taken and the parasitemia was determined by flow cytometry. Parasitemia on day 4 (in case of three or four day treatment) in % was compared to the untreated control group. All *in vivo* studies conducted at the Swiss TPH were adhering to local and national regulations of laboratory animal welfare in Switzerland (Permission number for housing: 1018H, and permission number 1731 for *Plasmodium berghei* mouse model).

BIBLIOGRAPHY

11 References

(1) Fauci, A. S.; Morens, D. M. The Perpetual Challenge of Infectious Diseases. *N. Engl. J. Med.* **2012**, *366*, 454–461.

(2) Lederberg, J. Infectious History. *Science* **2000**, *288*, 287–293.

(3) Guyer, B.; Freedman, M. A.; Strobino, D. M.; Sondik, E. J. Annual Summary of Vital Statistics: Trends in the Health of Americans During the 20th Century. *Pediatrics* **2000**, *106*, 1307–1317.

(4) Fauci, A. S.; Morens, D. M. Zika Virus in the Americas--Yet Another Arbovirus Threat. *N. Engl. J. Med.* **2016**, *374*, 601–604.

(5) World Health Organization. *Global Action Plan on Antimicrobial Resistance*; World Health Organization, Geneva, 2015; pp. 1–19.

(6) Hiramatsu, K.; Katayama, Y.; Matsuo, M.; Sasaki, T.; Morimoto, Y.; Sekiguchi, A.; Baba, T. Journal of Infection and Chemotherapy. *J. Infect. Chemother.* **2014**, *20*, 593–601.

(7) Diacon, A. H.; Pym, A.; Grobusch, M. P.; de los Rios, J. M.; Gotuzzo, E.; Vasilyeva, I.; Leimane, V.; Andries, K.; Bakare, N.; De Marez, T.; *et al.* Multidrug-Resistant Tuberculosis and Culture Conversion with Bedaquiline. *N. Engl. J. Med.* **2014**, *371*, 723–732.

(8) World Health Organization. *Global Tuberculosis Report 2015*; World Health Organization, Geneva, 2015; pp. 1–192.

(9) Tun, K. M.; Imwong, M.; Lwin, K. M.; Win, A. A.; Hlaing, T. M.; Hlaing, T.; Lin, K.; Kyaw, M. P.; Plewes, K.; Faiz, M. A.; *et al.* Spread of Artemisinin-Resistant Plasmodium Falciparum in Myanmar: a Cross-Sectional Survey of the K13 Molecular Marker. *Lancet Infect. Dis.* **2015**, *15*, 415–421.

(10) RTS, S. C. T. P. Efficacy and Safety of RTS,S/AS01 Malaria Vaccine with or Without a Booster Dose in Infants and Children in Africa: Final Results of a Phase 3, Individually Randomised, Controlled Trial. *The Lancet* **2015**, *386*, 31–45.

(11) Nathan, C.; Cars, O. Antibiotic Resistance--Problems, Progress, and Prospects. *N. Engl. J. Med.* **2014**, *371*, 1761–1763.

(12) McMichael, A. J. Globalization, Climate Change, and Human Health. *N. Engl. J. Med.* **2013**, *368*, 1335–1343.

(13) Altizer, S.; Ostfeld, R. S.; Johnson, P. T. J.; Kutz, S.; Harvell, C. D. Climate Change and Infectious Diseases: From Evidence to a Predictive Framework. *Science* **2013**, *341*, 514–519.

(14) World Health Organization. World Malaria Report 2014. *World Health Organization, Geneva* **2014**, 1–142.

(15) World Health Organization. World Health Statistics 2015. *World Health Organization, Geneva* **2015**, 1–164.

(16) Josling, G. A.; Llinás, M. Sexual Development in Plasmodium Parasites: Knowing When It's Time to Commit. *Nat. Rev. Micro.* **2015**, *13*, 573–587.

(17) Su, X.; Hayton, K.; Wellems, T. E. Genetic Linkage and Association Analyses for Trait Mapping in Plasmodium Falciparum. *Nat. Rev. Genet.* **2007**, *8*, 497–506.

(18) White, N. J.; Pukrittayakamee, S.; Hien, T. T.; Faiz, M. A.; Mokuolu, O. A.; Dondorp, A. M. Malaria. *Lancet* **2014**, *383*, 723–735.

(19) Cowman, A. F.; Berry, D.; Baum, J. The Cell Biology of Disease: the Cellular and Molecular Basis for Malaria Parasite Invasion of the Human Red Blood Cell. *J. Cell Biol.* **2012**, *198*, 961–971.
(20) Cowman, A. F.; Crabb, B. S. Invasion of Red Blood Cells by Malaria Parasites. *Cell* **2006**, *124*, 755–766.
(21) Beeson, J. G.; Drew, D. R.; Boyle, M. J.; Feng, G.; Fowkes, F. J. I.; Richards, J. S. Merozoite Surface Proteins in Red Blood Cell Invasion, Immunity and Vaccines Against Malaria. *FEMS Microbiol. Rev.* **2016**, 1–30.
(22) Weiss, G. E.; Gilson, P. R.; Taechalertpaisarn, T.; Tham, W.-H.; de Jong, N. W. M.; Harvey, K. L.; Fowkes, F. J. I.; Barlow, P. N.; Rayner, J. C.; Wright, G. J.; *et al.* Revealing the Sequence and Resulting Cellular Morphology of Receptor-Ligand Interactions During Plasmodium Falciparum Invasion of Erythrocytes. *PLoS Pathog.* **2015**, *11*, e1004670.
(23) Paul, A. S.; Egan, E. S.; Duraisingh, M. T. Host–Parasite Interactions That Guide Red Blood Cell Invasion by Malaria Parasites. *Curr. Opin. Hematol.* **2015**, *22*, 220–226.
(24) Koch, M.; Baum, J. The Mechanics of Malaria Parasite Invasion of the Human Erythrocyte - Towards a Reassessment of the Host Cell Contribution. *Cell Microbiol.* **2016**, *18*, 319–329.
(25) Boyle, M. J.; Richards, J. S.; Gilson, P. R.; Chai, W.; Beeson, J. G. Interactions with Heparin-Like Molecules During Erythrocyte Invasion by *Plasmodium Falciparum* Merozoites. *Blood* **2010**, *115*, 4559–4568.
(26) Das, S.; Hertrich, N.; Perrin, A. J.; Withers-Martinez, C.; Collins, C. R.; Jones, M. L.; Watermeyer, J. M.; Fobes, E. T.; Martin, S. R.; Saibil, H. R.; *et al.* Processing of Plasmodium Falciparum Merozoite Surface Protein MSP1 Activates a Spectrin-Binding Function Enabling Parasite Egress From RBCs. *Cell Host Microbe* **2015**, *18*, 433–444.
(27) Harris, P. K.; Yeoh, S.; Dluzewski, A. R.; O'Donnell, R. A.; Withers-Martinez, C.; Hackett, F.; Bannister, L. H.; Mitchell, G. H.; Blackman, M. J. Molecular Identification of a Malaria Merozoite Surface Sheddase. *PLoS Pathog.* **2005**, *1*, e29.
(28) Vogt, A. M.; Winter, G.; Wahlgren, M.; Spillmann, D. Heparan Sulphate Identified on Human Erythrocytes: a *Plasmodium Falciparum* Receptor. *Biochem. J.* **2004**, *381*, 593–597.
(29) Crick, A. J.; Theron, M.; Tiffert, T.; Lew, V. L.; Pietro Cicuta; Rayner, J. C. Quantitation of Malaria Parasite-Erythrocyte Cell-Cell Interactions Using Optical Tweezers. *Biophys. J.* **2014**, *107*, 846–853.
(30) Kobayashi, K.; Kato, K.; Sugi, T.; Takemae, H.; Pandey, K.; Gong, H.; Tohya, Y.; Akashi, H. Plasmodium Falciparum BAEBL Binds to Heparan Sulfate Proteoglycans on the Human Erythrocyte Surface. *J. Biol. Chem.* **2010**, *285*, 1716–1725.
(31) Kobayashi, K.; Takano, R.; Takemae, H.; Sugi, T.; Ishiwa, A.; Gong, H.; Recuenco, F. C.; Iwanaga, T.; Horimoto, T.; Akashi, H.; *et al.* Analyses of Interactions Between Heparin and the Apical Surface Proteins of Plasmodium Falciparum. *Sci. Rep.* **2013**, *3*, 3178–3188.
(32) Zhang, Y.; Jiang, N.; Lu, H.; Hou, N.; Piao, X.; Cai, P.; Yin, J.; Wahlgren, M.; Chen, Q. Proteomic Analysis of Plasmodium Falciparum Schizonts Reveals Heparin-Binding Merozoite Proteins. *J. Proteome Res.* **2013**, *12*, 2185–2193.
(33) Crosnier, C.; Bustamante, L. Y.; Bartholdson, S. J.; Bei, A. K.; Theron, M.; Uchikawa, M.; Mboup, S.; Ndir, O.; Kwiatkowski, D. P.; Duraisingh, M. T.; *et al.* Basigin Is a Receptor Essential for Erythrocyte Invasion by Plasmodium Falciparum. *Nature* **2011**, *480*, 534–537.
(34) Cooke, B.; Coppel, R.; Wahlgren, M. Falciparum Malaria: Sticking Up, Standing Out and Out-Standing. *Parasitol. Today* **2000**, *16*, 416–420.
(35) Mundwiler-Pachlatko, E.; Beck, H.-P. Maurer's Clefts, the Enigma of Plasmodium Falciparum. *Proc. Natl. Acad. Sci. USA* **2013**, *110*, 19987–19994.
(36) Voss, T. S.; Healer, J.; Marty, A. J.; Duffy, M. F.; Thompson, J. K.; Beeson, J. G.; Reeder, J. C.; Crabb, B. S.; Cowman, A. F. A Var Gene Promoter Controls Allelic Exclusion of Virulence Genes in Plasmodium Falciparum Malaria. *Nature* **2006**, *439*, 1004–1008.
(37) Ginsburg, H.; Stein, W. D. The New Permeability Pathways Induced by the

Malaria Parasite in the Membrane of the Infected Erythrocyte: Comparison of Results Using Different Experimental Techniques. *J. Membrane Biol.* **2004**, *197*, 113–134.

(38) Pouvelle, B.; Spiegel, R.; Hsiao, L.; Howard, R. J.; Morris, R. L.; Thomas, A. P.; Taraschi, T. F. Direct Access to Serum Macromolecules by Intraerythrocytic Malaria Parasites. *Nature* **1991**, *353*, 73–75.

(39) Goodyer, I. D.; Pouvelle, B.; Schneider, T. G.; Trelka, D. P.; Taraschi, T. F. Characterization of Macromolecular Transport Pathways in Malaria-Infected Erythrocytes. *Mol. Biochem. Parasitol.* **1997**, *87*, 13–28.

(40) Tahir, El, A.; Malhotra, P.; Chauhan, V. S. Uptake of Proteins and Degradation of Human Serum Albumin by Plasmodium Falciparum-Infected Human Erythrocytes. *Malar. J.* **2003**, *2*, 1–8.

(41) Bergmann-Leitner, E. S.; Duncan, E. H.; Angov, E. MSP-1p42-Specific Antibodies Affect Growth and Development of Intra-Erythrocytic Parasites of Plasmodium Falciparum. *Malar. J.* **2009**, *8*, 183–195.

(42) Urbán, P.; Valle-Delgado, J. J.; Mauro, N.; Marques, J.; Manfredi, A.; Rottmann, M.; Ranucci, E.; Ferruti, P.; Fernàndez-Busquets, X. Use of Poly(Amidoamine) Drug Conjugates for the Delivery of Antimalarials to Plasmodium. *J. Control. Release* **2014**, *177*, 84–95.

(43) Spillman, N. J.; Beck, J. R.; Goldberg, D. E. Protein Export Into Malaria Parasite–Infected Erythrocytes: Mechanisms and Functional Consequences. *Annu. Rev. Biochem.* **2015**, *84*, 813–841.

(44) Kappe, S. H. I.; Vaughan, A. M.; Boddey, J. A.; Cowman, A. F. That Was Then but This Is Now: Malaria Research in the Time of an Eradication Agenda. *Science* **2010**, *328*, 862–866.

(45) Dondorp, A. M.; Nosten, F.; Yi, P.; Das, D.; Phyo, A. P.; Tarning, J.; Lwin, K. M.; Ariey, F.; Hanpithakpong, W.; Lee, S. J.; *et al.* Artemisinin Resistance in *Plasmodium Falciparum* Malaria. *N. Engl. J. Med.* **2009**, *361*, 455–467.

(46) Amaratunga, C.; Lim, P.; Suon, S.; Sreng, S.; Mao, S. Dihydroartemisinin–Piperaquine Resistance in Plasmodium Falciparum Malaria in Cambodia: a Multisite Prospective Cohort Study. *Lancet Infect. Dis.* **2016**, *16*, 357–365.

(47) Miller, L. H.; Ackerman, H. C.; Su, X.-Z.; Wellems, T. E. Malaria Biology and Disease Pathogenesis: Insights for New Treatments. *Nat. Med.* **2013**, *19*, 156–167.

(48) Wells, T. N. C.; van Huijsduijnen, R. H.; Van Voorhis, W. C. Malaria Medicines: a Glass Half Full? *Nat. Rev. Drug Discov.* **2015**, *14*, 424–442.

(49) World Health Organization. Malaria Vaccine: WHO Position Paper-January 2016. *Wkly. Epidemiol. Rec.* **2016**, *91*, 33–51.

(50) Seder, R. A.; Chang, L. J.; Enama, M. E.; Zephir, K. L.; Sarwar, U. N.; Gordon, I. J.; Holman, L. A.; James, E. R.; Billingsley, P. F.; Gunasekera, A.; *et al.* Protection Against Malaria by Intravenous Immunization with a Nonreplicating Sporozoite Vaccine. *Science* **2013**, *341*, 1359–1365.

(51) Ishizuka, A. S.; Lyke, K. E.; DeZure, A.; Berry, A. A.; Richie, T. L.; Mendoza, F. H.; Enama, M. E.; Gordon, I. J.; Chang, L.-J.; Sarwar, U. N.; *et al.* Protection Against Malaria at 1 Year and Immune Correlates Following PfSPZ Vaccination. *Nat. Med.* **2016**, 1–13, doi:10.1038/nm.4110.

(52) Kester, K. E.; Cummings, J. F.; Ofori Anyinam, O.; Ockenhouse, C. F.; Krzych, U.; Moris, P.; Schwenk, R.; Nielsen, R. A.; Debebe, Z.; Pinelis, E.; *et al.* Randomized, Double-Blind, Phase 2a Trial of Falciparum Malaria Vaccines RTS,S/AS01B and RTS,S/AS02A in Malaria-Naive Adults: Safety, Efficacy, and Immunologic Associates of Protection. *J. Infect. Dis.* **2009**, *200*, 337–346.

(53) Richards, J. S.; Beeson, J. G. The Future for Blood-Stage Vaccines Against Malaria. *Immunol. Cell Biol.* **2009**, *87*, 377–390.

(54) Hoffman, S. L.; Billingsley, P. F.; James, E.; Richman, A.; Loyevsky, M.; Li, T.; Chakravarty, S.; Gunasekera, A.; Chattopadhyay, R.; Li, M.; *et al.* Development of a Metabolically Active, Non-Replicating Sporozoite Vaccine to Prevent Plasmodium Falciparum Malaria. *Hum. Vaccines* **2010**, *6*, 97–106.

(55) Tanner, M.; Greenwood, B.; Whitty, C. J. M.; Ansah, E. K.; Price, R. N.; Dondorp, A. M.; Seidlein, von, L.; Baird, J. K.; Beeson, J. G.; Fowkes, F. J. I.; *et al.* Malaria Eradication and Elimination: Views on How to Translate a Vision Into Reality. *BMC Med.* **2014**, *13*, 167–167.

(56) Hemingway, J.; Ranson, H.; Magill, A.; Kolaczinski, J. Averting a Malaria Disaster: Will Insecticide Resistance Derail Malaria Control? *The Lancet* **2016**, *387*, 1785–1788.
(57) Wu, Y.; Ng, D. Y. W.; Kuan, S. L.; Weil, T. Protein–Polymer Therapeutics: a Macromolecular Perspective. *Biomater. Sci.* **2015**, *3*, 214–230.
(58) Li, J.; Yu, F.; Chen, Y.; Oupický, D. Polymeric Drugs: Advances in the Development of Pharmacologically Active Polymers. *J. Control. Release* **2015**, *219*, 369–382.
(59) Palivan, C. G.; Goers, R.; Najer, A.; Zhang, X.; Car, A.; Meier, W. Bioinspired Polymer Vesicles and Membranes for Biological and Medical Applications. *Chem. Soc. Rev.* **2016**, *45*, 377–411.
(60) Siegwart, D. J.; Oh, J. K.; Matyjaszewski, K. ATRP in the Design of Functional Materials for Biomedical Applications. *Prog. Polym. Sci.* **2012**, *37*, 18–37.
(61) Gunkel-Grabole, G.; Sigg, S.; Lomora, M.; Lörcher, S.; Palivan, C. G.; Meier, W. P. Polymeric 3D Nano-Architectures for Transport and Delivery of Therapeutically Relevant Biomacromolecules. *Biomater. Sci.* **2015**, *3*, 25–40.
(62) Duncan, R. Polymer Therapeutics as Nanomedicines: New Perspectives. *Curr. Opin. Biotech.* **2011**, *22*, 492–501.
(63) Duncan, R.; Vicent, M. J. Polymer Therapeutics-Prospects for 21st Century: the End of the Beginning. *Adv. Drug Deliver. Rev.* **2013**, *65*, 60–70.
(64) Förster, S.; Antonietti, M. Amphiphilic Block Copolymers in Structure-Controlled Nanomaterial Hybrids. *Adv. Mater.* **1998**, *10*, 195–217.
(65) Tanford, C. *The Hydrophobic Effect: Formation of Micelles and Biological Membranes*; Wiley: New York, 1973; pp. 1–208.
(66) Tanford, C. The Hydrophobic Effect and the Organization of Living Matter. *Science* **1978**, *200*, 1012–1018.
(67) Israelachvili, J. N.; Mitchell, D. J.; Ninham, B. W. Theory of Self-Assembly of Hydrocarbon Amphiphiles Into Micelles and Bilayers. *J. Chem. Soc., Faraday Trans. 2* **1976**, *72*, 1525.
(68) Chandler, D. Interfaces and the Driving Force of Hydrophobic Assembly. *Nature* **2005**, *437*, 640–647.
(69) Southall, N. T.; Dill, K. A.; Haymet, A. D. J. A View of the Hydrophobic Effect. *J. Phys. Chem. B* **2002**, *106*, 521–533.
(70) Zhang, J.; Li, X.; Li, X. Stimuli-Triggered Structural Engineering of Synthetic and Biological Polymeric Assemblies. *Prog. Polym. Sci.* **2012**, *37*, 1130–1176.
(71) Israelachvili, J. N. Soft and Biological Structures. In *Intermolecular and Surface Forces*; Elsevier: London, 2011; pp. 535–576.
(72) Blanazs, A.; Armes, S. P.; Ryan, A. J. Self-Assembled Block Copolymer Aggregates: From Micelles to Vesicles and Their Biological Applications. *Macromol. Rapid Commun.* **2009**, *30*, 267–277.
(73) Antonietti, M.; Förster, S. Vesicles and Liposomes: a Self-Assembly Principle Beyond Lipids. *Adv. Mater.* **2003**, *15*, 1323–1333.
(74) Kita-Tokarczyk, K.; Grumelard, J.; Haefele, T.; Meier, W. Block Copolymer Vesicles—Using Concepts From Polymer Chemistry to Mimic Biomembranes. *Polymer* **2005**, *46*, 3540–3563.
(75) Discher, D. E.; Eisenberg, A. Polymer Vesicles. *Science* **2002**, *297*, 967–973.
(76) Cui, H.; Chen, Z.; Zhong, S.; Wooley, K. L.; Pochan, D. J. Block Copolymer Assembly via Kinetic Control. *Science* **2007**, *317*, 647–650.
(77) Einfalt, T.; Gunkel, G.; Spulber, M.; Najer, A.; Palivan, C. G. Supramolecular Architectures: Supramolecular Architectures From Self-Assembled Copolymers. In *CRC Concise Encyclopedia of Nanotechnology*; Kharisov, B. I.; Kharissova, O. V.; Ortiz-Mendez, U., Eds.; CRC Press, Taylor and Francis Group: Boca Raton, 2016; pp. 1055–1068.
(78) Discher, B. M. Polymersomes: Tough Vesicles Made From Diblock Copolymers. *Science* **1999**, *284*, 1143–1146.
(79) Mai, Y.; Eisenberg, A. Self-Assembly of Block Copolymers. *Chem. Soc. Rev.* **2012**, *41*, 5969–5985.
(80) Aoshima, S.; Kanaoka, S. A Renaissance in Living Cationic Polymerization. *Chem. Rev.* **2009**, *109*, 5245–5287.
(81) Braunecker, W. A.; Matyjaszewski, K. Controlled/Living Radical Polymerization: Features, Developments, and Perspectives. *Prog. Polym. Sci.*

2007, *32*, 93–146.
(82) Smith, A. E.; Xu, X.; McCormick, C. L. Stimuli-Responsive Amphiphilic (Co)Polymers via RAFT Polymerization. *Prog. Polym. Sci.* **2010**, *35*, 45–93.
(83) Hadjichristidis, N.; Iatrou, H.; Pitsikalis, M.; Sakellariou, G. Synthesis of Well-Defined Polypeptide-Based Materials via the Ring-Opening Polymerization of A-Amino Acid N-Carboxyanhydrides. *Chem. Rev.* **2009**, *109*, 5528–5578.
(84) Dechy-Cabaret, O.; Martin-Vaca, B.; Bourissou, D. Controlled Ring-Opening Polymerization of Lactide and Glycolide. *Chem. Rev.* **2004**, *104*, 6147–6176.
(85) Matyjaszewski, K. Atom Transfer Radical Polymerization: From Mechanisms to Applications. *Isr. J. Chem.* **2012**, *52*, 206–220.
(86) Onaca, O.; Enea, R.; Hughes, D. W.; Meier, W. Stimuli-Responsive Polymersomes as Nanocarriers for Drug and Gene Delivery. *Macromol. Biosci.* **2009**, *9*, 129–139.
(87) Lee, J. S.; Feijen, J. Polymersomes for Drug Delivery: Design, Formation and Characterization. *J. Control. Release* **2012**, *161*, 473–483.
(88) Koide, A.; Kishimura, A.; Osada, K.; Jang, W.-D.; Yamasaki, Y.; Kataoka, K. Semipermeable Polymer Vesicle (PICsome) Self-Assembled in Aqueous Medium From a Pair of Oppositely Charged Block Copolymers: Physiologically Stable Micro-/Nanocontainers of Water-Soluble Macromolecules. *J. Am. Chem. Soc.* **2006**, *128*, 5988–5989.
(89) Schatz, C.; Lecommandoux, S. Polysaccharide-Containing Block Copolymers: Synthesis, Properties and Applications of an Emerging Family of Glycoconjugates. *Macromol. Rapid Commun.* **2010**, *31*, 1664–1684.
(90) Schatz, C.; Louguet, S.; Le Meins, J.-F.; Lecommandoux, S. Polysaccharide-Block-Polypeptide Copolymer Vesicles: Towards Synthetic Viral Capsids. *Angew. Chem. Int. Ed.* **2009**, *48*, 2572–2575.
(91) Zhao, L.; Li, N.; Wang, K.; Shi, C.; Zhang, L.; Luan, Y. A Review of Polypeptide-Based Polymersomes. *Biomaterials* **2014**, *35*, 1284–1301.
(92) Egli, S.; Schlaad, H.; Bruns, N.; Meier, W. Functionalization of Block Copolymer Vesicle Surfaces. *Polymers* **2011**, *3*, 252–280.
(93) Pawar, P. V.; Gohil, S. V.; Jain, J. P.; Kumar, N. Functionalized Polymersomes for Biomedical Applications. *Polym. Chem.* **2013**, *4*, 3160–3176.
(94) Salva, R.; Le Meins, J.-F.; Sandre, O.; Brûlet, A.; Schmutz, M.; Guenoun, P.; Lecommandoux, S. Polymersome Shape Transformation at the Nanoscale. *ACS Nano* **2013**, *7*, 9298–9311.
(95) Magde, D.; Elson, E.; Webb, W. W. Thermodynamic Fluctuations in a Reacting System—Measurement by Fluorescence Correlation Spectroscopy. *Phys. Rev. Lett.* **1972**, *29*, 705–708.
(96) Rigler, R.; Mets, Ü.; Widengren, J.; Kask, P. Fluorescence Correlation Spectroscopy with High Count Rate and Low Background: Analysis of Translational Diffusion. *Eur. Biophys. J.* **1993**, *22*, 169–175.
(97) Rigler, P.; Meier, W. Encapsulation of Fluorescent Molecules by Functionalized Polymeric Nanocontainers: Investigation by Confocal Fluorescence Imaging and Fluorescence Correlation Spectroscopy. *J. Am. Chem. Soc.* **2006**, *128*, 367–373.
(98) Bacia, K.; Kim, S. A.; Schwille, P. Fluorescence Cross-Correlation Spectroscopy in Living Cells. *Nat. Methods* **2006**, *3*, 83–89.
(99) Schwille, P.; Haustein, E. Fluorescence Correlation Spectroscopy an Introduction to Its Concepts and Applications. *Anal. Chem.* **2009**, *94*, 1–33.
(100) Shi, X.; Foo, Y. H.; Sudhaharan, T.; Chong, S.-W.; Korzh, V.; Ahmed, S.; Wohland, T. Determination of Dissociation Constants in Living Zebrafish Embryos with Single Wavelength Fluorescence Cross-Correlation Spectroscopy. *Biophys. J.* **2009**, *97*, 678–686.
(101) Elson, E. L. Fluorescence Correlation Spectroscopy: Past, Present, Future. *Biophys. J.* **2011**, *101*, 2855–2870.
(102) Eggeling, C.; Ringemann, C.; Medda, R.; Schwarzmann, G.; Sandhoff, K.; Polyakova, S.; Belov, V. N.; Hein, B.; Middendorff, von, C.; Schönle, A.; *et al.* Direct Observation of the Nanoscale Dynamics of Membrane Lipids in a Living Cell. *Nature* **2009**, *457*, 1159–1162.
(103) Ihle, S.; Onaca, O.; Rigler, P.; Hauer, B.; Rodríguez-Ropero, F.; Fioroni, M.; Schwaneberg, U. Nanocompartments with a pH Release System Based on an

Engineered OmpF Channel Protein. *Soft Matter* **2011**, *7*, 532–539.
(104) Koynov, K.; Butt, H. J. Fluorescence Correlation Spectroscopy in Colloid and Interface Science. *Curr. Opin. Colloid In.* **2012**, *17*, 377–387.
(105) Itel, F.; Najer, A.; Palivan, C. G.; Meier, W. Dynamics of Membrane Proteins Within Synthetic Polymer Membranes with Large Hydrophobic Mismatch. *Nano Lett.* **2015**, *15*, 3871–3878.
(106) Itel, F.; Chami, M.; Najer, A.; Lörcher, S.; Wu, D.; Dinu, I. A.; Meier, W. Molecular Organization and Dynamics in Polymersome Membranes: a Lateral Diffusion Study. *Macromolecules* **2014**, *47*, 7588–7596.
(107) Egli, S.; Nussbaumer, M. G.; Balasubramanian, V.; Chami, M.; Bruns, N.; Palivan, C.; Meier, W. Biocompatible Functionalization of Polymersome Surfaces: a New Approach to Surface Immobilization and Cell Targeting Using Polymersomes. *J. Am. Chem. Soc.* **2011**, *133*, 4476–4483.
(108) Eigen, M.; Rigler, R. Sorting Single Molecules: Application to Diagnostics and Evolutionary Biotechnology. *Proc. Natl. Acad. Sci. USA* **1994**, *91*, 5740–5747.
(109) Einstein, A. Über Die Von Der Molekularkinetischen Theorie Der Wärme Geforderte Bewegung Von in Ruhenden Flüssigkeiten Suspendierten Teilchen. *Annalen der Physik (in German)* **1905**, *322*, 549–560.
(110) Einstein, A. *Investigations on the Theory of the Brownian Movement*; Fürth, R., Ed.; Dover Publications: New York, 1956; pp. 1–119.
(111) Haustein, E.; Schwille, P. Fluorescence Correlation Spectroscopy: Novel Variations of an Established Technique. *Annu. Rev. Biophys. Biomol. Struct.* **2007**, *36*, 151–169.
(112) Kapusta, P. *Absolute Diffusion Coefficients: Compilation of Reference Data for FCS Calibration. Picoquant Application Note*; Picoquant GmbH, 2010; pp. 1–2.
(113) Enderlein, J.; Gregor, I.; Patra, D.; Fitter, J. Art and Artefacts of Fluorescence Correlation Spectroscopy. *Curr. Pharm. Biotechnol.* **2004**, *5*, 155–161.
(114) Tcherniak, A.; Reznik, C.; Link, S.; Landes, C. F. Fluorescence Correlation Spectroscopy: Criteria for Analysis in Complex Systems. *Anal. Chem.* **2009**, *81*, 746–754.
(115) Ries, J.; Petrášek, Z.; García-Sáez, A. J.; Schwille, P. A Comprehensive Framework for Fluorescence Cross-Correlation Spectroscopy. *New J. Phys.* **2010**, *12*, 1–32.
(116) Bacia, K.; Schwille, P. Practical Guidelines for Dual-Color Fluorescence Cross-Correlation Spectroscopy. *Nat. Protoc.* **2007**, *2*, 2842–2856.
(117) Benda, A.; Beneš, M.; Mareček, V.; Lhotský, A.; Hermens, W. T.; Hof, M. How to Determine Diffusion Coefficients in Planar Phospholipid Systems by Confocal Fluorescence Correlation Spectroscopy. *Langmuir* **2003**, *19*, 4120–4126.
(118) Najer, A.; Wu, D.; Vasquez, D.; Palivan, C. G.; Meier, W. Polymer Nanocompartments in Broad-Spectrum Medical Applications. *Nanomedicine (Lond.)* **2013**, *8*, 425–447.
(119) Markovsky, E.; Baabur-Cohen, H.; Eldar-Boock, A.; Omer, L.; Tiram, G.; Ferber, S.; Ofek, P.; Polyak, D.; Scomparin, A.; Satchi-Fainaro, R. Administration, Distribution, Metabolism and Elimination of Polymer Therapeutics. *J. Control. Release* **2012**, *161*, 446–460.
(120) Brinkhuis, R. P.; Stojanov, K.; Laverman, P.; Eilander, J.; Zuhorn, I. S.; Rutjes, F. P. J. T.; van Hest, J. C. M. Size Dependent Biodistribution and SPECT Imaging of 111In-Labeled Polymersomes. *Bioconjugate Chem.* **2012**, *23*, 958–965.
(121) Venkataraman, S.; Hedrick, J. L.; Ong, Z. Y.; Yang, C.; Ee, P. L. R.; Hammond, P. T.; Yang, Y. Y. The Effects of Polymeric Nanostructure Shape on Drug Delivery. *Adv. Drug Deliver. Rev.* **2011**, *63*, 1228–1246.
(122) Lee, J. S.; Ankone, M.; Pieters, E.; Schiffelers, R. M.; Hennink, W. E.; Feijen, J. Circulation Kinetics and Biodistribution of Dual-Labeled Polymersomes with Modulated Surface Charge in Tumor-Bearing Mice: Comparison with Stealth Liposomes. *J. Control. Release* **2011**, *155*, 282–288.
(123) Canton, I.; Battaglia, G. Endocytosis at the Nanoscale. *Chem. Soc. Rev.* **2012**, *41*, 2718–2739.
(124) Jiskoot, W.; Schie, R. M. F.; Carstens, M. G.; Schellekens, H. Immunological Risk of Injectable Drug Delivery Systems. *Pharm. Res.* **2009**, *26*, 1303–1314.
(125) Monnard, P. A. Liposome-Entrapped Polymerases as Models for

Microscale/Nanoscale Bioreactors. *J. Membrane Biol.* **2003**, *191*, 87–97.

(126) Palivan, C. G.; Fischer-Onaca, O.; Delcea, M.; Itel, F.; Meier, W. Protein–Polymer Nanoreactors for Medical Applications. *Chem. Soc. Rev.* **2012**, *41*, 2800–2823.

(127) De Oliveira, H.; Thévenot, J.; Lecommandoux, S. Smart Polymersomes for Therapy and Diagnosis: Fast Progress Toward Multifunctional Biomimetic Nanomedicines. *Wiley Interdiscip. Rev. Nanomed. Nanobiotechnol.* **2012**, *4*, 525–546.

(128) Tanner, P.; Onaca, O.; Balasubramanian, V.; Meier, W.; Palivan, C. G. Enzymatic Cascade Reactions Inside Polymeric Nanocontainers: a Means to Combat Oxidative Stress. *Chem. Eur. J.* **2011**, *17*, 4552–4560.

(129) Vriezema, D. M.; Hoogboom, J.; Velonia, K.; Takazawa, K.; Christianen, P. C. M.; Maan, J. C.; Rowan, A. E.; Nolte, R. J. M. Vesicles and Polymerized Vesicles From Thiophene-Containing Rod-Coil Block Copolymers. *Angew. Chem. Int. Ed. Engl.* **2003**, *42*, 772–776.

(130) Nardin, C.; Thoeni, S.; Widmer, J.; Winterhalter, M.; Meier, W. Nanoreactors Based on (Polymerized) ABA-Triblock Copolymer Vesicles. *Chem. Commun.* **2000**, 1433–1434.

(131) Yamaoka, T.; Tabata, Y.; Ikada, Y. Distribution and Tissue Uptake of Poly (Ethylene Glycol) with Different Molecular Weights After Intravenous Administration to Mice. *J. Pharm. Sci.* **1994**, *83*, 601–606.

(132) Cabane, E.; Zhang, X.; Langowska, K.; Palivan, C. G.; Meier, W. Stimuli-Responsive Polymers and Their Applications in Nanomedicine. *Biointerphases* **2012**, *7*, 1–27.

(133) Schappacher, M.; Soum, A.; Guillaume, S. M. Synthesis of Polyester−Polypeptide Diblock and Triblock Copolymers Using Amino Poly(E-Caprolactone) Macroinitiators. *Biomacromolecules* **2006**, *7*, 1373–1379.

(134) Soo Choi, H.; Liu, W.; Misra, P.; Tanaka, E.; Zimmer, J. P.; Itty Ipe, B.; Bawendi, M. G.; Frangioni, J. V. Renal Clearance of Quantum Dots. *Nat. Biotechnol.* **2007**, *25*, 1165–1170.

(135) Balasubramanian, V.; Onaca, O.; Ezhevskaya, M.; Van Doorslaer, S.; Sivasankaran, B.; Palivan, C. G. A Surprising System: Polymeric Nanoreactors Containing a Mimic with Dual-Enzyme Activity. *Soft Matter* **2011**, *7*, 5595–5603.

(136) Nardin, C.; Hirt, T.; Leukel, J.; Meier, W. Polymerized ABA Triblock Copolymer Vesicles. *Langmuir* **2000**, *16*, 1035–1041.

(137) Trubetskoy, V. S.; Torchilin, V. P. Use of Polyoxyethylene-Lipid Conjugates as Long-Circulating Carriers for Delivery of Therapeutic and Diagnostic Agents. *Adv. Drug Deliver. Rev.* **1995**, *16*, 311–320.

(138) Immordino, M. L.; Dosio, F.; Cattel, L. Stealth Liposomes: Review of the Basic Science, Rationale, and Clinical Applications, Existing and Potential. *Int. J. Nanomed.* **2006**, *1*, 297–315.

(139) Knop, K.; Hoogenboom, R.; Fischer, D.; Schubert, U. S. Poly(Ethylene Glycol) in Drug Delivery: Pros and Cons as Well as Potential Alternatives. *Angew. Chem. Int. Ed.* **2010**, *49*, 6288–6308.

(140) Barz, M.; Luxenhofer, R.; Zentel, R.; Vicent, M. J. Overcoming the PEG-Addiction: Well-Defined Alternatives to PEG, From Structure–Property Relationships to Better Defined Therapeutics. *Polym. Chem.* **2011**, *2*, 1900–1918.

(141) Adams, N.; Schubert, U. S. Poly(2-Oxazolines) in Biological and Biomedical Application Contexts. *Adv. Drug Deliver. Rev.* **2007**, *59*, 1504–1520.

(142) Murdoch, C.; Reeves, K. J.; Hearnden, V.; Colley, H.; Massignani, M.; Canton, I.; Madsen, J.; Blanazs, A.; Armes, S. P.; Lewis, A. L.; *et al.* Internalization and Biodistribution of Polymersomes Into Oral Squamous Cell Carcinoma Cells in Vitro and in Vivo. *Nanomedicine (Lond.)* **2010**, *5*, 1025–1036.

(143) Hu, C. M. J.; Zhang, L.; Aryal, S.; Cheung, C.; Fang, R. H.; Zhang, L. Erythrocyte Membrane-Camouflaged Polymeric Nanoparticles as a Biomimetic Delivery Platform. *Proc. Natl. Acad. Sci. USA* **2011**, *108*, 10980–10985.

(144) Christian, D. A.; Garbuzenko, O. B.; Minko, T.; Discher, D. E. Polymer Vesicles with a Red Cell-Like Surface Charge: Microvascular Imaging and in Vivo Tracking with Near-Infrared Fluorescence. *Macromol. Rapid Commun.* **2010**,

31, 135–141.
(145) Kim, Y.; Tewari, M.; Pajerowski, J. D.; Cai, S.; Sen, S.; Williams, J.; Sirsi, S.; Lutz, G.; Discher, D. E. Polymersome Delivery of siRNA and Antisense Oligonucleotides. *J. Control. Release* **2009**, *134*, 132–140.
(146) Matsumura, Y.; Maeda, H. A New Concept for Macromolecular Therapeutics in Cancer Chemotherapy: Mechanism of Tumoritropic Accumulation of Proteins and the Antitumor Agent Smancs. *Cancer Res.* **1986**, *46*, 6387–6392.
(147) Alexis, F.; Pridgen, E.; Molnar, L. K.; Farokhzad, O. C. Factors Affecting the Clearance and Biodistribution of Polymeric Nanoparticles. *Mol. Pharmaceutics* **2008**, *5*, 505–515.
(148) Moghimi, S.; Hunter, A. Long-Circulating and Target-Specific Nanoparticles: Theory to Practice. *Pharmacol. Rev.* **2001**, *53*, 283–312.
(149) Petros, R. A.; DeSimone, J. M. Strategies in the Design of Nanoparticles for Therapeutic Applications. *Nat. Rev. Drug Discov.* **2010**, *9*, 615–627.
(150) Brinkhuis, R. P.; Rutjes, F. P. J. T.; van Hest, J. C. M. Polymeric Vesicles in Biomedical Applications. *Polym. Chem.* **2011**, *2*, 1449–1462.
(151) Anraku, Y.; Kishimura, A.; Kobayashi, A.; Oba, M.; Kataoka, K. Size-Controlled Long-Circulating PICsome as a Ruler to Measure Critical Cut-Off Disposition Size Into Normal and Tumor Tissues. *Chem. Commun.* **2011**, *47*, 6054–6056.
(152) Yang, X.; Grailer, J. J.; Rowland, I. J.; Javadi, A.; Hurley, S. A.; Steeber, D. A.; Gong, S. Multifunctional SPIO/DOX-Loaded Wormlike Polymer Vesicles for Cancer Therapy and MR Imaging. *Biomaterials* **2010**, *31*, 9065–9073.
(153) Saad, M.; Garbuzenko, O. B.; Ber, E.; Chandna, P.; Khandare, J. J.; Pozharov, V. P.; Minko, T. Receptor Targeted Polymers, Dendrimers, Liposomes: Which Nanocarrier Is the Most Efficient for Tumor-Specific Treatment and Imaging? *J. Control. Release* **2008**, *130*, 107–114.
(154) Kataoka, K.; Harada, A.; Nagasaki, Y. Block Copolymer Micelles for Drug Delivery: Design, Characterization and Biological Significance. *Adv. Drug Deliver. Rev.* **2001**, *47*, 113–131.
(155) Gaucher, G.; Dufresne, M.-H.; Sant, V. P.; Kang, N.; Maysinger, D.; Leroux, J.-C. Block Copolymer Micelles: Preparation, Characterization and Application in Drug Delivery. *J. Control. Release* **2005**, *109*, 169–188.
(156) Zhang, Q.; Re Ko, N.; Kwon Oh, J. Recent Advances in Stimuli-Responsive Degradable Block Copolymer Micelles: Synthesis and Controlled Drug Delivery Applications. *Chem. Commun.* **2012**, *48*, 7542–7552.
(157) Eetezadi, S.; Ekdawi, S. N.; Allen, C. The Challenges Facing Block Copolymer Micelles for Cancer Therapy: in Vivo Barriers and Clinical Translation. *Adv. Drug Deliver. Rev.* **2015**, *91*, 7–22.
(158) Renggli, K.; Baumann, P.; Langowska, K.; Onaca, O.; Bruns, N.; Meier, W. Selective and Responsive Nanoreactors. *Adv. Funct. Mater.* **2011**, *21*, 1241–1259.
(159) Peters, R. J. R. W.; Louzao, I.; van Hest, J. C. M. From Polymeric Nanoreactors to Artificial Organelles. *Chem. Sci.* **2012**, *3*, 335–342.
(160) van Oers, M. C. M.; Rutjes, F. P. J. T.; van Hest, J. C. M. Cascade Reactions in Nanoreactors. *Curr. Opin. Biotech.* **2014**, *28*, 10–16.
(161) Marguet, M.; Bonduelle, C.; Lecommandoux, S. Multicompartmentalized Polymeric Systems: Towards Biomimetic Cellular Structure and Function. *Chem. Soc. Rev.* **2012**, *42*, 512–529.
(162) Meng, F.; Zhong, Z. Polymersomes Spanning From Nano- to Microscales: Advanced Vehicles for Controlled Drug Delivery and Robust Vesicles for Virus and Cell Mimicking. *J. Phys. Chem. Lett.* **2011**, *2*, 1533–1539.
(163) Gaitzsch, J.; Appelhans, D.; Wang, L.; Battaglia, G.; Voit, B. Synthetic Bio-Nanoreactor: Mechanical and Chemical Control of Polymersome Membrane Permeability. *Angew. Chem. Int. Ed.* **2012**, *51*, 4448–4451.
(164) Spulber, M.; Najer, A.; Winkelbach, K.; Glaied, O.; Waser, M.; Pieles, U.; Meier, W.; Bruns, N. Photoreaction of a Hydroxyalkyphenone with the Membrane of Polymersomes: a Versatile Method to Generate Semipermeable Nanoreactors. *J. Am. Chem. Soc.* **2013**, *135*, 9204–9212.
(165) Ranquin, A.; Versées, W.; Meier, W.; Steyaert, J.; Van Gelder, P. Therapeutic Nanoreactors: Combining Chemistry and Biology in a Novel Triblock Copolymer Drug Delivery System. *Nano Lett.* **2005**, *5*, 2220–2224.

(166) Choi, H.-J.; Montemagno, C. D. Artificial Organelle: ATP Synthesis From Cellular Mimetic Polymersomes. *Nano Lett.* **2005**, *5*, 2538–2542.
(167) van Dongen, S. F. M.; Nallani, M.; Cornelissen, J. J. L. M.; Nolte, R. J. M.; van Hest, J. C. M. A Three-Enzyme Cascade Reaction Through Positional Assembly of Enzymes in a Polymersome Nanoreactor. *Chem. Eur. J.* **2008**, *15*, 1107–1114.
(168) Peters, R. J. R. W.; Marguet, M.; Marais, S.; Fraaije, M. W.; van Hest, J. C. M.; Lecommandoux, S. Cascade Reactions in Multicompartmentalized Polymersomes. *Angew. Chem. Int. Ed.* **2013**, *53*, 146–150.
(169) Martino, C.; Kim, S.-H.; Horsfall, L.; Abbaspourrad, A.; Rosser, S. J.; Cooper, J.; Weitz, D. A. Protein Expression, Aggregation, and Triggered Release From Polymersomes as Artificial Cell-Like Structures. *Angew. Chem. Int. Ed.* **2012**, *51*, 6416–6420.
(170) Langowska, K.; Palivan, C. G.; Meier, W. Polymer Nanoreactors Shown to Produce and Release Antibiotics Locally. *Chem. Commun.* **2013**, *49*, 128–130.
(171) Tanner, P.; Egli, S.; Balasubramanian, V.; Onaca, O.; Palivan, C. G.; Meier, W. Can Polymeric Vesicles That Confine Enzymatic Reactions Act as Simplified Organelles? *FEBS Lett.* **2011**, *585*, 1699–1706.
(172) Tanner, P.; Balasubramanian, V.; Palivan, C. G. Aiding Nature'S Organelles: Artificial Peroxisomes Play Their Role. *Nano Lett.* **2013**, *13*, 2875–2883.
(173) Ben-Haim, N.; Broz, P.; Marsch, S.; Meier, W.; Hunziker, P. Cell-Specific Integration of Artificial Organelles Based on Functionalized Polymer Vesicles. *Nano Lett.* **2008**, *8*, 1368–1373.
(174) Hammer, D. A.; Kamat, N. P. Towards an Artificial Cell. *FEBS Lett.* **2012**, *586*, 2882–2890.
(175) Marguet, M.; Edembe, L.; Lecommandoux, S. Polymersomes in Polymersomes: Multiple Loading and Permeability Control. *Angew. Chem. Int. Ed.* **2011**, *51*, 1173–1176.
(176) Marguet, M.; Sandre, O.; Lecommandoux, S. Polymersomes in "Gelly" Polymersomes: Toward Structural Cell Mimicry. *Langmuir* **2012**, *28*, 2035–2043.
(177) Wilson, D. A.; Nolte, R. J. M.; van Hest, J. C. M. Autonomous Movement of Platinum-Loaded Stomatocytes. *Nat. Chem.* **2012**, *4*, 268–274.
(178) Couvreur, P.; Vauthier, C. Nanotechnology: Intelligent Design to Treat Complex Disease. *Pharm. Res.* **2006**, *23*, 1417–1450.
(179) Huh, A. J.; Kwon, Y. J. "Nanoantibiotics": a New Paradigm for Treating Infectious Diseases Using Nanomaterials in the Antibiotics Resistant Era. *J. Control. Release* **2011**, *156*, 128–145.
(180) Brooks, B. D.; Brooks, A. E. Therapeutic Strategies to Combat Antibiotic Resistance. *Adv. Drug Deliver. Rev.* **2014**, *78*, 14–27.
(181) Mammen, M.; Choi, S. K. Polyvalent Interactions in Biological Systems: Implications for Design and Use of Multivalent Ligands and Inhibitors. *Angew. Chem. Int. Ed.* **1998**, *37*, 2754–2794.
(182) Baram-Pinto, D.; Shukla, S.; Gedanken, A.; Sarid, R. Inhibition of HSV-1 Attachment, Entry, and Cell-to-Cell Spread by Functionalized Multivalent Gold Nanoparticles. *Small* **2010**, *6*, 1044–1050.
(183) Bricarello, D. A.; Patel, M. A.; Parikh, A. N. Inhibiting Host–Pathogen Interactions Using Membrane-Based Nanostructures. *Trends Biotechnol.* **2012**, *30*, 323–330.
(184) Krachler, A. M.; Orth, K. Targeting the Bacteria-Host Interface: Strategies in Anti-Adhesion Therapy. *Virulence* **2013**, *4*, 284–294.
(185) Vonnemann, J.; Liese, S.; Kuehne, C.; Ludwig, K.; Dernedde, J.; Böttcher, C.; Netz, R. R.; Haag, R. Size Dependence of Steric Shielding and Multivalency Effects for Globular Binding Inhibitors. *J. Am. Chem. Soc.* **2015**, *137*, 2572–2579.
(186) Zaman, M.; Good, M. F.; Toth, I. Nanovaccines and Their Mode of Action. *Methods* **2013**, *60*, 226–231.
(187) Fang, R. H.; Zhang, L. Nanoparticle-Based Modulation of the Immune System. *Annu. Rev. Chem. Biomol. Eng.* **2016**, *7*, 1–22.
(188) Haas, S.; Hain, N.; Raoufi, M.; Handschuh-Wang, S.; Wang, T.; Jiang, X.; Schönherr, H. Enzyme Degradable Polymersomes From Hyaluronic Acid-Block-Poly(E-Caprolactone) Copolymers for the Detection of Enzymes of

Pathogenic Bacteria. *Biomacromolecules* **2015**, *16*, 832–841.
(189) Lane, D. D.; Su, F. Y.; Chiu, D. Y.; Srinivasan, S.; Wilson, J. T.; Ratner, D. M.; Stayton, P. S.; Convertine, A. J. Dynamic Intracellular Delivery of Antibiotics via pH-Responsive Polymersomes. *Polym. Chem.* **2015**, *6*, 1255–1266.
(190) Wayakanon, K.; Thornhill, M. H.; Douglas, C. W. I.; Lewis, A. L.; Warren, N. J.; Pinnock, A.; Armes, S. P.; Battaglia, G.; Murdoch, C. Polymersome-Mediated Intracellular Delivery of Antibiotics to Treat Porphyromonas Gingivalis-Infected Oral Epithelial Cells. *The FASEB Journal* **2013**, *27*, 4455–4465.
(191) Zhou, C.; Wang, M.; Zou, K.; Chen, J.; Zhu, Y.; Du, J. Antibacterial Polypeptide-Grafted Chitosan-Based Nanocapsules as an "Armed" Carrier of Anticancer and Antiepileptic Drugs. *ACS Macro Lett.* **2013**, *2*, 1021–1025.
(192) Savina, A.; Amigorena, S. Phagocytosis and Antigen Presentation in Dendritic Cells. *Immunol. Rev.* **2007**, *219*, 143–156.
(193) Scott, E. A.; Stano, A.; Gillard, M.; Maio-Liu, A. C.; Swartz, M. A.; Hubbell, J. A. Dendritic Cell Activation and T Cell Priming with Adjuvant- and Antigen-Loaded Oxidation-Sensitive Polymersomes. *Biomaterials* **2012**, *33*, 6211–6219.
(194) Lukianova-Hleb, E. Y.; Campbell, K. M.; Constantinou, P. E.; Braam, J.; Olson, J. S.; Ware, R. E.; Sullivan, D. J.; Lapotko, D. O. Hemozoin-Generated Vapor Nanobubbles for Transdermal Reagent- and Needle-Free Detection of Malaria. *Proc. Natl. Acad. Sci. USA* **2014**, *111*, 900–905.
(195) Santos-Magalhães, N. S.; Mosqueira, V. C. F. Nanotechnology Applied to the Treatment of Malaria. *Adv. Drug Deliver. Rev.* **2010**, *62*, 560–575.
(196) Dennis, E.; Peoples, V. A.; Johnson, F. Utilizing Nanotechnology to Combat Malaria. *J. Infect. Dis. Ther.* **2015**, *3*, 1–6.
(197) Aditya, N. P.; Vathsala, P. G.; Vieira, V.; Murthy, R. S. R.; Souto, E. B. Advances in Nanomedicines for Malaria Treatment. *Adv. Colloid Interfac.* **2013**, *201-202*, 1–17.
(198) Kuntworbe, N.; Martini, N.; Shaw, J.; Al-Kassas, R. Malaria Intervention Policies and Pharmaceutical Nanotechnology as a Potential Tool for Malaria Management. *Drug Dev. Res.* **2012**, *73*, 167–184.
(199) Tyagi, R. K.; Garg, N. K.; Sahu, T. Vaccination Strategies Against Malaria: Novel Carrier(S) More Than a Tour De Force. *J. Control. Release* **2012**, *162*, 242–254.
(200) Burkhard, P.; Lanar, D. E. Malaria Vaccine Based on Self-Assembling Protein Nanoparticles. *Expert Rev. Vaccines* **2015**, *14*, 1525–1527.
(201) Movellan, J.; Urbán, P.; Moles, E.; la Fuente, de, J. M.; Sierra, T.; Serrano, J. L.; Fernàndez-Busquets, X. Biomaterials. *Biomaterials* **2014**, *35*, 7940–7950.
(202) Pouvelle, B.; Gormley, J. A.; Taraschi, T. F. Characterization of Trafficking Pathways and Membrane Genesis in Malaria-Infected Erythrocytes. *Mol. Biochem. Parasitol.* **1994**, *66*, 83–96.
(203) Urbán, P.; Estelrich, J.; Cortés, A.; Fernàndez-Busquets, X. A Nanovector with Complete Discrimination for Targeted Delivery to Plasmodium Falciparum-Infected Versus Non-Infected Red Blood Cells in Vitro. *J. Control. Release* **2011**, *151*, 202–211.
(204) Urbán, P.; Estelrich, J.; Adeva, A.; Cortés, A.; Fernàndez-Busquets, X. Study of the Efficacy of Antimalarial Drugs Delivered Inside Targeted Immunoliposomal Nanovectors. *Nanoscale Res. Lett.* **2011**, *6*, 620–630.
(205) Moles, E.; Urbán, P.; Jiménez-Díaz, M. B.; Viera-Morilla, S.; Angulo-Barturen, I.; Busquets, M. A.; Fernàndez-Busquets, X. Immunoliposome-Mediated Drug Delivery to Plasmodium-Infected and Non-Infected Red Blood Cells as a Dual Therapeutic/Prophylactic Antimalarial Strategy. *J. Control. Release* **2015**, *210*, 217–229.
(206) Kirk, K. Membrane Transport in the Malaria-Infected Erythrocyte. *Physiol. Rev.* **2001**, *81*, 495–537.
(207) Marques, J.; Moles, E.; Urbán, P.; Prohens, R.; Busquets, M. A.; Sevrin, C.; Grandfils, C.; Fernàndez-Busquets, X. Application of Heparin as a Dual Agent with Antimalarial and Liposome Targeting Activities Toward Plasmodium-Infected Red Blood Cells. *Nanomed.-Nanotechnol.* **2014**, *10*, 1719–1728.
(208) Moles, E.; Fernàndez-Busquets, X. Loading Antimalarial Drugs Into Noninfected Red Blood Cells: an Undesirable Roommate for Plasmodium. *Future Med. Chem.* **2015**, *7*, 833–835.
(209) Isacchi, B.; Arrigucci, S.; Marca, G. L.; Bergonzi, M. C.; Vannucchi, M. G.;

Novelli, A.; Bilia, A. R. Conventional and Long-Circulating Liposomes of Artemisinin: Preparation, Characterization, and Pharmacokinetic Profile in Mice. *J. Lipos. Res.* **2011**, *21*, 237–244.

(210) Isacchi, B.; Bergonzi, M. C.; Grazioso, M.; Righeschi, C.; Pietretti, A.; Severini, C.; Bilia, A. R. Artemisinin and Artemisinin Plus Curcumin Liposomal Formulations: Enhanced Antimalarial Efficacy Against Plasmodium Berghei-Infected Mice. *Eur. J. Pharm. Biopharm.* **2012**, *80*, 528–534.

(211) Waknine-Grinberg, J. H.; Even-Chen, S.; Avichzer, J.; Turjeman, K.; Bentura-Marciano, A.; Haynes, R. K.; Weiss, L.; Allon, N.; Ovadia, H.; Golenser, J.; *et al.* Glucocorticosteroids in Nano-Sterically Stabilized Liposomes Are Efficacious for Elimination of the Acute Symptoms of Experimental Cerebral Malaria. *PLoS ONE* **2013**, *8*, e72722.

(212) Guo, J.; Waknine-Grinberg, J. H.; Mitchell, A. J.; Barenholz, Y.; Golenser, J. Reduction of Experimental Cerebral Malaria and Its Related Proinflammatory Responses by the Novel Liposome-Based B-Methasone Nanodrug. *BioMed Res. Int.* **2014**, *2014*, 1–8.

(213) Mura, S.; Nicolas, J.; Couvreur, P. Stimuli-Responsive Nanocarriers for Drug Delivery. *Nat. Mater.* **2013**, *12*, 991–1003.

(214) Kasozi, D.; Mohring, F.; Rahlfs, S.; Meyer, A. J.; Becker, K. Real-Time Imaging of the Intracellular Glutathione Redox Potential in the Malaria Parasite Plasmodium Falciparum. *PLoS Pathog.* **2013**, *9*, e1003782.

(215) Schafer, F. Q.; Buettner, G. R. Redox Environment of the Cell as Viewed Through the Redox State of the Glutathione Disulfide/Glutathione Couple. *Free Radic. Biol. Med.* **2001**, *30*, 1191–1212.

(216) Dubois, V. L.; Platel, D. F.; Pauly, G.; Tribouley-Duret, J. Plasmodium Berghei: Implication of Intracellular Glutathione and Its Related Enzyme in Chloroquine Resistance in Vivo. *Exp. Parasitol.* **1995**, *81*, 117–124.

(217) Vega-Rodríguez, J.; Pastrana-Mena, R.; Crespo-Lladó, K. N.; Ortiz, J. G.; Ferrer-Rodríguez, I.; Serrano, A. E. Implications of Glutathione Levels in the Plasmodium Berghei Response to Chloroquine and Artemisinin. *PLoS ONE* **2015**, *10*, e0128212.

(218) Paaijmans, K.; Fernàndez-Busquets, X. Antimalarial Drug Delivery to the Mosquito: an Option Worth Exploring? *Future Microbiol.* **2014**, *9*, 579–582.

(219) Reed, S. G.; Orr, M. T.; Fox, C. B. Key Roles of Adjuvants in Modern Vaccines. *Nat. Med.* **2013**, *19*, 1597–1608.

(220) Vekemans, J.; Leach, A.; Cohen, J. Development of the RTS,S/as Malaria Candidate Vaccine. *Vaccine* **2009**, *27S*, G67–G71.

(221) Mueller, M. S.; Renard, A.; Boato, F.; Vogel, D.; Naegeli, M.; Zurbriggen, R.; Robinson, J. A.; Pluschke, G. Induction of Parasite Growth-Inhibitory Antibodies by a Virosomal Formulation of a Peptidomimetic of Loop I From Domain III of Plasmodium Falciparum Apical Membrane Antigen 1. *Infect. Immun.* **2003**, *71*, 4749–4758.

(222) Draper, S. J.; Angov, E.; Horii, T.; Miller, L. H.; Srinivasan, P.; Theisen, M.; Biswas, S. Recent Advances in Recombinant Protein-Based Malaria Vaccines. *Vaccine* **2015**, *33*, 7433–7443.

(223) Vaughan, A. M.; Kappe, S. H. Malaria Vaccine Development: Persistent Challenges. *Curr. Opin. Immunol.* **2012**, *24*, 324–331.

(224) Bartlett, A. H.; Park, P. W. Heparan Sulfate Proteoglycans in Infection. In *Glycans in Diseases and Therapeutics*; Pavao, M. S. G., Ed.; Springer-Verlag: Berlin Heidelberg, 2011; pp. 31–62.

(225) Najer, A.; Wu, D.; Bieri, A.; Brand, F.; Palivan, C. G.; Beck, H.-P.; Meier, W. Nanomimics of Host Cell Membranes Block Invasion and Expose Invasive Malaria Parasites. *ACS Nano* **2014**, *8*, 12560–12571.

(226) Morens, D. M.; Folkers, G. K.; Fauci, A. S. The Challenge of Emerging and Re-Emerging Infectious Diseases. *Nature* **2004**, *430*, 242–249.

(227) Ashley, E. A.; Dhorda, M.; Fairhurst, R. M.; Amaratunga, C.; Lim, P.; Suon, S.; Sreng, S.; Anderson, J. M.; Mao, S.; Sam, B.; *et al.* Spread of Artemisinin Resistance in *Plasmodium Falciparum* Malaria. *N. Engl. J. Med.* **2014**, *371*, 411–423.

(228) World Health Organization. *World Health Statistics 2012*; World Health Organization, Geneva, 2012; pp. 1–176.

(229) McCormick, C. J.; Tuckwell, D. S.; Crisanti, A.; Humphries, M. J.; Hollingdale, M. R. Identification of Heparin as a Ligand for the a-Domain of *Plasmodium Falciparum* Thrombospondin-Related Adhesion Protein. *Mol. Biochem. Parasitol.* **1999**, *100*, 111–124.

(230) Vogt, A. M.; Barragan, A.; Chen, Q.; Kironde, F.; Spillmann, D.; Wahlgren, M. Heparan Sulfate on Endothelial Cells Mediates the Binding of *Plasmodium Falciparum*-Infected Erythrocytes via the DBL1alpha Domain of PfEMP1. *Blood* **2003**, *101*, 2405–2411.

(231) Vogt, A. M.; Pettersson, F.; Moll, K.; Jonsson, C.; Normark, J.; Ribacke, U.; Egwang, T. G.; Ekre, H.-P.; Spillmann, D.; Chen, Q. Release of Sequestered Malaria Parasites Upon Injection of a Glycosaminoglycan. *PLoS Pathog*. **2006**, *2*, 853–863.

(232) Adams, Y.; Freeman, C.; Schwartz-Albiez, R.; Ferro, V.; Parish, C. R.; Andrews, K. T. Inhibition of Plasmodium Falciparum Growth in Vitro and Adhesion to Chondroitin-4-Sulfate by the Heparan Sulfate Mimetic PI-88 and Other Sulfated Oligosaccharides. *Antimicrob. Agents Ch.* **2006**, *50*, 2850–2852.

(233) Hirsh, J.; Anand, S. S.; Halperin, J. L.; Fuster, V. Guide to Anticoagulant Therapy: Heparin : a Statement for Healthcare Professionals From the American Heart Association. *Circulation* **2001**, *103*, 2994–3018.

(234) Xiao, L.; Yang, C.; Patterson, P. S.; Udhayakumar, V.; Lal, A. A. Sulfated Polyanions Inhibit Invasion of Erythrocytes by Plasmodial Merozoites and Cytoadherence of Endothelial Cells to Parasitized Erythrocytes. *Infect. Immun.* **1996**, *64*, 1373–1378.

(235) Doolan, D. L.; Dobano, C.; Baird, J. K. Acquired Immunity to Malaria. *Clin. Microbiol. Rev.* **2009**, *22*, 13–36.

(236) Srinivasan, P.; Yasgar, A.; Luci, D. K.; Beatty, W. L.; Hu, X.; Andersen, J.; Narum, D. L.; Moch, J. K.; Sun, H.; Haynes, J. D.; *et al.* Disrupting Malaria Parasite AMA1-RON2 Interaction with a Small Molecule Prevents Erythrocyte Invasion. *Nat. Commun.* **2013**, *4*, 2261–2270.

(237) The RTS,S Clinical Trials Partnership. A Phase 3 Trial of RTS,S/AS01 Malaria Vaccine in African Infants. *N. Engl. J. Med.* **2012**, *367*, 2284–2295.

(238) Ewer, K. J.; O'Hara, G. A.; Duncan, C. J. A.; Collins, K. A.; Sheehy, S. H.; Reyes-Sandoval, A.; Goodman, A. L.; Edwards, N. J.; Elias, S. C.; Halstead, F. D.; *et al.* Protective $CD8^+$ T-Cell Immunity to Human Malaria Induced by Chimpanzee Adenovirus-MVA Immunisation. *Nat. Commun.* **2013**, *4*, 2836–2846.

(239) Look, M.; Bandyopadhyay, A.; Blum, J. S.; Fahmy, T. M. Application of Nanotechnologies for Improved Immune Response Against Infectious Diseases in the Developing World. *Adv. Drug Deliver. Rev.* **2010**, *62*, 378–393.

(240) Discher, B. M.; Won, Y.-Y.; Ege, D. S.; Lee, J. C.; Bates, F. S.; Discher, D. E.; Hammer, D. A. Polymersomes: Tough Vesicles Made From Diblock Copolymers. *Science* **1999**, *284*, 1143–1146.

(241) Graff, A.; Sauer, M.; Van Gelder, P.; Meier, W. Virus-Assisted Loading of Polymer Nanocontainer. *Proc. Natl. Acad. Sci. USA* **2002**, *99*, 5064–5068.

(242) Nazemi, A.; Haeryfar, S. M. M.; Gillies, E. R. Multifunctional Dendritic Sialopolymersomes as Potential Antiviral Agents: Their Lectin Binding and Drug Release Properties. *Langmuir* **2013**, *29*, 6420–6428.

(243) Passirani, C.; Barratt, G.; Devissaguet, J.-P.; Labarre, D. Long-Circulating Nanoparticles Bearing Heparin or Dextran Covalently Bound to Poly (Methyl Methacrylate). *Pharm. Res.* **1998**, *15*, 1046–1050.

(244) Zhang, J.; Shin, M. C.; David, A. E.; Zhou, J.; Lee, K.; He, H.; Yang, V. C. Long-Circulating Heparin-Functionalized Magnetic Nanoparticles for Potential Application as a Protein Drug Delivery Platform. *Mol. Pharmaceutics* **2013**, *10*, 3892–3902.

(245) Kumar, M.; Grzelakowski, M.; Zilles, J.; Clark, M.; Meier, W. Highly Permeable Polymeric Membranes Based on the Incorporation of the Functional Water Channel Protein Aquaporin Z. *Proc. Natl. Acad. Sci. USA* **2007**, *104*, 20719–20724.

(246) Liu, J.; Pervin, A.; Gallo, C. M.; Desai, U. R.; Van Gorp, C. L.; Linhardt, R. J. New Approaches for the Preparation of Hydrophobic Heparin Derivatives. *J. Pharm. Sci.* **1994**, *83*, 1034–1039.

(247) Sato, S.; Sakamoto, T.; Miyazawa, E.; Kikugawa, Y. One-Pot Reductive

Amination of Aldehydes and Ketones with A-Picoline-Borane in Methanol, in Water, and in Neat Conditions. *Tetrahedron* **2004**, *60*, 7899–7906.

(248) Stauch, O.; Schubert, R.; Savin, G.; Burchard, W. Structure of Artificial Cytoskeleton Containing Liposomes in Aqueous Solution Studied by Static and Dynamic Light Scattering. *Biomacromolecules* **2002**, *3*, 565–578.

(249) Boyle, M. J.; Wilson, D. W.; Richards, J. S.; Riglar, D. T.; Tetteh, K. K.; Conway, D. J.; Ralph, S. A.; Baum, J.; Beeson, J. G. Isolation of Viable Plasmodium Falciparum Merozoites to Define Erythrocyte Invasion Events and Advance Vaccine and Drug Development. *Proc. Natl. Acad. Sci. USA* **2010**, *107*, 14378–14383.

(250) Persson, K. E. M.; Lee, C. T.; Marsh, K.; Beeson, J. G. Development and Optimization of High-Throughput Methods to Measure *Plasmodium Falciparum*-Specific Growth Inhibitory Antibodies. *J. Clin. Microbiol.* **2006**, *44*, 1665–1673.

(251) Bijker, E. M.; Bastiaens, G. J.; Teirlinck, A. C.; van Gemert, G. J.; Graumans, W.; van de Vegte-Bolmer, M.; Siebelink-Stoter, R.; Arens, T.; Teelen, K.; Nahrendorf, W. Protection Against Malaria After Immunization by Chloroquine Prophylaxis and Sporozoites Is Mediated by Preerythrocytic Immunity. *Proc. Natl. Acad. Sci. USA* **2013**, *110*, 7862–7867.

(252) Najer, A.; Thamboo, S.; Duskey, J. T.; Palivan, C. G.; Beck, H.-P.; Meier, W. Analysis of Molecular Parameters Determining the Antimalarial Activity of Polymer-Based Nanomimics. *Macromol. Rapid Commun.* **2015**, *36*, 1923–1928.

(253) Feng, A.; Yuan, J. Smart Nanocontainers: Progress on Novel Stimuli-Responsive Polymer Vesicles. *Macromol. Rapid Commun.* **2014**, *35*, 767–779.

(254) Yildiz, U. H.; De Hoog, H.-P. M.; Fu, Z.; Tomczak, N.; Parikh, A. N.; Nallani, M.; Liedberg, B. Third-Party ATP Sensing in Polymersomes: a Label-Free Assay of Enzyme Reactions in Vesicular Compartments. *Small* **2013**, *10*, 442–447.

(255) Lomora, M.; Itel, F.; Dinu, I. A.; Palivan, C. G. Selective Ion-Permeable Membranes by Insertion of Biopores Into Polymersomes. *Phys. Chem. Chem. Phys.* **2015**, *17*, 15538–15546.

(256) The RTS,S Clinical Trials Partnership. Efficacy and Safety of RTS,S/AS01 Malaria Vaccine with or Without a Booster Dose in Infants and Children in Africa: Final Results of a Phase 3, Individually Randomised, Controlled Trial. *The Lancet* **2015**, *386*, 31–45.

(257) World Health Organization. World Health Statistics 2014. *World Health Organization, Geneva* **2014**, 1–177.

(258) Kim, S. A.; Heinze, K. G.; Bacia, K.; Waxham, M. N.; Schwille, P. Two-Photon Cross-Correlation Analysis of Intracellular Reactions with Variable Stoichiometry. *Biophys. J.* **2005**, *88*, 4319–4336.

(259) Sasaki, A.; Kinjo, M. Monitoring Intracellular Degradation of Exogenous DNA Using Diffusion Properties. *J. Control. Release* **2010**, *143*, 104–111.

(260) Najer, A.; Thamboo, S.; Palivan, C. G.; Beck, H.-P.; Meier, W. Giant Host Red Blood Cell Membrane Mimicking Polymersomes Bind Parasite Proteins and Malaria Parasites. *CHIMIA* **2016**, *70*, 288–291.

(261) Alban, S. Adverse Effects of Heparin. In *Handbook of Experimental Pharmacology*; Lever, R.; Mulloy, B.; Page, C. P., Eds.; Springer-Verlag Berlin Heidelberg, 2012; Vol. 207, pp. 211–264.

(262) World Health Organization. Severe and Complicated Malaria. World Health Organization Malaria Action Programme. *Trans. Roy. Soc. Trop. Med. Hyg.* **1986**, *80 (suppl.)*, 3–50.

(263) Osmond, R. I. W.; Kett, W. C.; Skett, S. E.; Coombe, D. R. Protein-Heparin Interactions Measured by BIAcore 2000 Are Affected by the Method of Heparin Immobilization. *Anal. Biochem.* **2002**, *310*, 199–207.

(264) Gorbet, M. B.; Sefton, M. V. Endotoxin: the Uninvited Guest. *Biomaterials* **2005**, *26*, 6811–6817.

(265) Dobrovolskaia, M. A.; Neun, B. W.; Clogston, J. D.; Ding, H.; Ljubimova, J.; McNeil, S. E. Ambiguities in Applying Traditional LimulusAmebocyte Lysate Tests to Quantify Endotoxin in Nanoparticle Formulations. *Nanomedicine (Lond.)* **2010**, *5*, 555–562.

(266) Scientific Support, U. S. Overcoming Assay Inhibition or Enhancement. *Lonza*

Walkersville Inc. **2012**, 1–3.
(267) Scientific Support, U. S. Limulus Amebocyte Lysate (LAL) Kinetic-QCL. *Lonza Walkersville Inc.* **2014**, 1–17.
(268) Goodman, A. L.; Forbes, E. K.; Williams, A. R.; Douglas, A. D.; de Cassan, S. C.; Bauza, K.; Biswas, S.; Dicks, M. D. J.; Llewellyn, D.; Moore, A. C.; *et al.* The Utility of Plasmodium Berghei as a Rodent Model for Anti-Merozoite Malaria Vaccine Assessment. *Sci. Rep.* **2013**, *3*, 1–13.
(269) Marques, J.; Vilanova, E.; Mourão, P. A. S.; Fernàndez-Busquets, X. Marine Organism Sulfated Polysaccharides Exhibiting Significant Antimalarial Activity and Inhibition of Red Blood Cell Invasionby. *Sci. Rep.* **2016**, *6*, 1–14.
(270) Najer, A.; Wu, D.; Nussbaumer, M. G.; Schwertz, G.; Schwab, A.; Witschel, M. C.; Schäfer, A.; Diederich, F.; Rottmann, M.; Palivan, C. G.; *et al.* An Amphiphilic Graft Copolymer-Based Nanoparticle Platform for Reduction-Responsive Anticancer and Antimalarial Drug Delivery. *Submitted* **2016**, 1–31.
(271) Tibbitt, M. W.; Dahlman, J. E.; Langer, R. Emerging Frontiers in Drug Delivery. *J. Am. Chem. Soc.* **2016**, *138*, 704–717.
(272) Torchilin, V. P. Multifunctional Nanocarriers. *Adv. Drug Deliver. Rev.* **2012**, *64*, 302–315.
(273) Cheng, C. J.; Tietjen, G. T.; Saucier-Sawyer, J. K. A Holistic Approach to Targeting Disease with Polymeric Nanoparticles. *Nat. Rev. Drug Discov.* **2015**, *14*, 239–247.
(274) Fang, J.; Nakamura, H.; Maeda, H. The EPR Effect: Unique Features of Tumor Blood Vessels for Drug Delivery, Factors Involved, and Limitations and Augmentation of the Effect. *Adv. Drug Deliver. Rev.* **2011**, *63*, 136–151.
(275) Cabral, H.; Makino, J.; Matsumoto, Y.; Mi, P.; Wu, H.; Nomoto, T.; Toh, K.; Yamada, N.; Higuchi, Y.; Konishi, S.; *et al.* Systemic Targeting of Lymph Node Metastasis Through the Blood Vascular System by Using Size-Controlled Nanocarriers. *ACS Nano* **2015**, *9*, 4957–4967.
(276) Wu, D.; Spulber, M.; Itel, F.; Chami, M.; Pfohl, T.; Palivan, C. G.; Meier, W. Effect of Molecular Parameters on the Architecture and Membrane Properties of 3D Assemblies of Amphiphilic Copolymers. *Macromolecules* **2014**, *47*, 5060–5069.
(277) Oerlemans, C.; Bult, W.; Bos, M.; Storm, G.; Nijsen, J. F. W.; Hennink, W. E. Polymeric Micelles in Anticancer Therapy: Targeting, Imaging and Triggered Release. *Pharm. Res.* **2010**, *27*, 2569–2589.
(278) Nicolas, J.; Mura, S.; Brambilla, D.; Mackiewicz, N.; Couvreur, P. Design, Functionalization Strategies and Biomedical Applications of Targeted Biodegradable/Biocompatible Polymer-Based Nanocarriers for Drug Delivery. *Chem. Soc. Rev.* **2013**, *42*, 1147–1235.
(279) Hoogenboom, R. Poly(2-Oxazoline)S: a Polymer Class with Numerous Potential Applications. *Angew. Chem. Int. Ed.* **2009**, *48*, 7978–7994.
(280) Lu, Y.; Sun, W.; Gu, Z. Stimuli-Responsive Nanomaterials for Therapeutic Protein Delivery. *J. Control. Release* **2014**, *194*, 1–19.
(281) Torchilin, V. P. Multifunctional, Stimuli-Sensitive Nanoparticulate Systems for Drug Delivery. *Nat. Rev. Drug Discov.* **2014**, *13*, 813–827.
(282) Kim, H. J.; Miyata, K.; Nomoto, T.; Zheng, M.; Kim, A.; Liu, X.; Cabral, H.; Christie, R. J.; Nishiyama, N.; Kataoka, K. siRNA Delivery From Triblock Copolymer Micelles with Spatially-Ordered Compartments of PEG Shell, siRNA-Loaded Intermediate Layer, and Hydrophobic Core. *Biomaterials* **2014**, *35*, 4548–4556.
(283) Li, Y.; Liu, T.; Zhang, G.; Ge, Z.; Liu, S. Tumor-Targeted Redox-Responsive Nonviral Gene Delivery Nanocarriers Based on Neutral-Cationic Brush Block Copolymers. *Macromol. Rapid Commun.* **2014**, *35*, 466–473.
(284) Yu, S.; Ding, J.; He, C.; Cao, Y.; Xu, W.; Chen, X. Disulfide Cross-Linked Polyurethane Micelles as a Reduction-Triggered Drug Delivery System for Cancer Therapy. *Adv. Healthcare Mater.* **2013**, *3*, 752–760.
(285) Huo, M.; Yuan, J.; Tao, L.; Wei, Y. Redox-Responsive Polymers for Drug Delivery: From Molecular Design to Applications. *Polym. Chem.* **2014**, *5*, 1519–1528.
(286) Thambi, T.; Deepagan, V. G.; Ko, H.; Suh, Y. D.; Yi, G.-R.; Lee, J. Y.; Lee, D. S.; Park, J. H. Biostable and Bioreducible Polymersomes for Intracellular Delivery

of Doxorubicin. *Polym. Chem.* **2014**, *5*, 4627–4634.
(287) Zhang, Q.; Aleksanian, S.; Noh, S. M.; Oh, J. K. Thiol-Responsive Block Copolymer Nanocarriers Exhibiting Tunable Release with Morphology Changes. *Polym. Chem.* **2013**, *4*, 351–359.
(288) Cheng, R.; Feng, F.; Meng, F.; Deng, C.; Feijen, J.; Zhong, Z. Glutathione-Responsive Nano-Vehicles as a Promising Platform for Targeted Intracellular Drug and Gene Delivery. *J. Control. Release* **2011**, *152*, 2–12.
(289) Narvekar, M.; Xue, H. Y.; Eoh, J. Y.; Wong, H. L. Nanocarrier for Poorly Water-Soluble Anticancer Drugs—Barriers of Translation and Solutions. *AAPS PharmSciTech* **2014**, *15*, 822–833.
(290) Witschel, M.; Rottmann, M.; Kaiser, M.; Brun, R. Agrochemicals Against Malaria, Sleeping Sickness, Leishmaniasis and Chagas Disease. *PLoS Negl. Trop. Dis.* **2012**, *6*, e1805.
(291) Witschel, M. C.; Rottmann, M.; Schwab, A.; Leartsakulpanich, U.; Chitnumsub, P.; Seet, M.; Tonazzi, S.; Schwertz, G.; Stelzer, F.; Mietzner, T.; *et al.* Inhibitors of Plasmodial Serine Hydroxymethyltransferase (SHMT): Cocrystal Structures of Pyrazolopyrans with Potent Blood- and Liver-Stage Activities. *J. Med. Chem.* **2015**, *58*, 3117–3130.
(292) Toughraï, S.; Malinova, V.; Masciadri, R.; Menon, S.; Tanner, P.; Palivan, C.; Bruns, N.; Meier, W. Reduction-Sensitive Amphiphilic Triblock Copolymers Self-Assemble Into Stimuli-Responsive Micelles for Drug Delivery. *Macromol. Biosci.* **2015**, *15*, 481–489.
(293) Jackson, K. E.; Klonis, N.; Ferguson, D. J. P.; Adisa, A.; Dogovski, C.; Tilley, L. Food Vacuole-Associated Lipid Bodies and Heterogeneous Lipid Environments in the Malaria Parasite, Plasmodium Falciparum. *Mol. Microbiol.* **2004**, *54*, 109–122.
(294) Nzila, A.; Okombo, J.; Becker, R. P.; Chilengi, R.; Lang, T.; Niehues, T. Anticancer Agents Against Malaria: Time to Revisit? *Trends Parasitol.* **2010**, *26*, 125–129.
(295) Hooft van Huijsduijnen, R.; Guy, R. K.; Chibale, K.; Haynes, R. K.; Peitz, I.; Kelter, G.; Phillips, M. A.; Vennerstrom, J. L.; Yuthavong, Y.; Wells, T. N. C. Anticancer Properties of Distinct Antimalarial Drug Classes. *PLoS ONE* **2013**, *8*, e82962.
(296) Alonso, P. L.; Brown, G.; Arevalo-Herrera, M.; Binka, F.; Chitnis, C.; Collins, F.; Doumbo, O. K.; Greenwood, B.; Hall, B. F.; Levine, M. M.; *et al.* A Research Agenda to Underpin Malaria Eradication. *PLoS Med.* **2011**, *8*, e1000406.
(297) Howes, R. E.; Piel, F. B.; Patil, A. P.; Nyangiri, O. A.; Gething, P. W.; Dewi, M.; Hogg, M. M.; Battle, K. E.; Padilla, C. D.; Baird, J. K.; *et al.* G6PD Deficiency Prevalence and Estimates of Affected Populations in Malaria Endemic Countries: a Geostatistical Model-Based Map. *PLoS Med.* **2012**, *9*, e1001339.
(298) Baird, J. K. Primaquine Toxicity Forestalls Effective Therapeutic Management of the Endemic Malarias. *Int. J. Parasitol.* **2012**, *42*, 1049–1054.
(299) Angelova, M. I.; Dimitrov, D. S. Liposome Electroformation. *Faraday Discuss. Chem. Soc.* **1986**, *81*, 303–311.
(300) Farndale, R. W.; Sayers, C. A.; Barrett, A. J. A Direct Spectrophotometric Microassay for Sulfated Glycosaminoglycans in Cartilage Cultures. *Connect. Tissue Res.* **1982**, *9*, 247–248.
(301) Barbosa, I.; Garcia, S.; Barbier-Chassefière, V.; Caruelle, J.-P.; Martelly, I.; Papy-García, D. Improved and Simple Micro Assay for Sulfated Glycosaminoglycans Quantification in Biological Extracts and Its Use in Skin and Muscle Tissue Studies. *Glycobiology* **2003**, *13*, 647–653.
(302) Kim, B.-S.; Hong, D.-J.; Bae, J.; Lee, M. Controlled Self-Assembly of Carbohydrate Conjugate Rod−Coil Amphiphiles for Supramolecular Multivalent Ligands. *J. Am. Chem. Soc.* **2005**, *127*, 16333–16337.
(303) Hulme, E. C.; Trevethick, M. A. Ligand Binding Assays at Equilibrium: Validation and Interpretation. *Brit. J. Pharmacol.* **2010**, *161*, 1219–1237.
(304) Mphande, F.; Nilsson, S.; Bolad, A. Culturing of Erythrocytic Asexual Stages of Plasmodium Falciparum and P. Vivax. In *Methods in malaria research*; Ljungström, I.; Moll, K.; Perlmann, H.; Scherf, A.; Wahlgren, M., Eds.; MR4/ATCC: Manassas, 2008; pp. 1–10.
(305) Dorn, A.; Stoffel, R.; Matile, H.; Bubendorf, A.; Ridley, R. G. Malarial

Haemozoin/B-Haematin Supports Haem Polymerization in the Absence of Protein. *Nature* **1995**, *374*, 269–271.

(306) Lambros, C.; Vanderberg, J. P. Synchronization of Plasmodium Falciparum Erythrocytic Stages in Culture. *J. Parasitol.* **1979**, *65*, 418–420.

(307) Huber, W.; Koella, J. C. A Comparison of Three Methods of Estimating EC50 in Studies of Drug Resistance of Malaria Parasites. *Acta Trop.* **1993**, *55*, 257–261.

(308) Rivadeneira, E. M.; Wasserman, M.; Espinal, C. T. Separation and Concentration of Schizonts of Plasmodium Falciparum by Percoll Gradients. *J. Protozool.* **1983**, *30*, 367–370.

(309) Tokuyasu, K. T. A Technique for Ultracryotomy of Cell Suspensions and Tissues. *J. Cell Biol.* **1973**, *57*, 551–565.

(310) Gustafsson, M. G. Surpassing the Lateral Resolution Limit by a Factor of Two Using Structured Illumination Microscopy. *J. Microsc.* **2000**, *198*, 82–87.

(311) Schermelleh, L.; Carlton, P. M.; Haase, S.; Shao, L.; Winoto, L.; Kner, P.; Burke, B.; Cardoso, M. C.; Agard, D. A.; Gustafsson, M. G. L.; *et al.* Subdiffraction Multicolor Imaging of the Nuclear Periphery with 3D Structured Illumination Microscopy. *Science* **2008**, *320*, 1332–1336.

ACKNOWLEDGMENTS

First of all, I would like to kindly thank my PhD supervisor Prof. Dr. Wolfgang Meier for the opportunity to do my PhD research in his group, providing an excellent environment for fruitful research. Next, I am very grateful to my PhD co-supervisors Prof. Dr. Cornelia G. Palivan and Prof. Dr. Hans-Peter Beck (Swiss Tropical and Public Health Institute) for many advises, interesting discussions, and assistance in writing manuscripts. I am also greatly honored that Prof. Dr. Abhay Pandit (National University of Ireland, Galway) accepted to be the co-referee for my PhD thesis; go raibh míle maith agat!

Furthermore, I would like to greatly acknowledge the nice and productive group atmospheres I have met in both, the chemistry laboratories and at the Swiss Tropical and Public Health Institute. Many people were involved in these projects; without them this progress would have never happened. I would like to extend my sincerest thanks and appreciation to everyone who has been involved, especially people who I forgot to mention herein.

I would like to kindly thank our great chemists Dr. Dalin Wu, Sven Kasper, and Samuel Lörcher for synthesizing PMOXA-*g*(SS)-PCL, PMOXA-*b*-PCL, and PMOXA-*b*-PDMS-*b*-PMOXA and for inspiring discussions. For cell experiments with HeLa cells I would like to thank Dr. Jason T. Duskey, Dr. Martin G. Nussbaumer, and Sagana Thamboo. Mihai Lomora is thanked for help with stopped-flow measurements. Dr. Severin J. Sigg and Pascal Richard are thanked for collaboration on the MRI-project. Andrej Bieri (C-CINA, University of Basel) is acknowledged for cryo-TEM imaging. I also thank the two master students I supervised during my PhD thesis, Alexandra Wiesler and Sagana Thamboo, for their hard work and I wish them all the best for their own PhD thesis.

From the Swiss TPH, I would like to thank Dr. Sebastian Rusch for assistance with *Plasmodium* cultures and performing mouse experiments showing preliminary "vaccine-like" action. Françoise Brand is kindly acknowledged for TEM preparation and imaging of parasite-nanomimic complexes. Then, I greatly thank Dr. Matthias Rottmann for nice discussions and for organizing part of the *in vitro*

and *in vivo* tests with malaria models, and his team, including Anja Schäfer, Christoph Fischli, and Ursula Lehmann, for performing the experiments.

Dr. Evelina Angov (Division of Malaria Vaccine Development, Walter Reed Army Institute of Research, Silver Spring, MD, USA) is kindly acknowledged for providing *Pf*MSP1$_{42}$. I further thank the Imaging Core Facility (IMCF, University of Basel), and in particular Dr. Alexia Isabelle Loynton-Ferrand for technical assistance provided on the OMX microscope. Prof. H. Stahlberg (C-CINA, University of Basel) is acknowledged for providing access to electron microscopes. Prof. Dimitrios Tsakiris (University Hospital) is thanked for anticoagulation tests. Gabriele Persy, Vesna Olivieri and Ursula Sauder are thanked for assistance on TEMs. My mentor on FCS/FCCS, Dr. Per Rigler (Zeiss AG), is kindly thanked for introducing me to these interesting techniques and many interesting discussions. Dr. Peter Eckard (Unitectra) is thanked for help with patenting. The collaborators on the drug delivery project, Geoffrey Schwertz (ETHZ), Anatol Schwab (ETHZ), Matthias C. Witschel (BASF), and Prof. François Diederich (ETHZ), are kindly acknowledged for synthesizing and providing the SHMT inhibitor (±)-**1** and discussions on the manuscript.

Tobias Najer is thanked for designing the artistic illustration of the concepts and creating the layout of this thesis (Tobias Najer Grafikdesign + Illustration). Dr. Bernard A. Goodman (Guangxi University), Dr. Lionel Maurizi, Dr. Jens Gaitzsch, Dr. Gesine Gunkel-Grabole, Elliot Smith, and Dr. Cora-Ann Schönenberger are thanked for proofreading manuscripts and parts of this thesis.

The Swiss National Science Foundation, NCCR “Molecular Systems Engineering”, and the University of Basel are kindly acknowledged for financial support.

Finally, I would like to thank my family, and especially my parents Roland and Luzia Najer-Stadelmann, for the unlimited support they have given me throughout my whole life. I further thank all my friends, and especially my flat mates for a wonderful PhD time. At the very end, I wish to thank my lovely girlfriend Franziska Stampfli for all the support she has given me also during difficult and stressful times.

Big thanks to everyone again!